THE GEOLOGICAL SOCIETY OF AMERICA

BULLETIN

ISSN 0016-7606 VOLUME 114 NUMBER 3 MARCH 2002

IN THIS ISSUE:
Syntectonic deposits and punctuated limb rotation in a submarine fold

Syntectonic deposits and punctuated limb rotation in an Albian submarine transpressional fold (Mutriku village, Basque-Cantabrian basin, northern Spain)

L.M. Agirrezabala*
Estratigrafia eta Paleontologia Saila, Euskal Herriko Unibertsitatea, 644 postakutxa, 48080 Bilbao, Spain

H.G. Owen
Natural History Museum, Cromwell Road, London SW7 5BD, UK

J. García-Mondéjar
Estratigrafia eta Paleontologia Saila, Euskal Herriko Unibertsitatea, 644 postakutxa, 48080 Bilbao, Spain

ABSTRACT

Deep-water syntectonic deposits and angular unconformities record the denudation and deformation history of the middle Cretaceous Aitzeta structure, interpreted here as a monoclinal syncline associated with the high-angle reverse Mutriku fault (Basque-Cantabrian basin, northern Spain). Sedimentological and structural analyses, combined with a precise chronostratigraphy based on ammonites, permit us to document in detail the history of this syncline during ~0.53 m.y. (Late Albian, *Callihoplites auritus* Subzone). Tectonism occurred during two major and two minor short-lived pulses. The sedimentary signatures of these pulses include unconformities and resedimented deposits derived from the uplifted rocks, showing inverted clast stratigraphy. In contrast, intervening phases of tectonic calm were characterized by gentle hemipelagic sedimentation. The major tectonic pulses were characterized by strong rotation and uplift of the syncline limb. The two major pulses coincided with the lower and upper limits of the *auritus* Subzone, respectively, and resulted in the following limb-rotation and uplift values: 42° and 250 m in the first pulse and 66° and 100–140 m in the second pulse. A maximum duration of 0.12 m.y. for each major pulse has been calculated, from which limb-rotation and uplift rates of 0.35°/k.y. and 2.08 m/k.y. (first pulse) and 0.55°/k.y. and 0.83–1.16 m/k.y. (second pulse) are estimated. Growth strata and angular unconformity geometries, temporal variation of deformation rates, and bedding-parallel faulting indicate folding by progressive limb rotation and associated flexural slip. Local northwest-southeast compression is deduced in formation of the Aitzeta syncline. The presence of bedding-parallel oblique faulting and minor drag folds suggests a component of right-oblique movement along the Mutriku fault.

Keywords: Albian, Basque, folding, rates, sedimentation, transpression.

INTRODUCTION

Precisely dated deposits that correlate with the growth of tectonic structures provide a record of deformation histories. In the peri-Atlantic Mesozoic Basque-Cantabrian basin, northern Spain (Boillot and Malod, 1988), the deposition of deep-water strata and the development of angular unconformities flanking the Albian Aitzeta structure (Figs. 1 and 2) permit us to establish its deformation history. This local structure appears on a geologic map as a fossilized homoclinal overturned succession and is interpreted here as the overturned limb of a fault-related monoclinal syncline with a buried hinge. Biostratigraphical data, based on ammonites and foraminifera, provide a high-resolution temporal framework, which is used to both reconstruct the depositional and deformation history and to determine deformation rates in the Aitzeta structure.

Fault-related growth folds and linked growth strata have been widely documented in Cenozoic foreland basins. Fewer cases have been reported from strike-slip basins. Field and modeling studies support two contrasting, geometrically based kinematic models: instantaneous limb rotation and progressive limb rotation. The former model is based upon kink-band migration and displays constant dips on the fold limbs (Suppe, 1983; Suppe et al., 1997). The second model produces limb rotation and increasing limb dips during growth (Riba, 1976; Holl and Anastasio, 1993; Hardy and Poblet, 1994; Vergés et al., 1996; Schneider et al., 1996). In the case of the Cretaceous Aitzeta syncline, the geometry of its preserved growth strata suggests an origin of progressive limb rotation. However, this geometry was produced by repeated pulses of nearly instantaneous limb rotation that are recorded in angular unconformities in syntectonic sedimentary deposits.

This study is based on detailed sedimentological and structural mapping at 1:5000 scale, measurements of stratigraphic sections, biostratigraphic dating of sedimentary units, facies analysis, and construction of structural cross sections. The major tectonic phases recognized within the Aitzeta area occurred during a period of ~0.53 m.y. (*Callihoplites auritus* ammonite Subzone of the European province zonation of the late Albian). The estimated local compressive deformation took place in a general strike-slip regime (Choukroune and Mattauer, 1978). Thus, this example will be useful for comparison with deformation rates in similar regimes, both modern and ancient.

*E-mail: gppagmul@lg.ehu.es.

GSA Bulletin; March 2002; v. 114; no. 3; p. 281–297; 12 figures; 3 tables.

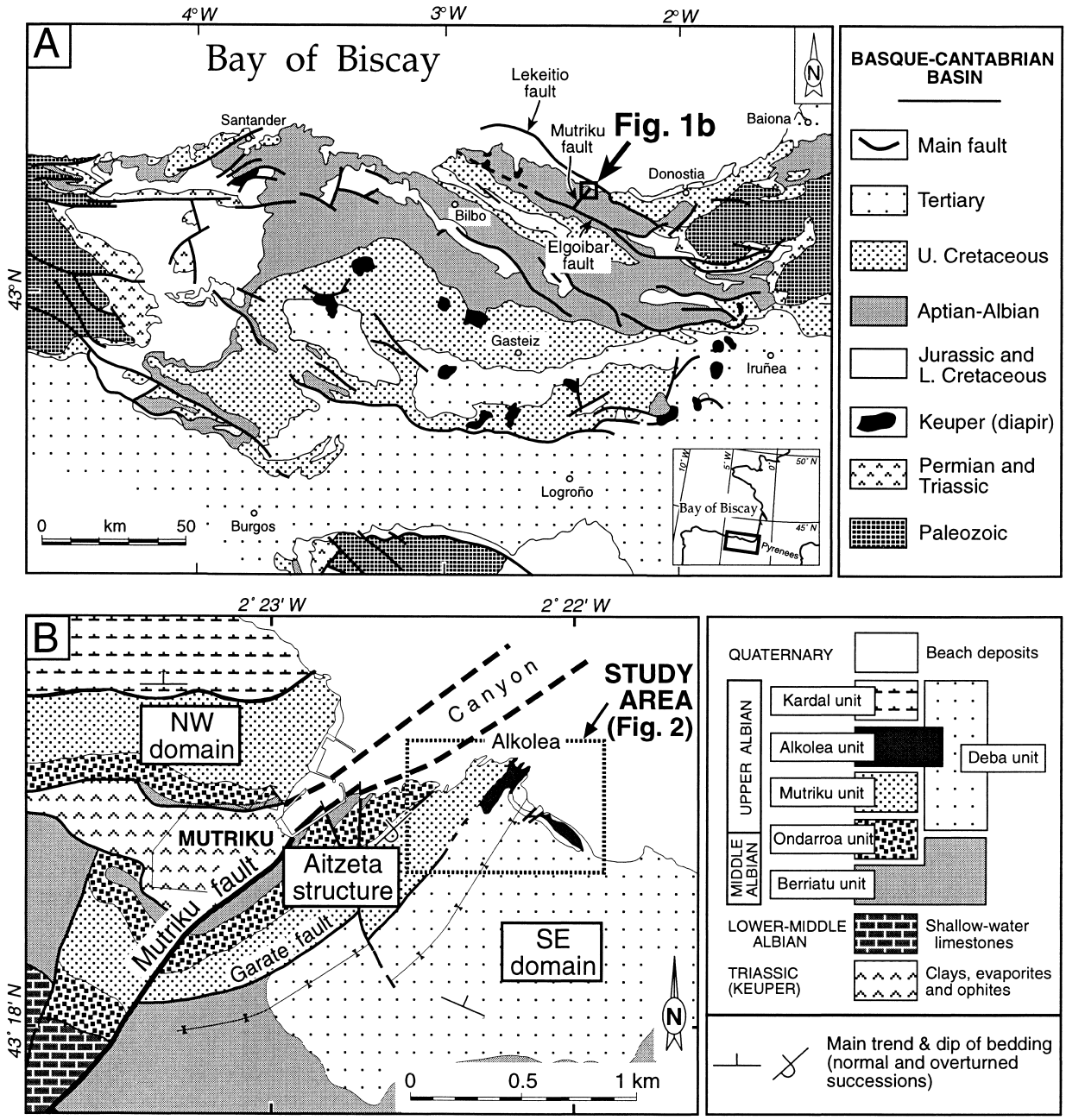

Figure 1. (A) Simplified geologic map of the Basque-Cantabrian region with location of B. (B) Simplified geologic map of the Mutriku area. The square indicates the area of study (Fig. 2).

GEOLOGIC SETTING

The Aitzeta structure is located close to the coastal Mutriku village in the northeastern part of the Basque-Cantabrian region (Fig. 1). During Cretaceous time the area was located on the southwestern European plate margin, which was created by oblique opening of the Bay of Biscay rift. This rift was affected by major sinistral strike-slip deformation (e.g., Choukroune and Mattauer, 1978), which included the development of short-lived compressional tectonic structures like Aitzeta.

In map view, the Aitzeta structure appears as a fossilized overturned homocline, interpreted here as the rotated limb of a monoclinal syncline (Figs. 1 and 2). It reaches 2 km (minimum) in strike length and 0.5 km (maximum) in dip-direction width and strikes northeast. The high-angle Mutriku and Garate faults separate the Aitzeta structure from two little-deformed domains, one to the northwest and another to the southeast (Fig. 1B). A cover of syntectonic deposits overlaps the eastern margin of the structure. These deposits record the punctuated growth of the Aitzeta syncline during the late Albian *auritus* Subzone, a time interval of ~0.53 m.y.

Tertiary deformation was relatively weak in the study area (Figs. 1 and 2). It consisted of (1) reactivation of the Cretaceous Mutriku fault and diapirism of Triassic evaporites, (2) reactivation of the monoclinal syncline and

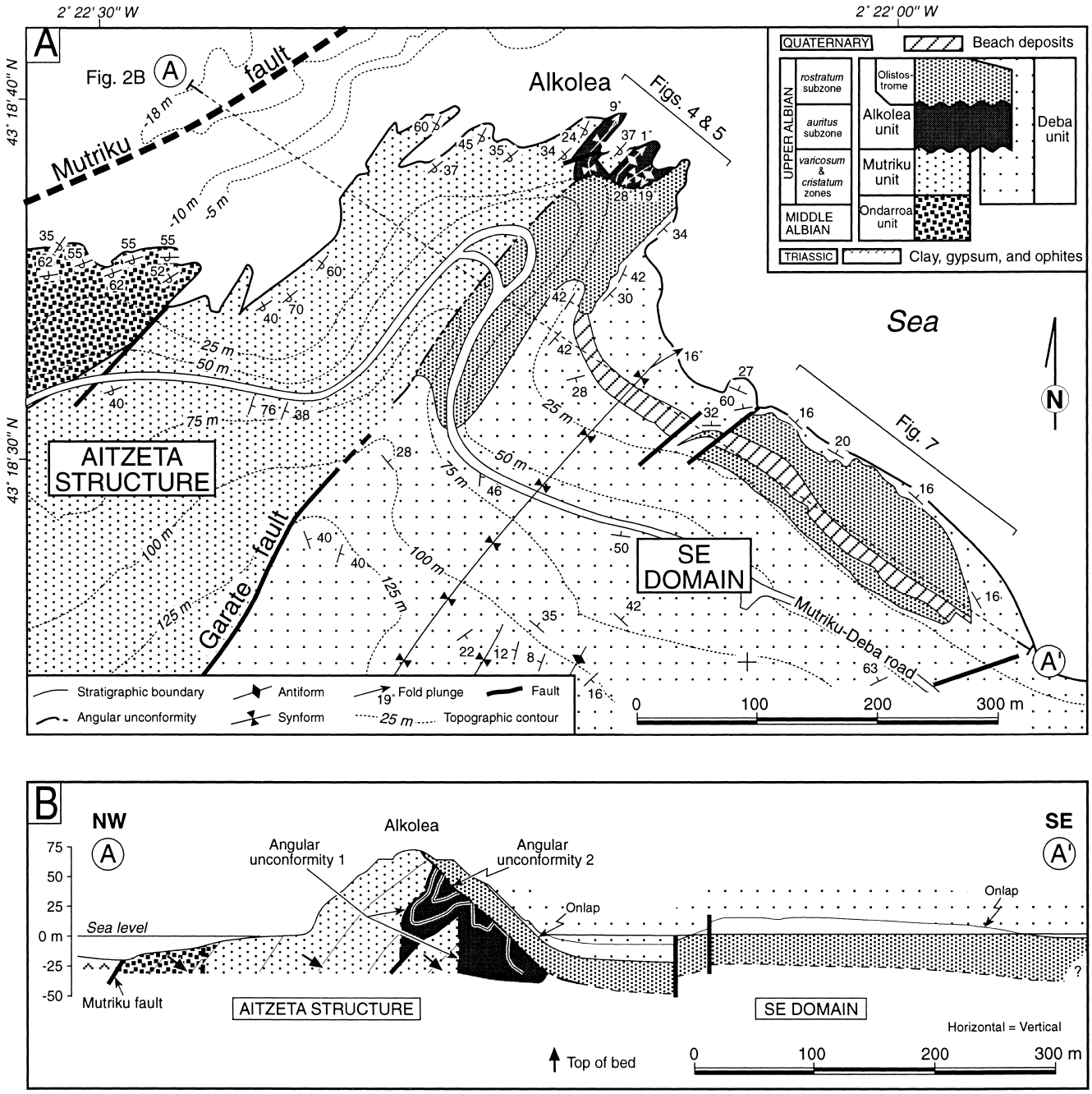

Figure 2. (A) Geologic map of the study area, showing locations of Figures 2B, 4, 5, and 7. (B) Noninterpretive shallow A–A′ cross section. The submarine northwesternmost part has been projected from coastal data. Bold arrows in B indicate tops of beds.

tilting of its hinge line (average plunge: 23° toward 073°), and (3) appearance of northeast-trending minor faults and gentle folds of meter to decameter scale. This paper focuses on the late Albian deformation.

STRATIGRAPHY

Figure 3 shows two representative stratigraphic sections of the study area in both the Aitzeta and southeast domains. Five lithostratigraphic units of Middle Albian–Late Albian age (Berriatu, Ondarroa, Mutriku, Alkolea, and Deba, respectively) are recognized (Table 1). Complex stratigraphy and geometric relationships among the units are observed in the key outcrop of Alkolea point (Figs. 2, 4, and 5). The units are composed of the following main lithofacies: Berriatu unit—marls, limestone megabreccias, lutites, and sandstones; Ondarroa unit—siliciclastic conglomerates, sandstones, and lutites; Mutriku unit—bioturbated muddy sandstones; Alkolea unit—megabreccias, marls, and limestones (Figs. 4 and 6, A–C, and Table 2); and Deba unit—alternating sandstones and lutites (Figs. 6D and 7).

The units are grouped into three distinct sequences: An early middle Albian (*Lyelliceras lyelli* Subzone) to early late Albian (*Hysteroceras varicosum* Zone) pretectonic sequence,

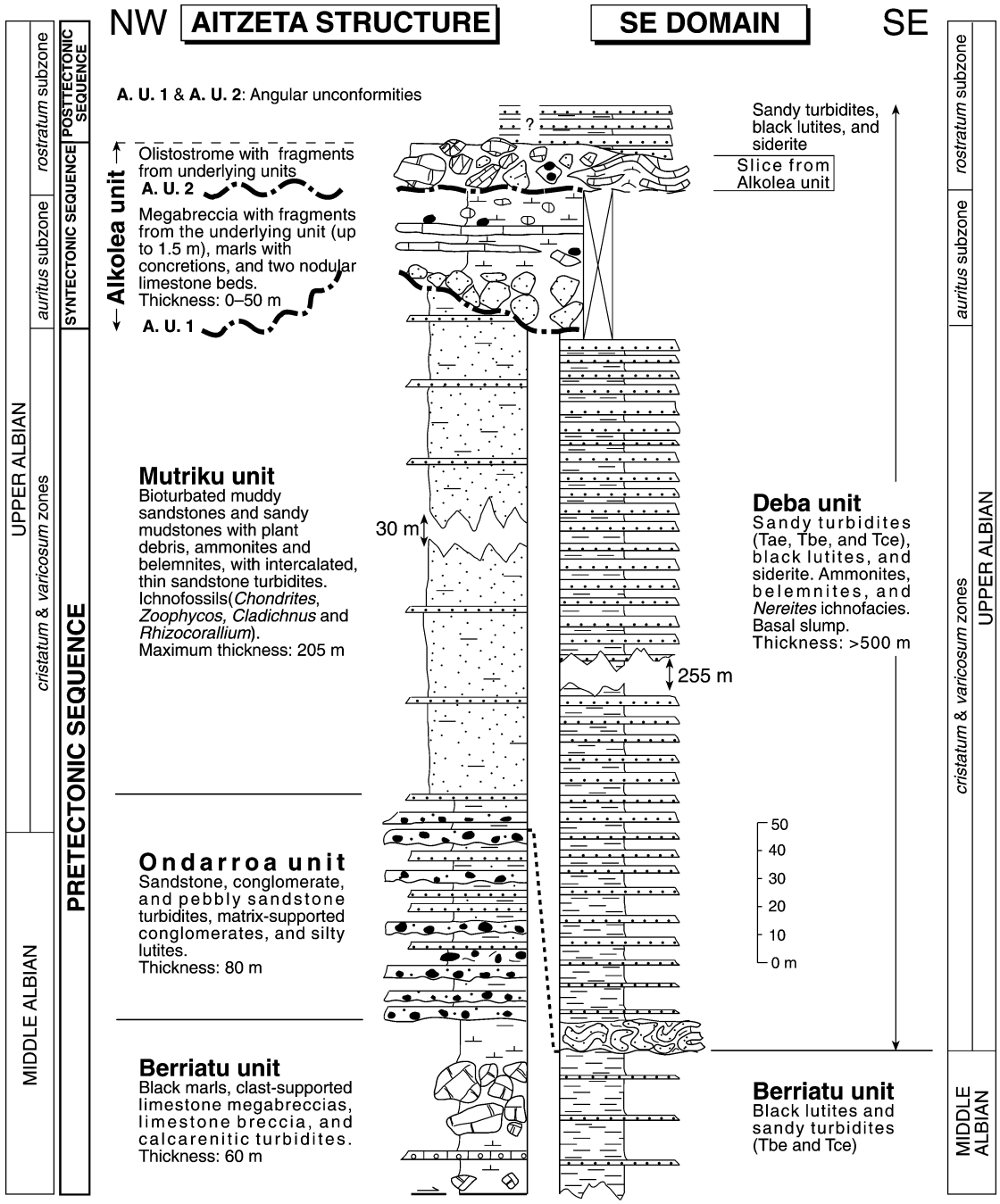

Figure 3. Schematic stratigraphic sections of the Aitzeta structure and southeast domain, with indication of pretectonic, syntectonic, and posttectonic sequences; ammonite biozonation; and angular unconformities. Sbz.—subzone, SQ.—sequence, syntect.

a middle late Albian (*Callihoplites auritus* Subzone) syntectonic sequence, and a late late Albian (*Mortoniceras rostratum* Subzone) posttectonic sequence. We utilize the prefixes pre-, syn-, and post- to refer to the phases of tectonic development of the Aitzeta structure and the succession of sedimentary sequences deposited during those phases. The syntectonic sequence reflects the main phase of deformation and creation of the Aitzeta structure, and that sequence is described in detail in this paper. Accurate chronostratigraphy of the sedimentary units is based on ammonites and foraminifera fossils and is given in the faunal Appendix Table A1. The ammonite zonation for the late Albian used here follows that given in López-Horgue et al. (1999) for the northern Tethyan region. The exception to this approach is the use of the European province *Callihoplites auritus* Subzone (= *Mortoniceras (Mortoniceras) inflatum* Zone sensu stricto of the Tethyan zonation). The exception is used to facilitate discussion of the chronometry and the tectonic phases in relation to the dating work of Gradstein et al. (1994). Stratigraphy of the area has been established in Agirrezabala (1996). Dating, description, and interpretation of the sequences, units, and subunits are summarized in the Table 1.

TABLE 1. SEQUENCES, UNITS, AND SUBUNITS

Sequences, units, and subunits and dating interpretation	Description	Interpretation
Pretectonic sequence		
Berriatu unit Early middle Albian (*L. lyelli* Subzone)	>60 m thick. In the Aitzeta domain, unit consists of black marls and lutites, limestone megabreccias with ≤6-m-long olistoliths, and discrete calcarenitic turbidites. In the southeast domain, unit is composed of black lutites and thin-bedded turbidite sandstones.	Deep-water submarine slope
Ondarroa unit Middle to early late Albian (*D. cristatum* Zone)	80 m thick. Unit is found only in the Aitzeta domain and is composed of sandstone, pebbly sandstone, and conglomerate turbidite beds alternating with lutites. Conglomerates consist of quartzite and ≤15-cm-long quartz clasts.	Inner part of a coarse-grained turbidite system
Mutriku unit Late Albian (*H. varicosum* Zone)	205 m thick (original thickness: ~250 m). Unit is found only in the Aitzeta domain and is separated from the overlying syntectonic Alkolea unit by an angular unconformity (1 in Fig. 4). This unit is composed of highly bioturbated muddy sandstones, sandy lutites with ammonites, and sparse thin-bedded turbidite sandstones.	Deep-water paleohigh
Deba unit Early late Albian (*D. cristatum* Zone–*H. varicosum* Zone)	~450 m. Unit is present only in the southeast domain and is composed of alternating black lutites and sandy, plane-parallel, thin- and medium-bedded turbidites with a basal slump. Abundant trace fossils of *Nereites* ichnofacies. Coarsening- and thickening-upward succession.	Outer part of a prograding turbidite system in a deep submarine trough
Syntectonic sequence		
Alkolea unit Late Albian (*C. auritus* Subzone). This unit is subdivided into the following four superposed subunits (Fig. 4):	11–50 m thick. At Alkolea Point (Fig. 4), the unit thickness is quickly reduced to 11 m to the northwest at the cliff top (Fig 2B). The lower boundary is the faulted angular unconformity 1, originally dipping 5° toward 123° (angle with the overlying limestone beds); the underlying Mutriku unit shows tectonic rotation of 42° toward 125° (Figs. 4 and 5C). The upper boundary is an unconformity surface, separating this unit from the posttectonic Deba unit (onlapping turbidites in Fig. 4B).	
Subunit A	0–10 m thick. Subunit is faulted, completely disappearing toward the northwest. Its lower contact is angular unconformity 1, and its upper contact is a conformable surface with subunit B (Figs. 4 and 5C). Subunit is a clast-supported breccia with angular sandstones and ≤3.4-m-long lutite boulders and lutite matrix (Fig. 6A).	Erosion of the underlying rotated rocks and downslope (southeastward) resedimentation as a cohesive debris-flow deposit
Subunit B	0–2.5 m thick. This folded subunit rests conformably on subunit A southeastward and unconformably on Mutriku unit northwestward (angular unconformity 1) (Fig. 4). Subunit disappears completely northwestward, being truncated by angular unconformity 2. Subunit is composed of two similar marl-limestone couplets, the lower B_1 and the upper B_2. They merge to the northwest, and couplet B_1 is missing to the southeast, although blocks of subunit B rest on subunit A. Limestones are nodular and micritic with planktonic fossils, and they have sharply irregular tops with ≤10-cm-long quartzite clasts, borings, local Fe-rich crust, ammonites, rare corals, bivalves, and reworked concretions encrusted by sponges.	Hemipelagic deposition with two phases of hardground formation. Resedimentation; also bypassing of siliciclastic sediments on hardground tops
Subunit C	0–15 m thick. Subunit C is concordant with subunit B, and both appear strongly folded. Folds are truncated below angular unconformity 2, and synclines show maximum thickness. Subunit is composed mainly of gray marls with sparse limestone concretions. In the southeast, subunit has a 90-cm-thick nodular limestone orthobreccia (≤42-cm-long clasts) and sandy marls (Fig. 4).	Hemipelagic deposition with sporadic resedimentation on a southeast-oriented talus slope
Subunit D	12 m thick. Subunit is an olistostrome that crops out at Alkolea and in the southeast domain (Fig. 2). At Akolea, the subunit's base is angular unconformity 2, resting on subunits B and C and the overturned Mutriku unit (Figs. 2, 4, and 5B). Top of subunit D is an unconformity onlapped by posttectonic Deba unit toward the northwest. Subunit D is composed of a massive, disorganized, clast-supported, polymictic, and heterometric breccia with ≤12-m-long olistoliths (Fig. 6C). The matrix consists of sandy marls and lutites, similar to some crushed clasts derived from Mutriku unit. Table 2 summarizes composition, maximum size, and source rock of the main clasts. In southeast domain (Fig. 2), the olistostrome consists of a single 12-m-thick and 230-m-long (minimum) slab of marls and nodular limestones, entirely corresponding to subunit C (Fig. 7). Its top is onlapped by the posttectonic Deba unit. Three northeast-striking internal anticlines (I, II, and III, Fig. 7) indicate that the transport direction of the slab was toward the southeast.	Transport by cohesive debris flow and free translation of individual blocks. Deposition in a southeast-dipping submarine slope at the end of a phase of rotation, uplift, and denudation of the underlying units
Posttectonic sequence		
Posttectonic Deba unit Late Albian (*M. rostratum* Subzone)	~25 m (minimum).This subunit wedges out and onlaps toward the northwest onto the top of the subunit D of the Alkolea unit (Figs. 6C and 7). Subunit is made up of turbidite sandstones and lutites in couplets, with sand:lutite ratios of 2:1 (Fig. 6D). Sandstone beds are 2–50 m thick and present Tb to Tbe Bouma sequences.	Outer part of a turbidite system

STRUCTURE

Southeast of the Mutriku fault, the main Albian structure of the area beneath angular unconformity 2 consists of two structurally distinct domains: the uplifted Aitzeta structure and the undeformed southeast domain (Figs. 1B and 2). The uplifted Aitzeta structure reveals an overturned homoclinal succession of pretectonic units. The narrow transition zone between the Aitzeta and southeast domains in the southern part of the area coincides with the northeast-trending Garate fault that cuts only pretectonic units. In the northeastern coastal area (Alkolea), in which the shallowest structural level is observed, syntectonic deposits overlie and overlap the structure of the transition zone, which is therefore hidden.

The superb Alkolea sea-cliff exposure is the only part of the area where the Aitzeta structure is overlain by syntectonic deposits of *auritus* Subzone age (Figs. 2 and 4). Structural analysis of this key outcrop permits the establishment of some of the deformation mechanisms that operated during uplift of the Aitzeta structure and their ages. In this outcrop, both the pretectonic sequence and subunit A of the syntectonic sequence show brittle deformation or faulting, whereas subunits B and C of the syntectonic sequence show marly deposits with ductile deformation or folding. The analysis of all these faults and folds shows that they formed simultaneously following deposition of the highest preserved unit of the *auritus*

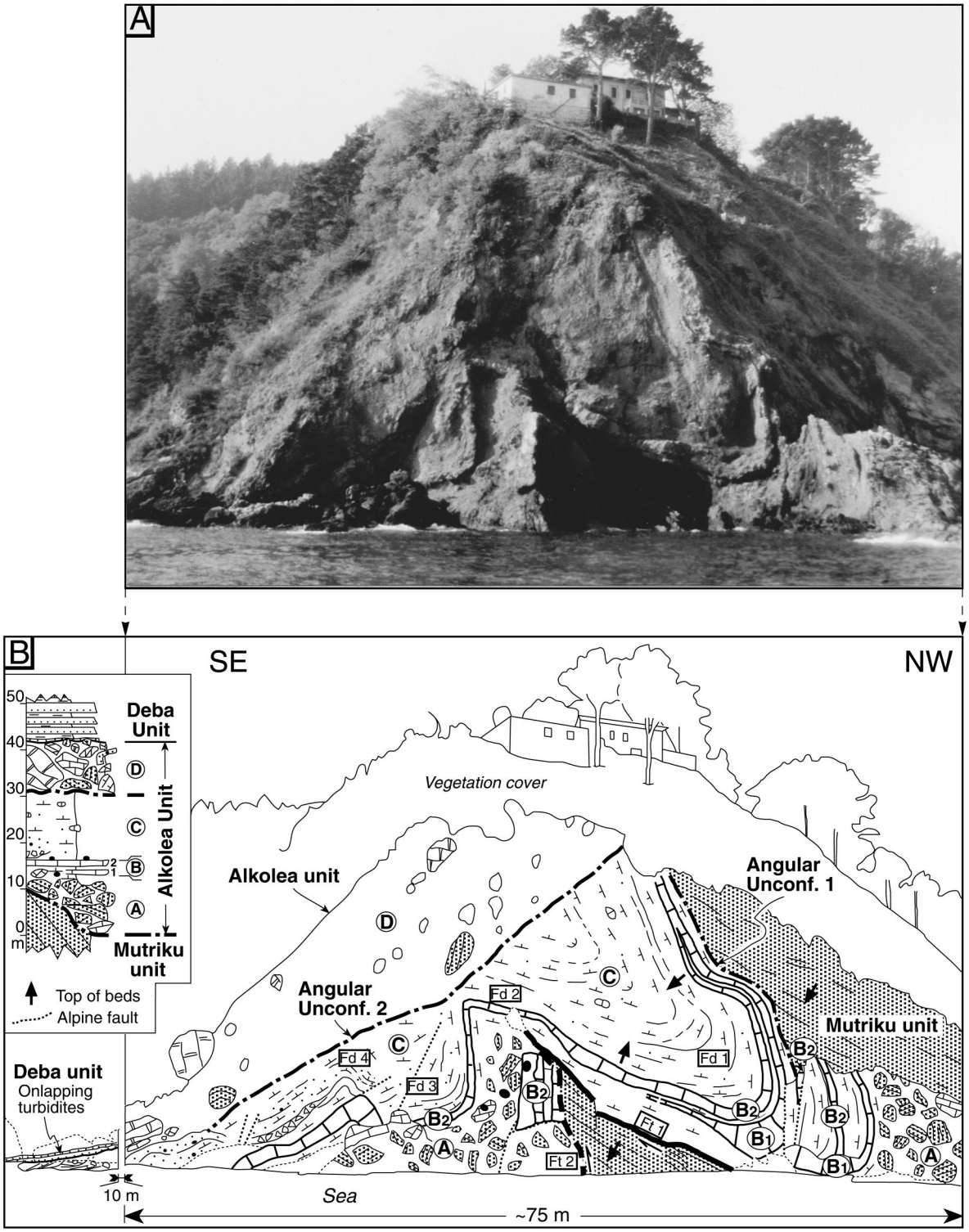

Figure 4. View of the Alkolea point outcrop from the sea. (A) Photograph. (B) Sketch showing lithostratigraphic units (Mutriku, Alkolea, and Deba), subunits (A–D), angular unconformities (1–2), faults (Ft 1–2), and folds (Fd 1–4). The southeasternmost part of the drawing lies 10 m outside of the photograph. Arrows indicate top of beds. Note that the bottom of the outcrop is not a perfectly vertical wall and that some elements are on different planes. Inset shows the vertical arrangement of lithostratigraphic units and subunits.

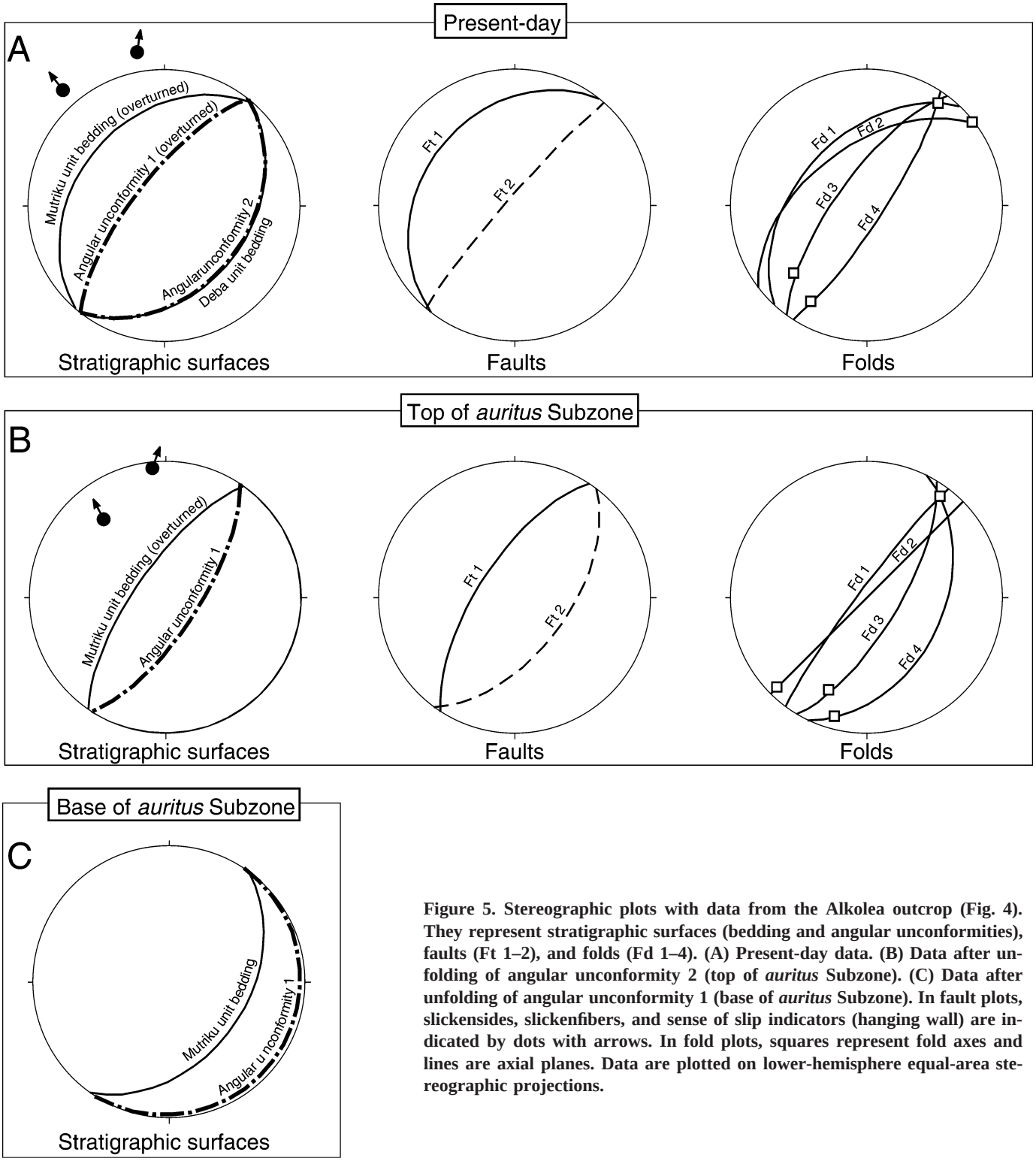

Figure 5. Stereographic plots with data from the Alkolea outcrop (Fig. 4). They represent stratigraphic surfaces (bedding and angular unconformities), faults (Ft 1–2), and folds (Fd 1–4). (A) Present-day data. (B) Data after unfolding of angular unconformity 2 (top of *auritus* Subzone). (C) Data after unfolding of angular unconformity 1 (base of *auritus* Subzone). In fault plots, slickensides, slickenfibers, and sense of slip indicators (hanging wall) are indicated by dots with arrows. In fold plots, squares represent fold axes and lines are axial planes. Data are plotted on lower-hemisphere equal-area stereographic projections.

Subzone (subunit C) and before the olistostrome deposits of the *rostratum* Subzone (subunit D). The following description of faults and folds is made on the basis of restored data (Fig. 5).

Faults

Two northeast-striking faults (average 034°), faults 1 and 2, are present in the Alkolea outcrop (Figs. 4 and 5B). Fault 1 dips 68° toward 303° (dip direction), is parallel to the bedding of the Mutriku unit, cuts angular unconformity 1, and shows slickenlines, slickenfibers, and small steps indicating hanging-wall movement toward 332° and 019° (ends of

TABLE 2. OLISTOSTROME CLASTS AT ALKOLEA

Clast lithology	Other features	Maximum size (m)	Provenance
Urgonian limestone	Micritic, calcarenitic textures and breccia. Partial silicification and dolomitization. Fauna of late early to early middle Albian (see Appendix)	12.0	Berriatu unit
Dolomite	Local silicification	1.0	Berriatu unit
Bedded limestone	Sponge spicules, benthic foraminifera, and sand particles	1.8	Berriatu unit
Pebbly sandstone	Quartz pebbles as large as 3 cm	2.2	Ondarroa unit
Muddy sandstone	Bioturbation and inoceramids	4.6	Mutriku unit
Bedded carbonaceous sandstone	Carbonaceous lamina	2.2	Mutriku unit (?)
Nodular limestone	Asphalt fills and impregnations	5.4	Alkolea unit, subunit B
Marl	Massive	4.6	Alkolea unit, subunit C

spectrum values) (Fig. 5B). Based on directions of the slickenlines and slickenfibers, the calculated components are 50 m for the normal dip slip and 10–71 m for the dextral strike slip. The strike-slip component is 20%–142% of the dip-slip component; therefore, this bedding-plane fault is classified as a dextral normal-slip fault.

Fault 2 dips 58° toward 126° and is parallel to the angular unconformity 1. It forms a 1–2-m-wide fault zone containing calcite veins that are oriented parallel to the fault and that fill right-stepping, en echelon extensional fractures. Although no criteria to quantify slip components have been found, absence of stratigraphic separation across this fault sug-

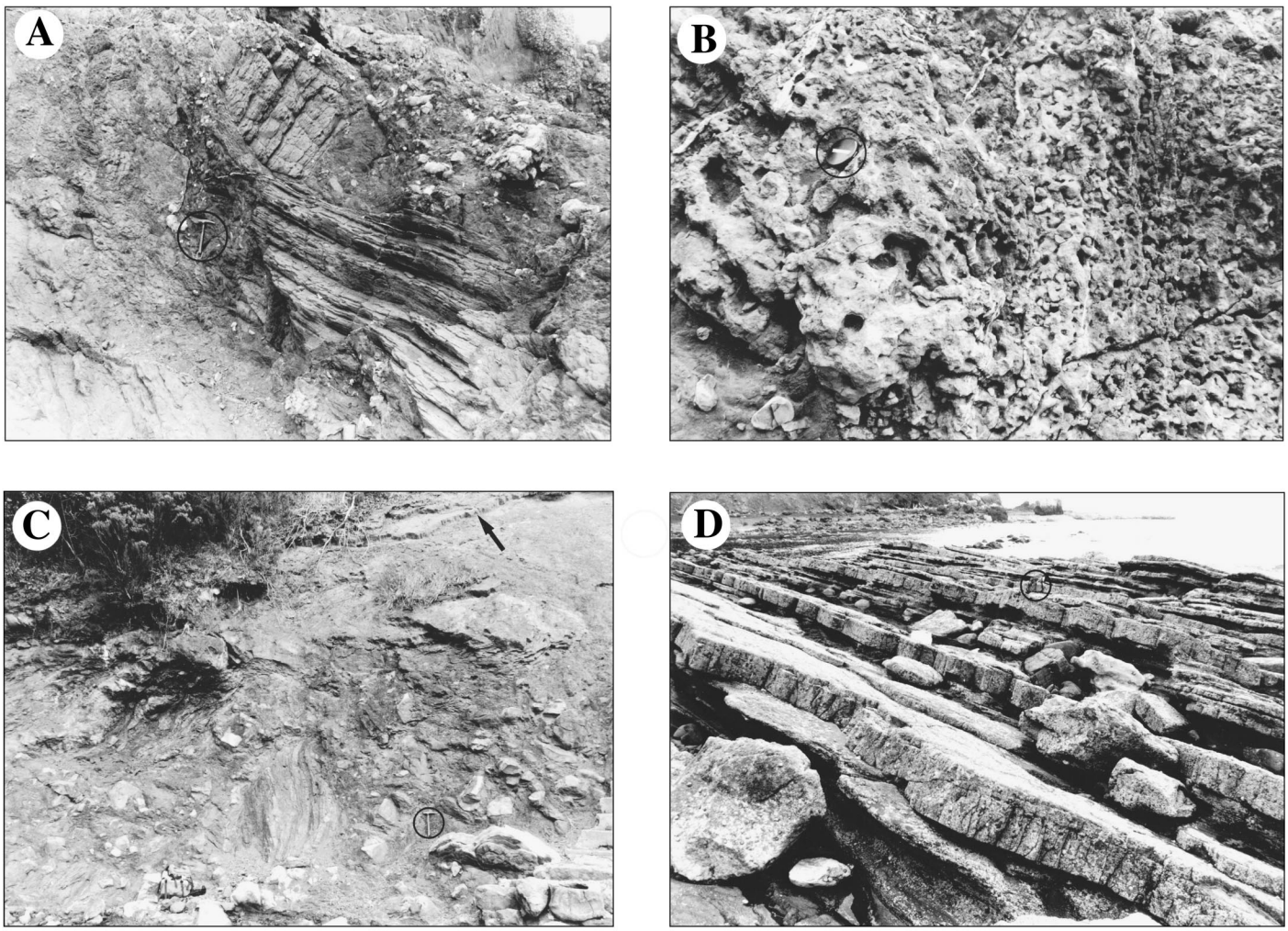

Figure 6. (A) Lowermost massive, disorganized breccia from the Alkolea unit (subunit A, as in outcrop shown in Fig. 4), mainly composed of muddy sandstone fragments from the underlying Mutriku unit (encircled hammer for scale). (B) Plan view of the top of the uppermost nodular limestone from the Alkolea unit (subunit B_2) showing nodular aspect and some borings (encircled lens cap for scale). (C) Alkolea unit olistostrome (subunit D) in Alkolea locality showing massive, disorganized, polymictic megabreccia with angular fragments of the underlying Alkolea (subunits B and C), Mutriku, Ondarroa, and Berriatu units. Note overlying sandstone turbidites from the Deba unit (arrow at top of the photograph; encircled hammer for scale). (D) General aspect of turbiditic sandstone-lutite couplets from the Deba unit (posttectonic sequence). The Alkolea outcrop is shown in the background (encircled backpack for scale).

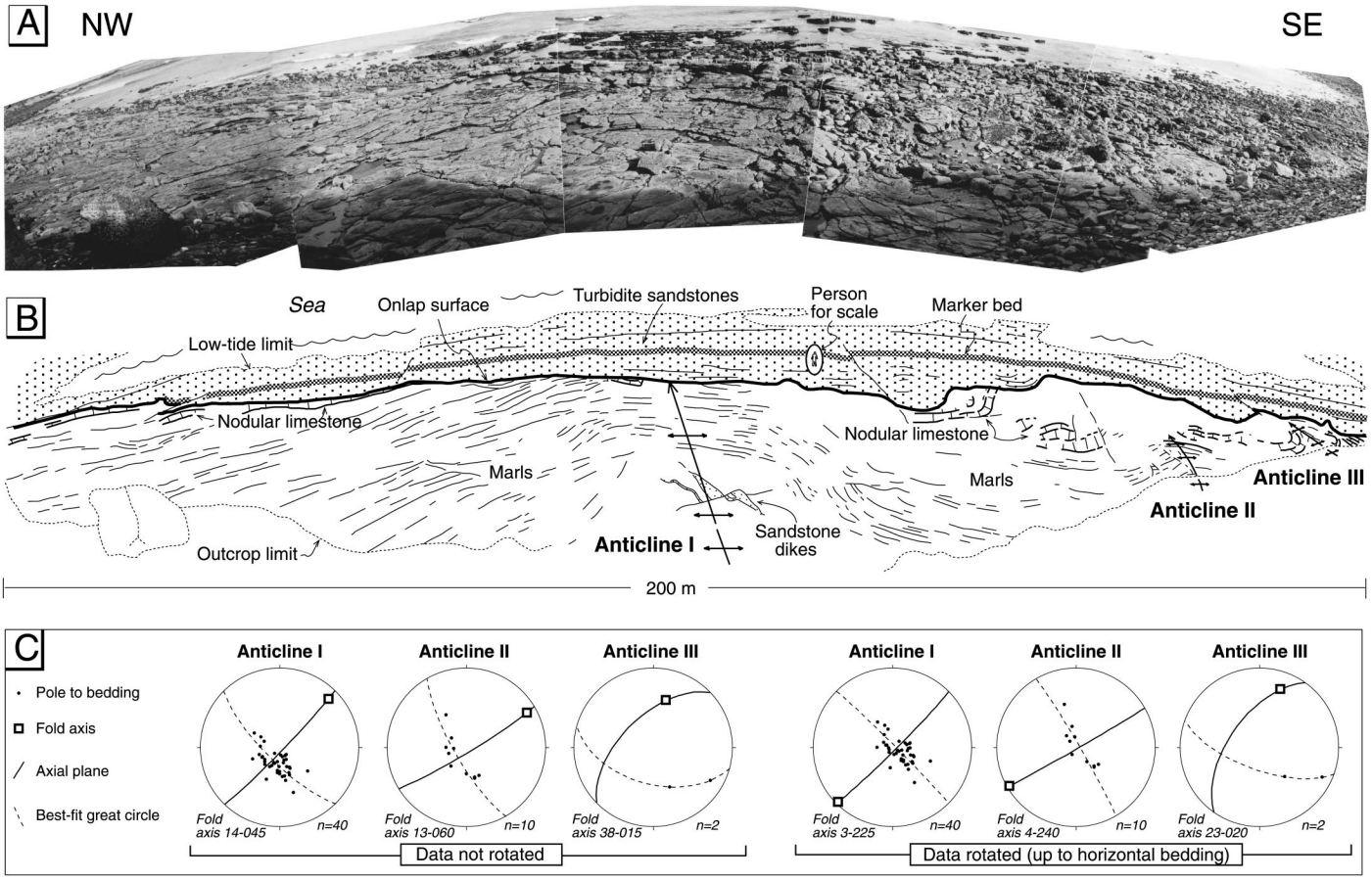

Figure 7. (A) Photograph and (B) sketch of the wave-cut platform in southeast domain showing an olistostromal slab (subunit D of the Alkolea unit) composed of folded marls and nodular limestones from subunits B and C of the Alkolea unit. Turbidite sandstones (Deba unit) onlap the top of the slab northwestward (note turbiditic marker bed). A person for scale is standing in the center background (see location in sketch). Location of outcrop is shown in Figure 2A. (C) Poles to bedding plots of data from the three main anticlines (I, II, and III) of the slab, both for present-day (data not rotated) and late Albian (data rotated) times. Data plotted on lower-hemisphere equal-area stereographic projections.

gests very little slip movement. Data suggest that it corresponds to the angular unconformity 1, slightly sheared by left-lateral movements, similarly to other, Tertiary, small-scale faults of the area (Fig. 5B).

Fault 1 and angular unconformity 1 end and coalesce upward, bounding a triangular wedge of Mutriku unit rocks several tens of meters high and wide. The dip of beds in this wedge is identical to that of the beds of the same unit to the west. This triangular wedge was formed by bedding-plane faulting (fault 1) of the Mutriku unit that cut and repeated the angular unconformity 1 surface.

Folds

The marly subunits B and C of the Alkolea unit show four northeast-trending folds (average 035°), folds 1–4, which range from a few meters to a few tens of meters in amplitude (Figs. 4 and 5B). The continuity of the folded unit with the underlying rocks and the geometric relationship between folds and underlying faults suggest that the folds are of tectonic origin and are not slump folds. The shortening estimate for this folding is 50 m (48%).

Folds 1 and 2 are tens of meters wide, tight (interlimb angles: 50°–60°), overturned, with subhorizontal axes and axial planes striking 037° and 045°, respectively. Fold 1 also shows important thickening of weak rocks (marls) in the axial zone together with slickenfibers on bedding surfaces, indicating a flexural-slip fold mechanism. Geometry and trend of folds 1 and 2 are clearly conditioned by the shape of the underlying triangular wedge: (1) the strikes of both axial planes, the lower fault (fault 1), and bedding are subparallel; (2) the fold limbs (fold 2) are subparallel to the wedge boundaries; and (3) the anticlinal hinge (fold 2) is located above the top of the triangular wedge, the synclinal hinge (fold 1) coinciding with the cut-off plane of the hanging wall (Figs. 4 and 5B). These geometric relationships suggest that folds 1 and 2 are drape folds created by uplift of the underlying triangular wedge.

Folds 3 and 4 are only a few meters wide, with axial planes that dip 71° toward 121° and 43° toward 116° and axes plunging 18° toward 198°, respectively. The style of these folds varies from tight (interlimb angle 40°), box-like geometry in the case of fold 3, to an open (interlimb angle 86°), chevron-like fold in the case of fold 4. The mean strike of the axial surfaces is oriented at 6° to the strike of the fault 1 and, unlike major folds 1 and 2, folds 3 and 4 are not obviously associated with an underlying fault. Although alternative interpretations are possible, the observed obliquity can be explained easily by drag folds consis-

TABLE A1. FOSSIL CONTENT AND DATING

Sequences and units and dating interpretation	Fossils	Horizons	Other authors and comments
Pretectonic sequence: early middle Albian (*Lyelliceras lyelli* Subzone) to early late Albian (*Hysteroceras varicosum* Zone)			
Berriatu unit: early middle Albian (*L. lyelli* Subzone)			
	Locality: Elantxobe		
	Metahamites cf. *elegans* (d'Orbigny) (ELAN-1)	A	
	Kossmatella cf. *muhlenbecki* (Fallot) (ELAN-2, 6, 11)	A	
	Locality: Ea		
	Metahamites sp. (EA-9)	B	
	Parasilesites cf. *kilianiformis* (Fallot) (EA-8)	B	
	Kossmatella sp. (EA-12)	B	
	Eogaudryceras sp. (EA-5)	B	
	Locality: Lekeitio		
	Hemiptychoceras gaultinum (Pictet) (LEK-18)	D	
	Kossmatella agassizianum (Pictet) (LEK-30, 35)	D	
	Lyelliceras pseudolyelli (Parona and Bonarelli) (LEK-50)	D	
	Lyelliceras cf. *lyelli* (d'Orbigny) (LEK-37, F-16)	D	
	Lyelliceras cf. *gevreyi* (Jacob) (LEK-4, 10, 20, 49)	D	
	Lyelliceras sp. *peruvianum*-group (F-16')	D	
	Cleoniceras (Cleoniceras) cf. *devisensis* Spath (LEK-47)	D	
Ondarroa unit:: middle to early late Albian (*Dipoloceras cristatum* Zone)			
	Locality: Etxebarri (8 km south of Ondarroa)		Horizon F (approx.): Reitner (1987) recorded *Ticinella* cf. *primula* Luterb.
	Puzosia sp. (ETX-2)	F	
	Oxytropidoceras (Oxytropidoceras) sp. (ETX-1)	F	Horizon G, in clasts: Reitner (1987) recorded *Orbitolina (Mesorbitolina) texana* (Roemer), *Simplorbitolina conulus* Schr., and *Orbitolina (Mesorbitolina) subconcava* Leym.
	Locality: Ondarroa		
	Puzosia sp. (OND-5)	G	
	In uppermost clasts:		
	Neorbitolinopsis conulus (Douvillé) (OND-1)	G	
	Orbitolina (Mesorbitolina) aperta (primitive form) (Erman) (OND-1)	G	
	Hensonina lenticularis (Henson) (OND-1)	G	
Ea unit: early middle Albian (*L. lyelli* Subzone)			
	Locality: Ea		
	Dipoloceroides sp. (EA-13)	C	
	Locality: Lekeitio		
	Kossmatella agassizianum (Pictet) (LEK-41)	E	
	Lyelliceras cf. *gevreyi* (Jacob) (LEK-44)	E	
	Protanisoceras (Protanisoceras) sp. (LEK-45)	E	
Mutriku unit: late Albian (*Hysteroceras varicosum* Zone)			
	Locality: Mutriku		Horizon H: Gómez de Llarena (1958) recorded *Actinoceramus concentricus* (Parkinson).
	Puzosia mayoriana (Pictet) (JMNS-18)	J	
	Puzosia cf. *provincialis* (Parona AND Bonarelli) (MUTR-12)	L	Horizon K (approx.): Plestch (1990) recorded *Hypophylloceras velledae, Idiohamites turgidus,* and *Anisoceras arrogans.*
	Hysteroceras cf. *varicosum* (J. Sowerby) (MUTR-1)	L	
	Mortoniceras (Mortoniceras) sp. (GA-841)	L	
	Hamites sp. (MUTR-6)	L	Horizon L (approx.): Gómez de Llarena (1958) recorded *Puzosia mayoriana* (d'Orbigny) and *Mortoniceras (Mortoniceras) potternense* var. *evoluta* Spath. Plestch (1990) recorded *Pachydesmoceras* cf. *denisonianum* and *Mortoniceras evolutum*
			Upper part of the unit:: Reitner (1987) recorded *Idiohamites* sp., *Mortoniceras* sp., *Biticinella roberti,* and *Actinoceramus concentricus*
Pretectonic Deba unit: late Albian (*Dipoloceras cristatum* and *H. varicosum* Zones)			
	Locality: Deba		Horizon I: Rat (1959) recorded *Kossmatella, Dipoloceras*? , and *Epihoplites*? . Feuillée (1967) recorded *Thalmanninella trochoidea* (Gandolfi), *Thalmanninella ticinensis* (Gandolfi), and *Ticinella roberti* Gandolfi. Magniez and Rat (1972) recorded *Hedbergella planispira* (Tappen), *Hedbergella infracretacea* (Glaessner)? , *Hedbergella delrioensis* (Carsey), and *Favusella washitensis* (Carsey)
	Kossmatella cf. *schindewolfi* Wiedmann AND Dieni (DEBA-1, 2)	I	
	Hemiptychoceras sp. (DEBA-7)	I	
	Puzosia (*Puzosia)* sp. (DEBA-5)	I	
	Oxytropidoceras (Oxytropidoceras) cf. *cantianum* Spath (DEBA-6)	I	
	Hysteroceras sp. (DEBA-4)	I	

tent with a dextral-wrench model rather than other fold types.

The geometries of folds in the Alkolea unit and faults in the Mutriku unit are considered to be due to the differences in the mechanical behavior of their respective lithologies. Important early-diagenetic calcite cementation of the Mutriku muddy sandstones favored their early lithification and brittle behavior. The Alkolea unit, on the other hand, behaved differently because of the predominance of marls in it, deposited shortly before their deformation.

PHASES OF SEDIMENTATION AND TECTONIC DEFORMATION

Integrated stratigraphic, sedimentological, and structural analyses permit us to distinguish different phases in the tectono-sedimentary evolution of the Aitzeta structure. The timing and general features of these phases are described in 10 schematic cross sections (numbered in Fig. 8). Four phases of active tectonism (1, 3, 5, 8–9) characterized by rotation, faulting, folding, and uplift are represented by angular unconformities, erosion surfaces, and resedimentation deposits. The tectonic pulses are separated by intervening phases of tectonic calm and gentle sedimentation (2, 4, 6–7, 10).

TABLE A1. *(Continued.)*

Sequences and units and dating interpretation	Fossils	Horizons	Other authors and comments
Syntectonic sequence: late Albian (*Callihoplites auritus* Subzone)			
Alkolea unit: late Albian (*C. auritus* Subzone = *Mortoniceras inflatum* Zone of the Tethyan zonation)			
	Locality: Alkolea		
	Hamitoides cf. *studerianus* Pictet (ALK-3)	N	Top of hardground
	Cantabrigites cf. *nanoides* Wiedmann (ALK-2)	N	Top of hardground
	Lechites sp. (ALK-1)NTop of hardground		
	In limestone clasts in the upper olistostrome (limestone of late early to early middle Albian age):		Horizon M: Plestch (1990) recorded *Rotalipora subticinensis* and *Hedbergella* gr. *planispira*
	Simplorbitolina conulus Schroeder (ALK-6)	Q	
	Simplorbitolina manasi Ciry and Rat (ALK-6)	Q	
	Orbitolina (M.) subconcava Leymerie (LEK-45)	Q	
	Coskinolinella santanderensis Ramirez del Pozo (ALK-5)	Q	
	Hensonina lenticularis Henson (ALK-6, LEK-45)	Q	
Posttectonic sequence: In marls of Kardal unit underlain by Alkolea unit and laterally equivalent of Deba unit, outcropping ~1 km westward from study area.			
Late Albian, early *Stoliczkaia dispar* Zone, *Mortoniceras rostratum* Subzone			
	Locality: Mutriku		
	Anisoceras cf. *perarmatum* (Pictet and Campiche) (JMNS-2, 3)	P	Horizon O: Plestch (1990) recorded *Hemiptychoceras* sp., *Praeglobotruncana* cf. *stephani, Ammodiscus gaultinus,* and *Hedbergella simplex*
	Anisoceras picteti Spath (JMNS-4, 7)	P	
	Anisoceras pseudoelegans (Pictet and Campiche) (JMNS-21)	P	
	Mortoniceras (M.) alstonense (Breistroffer) (JMNS-9,11)	P	
	Mortoniceras (Mortoniceras) arietiforme group Spath (JMNS-14)	P	
	Mortoniceras (Mortoniceras) rugosum Spath (JMNS-12)	P	
	Mortoniceras (Mortoniceras) cf. *pachys* (Seeley) (JMNS-15)	P	
	Mortoniceras (Mortoniceras) sp. (JMNS-13)	P	
	Anisoceras saussureanum (Pictet) (JMNS-1, 6)	P and R	
	Anisoceras armatum (J. Sowerby) (JMNS-5)	R	

Phase 1

The Aitzeta structure was initiated with uplift and tilting (42° toward 125°) of the pretectonic units. Subsequent erosional truncation of the Mutriku unit created angular unconformity 1 (surface dip: 5° toward 123°). Fragments of the Mutriku unit were resedimented downslope (southeast) as a debris-flow breccia, forming a wedge-shaped body (Alkolea unit, subunit A) that pinched out toward the uplifted area (northwest).

Phase 2

Under calm tectonic conditions, hemipelagic marls and nodular limestones (Alkolea unit, subunit B_1) were deposited, producing a condensed interval. These sediments draped both the breccia and the angular unconformity formed during phase 1.

Phase 3

Downslope bypassing of sediments derived from the underlying Ondarroa unit by gravity flows caused erosion of the sea bottom and exposure, local fragmentation, and resedimentation of the hemipelagic nodular limestones of phase 1 (Alkolea unit, subunit B_1). These flows deposited scattered quartzite clasts up to 10 cm long derived from the Ondarroa unit and muddy sandstone clasts derived from the Mutriku unit. These clasts record the exposure and erosion of the two pretectonic units. Exposure of the Ondarroa unit and development of gravity flows reflect a gentle tectonic pulse of uplift in the Aitzeta structure. The exposure of the Ondarroa unit implies that at least 250 m of the overlying Mutriku unit must have been removed by erosion during phases 1 and 3. Consequently, a minimum amount of 250 m (equivalent to eroded thickness) of accumulated uplift is estimated for the Aitzeta structure during these phases.

Phase 4

A second condensed section consisting of hemipelagic marls and nodular limestones (subunit B_2 of the Alkolea unit) was deposited under calm tectonic conditions.

Phase 5

Gravity flows carrying quartz and quartzite clasts from the Ondarroa unit caused erosion of the seafloor and local reworking of the previously formed nodular limestone (subunit B_2 of the Alkolea unit). These flows left a lag of scattered siliciclastic clasts (up to 10 cm long) on the top of the limestone. Although there is no geometric evidence of tectonic deformation during this phase within the studied area, it is likely that uplift in the source area promoted the gravity flows and erosion of the underlying Ondarroa unit in a phase similar to that proposed for phase 3.

Phase 6

Exposure of the nodular limestone (subunit B_2 of the Alkolea unit) on the seafloor without further sediment accumulation led to the formation of a hardground. This was bored, encrusted by corals and sponges, colonized by bivalves, and covered with an iron crust and specimens of nektonic fauna (belemnites and ammonites) (Fig. 6B). All these features suggest a relatively long-lasting period of submarine exposure of the hardground during tectonic quiescence.

Phase 7

Renewed sedimentation under calm tectonic conditions resulted in accumulation of concretionary marls (subunit C of the Alkolea unit). Sandy marls and sandstones were deposited on the lower part of the slope along with scarce small-scale gravity flow deposits.

Phase 8

A major pulse of tectonic activity caused uplift and 66° (72° toward 305°) of tilting and overturning of the pretectonic units of the Aitzeta structure. Along the margin of the uplifted structure, at the structurally shallowest depth, a bedding-parallel fault affecting pretectonic units created decameter-scale drape folds parallel to it within the overlying deposits (subunits B and C of the Alkolea unit).

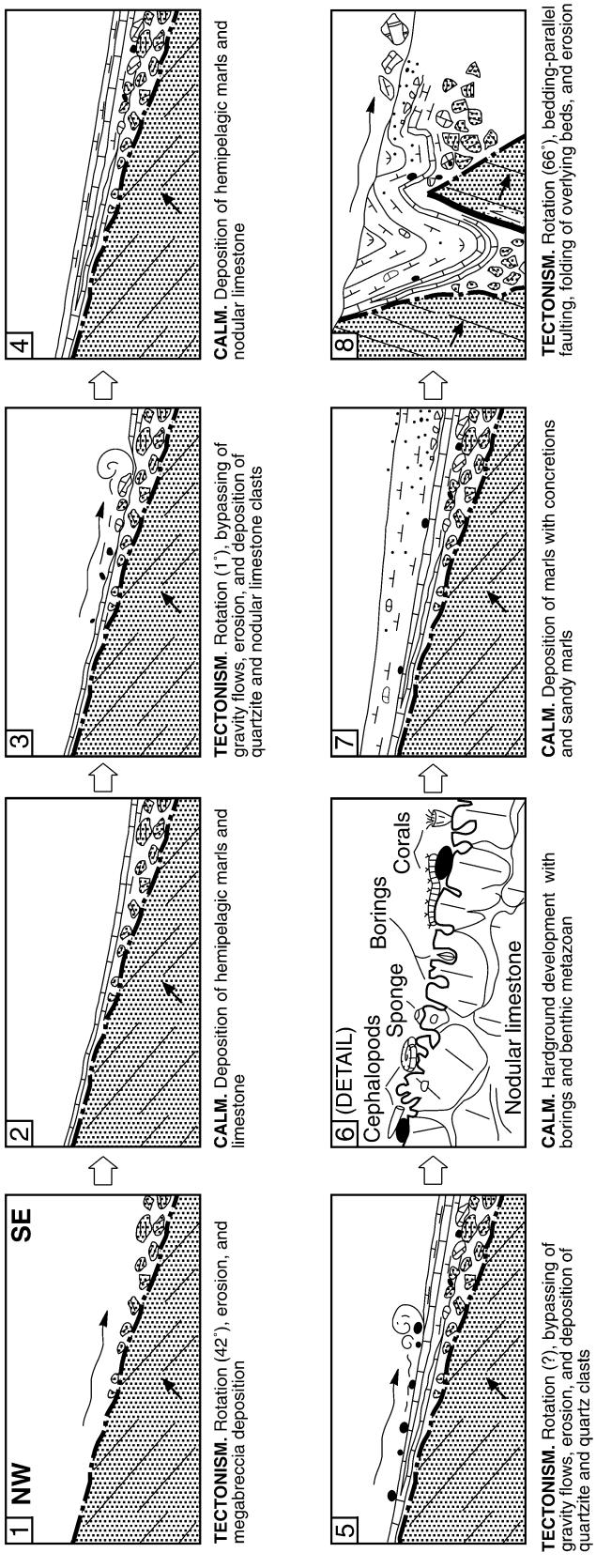

Figure 8. Tectono-sedimentary evolution of the studied area represented in 10 northwest-southeast cross sections. The sequential arrangement shows an alternation of phases of tectonic deformation (1, 3, 5, 8–9) indicated by erosion and resedimented deposits and tectonic calm (2, 4, 6–7, 10) indicated by hemipelagic deposits. Cartoons 1–8 correspond to the Alkolea locality, and cartoons 9–10 represent the whole study area. Long and wavy arrows represent currents. Short and bold arrows indicate tops of beds.

Associated dextral normal-slip movement caused development of the meter-scale drag folds oriented obliquely at 6° to the bedding-parallel fault. The folded materials were shortened by 50 m (48%) as they were uplifted and strongly truncated by erosion (angular unconformity 2). As a consequence, the lowermost pretectonic unit, the Berriatu, was exhumed. A calculation of the minimum accumulated uplift required to achieve this exhumation during the tectonically active phases 1, 3, 5, and 8 gives a range of 350–390 m (equivalent to the eroded thickness).

Phase 9

Fragments of the pretectonic units and the three syntectonic subunits A–C were transported downslope to the southeast and deposited at the base of the submarine slope as a polygenic and chaotic olistostrome (subunit D of the Alkolea unit). This unit contains blocks as long as 230 m (minimum length at outcrop) and covers and preserves the underlying structure. Its formation marked the end of the previous phase 8.

Phase 10

Tabular sandy turbidites (posttectonic Deba unit), corresponding to a submarine fan of northern provenance, progressively onlapped the top of the previously deposited olistostrome to the northwest. They probably also covered a great proportion of the uplifted structure, sealing the tectonic structure described completely.

Finally, in post–*auritus* Subzone time (? Tertiary), successions of the Aitzeta structure and the most closely adjacent southeast domain tilted 37° toward the southeast.

INTERPRETATION OF THE STRUCTURE

Stratigraphic and structural data from the Aitzeta structure and its surrounding areas indicate that it can be regarded as a southeast-facing monoclinal syncline produced by the Mutriku fault (Fig. 9). This fold is not evident from the cartography because the hinge zone is buried by syntectonic deposits and it is sheared by the Garate fault to the southwest (Figs. 1B and 2). Examination of the geologic maps (Figs. 1B and 2) suggests that this structure can be interpreted as a pressure ridge situated between the Mutriku and Garate faults, with homoclinal overturning of the inner successions. However, the data we present best fit a fold interpretation. A monoclinal syncline interpretation is supported by the following observations:

1. Bedding-plane faulting of the pretectonic sequence cuts the overlying angular unconformity 1 and caused folding (drape folds) of the syntectonic deposits. This event is interpreted to have resulted from reactivation of a flexural-slip fold. Kinematic indicators show normal faulting in the overturned limb consistent with the expected sense of flexural slip for the syncline. Structures similar in character and size, linked to reactivated folds, were described by Alonso (1989).

2. In the northeast part of the transition zone between the Aitzeta structure and southeast domain there is no evidence of significant faulting, and pre-, syn- and posttectonic sequences show overall continuity between the domains. Therefore, the Aitzeta structure in that area was not associated with significant faulting.

3. The Garate fault is a branch of the major Mutriku fault created at a bend in the latter. It shows a progressive decrease in apparent slip northeastward, becoming zero in the coastal area (Figs. 1B and 2). Thus, the Garate fault is interpreted as being the result of local shearing on the hinge of the syncline during the latest folding stage (latest *auritus* Subzone).

4. Post–*auritus* Subzone rotation of the Aitzeta succession created the mapped syncline (Figs. 1B and 2), a fold whose axial surface is parallel to the boundary of Aitzeta domain. It is inferred that this fold originated by reactivation of a previous Albian syncline.

5. Overturning of the Aitzeta succession by fold-limb rotation is the simplest explanation of the surface structure seen. Strong tilting of a fault-bounded block does not provide an easy solution to the space problems at depth required by such a model.

In monoclinal structures, the development of anticline-syncline pairs is common. In this case, the absence of either tectonic deformation or significant unconformities in coeval deposits of the northwest domain indicates the lack of a deformation regime in that area. This observation, together with the large uplift and denudation of the rotated limb of the Aitzeta syncline, suggests that the Mutriku fault cut the whole sedimentary cover during the development of the structure (Fig. 9, B–C). Stratigraphic and structural data suggest that reverse slip on the northwest-dipping Mutriku fault caused down dropping of the footwall and the growth of the Aitzeta syncline southeast of the fault.

The growth strata and angular unconformities developed during the *auritus* Subzone show increased dip with age, indicating that the syncline grew by progressive limb rotation rather than by instantaneous limb rotation (Fig. 9B). Folds undergoing progressive limb rotation have been documented in detachment folds of foreland basins (Hardy and Poblet, 1994; Vergés et al., 1996) and in monoclines that originated from basement-involved blind reverse faults from strike-slip basins (Schneider et al., 1996). We propose that the Aitzeta syncline similarly formed in response to reverse slip on the high-angle emergent Mutriku fault.

The Aitzeta syncline formation suggests local northwest-southeast compression related to the northeastern part of the Mutriku fault. This fault is subperpendicular to the major northwest-trending Elgoibar and Lekeitio faults (Figs. 1A and 10), which are parallel to the basin axis and had an important role during the Cretaceous (García-Mondéjar et al., 1996). On the basis of sedimentological and structural data, such as horst-and-graben basin configuration, en echelon drag folds (Fig. 10), and strike-slip kinematic indicators (in the case of the Elgoibar fault), these two regional faults have been attributed to a sinistral strike-slip regime, consistent with the Pyrenean sinistral wrench system (Agirrezabala, 1996; Agirrezabala and García-Mondéjar, 2001). The northwest-southeast compression attributed to the northeastern part of the Mutriku fault does not conform to the strain ellipse of overall northwest-southeast sinistral wrench, but it can be explained by differential motion between the blocks separated by the Mutriku fault (Fig. 10, inset). In this way, higher strike-slip rates of the northwest block (hanging wall) with respect to the southeast block (footwall) along the Lekeitio fault would have caused compression perpendicular to the Mutriku fault and uplift of the hanging wall.

Although no piercing lines were observed, we consider that a dextral component was also involved in the development of the monocline (Fig. 10). This interpretation is based on the following arguments: (1) dextral-oblique flexural-slip horizons in the pretectonic sequence are compatible with transpression (oblique flexural slip has been documented in folds of transpressive regimes, e.g., Tanner, 1989) and (2) oblique folds (drag folds) in the syntectonic sequence are consistent with a dextral wrench model. In agreement with such a model, the subordinate Mutriku fault is consistent in both orientation and dextral component with the expected antithetic movement in that wrench system.

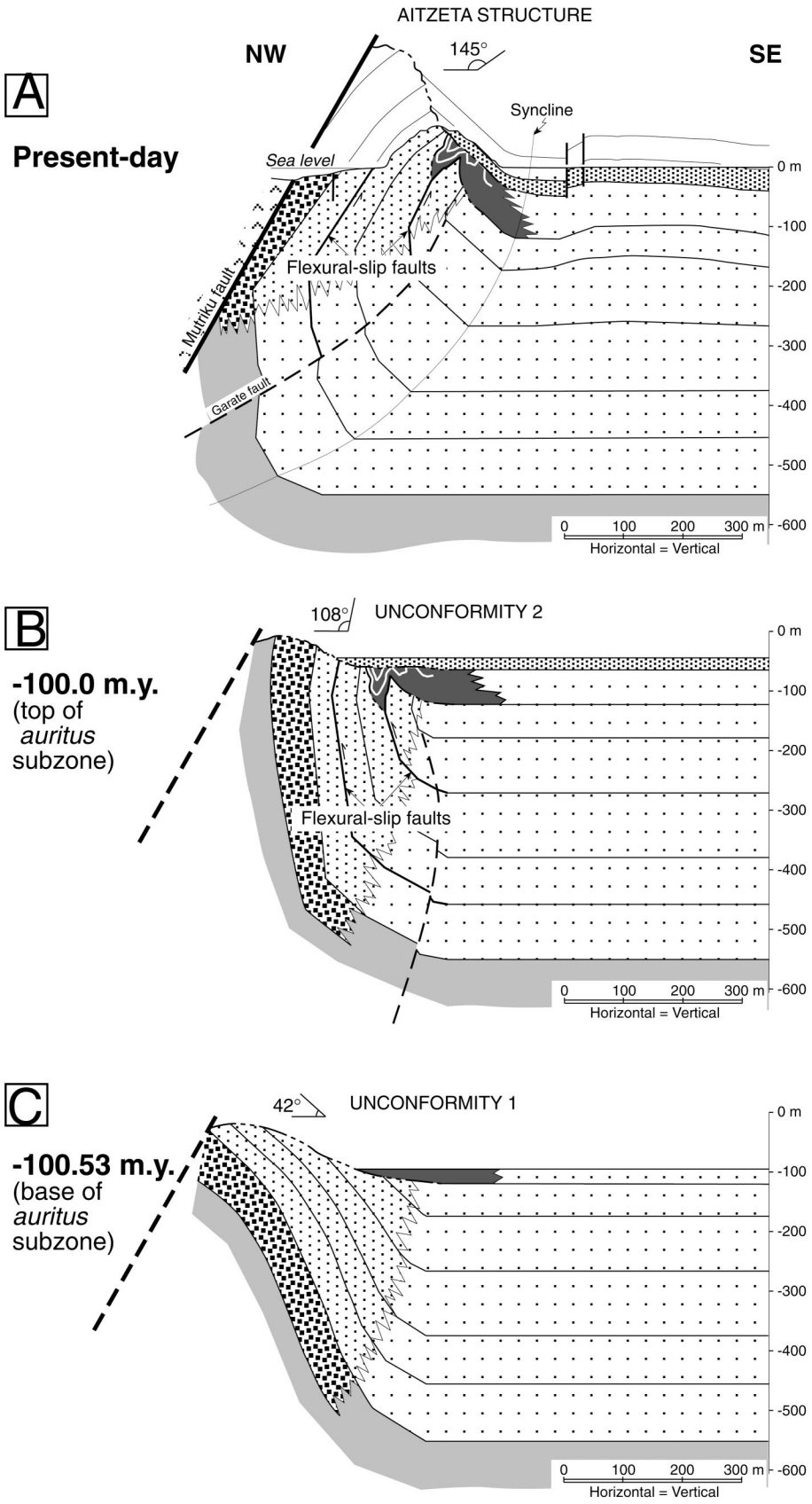

Figure 9. Interpretive A–A′ cross section of the Aitzeta structure for three different times (location in Fig. 2). (A) Present-day geometry. (B) Unfolded geometry at −100.0 m.y. (top of *auritus* Subzone) corresponding to the second major tectonic pulse (phases 8 + 9 of Fig. 8). (C) Unfolded geometry at −100.53 m.y. (base of *auritus* Subzone) corresponding to the first major tectonic pulse (phase 1 of Fig. 8). In B and C, the present-day Mutriku fault (dashed; without restoration) is located only for reference.

DEFORMATION RATES

Chronology of the Tectonic Pulses

Biostratigraphic data from the pre-, syn- and posttectonic units permit us to establish an intra–*auritus* Subzone age for the syntectonic Alkolea unit described here (see appendix) and, therefore, for all the sedimentation and tectonic deformation phases recorded by the unit. This age correlates with similar evidence from elsewhere in western Europe for tectonic activity and accompanying erosion of sediments at the beginning and end of the *auritus* Subzone (Owen, 1976; Wiedmann and Owen, 2001). Geographically widespread sequence boundaries in the Boreal, European, and Tethyan provinces at the beginning and end of the *auritus* Subzone have been recognized by Hardenbol et al. (1998). The duration of the *auritus* ammonite Subzone in the calibration scale of Gradstein et al. (1994) is 0.53 m.y. (from 100.53 to 100 Ma). Estimating absolute durations of the individual phases of sedimentation and tectonic deformation that occurred within the *auritus* Subzone can be very difficult, as they all fall below the resolution threshold and error range of any radiometrically established age. Moreover, no astronomically driven depositional cycles have been found in the Basque-Cantabrian basin successions of that age. Nevertheless, we have made an estimation of the timing of the principal tectonic phases (Fig. 11) in order to calculate rates of tectonic deformation. This estimation of timing relies on the following arguments and assumptions.

1. Each of the four phases of tectonic deformation distinguished in the Aitzeta area is represented by an unconformity and its related resedimented deposits. Therefore, the time spans of the phases of tectonic deformation correspond with sedimentation hiatuses in the uplifted structure. If we assume that strain rates did not vary much and, therefore, the time span of these hiatuses is proportional to

the intensity of the corresponding tectonic deformation, the duration of the two major phases of tectonic deformation bounding the *auritus* Subzone (cartoons 1 and 8 in Fig. 8, represented by the angular unconformities 1 and 2) is assumed to be much longer than the other corresponding two minor tectonic phases (cartoons 3 and 5, in Fig. 8). On the basis of this assumption and considering the difficulty of attributing durations to the two minor tectonic phases, we consider them negligible for calculation purposes.

2. The intervening phases of tectonic calm are represented mainly by deposition of hemipelagic deposits (phases 2, 4, and 6–7 in Fig. 8). The duration of all sedimentation phases can be estimated by using average sedimentation rates for modern and ancient hemipelagic sediments (~0.0648 m/k.y.; Fig. 17 in Scholle et al., 1983). Given that the maximum thickness of hemipelagic deposits preserved in Alkolea is 17.5 m, ~0.29 m.y. are indicated for their deposition (Fig. 11). This calculated interval is not the maximum, because the upper part of the hemipelagic deposits is lacking (erosion and truncation after rotation related to angular unconformity 2).

In summary, if the *auritus* Subzone spans 0.53 m.y., and of this, 0.29 m.y. (minimum) represents the phases of tectonic calm (sedimentation), the duration of all tectonic phases or hiatuses is 0.24 m.y. (maximum). As there are two main tectonic phases, each of the phases is arbitrarily assumed to span 0.12 m.y. (maximum, Fig. 11). If we consider this estimated time span to be valid, the rates of tectonic deformation of the Aitzeta syncline can be estimated (Fig. 11).

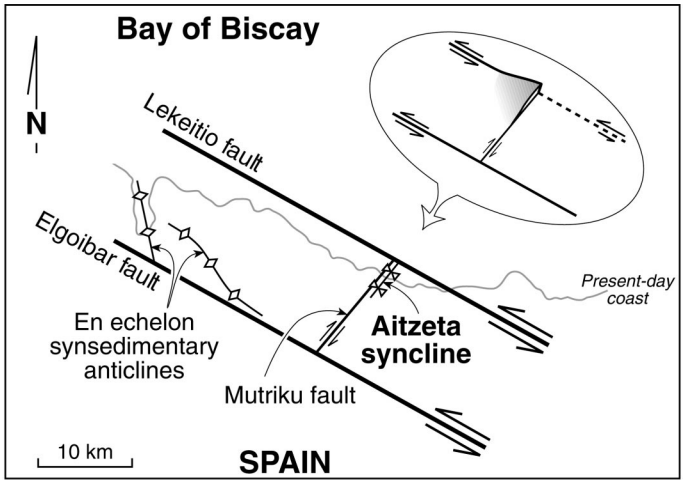

Figure 10. Schematic synsedimentary tectonic pattern of the region for middle Cretaceous time. The Aitzeta syncline and Mutriku fault are structures associated with a general sinistral strike-slip system (i.e., the Lekeitio and Elgoibar faults). Inset shows a model for the northeastern part of the Mutriku fault, where northwest-southeast compression and uplift result from differential slip rates along the Lekeitio fault.

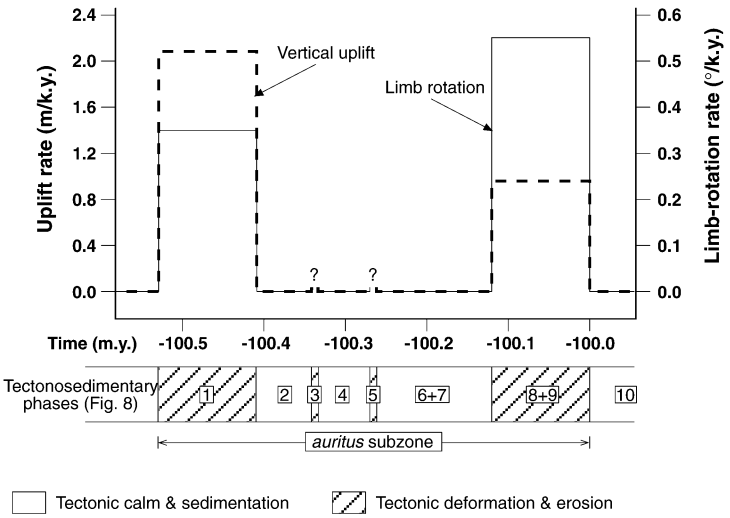

Figure 11. Rates of limb rotation and uplift during growth of the Aitzeta syncline. Chronostratigraphic distribution of the tectono-sedimentary phases represented in Figure 8 is shown. Time scale based on Gradstein et al. (1994).

Limb-Rotation Rates

Limb rotation in the Aitzeta syncline can be demonstrated, geometrically, for at least two major pulses and one minor pulse. For the purpose of calculating rates, only the two major limb-rotation pulses have been considered, because estimating the time span of the minor pulse is very difficult. The first pulse of limb rotation occurred in tectono-sedimentary phase 1 (Figs. 8, 9C, and 11), reaching a value of 42°. If a maximum duration of 0.12 m.y. is assumed for this pulse, the minimum limb-rotation rate calculated is 0.35°/k.y. The second major pulse corresponds to tectono-sedimentary phases 8 and 9 (Figs. 8, 9B and 11), with 66° of limb rotation. If a time span of 0.12 m.y. is also supposed for the second major pulse, the minimum limb-rotation rate calculated is 0.55°/k.y.

Uplift Rates

Progressive exhumation of the pretectonic units and their erosion in the uplifted fold limb are demonstrated by the presence of intraclasts in the resedimented deposits of the syntectonic unit. The total thickness of eroded units has been estimated on the basis of the difference in maximum measured thickness of the pretectonic units and the residual thicknesses after erosion. This calculation gives only a minimum value, because erosion did not balance the tectonically generated topographic uplift and a residual relief was preserved before burial by posttectonic sediments.

Two main uplift pulses occurred in the northwest limb of the Aitzeta syncline. The first took place during tectono-sedimentary phase 1 (Figs. 8, 9C, and 11), with the result that most of the original thickness of the pretectonic Mutriku unit (250 m thick) was eroded away. Erosion of this unit is indicated by the presence of redeposited fragments of the underlying Ondarroa unit in the unit being formed (Alkolea unit, subunit B) by the next

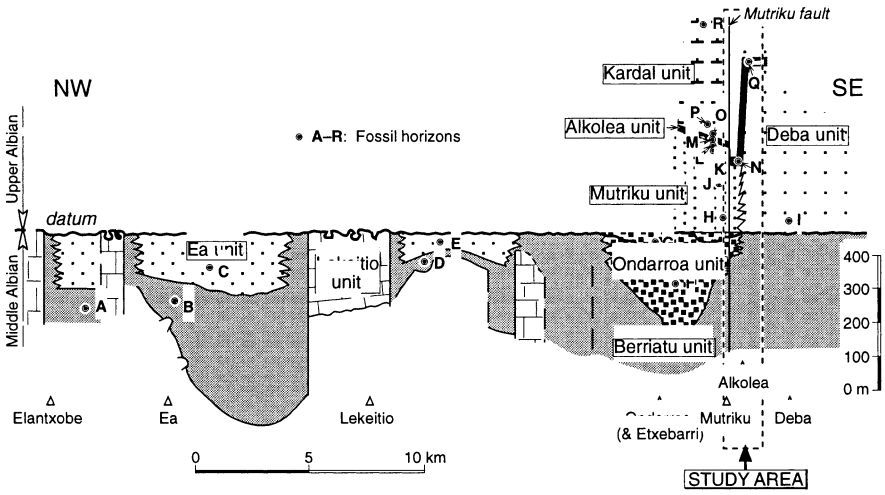

Figure A1. Schematic stratigraphic cross section of the Middle Albian–Upper Albian rocks from the Basque coast between Elantxobe and Deba, showing the relationship between different lithostratigraphic units and the stratigraphic location of the localities and fossil horizons (A–R) reported in Table A1 (modified from Agirrezabala, 1996).

minor tectonic pulse (Figs. 8 and 11, phase 3). The small amount of tectonic deformation and the apparent short-lived character of this minor pulse suggest that it involved little erosion and that the Mutriku unit had been largely eroded away during the earlier main-uplift phase. Thus, a minimum tectonic uplift of 250 m (eroded thickness) can be attributed to the first main pulse, giving a rate of 2.08 m/k.y.

The second main pulse of tectonic uplift occurred during tectono-sedimentary phases 8 and 9 (Figs. 8, 9B, and 11). At the end of this pulse, erosion had reduced the thickness of the Ondarroa unit by 100–140 m and had incised down to the lowermost Berriatu unit of limestone megabreccias. Consequently, this pulse implies an absolute uplift of 100–140 m and a tectonic uplift rate of 0.83–1.16 m/k.y.

Calculated rates show a nonlinear relationship between limb-rotation and uplift values (Fig. 11). Thus, from the first main tectonic pulse to the second, the limb-rotation rate increased (from 0.35°/k.y. to 0.55°/k.y.), yet the uplift rate decreased (from 2.08 m/k.y. to 0.83–1.16 m/k.y.). Decrease of uplift rate does not necessarily imply a decrease in tectonic activity. It can be explained by rapid initial crestal uplift followed by reduction of uplift rate as the fold tightened progressively and the limb overturned. This nonlinear relationship is consistent with progressive limb rotations postulated for theoretical models (Hardy and Poblet, 1994) and with other field examples (Holl and Anastasio, 1993; Vergés et al., 1996).

CONCLUSIONS

Deep-water syntectonic deposits and angular unconformities record the growth history of the Aitzeta structure. Biostratigraphic data based on ammonites provide a temporal framework for the analysis of deformation and sedimentation rates and permit reconstruction of a detailed history of structure growth. Although it is not evident from the surface mapping, structural and stratigraphic data support the interpretation of the Aitzeta structure as a fault-related syncline. It is a northeast-trending, southeast-facing, monoclinal syncline formed in response to reverse slip on the northwest-dipping, high-angle Mutriku fault. The Aitzeta syncline was mainly formed in response to local northwest-southeast compressive stress along the Mutriku fault. Nevertheless, oblique flexural-slip faults and drag folds suggest that dextral oblique movements took place at the same time. This right-lateral component is consistent with the expected antithetic movement interpreted for the wrench system of the Basque-Cantabrian basin as a whole.

Deformation of the uplifted limb was punctuated and took place during the *Callihoplites auritus* ammonite Subzone (late Albian), a period of ~0.53 m.y. Growth strata and angular unconformities show increasing dip with age, indicating that the syncline grew by progressive limb rotation rather than by instantaneous limb rotation. Bedding-plane faulting within the limb demonstrates that the fold grew by a flexural-slip mechanism. In addition, preserved tectonic structures and inverted clast stratigraphy prove the following: (1) total uplift is equal to or greater than the total exhumation of older units (350–390 m), (2) bedding was overturned (108° of total limb rotation), (3) reactivation of the syncline caused complex tectonic deformation, and (4) the limb was eroded, and exhumed deposits were resedimented.

Two major and two minor tectonic pulses occurred during the *auritus* Subzone time span, each separated by phases of tectonic calm and gentle hemipelagic sedimentation. The two major tectonic pulses coincided with the beginning and the end of the *auritus* Subzone. On the basis of conservative estimations, the maximum duration of each major pulse was 0.12 m.y. The first major pulse caused uplift of 250 m at a minimum rate of 2.08 m/k.y. and limb rotation of 42° at a minimum rate of 0.35°/k.y. The second major pulse caused uplift of 100–140 m at a minimum rate of 0.83–1.16 m/k.y. and limb rotation of 66° at a minimum rate of 0.55°/k.y. The deduced nonlinear relationship between the rates of uplift and limb rotation—the limb-rotation rate increased but the uplift rate decreased—is to be expected in folds undergoing progressive limb rotation.

APPENDIX. FOSSIL CONTENT AND DATING

Ammonites are comparatively rare; they are indigenous to the sediment in which they were buried and are not always well preserved. However, they, with the associated microfossils, have provided the basis of an accurate dating of the various units. Table A1 displays the various units' fossils, their dating, the location of specimens in specific horizons, and references to other authors for sequences and units laterally equivalent to those described in this paper. Figure A1 shows the stratigraphic location of fossiliferous horizons (A–R) reported in Table A1. The specimens listed in Table A1 are found in the collections of the Euskal Herriko Unibertsitatea, Estratigrafia eta Paleontologic Saila (EHUEPS), Leioa (Bizkaia, Spain).

ACKNOWLEDGMENTS

This research was supported by the Basque Government Project PI96/64 and the Basque Country University Project G39/98. We thank J.M. Narbaez Amasorrain for kindly giving us facilities to study several specimens of ammonites from his private collection. Adolfo Uriarte kindly supplied unpublished bathymetric data from the Mutriku Canyon. We appreciate constructive discussion with Gabriel Gutiérrez-Alonso and his comments on the structure. We are grateful to Andrew Meigs and Kari Bassett for their reviews of this paper that raised significant issues in the clarification of the interpretation of the structure. However, we are solely responsible for the content herein. We also thank Allen Glazner and Rebecca Dorsey for their constructive editorial reviews.

REFERENCES CITED

Agirrezabala, L.M., 1996, El Aptiense–Albiense del Nor-Vizcaíno entre Gernika y Azpeitia [Ph.D. thesis]: Bilbao, Spain, Euskal Herriko Unibertsitatea, 429 p.

Agirrezabala, L.M., and García-Mondéjar, J., 2001, Kinematic indicators and mineralization on the Elgoibar fault (Basque-Cantabrian basin): Geogaceta, v. 30.

Alonso, J.L., 1989, Fold reactivation involving angular unconformable sequences: Theoretical analysis and natural examples from the Cantabrian Zone (northwest Spain): Tectonophysics, v. 170, p. 57–77.

Boillot, G., and Malod, J., 1988, The north and north-west Spanish continental margin: A review: Revista de la Sociedad Geológica de España, v. 1, p. 295–316.

Choukroune, P., and Mattauer, M., 1978, Tectonique des plaques et Pyrénnées: Sur le fonctionnement de la faille transformante nord-pyrénéenne; comparaisons avec des modèles actuels: Bulletin de la Société Géologique de France, ser. 5, v. 20, p. 689–700.

Feuillée, P., 1967, Le Cénomanien des Pyrénées basques aux Asturies. Essai d'analyse stratigraphique: Mémoir de la Société Géologique de France, v. 46, 343 p.

García-Mondéjar, J., Agirrezabala, L.M., Aranburu, A., Fernández-Mendiola, P.A., Gómez-Pérez, I., López-Horgue, M., and Rosales, I., 1996, Aptian–Albian tectonic pattern of the Basque-Cantabrian basin (northern Spain): Geological Journal, v. 31, p. 13–45.

Gómez de Llarena, J., 1958, Datos paleontológicos del Flysch litoral de Guipuzcoa: El Vraconiense de septarias de Motrico: Notas y Comunicaciones del Instituto Geológico y Minero de España, v. 50, no. 2, p. 5–21.

Gradstein, F.M., Agterberg, F.T., Ogg, J.G., Hardenbol, J., van Veen, P., Thierry, J., and Huang, Z., 1994, A Mesozoic time scale: Journal of Geophysical Research, v. 99B, p. 24051–24074.

Hardenbol, J., Thierry, J., Farley, M.B., Jacquin, T., Graciansky, P.C., and Vail, P.R., 1998, Mesozoic and Cenozoic chronostratigraphic framework of European basins, *in* Graciansky, P.C., Hardenbol, J., Jacquin, T., and Vail, P.R., eds., Mesozoic and Cenozoic sequence stratigraphy of European basins: SEPM (Society for Sedimentary Geology) Special Publication 60, p. 3–13.

Hardy, S., and Poblet, J., 1994, Geometric and numerical model of progressive limb rotation in detachment folds: Geology, v. 22, p. 371–374.

Holl, J.E., and Anastasio, D.J., 1993, Paleomagnetically derived folding rates, southern Pyrenees, Spain: Geology, v. 21, p. 271–274.

López-Horgue, M.A., Owen, H.G., Rodriguez-Lázaro, J., Orue-Etxebarria, X., Fernández-Mendiola, P.A., and García-Mondéjar, J., 1999, Late Albian–early Cenomanian stratigraphic succession near Estella-Lizarra (Navarra, central northern Spain) and its regional and interregional correlation: Cretaceous Research, v. 20, p. 369–402.

Magniez, F., and Rat, P., 1972, Les foraminifères des formations à spongiaires et Tritaxia dans l'Aptien–Albien Cantabrique (Espagne): Revista Española de Micropaleontología, special issue, XXX Aniversario Empresa Nacional Adaro, p. 159–178.

Owen, H.G., 1976, The stratigraphy of the Gault and Upper Greensand of the Weald: Proceedings of the Geologists' Association, v. 86, p. 475–498.

Plestch, T., 1990, Kartierung, Sedimentologie und Stratigraphie im ''Schwarzen Flysch von Deva'' bei Saturraran, Prov. Bizkaia/Gipuzkoa, N-Spanien [M.Sc. thesis]: Tübingen, Germany, University of Tübingen, 103 p.

Rat, P., 1959, Les pays crétacés Bascocantabriques (Espagne) [Thèse doctorale]: Dijon, France, Publications de l'Université de Dijon, v. 23, 525 p.

Reitner, J., 1987, Mikrofazielle, paläokologische und paläogeographische analyse ausgewählter Vorkommen flachmariner Karbonate im Basko-Kantabrischen Strike-Slip Fault Becken System (Nord-spanien) an der Wenden von der Unterkreide zur Oberkreide: Documenta Naturae, v. 40, p. 1–239.

Riba, O., 1976, Syntectonic unconformities of the Alto Cardener, Spanish Pyrenees: A genetic interpretation: Sedimentary Geology, v. 15, p. 213–233.

Schneider, C.L., Hummon, C., Yeats, R.S., and Huftile, G.L., 1996, Structural evolution of the northern Los Angeles basin, California, based on growth strata: Tectonics, v. 15, p. 341–355.

Scholle, P.A., Arthur, M.A., and Ekdale, A.A., 1983, Pelagic environment, *in* Scholle, P.A., Bebout, D.G., and Moore, C.H., eds., Carbonate depositional environments: American Association of Petroleum Geologists, p. 620–691.

Suppe, J., 1983, Geometry and kinematics of fault-bend folding: American Journal of Science, v. 283, p. 684–721.

Suppe, J., Sàbat, F., Muñoz, J.A., Poblet, J., Roca, E., and Vergés, J., 1997, Bed-by-bed fold growth by kink-band migration: Sant Llorenç de Morunys, eastern Pyrenees: Journal of Structural Geology, v. 19, p. 443–461.

Tanner, P.W.G., 1989, The flexural-slip mechanism: Journal of Structural Geology, v. 11, p. 635–655.

Vergés, J., Burbank, D.W., and Meigs, A., 1996, Unfolding: An inverse approach to fold kinematics: Geology, v. 24, p. 175–178.

Wiedmann, J., and Owen, H.G., 2001, Late Albian ammonite biostratigraphy of the Kirchrode I borehole, Hannover, Germany: Paleogeography, Paleoclimatology, Paleoecology, v. 174, p. 161–180.

MANUSCRIPT RECEIVED BY THE SOCIETY JUNE 28, 2001
REVISED MANUSCRIPT RECEIVED AUGUST 22, 2001
MANUSCRIPT ACCEPTED OCTOBER 26, 2001

Printed in the USA

Organic Geochemistry 39 (2008) 1185–1188

Contents lists available at ScienceDirect

Organic Geochemistry

journal homepage: www.elsevier.com/locate/orggeochem

Geochemical correlation of pyrobitumen fills with host mid-Cretaceous Black Flysch Group (Basque-Cantabrian Basin, western Pyrenees)

Luis M. Agirrezabala [a,*], Carmen Dorronsoro [b], Albert Permanyer [c]

[a] Estratigrafia eta Paleontologia Saila, Euskal Herriko Unibertsitatea, 644 P.K., 48080 Bilbo, The Basque Country, Spain
[b] Kimika Aplikatua Saila, Euskal Herriko Unibertsitatea, 1072 P.K., 20080 Donostia, The Basque Country, Spain
[c] Departament de Geoquímica, Petrologia i Prospecció Geològica, Universitat de Barcelona, Martí i Franquès s/n, 08028 Barcelona, Catalonia, Spain

ARTICLE INFO

Article history:
Received 4 September 2007
Received in revised form 18 March 2008
Accepted 19 March 2008
Available online 27 March 2008

ABSTRACT

Abundant syndepositional pyrobitumen fills occur within Albian hydrothermal vent carbonates of the organic-rich Black Flysch Group in the Basque-Cantabrian Basin, indicating that these carbonates were charged with oil during Albian times. A carbon isotopic study of pyrobitumens and samples of candidate oil generating rocks (Jurassic and Albian host rock units) as well as Carboniferous-sourced condensate was undertaken to test an Albian source hypothesis for the pyrobitumens. On the basis of similar isotopic ratio values, the pyrobitumens show a strong positive correlation with the host Black Flysch Group. This is supported by Stahl-type curves and a Sofer plot, which show that the pyrobitumens best match the host Albian deposits, whereas the Jurassic source rock and the Carboniferous sourced condensate plot separately. This new Albian pyrobitumen-source correlation demonstrates the existence of an oil generating rock unrecognised till now in the Basque-Cantabrian Basin – the mid-Cretaceous Black Flysch Group.

1. Introduction

Albian authigenic carbonates containing abundant pyrobitumen fills crop out near the village of Mutriku in the northern margin of the Basque-Cantabrian Basin (western Pyrenees). The carbonates and pyrobitumen fills occur within the organic rich Black Flysch Group, which is composed of deep water siliciclastic turbiditic deposits. A recent interdisciplinary study has interpreted these carbonate deposits as by-products of the oxidation of oil-rich hydrothermal fluids vented at the Albian seabed, suggesting a hydrothermal petroleum generation at shallow depth sourced from host organic-rich deposits (Agirrezabala, 2007, unpublished results; Agirrezabala et al., 2007). The aim of this paper was to investigate the hypothesis of an Albian source by means of carbon isotopic analysis of the pyrobitumens, the candidate oil generating rocks (Jurassic black shales and Albian Black Flysch Group deposits) and the hydrocarbons in the basin (Carboniferous-sourced Gaviota condensate). The Jurassic and Carboniferous rocks constitute the source of commercial oil and gas accumulations, respectively, in the basin (Quesada et al., 1997; Martínez del Olmo and Mallo, 2002), whereas the Albian Black Flysch Group has never been proposed as a potential oil generating rock.

2. Geological setting

The Middle Albian-Lower Cenomanian Black Flysch Group is an extensive unit represented in the overall Pyrenean region and composed of deep water siliciclastic turbidites and hemipelagic deposits. In the Basque-Cantabrian Basin, these deposits are organic rich [total organic carbon (TOC) around 1%] and filled small, confined strike-slip subbasins, where seabed sub oxic conditions favoured preservation of the abundant organic input. Both petrographic analysis and the presence of abundant macroscopic woody fragments and trunks (up to 1.8 m in length) suggest a mainly terrestrial origin for the organic matter. Some

* Corresponding author. Tel.: +34 946015425; fax: +34 946013500.
E-mail address: l.agirrezabala@ehu.es (L.M. Agirrezabala).

0146-6380/$ - see front matter © 2008 Elsevier Ltd. All rights reserved.
doi:10.1016/j.orggeochem.2008.03.012

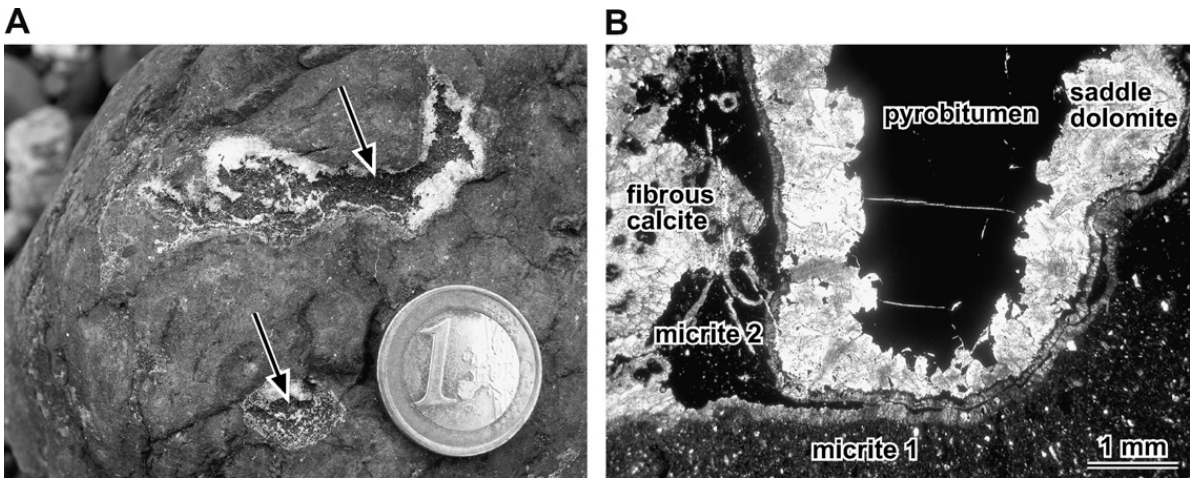

Fig. 1. Albian hydrothermal vent carbonates with pyrobitumen fills. (A) Outcrop photograph of pyrobitumens (arrows) filling tubular structures. (B) Microphotograph of a carbonate tubular structure showing the main carbonate phases and the youngest pyrobitumen fill.

sub-basin bounding active faults channelized the expulsion of hydrothermal fluids rich in hydrocarbons. The expulsion occurred contemporaneously with intense volcanism in the basin. Oxidation of the vented hydrocarbons led to the formation at or near the seabed of isotopically depleted authigenic carbonates, which contain the abundant pyrobitumen fills studied here (Agirrezabala, 2007, unpublished results; Agirrezabala et al., 2007). These carbonate deposits were buried by a very thick (~8000 m) latest Albian-Middle Eocene succession and subsequently folded and faulted during the Late Eocene basin inversion (Gómez et al., 2002). Host Black Flysch deposits in the study area have a vitrinite reflectance of 2.13%.

The pyrobitumens appear as black, solid, brittle masses up to 7 cm long and display a concoidal fracture when broken (Fig. 1A). They usually fill voids lined by hydrothermal calcites and saddle dolomite (Fig. 1A and B) with oxygen isotopic signatures indicative of formation temperatures up to 109 °C. Under epifluorescence microscopy (UV) the samples do not show any fluorescence, in accord with their overmature stage.

3. Materials and methods

A set of 11 samples of pyrobitumen-rich carbonates, 17 samples of Jurassic and Albian candidate oil generating rocks, as well as one Carboniferous-sourced condensate (Gaviota field) were studied. All the rock samples were submitted to Rock-Eval pyrolysis following the technique described by Espitalié et al. (1985a, b, 1986). Of these, five samples were selected on the basis of their TOC content and stratigraphic position and analysed for their stable carbon isotopic composition: two pyrobitumen samples extracted from centimetric pyrobitumen fills using a hand held microdrill, one sample from each candidate Jurassic and Albian oil generating rocks and one Carboniferous-sourced condensate. Carbon isotope measurements of the whole oil as well as whole extracts, saturated and aromatic hydrocarbon fractions, and NSO compounds were performed using a Thermo Finnigan Series 1112 elemental analyser coupled to a Finnigan Mat Delta C mass spectrometer. The reference materials were graphite (USGS24), saccharose (IAEA-CH6), polyethylene (IAEACH7) and oil (NBS-22).

Table 1
Rock-Eval pyrolysis results from rock samples (HI, hydrogen index; OI, oxygen index; TPI, total production index; RC, residual carbon)

Sample	S1[a]	S2[a]	S3[a]	TOC (%)	HI[b]	OI[c]	T_{max} (°C)	TPI	RC
Albian pyrobitumen-rich vent carbonates									
HH-11	0.07	0.08	0.09	1.12	7	8	526	0.47	1.11
HH-12	0.08	0.36	0.23	1.91	19	12	537	0.18	1.87
HH-13	0.1	0.35	0.29	3.15	11	9	536	0.22	3.11
HH-14	0.07	0.1	0.26	1.25	8	21	529	0.41	1.24
HH-15	0.08	0.44	0.34	3.19	14	11	556	0.15	3.15
HH-16	0.12	0.54	0.4	2.9	19	14	545	0.18	2.85
HH-17	0.11	0.39	0.14	3	13	5	521	0.22	2.96
HH-34	0.26	0.32	0.15	3.17	10	5	482	0.45	3.12
HH-35	0.06	0.16	0.15	0.98	16	15	552	0.27	0.96
HH-36	0.24	0.44	0.42	3.27	13	13	563	0.35	3.21
HH-37	0.06	0.38	0.13	2.16	18	6	556	0.14	2.12
Albian Black Flysch Group deposits									
BURU-1	0.02	0.05	0.16	1.64	3	10	563	0.29	1.63
BURU-2	0.03	0.07	0.05	1.1	6	5	563	0.3	1.09
BURU-3	0.03	0.04	0.04	1	4	4	514	0.43	0.99
BURU-4	0.02	0.02	0.09	0.69	3	13	446	0.5	0.69
BURU-5	0.03	0.07	0.06	0.65	11	9	550	0.3	0.64
BURU-6	0.08	0.04	0.03	0.69	6	4	463	0.67	0.68
SAT-1	0.02	0.01	0.17	0.5	2	34	463	0.67	0.5
SAT-2	0.02	0.02	0.15	0.43	5	35	473	0.5	0.43
SAT-3	0.02	0.16	0.07	1.16	14	6	533	0.11	1.15
SAT-4	0.02	0.05	0.26	1.49	3	17	572	0.29	1.48
HH-25	0.04	0.09	0.16	0.78	12	21	527	0.31	0.77
HH-26	0.03	0.06	0.08	0.84	7	10	528	0.33	0.83
HH-27	0.04	0.07	0.1	0.9	8	11	521	0.36	0.89
HH-28	0.04	0.07	0.05	1	7	5	529	0.36	0.99
Jurassic black shales									
CP-1	0.03	0.02	0.3	0.44	5	68	525	0.6	0.44
CP-5	0.02	0.12	0.74	7.85	2	9	591	0.14	7.84
CP-6	0.03	0.12	0.6	5.05	2	12	589	0.2	5.04

[a] S1, S2 = mg HC/g rock; S3 = mg CO_2/g rock.
[b] HI = mg HC/g TOC.
[c] OI = mg CO_2/g TOC.

4. Results and discussion

Rock-Eval pyrolysis results for all the rock samples show high T_{max} values and low hydrogen index (HI) values (Table 1). Nevertheless, extremely low S2 yields (<0.2 mg HC/g rock) make T_{max} values unreliable (Espitalié et al., 1985a, b, 1986). The Albian vent carbonate samples yielded relatively high TOC values (up to 3.27%) consistent with their abundant pyrobitumen fills. Mean TOC value from the host Black Flysch Group is around 1% (0.43–1.64%), sufficient to constitute an oil-generating unit. The Jurassic black shales afforded values up to 7.85% and constitute the best oil source rock in the basin.

Carbon isotopic composition was determined firstly for whole pyrobitumen, condensate and source rock extracts, and secondly for saturated and aromatic hydrocarbons and polar (NSO) compounds (Table 2). All samples, except GAV-1 condensate, are rich in sulfur, which could have interfered with the isotopic measurements and caused a small deviation in mass balance. Genetic relationships between hydrocarbons and their sources may be deduced by using Stahl type (Stahl, 1978) and Sofer plots (Sofer, 1984) (Fig. 2A and B). These diagrams show that the pyrobitumens are genetically related and best match the Albian oil generating rock. The Jurassic source rock and the Carboniferous-sourced condensate plot separately. According to Schoell et al. (1990), there is a negligible isotopic fractionation between organic source and hydrocarbons produced during hydrothermal alteration. Therefore, the $\delta^{13}C_{whole}$ value of the pyrobitumen can be used to constrain the source from which it was derived. The extracts from the pyrobitumen and the Albian Black Flysch samples exhibit similar mean $\delta^{13}C_{whole}$ values (−25.28‰ and −25.02‰, respectively), which coincide with contempora-

Table 2
Extract composition and $\delta^{13}C$ values (vs. PDB) for whole extracts, saturated and aromatic fractions, and NSO compounds

Sample	Extract				$\delta^{13}C$‰			
	EOM[a] (mg)	Sat (%)	Aro (%)	NSO (%)	Whole	Sat	Aro	NSO
Albian pyrobitumen fill (HH-34a)	4.06	15.27	11.58	73.15	−25.26	−27.19	−23.90	−27.34
Albian pyrobitumen fill (HH-36a)	2.72	17.47	11.15	71.38	−25.30	−27.41	−23.79	−27.51
Black Flysch Group deposits (BURU-5)	3.70	25.95	11.89	62.16	−25.02	−27.01	−25.09	−26.60
Jurassic black shales (CP-5)	8.49	11.31	1.53	87.16	−27.83	−27.00	−27.90	−28.40
Carboniferous-sourced condensate (GAV-1)	11.69	62.50	36.39	1.11	−23.26	−24.02	−22.93	nd[b]

[a] Extractable organic matter.
[b] Not determined.

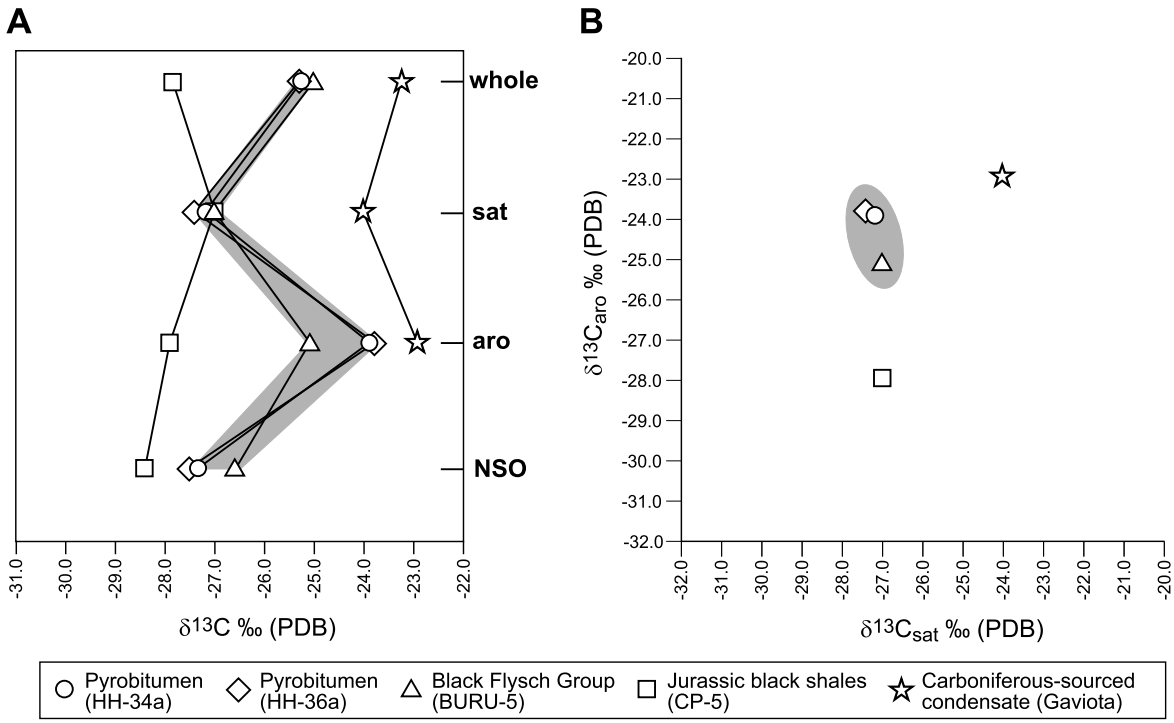

Fig. 2. Carbon isotopic composition of whole, saturated and aromatic hydrocarbon fractions and NSO compounds for pyrobitumens, Black Flysch Group, Jurassic source rock and Carboniferous-sourced condensate. (A) Stahl type curves. (B) Sofer type $\delta^{13}C_{sat}$ vs. $\delta^{13}C_{aro}$ diagram. Shadow areas indicate field range for pyrobitumen and Black Flysch Group.

neous Late Albian terrestrial organic matter values from North Atlantic Ocean (Hofmann et al., 2000). The Jurassic source rock ($\delta^{13}C_{whole}$ −27.83‰) and Carboniferous Gaviota condensate ($\delta^{13}C_{whole}$ −23.26‰) afforded isotopic values which clearly differentiate them from the pyrobitumen value. On the other hand, they are in accord with the isotope signatures of the Jurassic oil from the Ayoluengo field (Quesada et al., 1997) and worldwide Carboniferous coals and fossil plants (e.g. Beerling et al., 2002), respectively.

The carbon isotopic compositions of saturated and aromatic fractions and NSO compounds for the pyrobitumen samples (mean values: $\delta^{13}C_{sat}$ −27.30‰, $\delta^{13}C_{aro}$ −23.84‰, $\delta^{13}C_{NSO}$ −27.42‰) and host Black Flysch samples ($\delta^{13}C_{sat}$ −27.01‰, $\delta^{13}C_{aro}$ −25.09‰, $\delta^{13}C_{NSO}$ −26.60‰) are similar, with slightly depleted $^{13}C_{aro}$ and enriched $^{13}C_{NSO}$ values for the latter (Fig. 2A and B). Normally, oils show $\delta^{13}C$ variations of up to 1.5‰ relative to their source rock (Peters and Moldowan, 1993). In fact, this is observed for the pyrobitumen extract when compared with its Black Flysch host. The saturated and aromatic fractions and NSO compounds of the pyrobitumens clearly obey this "1.5‰ maximum difference rule" when compared with the same fractions and compounds from the Albian Black Flysch Group. On the other hand, the Jurassic source rock shows a similar saturated fraction signature ($\delta^{13}C_{sat}$ −27.00‰) but isotopically much lighter aromatic fractions ($\delta^{13}C_{aro}$ −27.90‰) and NSO compounds ($\delta^{13}C_{NSO}$ −28.40‰) than those of the pyrobitumen. In contrast, both saturated ($\delta^{13}C_{sat}$ −24.02‰) and aromatic ($\delta^{13}C_{aro}$ −22.93‰) hydrocarbons of the Carboniferous condensate show a clear ^{13}C enrichment when compared with the pyrobitumen samples (Fig. 2A and B). Therefore, the isotopic dissimilarity between the pyrobitumens and both Jurassic and Carboniferous samples suggests that neither were a source for the pyrobitumens.

5. Conclusions

The carbon isotopic compositions of whole extracts as well as saturated and aromatic fractions and NSO compounds of the Albian pyrobitumen fills correlate positively with those of the host Black Flysch Group, whereas both Jurassic candidate source rock and Carboniferous-sourced Gaviota condensate display a clear isotopic dissimilarity. This pyrobitumen-source correlation demonstrates the existence of a previously unrecognised petroleum-generating unit, the organic rich Black Flysch Group. On the other hand, the syndepositional character of the pyrobitumen fills and their association with high temperature carbonates provide evidence for a link between hydrothermal activity and generation and expulsion of petroleum.

Acknowledgements

The study was funded by the Euskal Herriko Unibertsitatea (Projects EHU06/62, UNESCO06/03 and 9UPV00121.310-13556/2001) and the Ministerio de Educación y Ciencia (Projects CGL2006-05491/BTE and BTE2003-04823). The authors acknowledge Repsol-YPF for providing the Gaviota condensate. They are grateful to Mrs M. Sibila for the analytical work. H. Cander and C. Boreham are sincerely thanked for reviewing the manuscript.

Guest Associate Editor—**A. Milkov**

References

Agirrezabala, L.M., 2007. Geochemistry of ancient vent deposits as record of the temporal and spatial evolution of expulsed fluids: a case study from west Pyrenees. Abstract. In: 23rd International Applied Geochemistry Symposium (IAGS), Oviedo. p. 108.

Agirrezabala, L.M., Dorronsoro, C., Permanyer, A., 2007. Mid-Cretaceous hydrothermal petroleum generation and expulsion in the Basque-Cantabrian Basin (western Pyrenees). Abstract. In: 23rd International Applied Geochemistry Symposium (IAGS), Oviedo. p. 109.

Beerling, D.J., Lake, J.A., Berner, R.A., Hickey, L.J., Taylor, D.W., Royer, D.L., 2002. Carbon isotope evidence implying high O_2/CO_2 ratios in the Permo-Carboniferous atmosphere. Geochimica et Cosmochimica Acta 66, 3757–3767.

Espitalié, J., Deroo, G., Marquis, F., 1985a. La pyrolyse Rock-Eval et ses applications. Part I. Revue de l'Institut Français du Pétrole 40, 563–578.

Espitalié, J., Deroo, G., Marquis, F., 1985b. La pyrolyse Rock-Eval et ses applications. Part II. Revue de l'Institut Français du Pétrole 40, 755–784.

Espitalié, J., Deroo, G., Marquis, F., 1986. La pyrolyse Rock-Eval et ses applications. Part III. Revue de l'Institut Français du Pétrole 41, 73–89.

Gómez, M., Vergés, J., Riaza, C., 2002. Inversion tectonics of the northern margin of the Basque Cantabrian Basin. Bulletin de la Société Géologique de France 173, 449–459.

Hofmann, P., Ricken, W., Schwark, L., Leythaeuser, D., 2000. Carbon–sulfur–iron relationships and $\delta^{13}C$ of organic matter for late Albian sedimentary rocks from the North Atlantic Ocean: paleoceanographic implications. Palaeogeography, Palaeoclimatology, Palaeoecology 163, 97–113.

Martínez del Olmo, W., Mallo, J.M., 2002. Non-renewable energy resources: oil and gas. In: Gibbons, W., Moreno, T. (Eds.), Geology of Spain. Blackwell, pp. 494–499.

Peters, K.E., Moldowan, J.M., 1993. The Biomarker Guide: Interpreting Molecular Fossils in Petroleum and Ancient Sediments. Prentice Hall, Englewood Cliffs, NJ.

Quesada, S., Dorronsoro, C., Robles, S., Chaler, R., Grimalt, J.O., 1997. Geochemical correlation of oil from Ayoluengo field to Liassic black shale units in the southwestern Basque-Cantabrian Basin (northern Spain). Organic Geochemistry 27, 25–40.

Schoell, M., Hwang, R.J., Simoneit, B.R.T., 1990. Carbon isotope composition of hydrothermal petroleums from Guaymas Basin, Gulf of California. Applied Geochemistry 5, 65–69.

Sofer, Z., 1984. Stable carbon isotope composition of crude oils: application to source depositional environment and petroleum alteration. American Association of Petroleum Geologists Bulletin 66, 31–49.

Stahl, W.J., 1978. Source rock-crude oil correlation by isotopic type-curves. Geochimica et Cosmochimica Acta 42, 1573–1577.

Sedimentology (2009) **56,** 969–996 doi: 10.1111/j.1365-3091.2008.01013.x

Mid-Cretaceous hydrothermal vents and authigenic carbonates in a transform margin, Basque-Cantabrian Basin (western Pyrenees): a multidisciplinary study

LUIS M. AGIRREZABALA
Estratigrafia eta Paleontologia Saila, Euskal Herriko Unibertsitatea, 644 P.K., E-48080 Bilbo, The Basque Country, Spain (E-mail: l.agirrezabala@ehu.es)

Associate Editor: John Reijmer

ABSTRACT

A comprehensive study of authigenic carbonates and associated fauna in Late Albian organic-rich, deep-water deposits (the Black Flysch Group) reveals that carbonate precipitation was a by-product of the anaerobic oxidation of hydrocarbon-rich hydrothermal fluids. The authigenic carbonates are exposed along the Kardala and Alkolea sea cliffs in the western Pyrenees. The two vent carbonates occur 1 km apart adjacent to the synsedimentary, right-reverse Mutriku fault, but in contrasting structural domains: the Kardala carbonates occur on a structural ridge (hangingwall) and the Alkolea carbonates are positioned at the base of an erosional scarp (folded downward footwall). The similarity in pattern of the carbonate phases and complex paragenetic events for both vent precipitates implies that hydrothermal fluid generation processes and pore-water evolution during early and late diagenesis were similar. Nevertheless, a comparison of the geochemistry, fossil fauna and morphology of carbonate structures of both precipitates suggests that the vented hydrocarbon type, flow intensity and temperature of hydrothermal fluids were different. At the Kardala vent, intense focused flow of hot (up to 109 °C), oil-rich fluids were generated, allowing the development of a relatively abundant chemosynthesis-based fauna. In contrast, at the Alkolea vent, diffuse flows of warm, thermogenic methane-rich fluids were expelled to the sea floor and no chemosynthetic fauna developed. These differences are related to the contrasting structural setting of each locality. Similar $\delta^{13}C_{org}$ values for both pyrobitumen-fills and host unit organic matter suggest that the hydrocarbon source was the Black Flysch Group. Contact alteration of these organic-rich sediments by syndepositional hydrothermal fluids generated hydrothermal petroleum (oil and gas hydrocarbons) which probably migrated updip to the sea floor by contemporary compression tectonics.

Keywords Authigenic carbonate, Basque-Cantabrian Basin, hydrothermal vent, mid-Cretaceous, Pyrenees, transform margin.

INTRODUCTION

Hydrothermal vent and cold-seep carbonates are associated with fluid flow along active and passive continental margins worldwide (Campbell, 2006). Carbonate precipitation is a by-product of microbial activity which causes anaerobic oxidation of methane (AOM) (Boetius *et al.*, 2000; Valentine, 2002). Hydrothermal vents are discharges of warm to hot fluids derived from interactions between hot igneous rocks and circulating sea water. In contrast, hydrocarbon seeps are usually discharges of cold fluids rich in hydrocarbons released from buried sedimentary basins (Campbell, 2006). Modern vent and seep biota are dominated by chemoautotrophic

microbes and communities of mega-invertebrates, some with endosymbiotic bacteria (reviewed in Van Dover, 2000). Analogous rocks have been reported from ancient marine deposits of Early Archaean to Quaternary age worldwide (reviewed in Campbell, 2006). Stratigraphic, structural, petrological, textural, geochemical and palaeontological characteristics and molecular biomarkers are used for identifying ancient hydrothermal vent and seep carbonates (Beauchamp & von Bitter, 1992; Campbell & Bottjer, 1993; Little *et al.*, 1998; Campbell *et al.*, 2002; Flügel, 2004; Peckmann & Thiel, 2004; Campbell, 2006). In contrast to numerous Cenozoic examples, the Mesozoic record of vents and seeps is rather sparse (Beauchamp & Savard, 1992; Gaillard *et al.*, 1992; Campbell & Bottjer, 1993; Kelly *et al.*, 1995, 2000; Kauffman *et al.*, 1996; Campbell *et al.*, 2002; Gómez-Pérez, 2003; Little *et al.*, 2004). Moreover, ancient hydrothermal vents are less abundant than cold seeps, and only four Mesozoic examples have been reported worldwide (Campbell, 2006).

Most of the fluids associated with cold seeps have their origin in deeply buried hydrocarbon reservoirs which emerge through various permeable pathways such as faults, other fractures and sedimentary discontinuities (Orange *et al.*, 1999). In some hydrothermal vents, liquid and gaseous hydrocarbons originate from hydrothermal alteration of organic-rich sediments at shallow depth, as documented in the Guaymas Basin (Einsele *et al.*, 1980; Simoneit & Lonsdale, 1982) and the Northern Pacific Ocean (Rushdi & Simoneit, 2002a,b). The petrological and geochemical characteristics of hydrocarbon-derived precipitates are controlled largely by the nature of the fluids and flow pathways (Levin, 2005). In modern vents and seeps, the type of escaping hydrocarbon determines the magnitude of the carbon isotope depletion of the resulting precipitates (Aharon, 2000), whereas fluid temperature among other factors (e.g. diagenesis, mineralogy, meteoric water, hydrate dissociation, salinity) is recorded by the oxygen isotopic signature. Fluid flow intensity at the sea floor is reflected in the abundance of mega-fauna (Sibuet & Olu, 1998; Judd & Hovland, 2007) and the morphology of the carbonate structures (Orange *et al.*, 1999). This multidisciplinary study characterizes and interprets mid-Cretaceous authigenic carbonates from the Kardala and Alkolea in the western Pyrenees. The present study demonstrates that the authigenic carbonates are the by-products of hydrocarbon-rich hydrothermal fluids adjacent to the synsedimentary Mutriku fault. To identify and characterize relationships between geological, geochemical and biological processes, a number of complementary methodologies have been employed, including sedimentological and stratigraphic field studies, fossil biota characterization, petrological and stable isotopic analyses of carbonate phases, and characterization and isotopic analysis of organic matter. On the basis of the results obtained, the main controls in the formation of both the Kardala and Alkolea authigenic carbonates are interpreted and discussed in terms of the nature of fluids (composition and temperature), relative intensity of flows, hydrocarbon source and fluid expulsion process.

GEOLOGICAL SETTING

At the Kardala and Alkolea localities, authigenic carbonates crop out near the coastal village of Mutriku in the northern margin of the Basque-Cantabrian Basin (Fig. 1). This Mesozoic basin is 200 km long and trends east–west in the westernmost part of the Pyrenean realm, which originated by rifting related to the Cretaceous opening of the Bay of Biscay and the eastward drift of the Iberian plate (Montadert *et al.*, 1974). During the mid-Cretaceous, the northern margin of the Basque-Cantabrian Basin and the overall Pyrenean realm were affected by transtension due to sinistral strike–slip deformation, which created numerous small sub-basins that were filled with siliciclastic, deep-water, organic-rich turbiditic deposits (Puigdefábregas & Souquet, 1986; Agirrezabala, 1996). These deposits constitute the Middle Albian–Lower Cenomanian Black Flysch Group which extends along the entire Pyrenean realm (Souquet *et al.*, 1985). In the study area, the Black Flysch Group is subdivided into seven informal lithostratigraphic units (Agirrezabala, 1996; Agirrezabala *et al.*, 2002) (Figs 1B and 2). The Kardala and Alkolea carbonates occur in the Kardala and Alkolea units, respectively, and are composed of lutites, nodular carbonates and local breccias. Stratigraphic, sedimentological and structural data, as well as the tectono-sedimentary interpretations relative to these units, have already been documented in detail by Agirrezabala (1996) and Agirrezabala *et al.* (2002, 2003).

The Kardala and Alkolea authigenic carbonates are dated within the *Callihoplites auritus* ammonite Subzone (European province zonation of the Late Albian) *pro parte* (Agirrezabala, 1996;

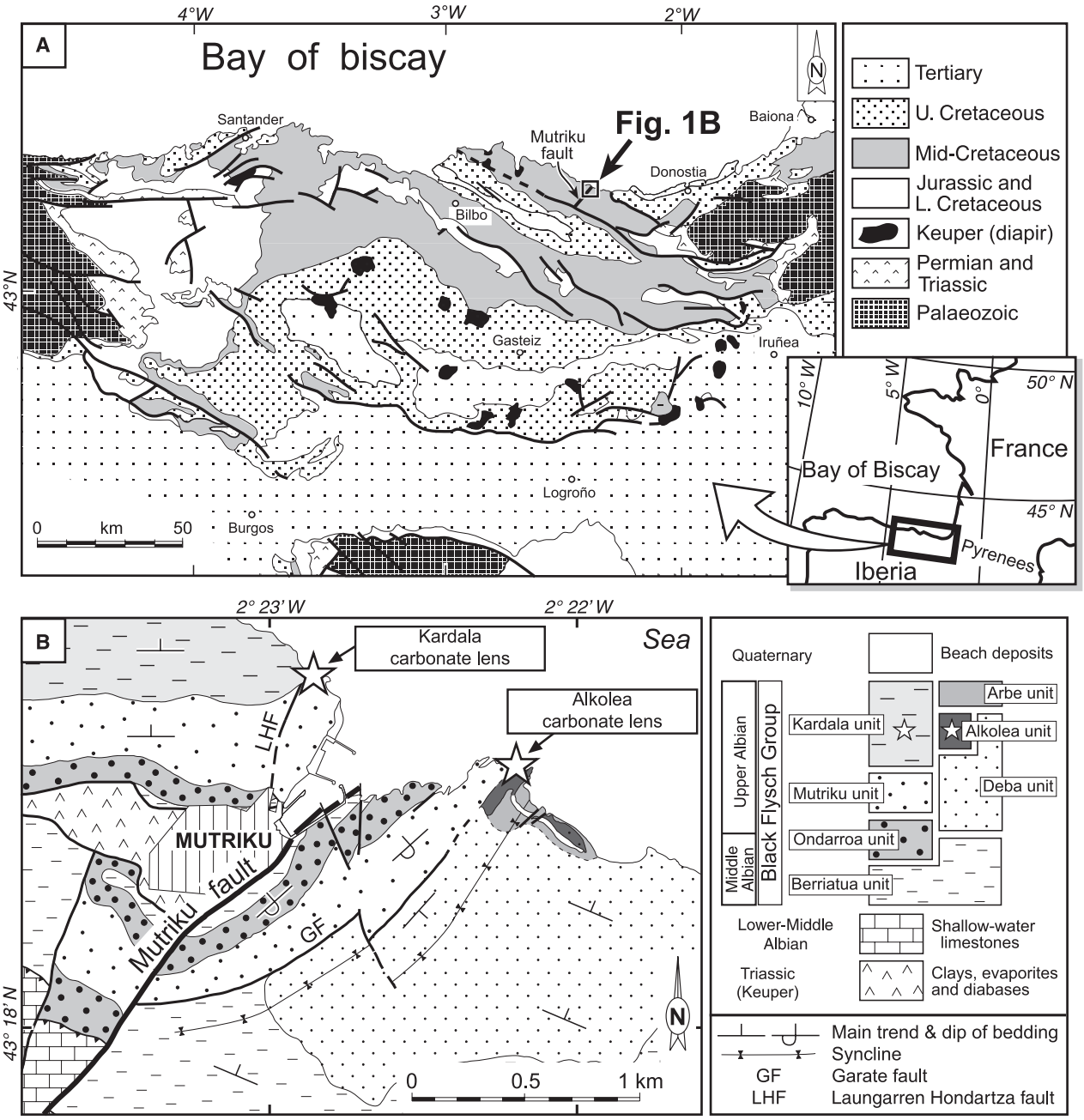

Fig. 1. (A) Geological map of the Basque-Cantabrian Basin in the western Pyrenees with an indication of the study area. (B) Detailed geology of the two authigenic carbonate lenses (stars) of this study.

Agirrezabala *et al.*, 2002, 2003) and, therefore, they were formed within a maximum period of 1·3 Myr (Ogg *et al.*, 2004). The outcrops of the Kardala and Alkolea carbonate occur 1 km apart, next to and on both sides of the north-east-trending Mutriku fault, a high-angle, right-reverse fault which was active during authigenic carbonate precipitation (Figs 1 and 3A) (Agirrezabala *et al.*, 2002). During this period, the Kardala carbonates precipitated on the uplifted north-western hangingwall (Agirrezabala, 1996), adjacent to a minor fault (Laugarren Hondartza fault; Figs 1B and 3A). Contemporaneously, on the south-eastern footwall, the south-east-dipping Aitzeta monoclinal syncline developed in two main pulses that were recorded in the deposits as two high-angle, angular unconformities (AU1 and AU2, base and top of the *C. auritus* Subzone, respectively; Figs 2 and 4A) (Agirrezabala *et al.*, 2002). Both unconformities are overlain by resedimented blocks derived from denudated underlying units. The Alkolea carbonates overlie and

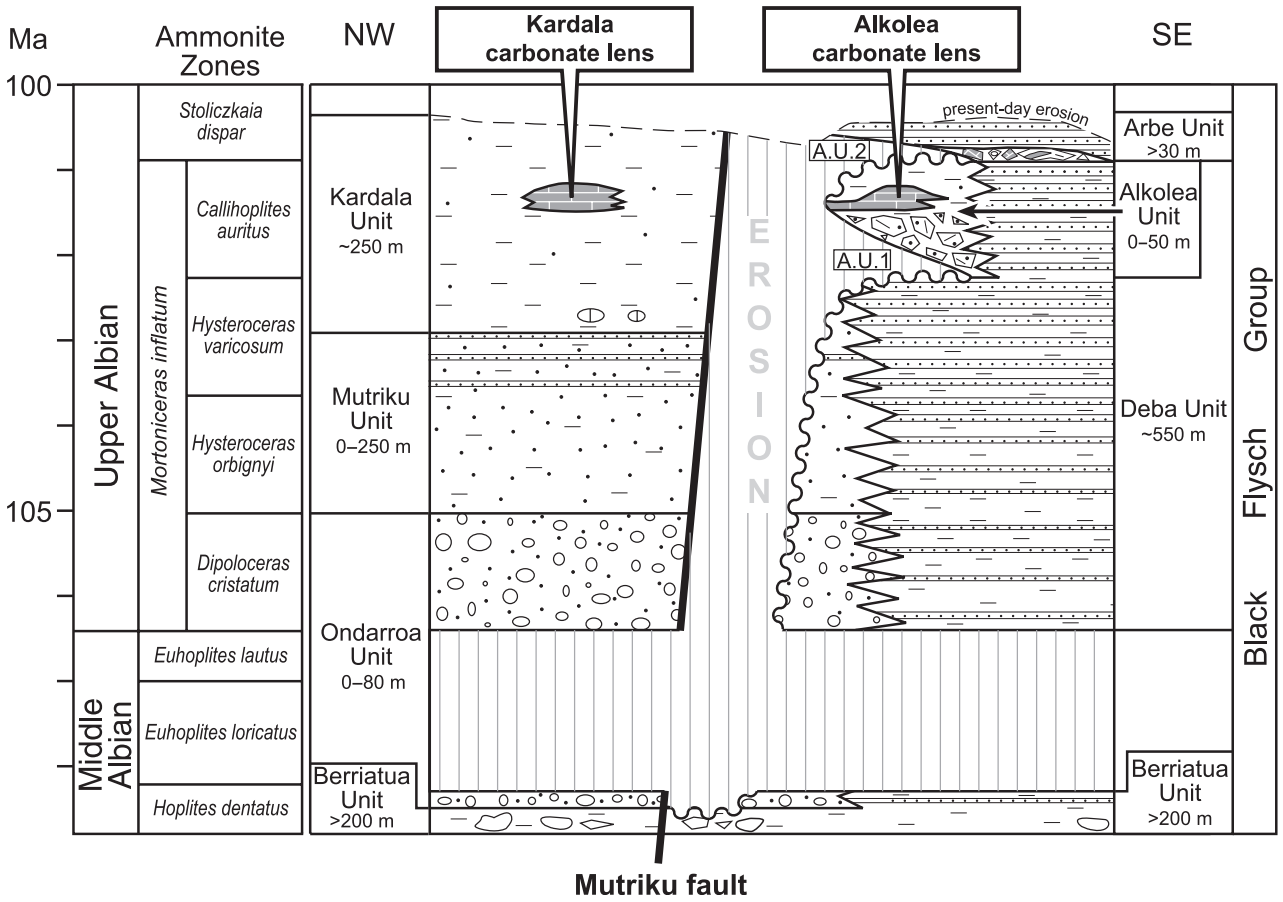

Fig. 2. Basic stratigraphy of the Black Flysch Group in the study area (modified from Agirrezabala *et al.*, 2002) with an indication of the Kardala and Alkolea authigenic carbonates, syndepositional Mutriku fault and two angular unconformities (A.U.1 and A.U.2).

onlap the older angular unconformity (AU1) and are truncated by the younger unconformity (AU2). Given the north-east trend of the Aitzeta monoclinal syncline, local north-west to south-east compression is deduced in its formation (Agirrezabala *et al.*, 2002).

METHODS

A total of 115 thin sections (35 × 20 mm and 85 × 40 mm) were examined by plane-polarized, cross-polarized, epifluorescence [ultraviolet (UV)] and reflected light microscopy. The observation of thin sections using a white background under reflected light allowed pure carbonates to be distinguished from those containing pyrite and organic matter, each of which displays a characteristic reflection pattern (Folk, 1987). Pyrite occurs as highly metallic, brassy yellow minerals and organic matter occurs as black masses. Thirteen thin sections were also stained with a mixture of potassium ferricyanide and alizarin red to differentiate among mineral phases of carbonate. X-ray diffraction (XRD) analysis of seven powdered mineral samples was carried out using an automated Philips PW1710 diffractometer (Philips Co., Eindhoven, The Netherlands). Semi-quantitative estimates were made from peak areas on XRD patterns (Schultz, 1964). Total organic carbon content (TOC; wt%) was measured by a duplicated analysis of 41 samples (limestones and lutites) with a FlashEA 1112 (ThermoFinnigan) elemental analyzer (Thermo Fisher Scientific Co., Waltham, MA, USA) after acid removal of carbonates by using hot (80 °C) hydrochloric acid. Systematic sampling was used to obtain representative TOC logs through both authigenic carbonates and host deposits. Volumetrically major carbonate phases were selected for oxygen and carbon isotope analyses. Thirty-six samples were taken from the surfaces of polished blocks using a hand-held microdrill under a binocular microscope. For extraction of

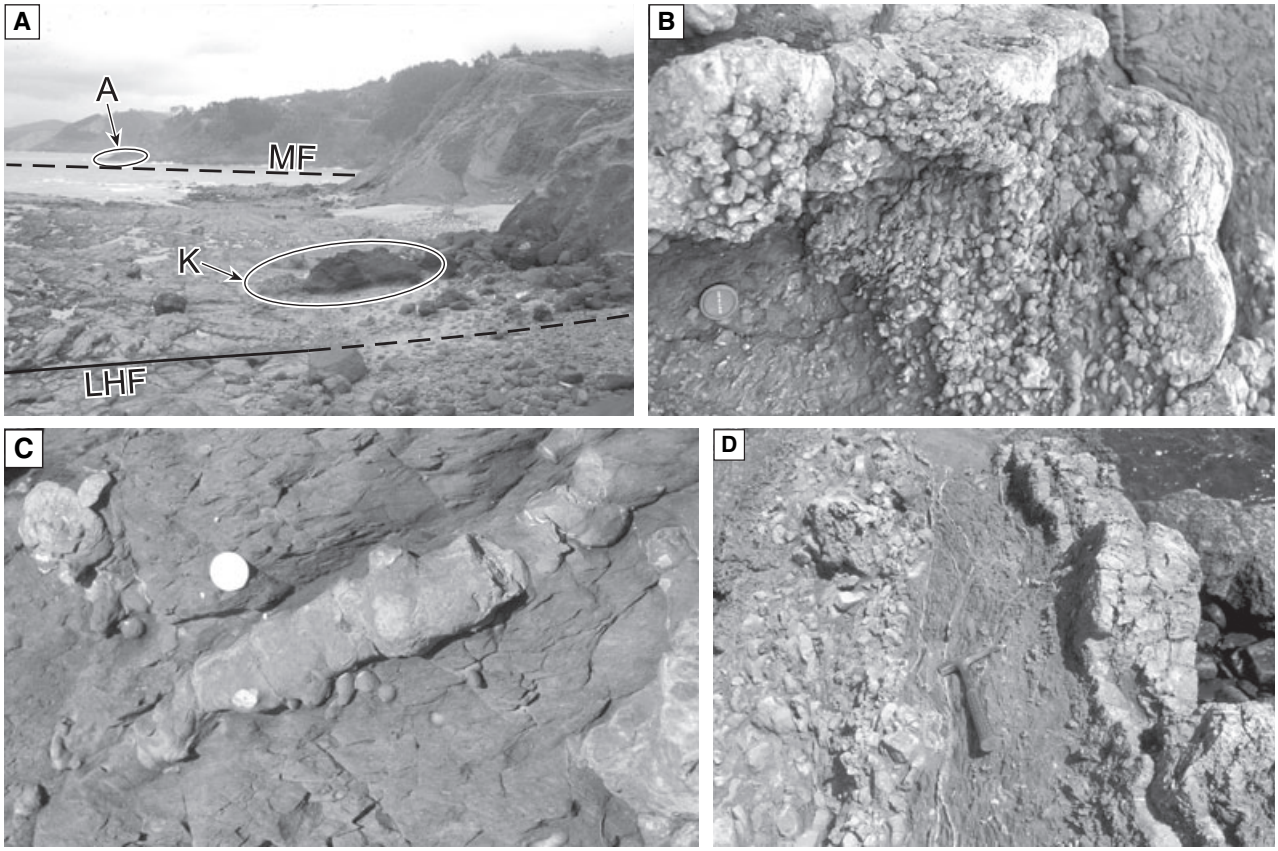

Fig. 3. Outcrops and typical field characteristics of the studied authigenic carbonates. (A) Kardala 'K' and Alkolea 'A' carbonate lenses (encircled) and traces of the syndepositional Mutriku and Laugarren Hondartza faults (MF and LHF, respectively). Outcrop width (middle part) is *ca* 70 m. (B) Outcrop of disturbed concretionary carbonates and interbedded lutites from the Kardala site. Lens cap is 5·5 cm in diameter. (C) Tubular carbonate concretion and host lutites from the Kardala carbonates. Coin is 2·2 cm in diameter. (D) Vent carbonate breccia (left), autochthonous vent carbonates (right) and intervening lutites (centre) at the Alkolea site. Sub-vertical bedding, top to the right. Hammer is 34 cm in length.

CO_2 from each sample standard techniques were followed (McCrea, 1950; Craig, 1957); the sample was allowed to react with orthophosphoric acid (90 °C), and analysed in an ISOCARB device attached to a VG-Isotech SIRA-II^{TM} mass spectrometer (both VG Isogas Co., Middlewich, UK). Accuracy was monitored by repeated analysis of both internal and international (NBS-19) carbonate standards under identical analytical conditions. For both carbon and oxygen, laboratory precision was better than ±0·2‰. Organic carbon samples for stable isotope determinations were combusted with a EuroVector elemental analyzer linked to an ISOPRIME (GV Instruments Ltd, Manchester, UK) mass spectrometer. Isotope results are given in the usual delta notation relative to Vienna Pee Dee Belemnite (PDB). Details about laboratory methods employed for expanded gas chromatography are presented in Chaler *et al.* (2005).

DESCRIPTION OF AUTHIGENIC CARBONATES

The mid-Cretaceous Kardala and Alkolea authigenic carbonates occur as stacked carbonate beds enclosed in recessive hemipelagic silty to sandy lutites of the turbiditic, deep-water Black Flysch Group (Figs 2, 3A and 4). Lens morphology of these carbonates can be verified by both outcrop (Kardala, Fig. 4B) and stratigraphic criteria (correlation of carbonates with contemporaneous lutites and sandy turbidites; Fig. 2). At the outcrop scale, the Kardala and Alkolea mounds are composed of stacked lenticular to tabular carbonate beds separated by interbedded sandy to silty lutites similar to the enclosing deposits (Fig. 4), which thus suggest separate episodes of carbonate precipitation. The authigenic carbonates are isotopically light in ^{13}C (2·25‰ to −41·50‰), have a high carbonate content (67·7%

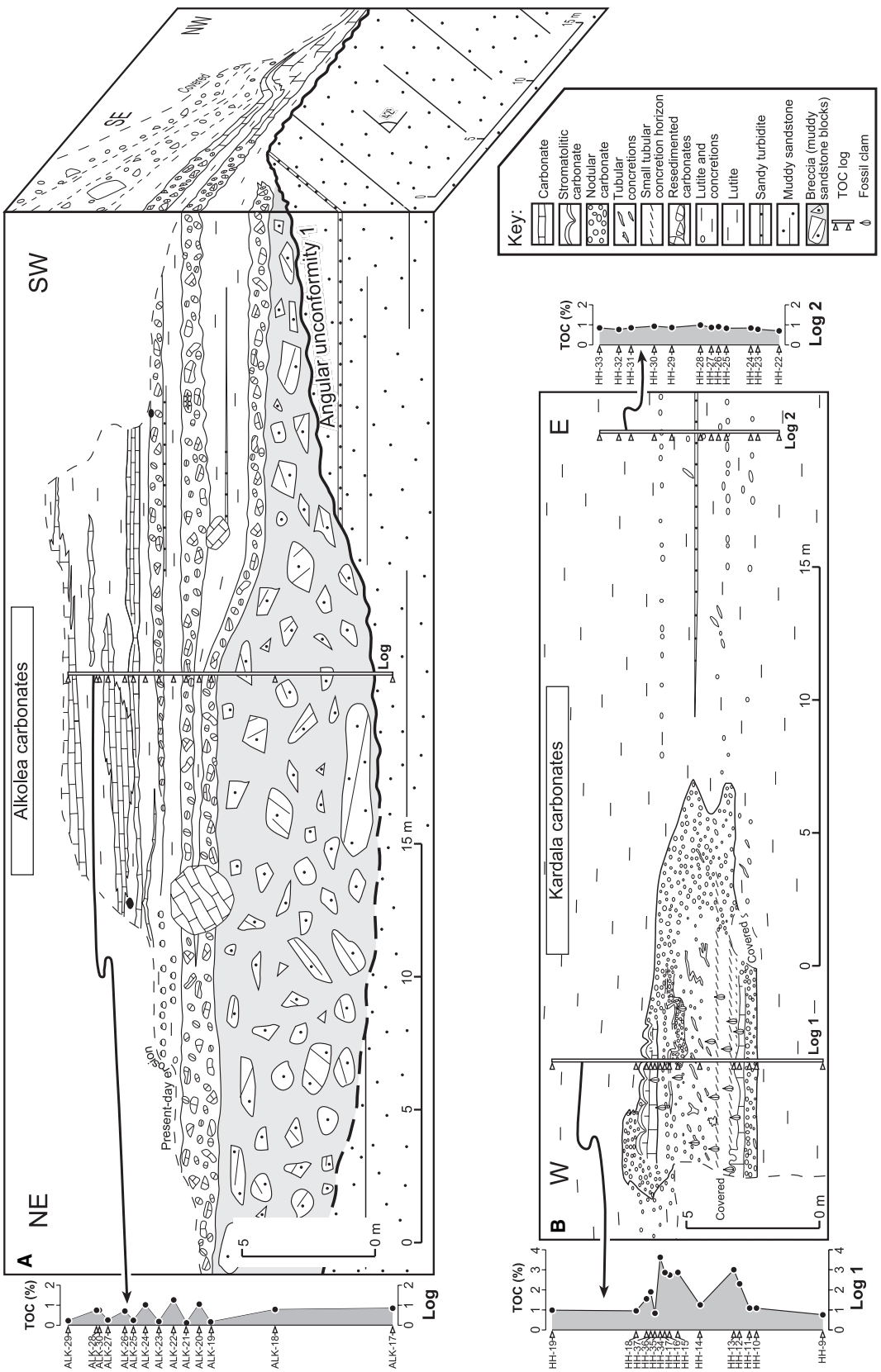

Fig. 4. Detailed stratigraphic cross-sections, facies and total organic carbon (TOC) logs of studied authigenic carbonates and host deposits at the Alkolea (A) and Kardala (B) sites.

$CaCO_3$ on average, up to 89%) compared with the enclosing shale deposits (8% $CaCO_3$ on average) and show diverse structures such as nodules, tubular concretions, stromatolites and septarias (concretions displaying a mineralized crack set).

At Kardala, the carbonate precipitates constitute a lens up to 5 m thick and 16 m long (minimum) composed of oil-stained nodular limestones, locally deformed, carbonate concretions and tubular structures with abundant solid bitumen-fills, as well as interbedded silty lutites (Figs 3A to C and 4B). The inner part is composed of massive to tightly packed nodular carbonates and tubular carbonate concretions. The outer part consists of nodular carbonates and concretion-rich lutites. The tubular structures show a preferential orientation dipping on average 20° towards the west-north-west (after bedding restoration). These directions are sub-perpendicular to the north-east-trending structural ridge and faults. The carbonates include a relatively abundant fossil biota and have high TOC values (up to 3·62%). Contact with the embedding rocks is gradational, showing a progressive lateral decrease in carbonate concentration. In contrast, the fossil fauna found in the carbonates is absent in the enclosing silty lutites which are characterized by low TOC values (*ca* 1%), similar to the background TOC value of the Black Flysch Group (Agirrezabala *et al.*, 2008) (Fig. 4B). A thin (0 to

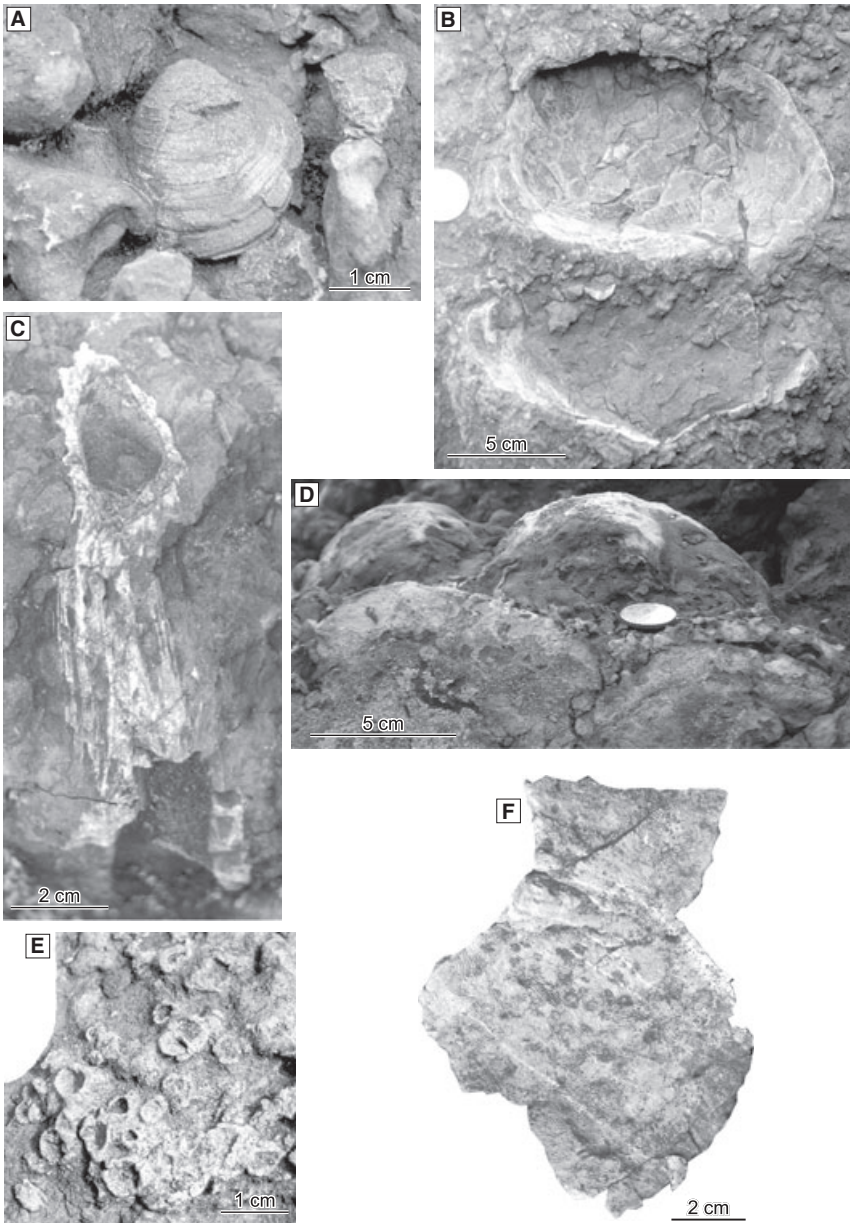

Fig. 5. Fossil biota from the Kardala (A) to (D) and the Alkolea carbonates (E) and (F). (A) ?*Codakia* (*Epilucina*) sp., articulated lucinid specimen. (B) Large clam, interior of disarticulated valves. (C) Radiolitid rudist. (D) Hemispherical stromatolites showing internal lamination (lower half). (E) Cluster of vuggy carbonate structures with a cup-like shape attributed to fossil sponges, top view. (F) Plate-like coral, top view.

3 cm thick) turbidite sandstone pinches out towards the fossil-rich carbonates, suggesting that the carbonate lens formed a relief on the sea bottom during turbidite deposition (Fig. 4B).

At Alkolea, the authigenic carbonates and interbedded lutites rest on an (high-angle) angular unconformity (AU1) and on an intraformational megabreccia composed of muddy sandstone blocks; both carbonates and lutites wedge out and onlap the angular unconformity towards the north-west (Fig. 4A), suggesting increasing sea floor relief in the same direction. The top and lateral contacts with the host lutites are not preserved because of modern erosion. The minimum dimensions of the carbonate lens are 8 m thick and 40 m long, and internally it shows two superimposed and partially equivalent parts (Fig. 4A). The lower part is composed of carbonate breccias and interbedded lutites; carbonate breccias consist of angular fragments of nodular carbonates (up to 2·5 m long) and rounded septarias (up to 80 cm long) embedded in a mudstone matrix with rare lutite clasts (Fig. 3D). The upper part is composed of undisturbed, autochthonous tabular to lenticular carbonates with both plane-parallel and vuggy massive stratification, and interbedded lutites (Figs 3D and 4A). In contrast to what has been observed at the Kardala site mound, bivalve fauna and tubular carbonate concretions are absent at the Alkolea site, where carbonate TOC values are very low (Fig. 4A).

FOSSIL BIOTA

The authigenic carbonates at Kardala have relatively abundant benthonic macrofossils dominated by bivalves (lucinids and large clams), rare gastropods, a single coral, a rudist and stromatolites (Fig. 5A to D), whereas the enclosing lutites are devoid of macrobenthonic fauna. In contrast, at the Alkolea locality the aforementioned fauna is absent and only calcified sponges and a coral have been observed (Fig. 5E and F). Other associated fossils which are present at both localities are small ammonites (*Hamitoides* cf. *studerianus* Pictet, *Cantabrigites* cf. *nanoides* Wiedmann and *Lechites* sp.), belemnites, wood fragments, radiolarians, planktonic and benthonic foraminifera, sponge spicules, echinoid fragments, and faecal pellets. Burrows and borings are also present.

At Kardala, the fossil assemblage is composed mainly of scattered, relatively abundant lucinid and scarcer large clams (Fig. 5A and B) often with both valves still attached. The distribution of these bivalves is restricted to the inner carbonates of the structure (Fig. 4B). Infaunal lucinid bivalves, classified tentatively as *Codakia* (*Epilucina*) sp. occur throughout the carbonate lens. The bivalves are 8 to 27 mm long (average 18 mm), most of them are closed-valved and show no apparent preferred orientation (Fig. 5A). Large clams are restricted to the south-western part of the carbonate lens. Shells are up to 152 mm long, moderately thick, oval–oblong and present a surface with fine irregular growth lines (Fig. 5B); their identification is problematic because their dentition type has not been observed.

Two individual gastropods (abyssochrysid?, trochoid?) have been found in the Kardala carbonate lens. The small fossil coral found at Kardala resembles specimens of *Discocyathus* (Moore, 1956), a solitary, discoid coral. The fossil exhibits a flat, circular corallum base 13 mm in diameter, lobate septa and a distal side with calicular pit. The rudist bivalve is a cup-shaped, 12 cm long radiolitid, which shows no evidence of transport or reworking (Fig. 5C). This occurrence is thought to be the first time that a rudist has been documented in vent-related or seep-related precipitates. The stromatolites are laterally linked carbonate hemispheroids up to 50 cm wide with convex-up internal lamination (Fig. 5D); they are restricted to the uppermost part of the Kardala carbonate lens (Fig. 4B).

At the Alkolea locality only a plate-like coral (Fig. 5F) and structures assigned tentatively to sponges (Fig. 5E) were found. These sponges, millimetres to centimetres in diameter, constitute irregular, vuggy carbonate structures, typically with cup-like shapes; they are present as both solitary individuals and clusters.

CARBONATE PETROLOGY AND PARAGENESIS

Petrological analyses of both the Kardala and the Alkolea carbonates revealed the occurrence of complex paragenetic sequences for carbonates from both sites. The sequence includes 12 events corresponding to four major carbonate phases, a major asphalt fill, nine minor phases (carbonate and quartz cements, and siliciclastic fill) and six corrosion/fracturing events. A petrographic description of all the mineral phases is summarized in Table 1 and the proposed timing of the different diagenetic events is illustrated in Fig. 6. The order of the paragenetic events has been

Table 1. Petrographic characteristics of mineral phases from the Kardala and Alkolea carbonates of this study with an indication of the figure numbers.

Paragenetic mineral phase	Petrographic character	Crystal morphology	Crystal size	Occurrence*	Figure
Micrite 1 (m1)	Brown/grey, microcrystalline; siliciclastics (quartz, feldspar, mica, clay), pyrite, benthonic and planktonic microfossils, sponge spicules, wood fragments; ± oil stains, peloids, macrofossils, bioturbation, microspar, texture grumeleuse, stromatolithic lamination	Anhedral	Micrite < 4 μm; microspar 5–20 μm	K, A	7A–F; 8A,C,D; 9A,B,D
Brown calcite (b)	Brown, as lining laminae or as aggraded mass	Anhedral	20–150 μm; 50–200 μm thick laminae	K, A	8A,C,D
Fibrous calcite 1 (f1)	Light yellow/buff; as growth cements in pores (layers, coatings); radiating fibre fans, undulose extinction, rhomb-tip terminations; clear areas with inclusion-rich (oil) bands and trails; locally recrystallized and/or dolomitized	Coarse to fine radial fibrous; radiaxial fibrous; locally tabular habits	Up to 3 mm thick botryoids	K, A	7F; 8A–E; 9A
Peloidal calcite (p)	Brown/grey; micritic peloids and microsparitic cement as pore-fills and coatings; fenestral clotted fabric; detritic-free; pyrite-rich peloids with gradational boundaries (microbial?)	Anhedral	< 4 μm; microspar areas 5–20 μm	K	8A,B
Sparry calcite (s)	Clear; as fills in pores; usually dentate	Subhedral rhombs to anhedral	Up to 160 μm	K, A	7A,B,D; 9B
Micrite 2 (m2)	Dark brown/grey, microcrystalline; pyrite (± pellets); as geopetal fills (± clear spar, quartz grains; or as thin linings in pores (microbial?)	Anhedral	Micrite < 4 μm; microspar 5–15 μm	K, A	8A,D
Isopachous calcite (i)	Light to dark brown; inclusion-rich (oil), very turbid (± clear regions); as thin laminae lining pores, radiating fibre fans, undulose extinction, ± pellets	Radial fibrous; radiaxial fibrous; also adjacent tabular habits	Up to 600 μm thick botryoids	K	8D
Saddle dolomite (sd)	Clear with inclusion-rich turbid areas; as pore-filling cement, coarse crystals with undulose extinction, ± intercrystalline pyrobitumen (py)	Conspicuous, curved crystal faces	Up to 2 mm; variable thickness (up to 2·5 mm)	K	7A; 8A,D–F; 9A
Pyrobitumen (py)	Black; irregular, homogeneous masses filling voids, ± internal blocky calcite or saddle dolomite spherules and fracture-fills		Up to 2 cm thick masses	K, A	7A,C; 8D–F; 9A
Sulphates and carbonates mixture (sc)	Complex mixture; as replacive or void-filling cement	Anhedral to euhedral	Up to 1 dm thick masses	A	9B
Blocky calcite (bl)	Clear (± poikilotopic); as cements filling fractures and subspherical cavities (gas bubbles?) within pyrobitumen (py)	Euhedral	Up to 1·1 mm	K, A	9A,C

Table 1. (*Continued*)

Paragenetic mineral phase	Petrographic character	Crystal morphology	Crystal size	Occurrence*	Figure
Quartz (q)	Coarse, limpid to poikilotopic (organics); as pore-filling cement	Euhedral to anhedral	Up to 1·5 mm	K, A	9C
Fibrous calcite 2 (f2)	Clear; as vein-filling cements, very fine fibres, perpendicular (± oblique, curved) to fracture walls	Euhedral	Up to 1·1 mm thick veins	K, A	9D

*K, Kardala; A, Alkolea.

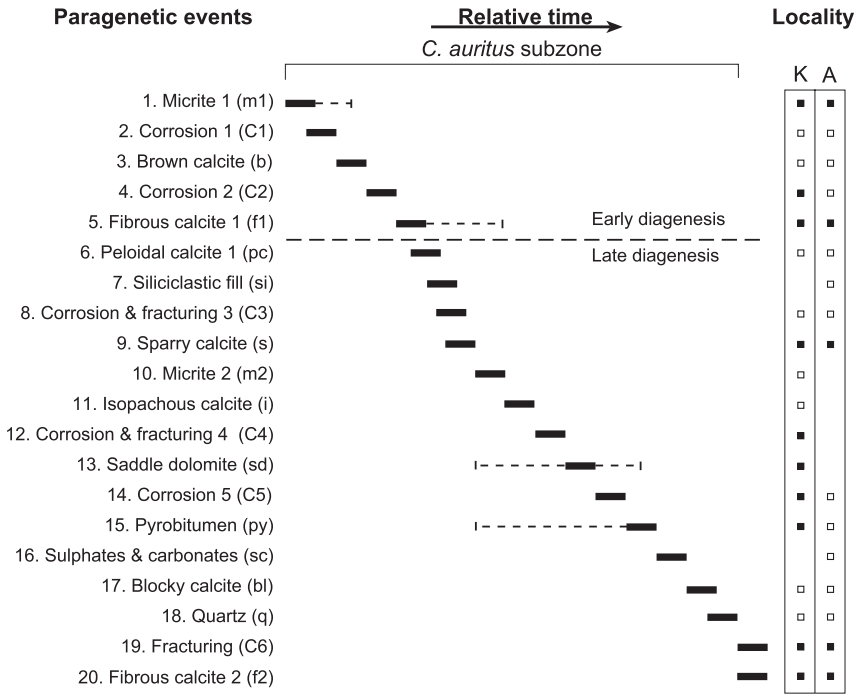

Fig. 6. Relative timing and geographic distribution of the 20 paragenetic events recorded in the two carbonate lenses of this study. Events 1 to 18 took place during *C. auritus* ammonite Subzone *pro parte*, i.e. a maximum duration of 1·3 Myr. Approximate separation between early and late diagenesis is shown. Thick lines indicate the relative duration of each event and thin lines indicate the probable maximum extent. Columns to the right show the geographic distribution (K, Kardala; A, Alkolea) and relative occurrence (filled square, major; open square, minor) of the events.

established by combining the following criteria: cross-cutting (including replacement) and overgrowth relationships, habits of minerals and the spatial distribution of all solids. Most events (1 to 18) of the paragenetic sequence are post-dated by the overlying megabreccia (Alkolea site; Fig. 2), indicating that they occurred within the early Late Albian *C. auritus* Subzone (Agirrezabala *et al.*, 2002). In this respect, many resedimented blocks of the overlying megabreccia are composed of authigenic carbonates showing most of the paragenetic phases cross-cut and post-dated by fissures filled with matrix lutite. The most complete record of the paragenetic events was observed in the carbonate tubular concretions. Based on petrographic and geochemical analyses, the events of the paragenetic sequence have been grouped tentatively into early and late diagenetic stages. Early diagenetic events are unrestricted spatially and their characteristics (borings, bioturbation and low-temperature cements) suggest that they are sea floor and shallow sub-sea floor-related events. Late diagenetic phases are pore-filling cements formed by high-temperature fluids which indicate burial conditions.

Early diagenesis

The earliest paragenetic event (event 1; Fig. 6) corresponds to micrite 1 formation in the background siliciclastic mud sediments, simultaneous with bioturbation and colonization of benthonic macro-invertebrates. This detrital-rich micrite constitutes the volumetrically most important phase. It exhibits a brown to grey colour with common oil-stained darker areas. Mineralogical composition determined by XRD analysis is calcite (67·7%), detrital clay minerals and mica (13%

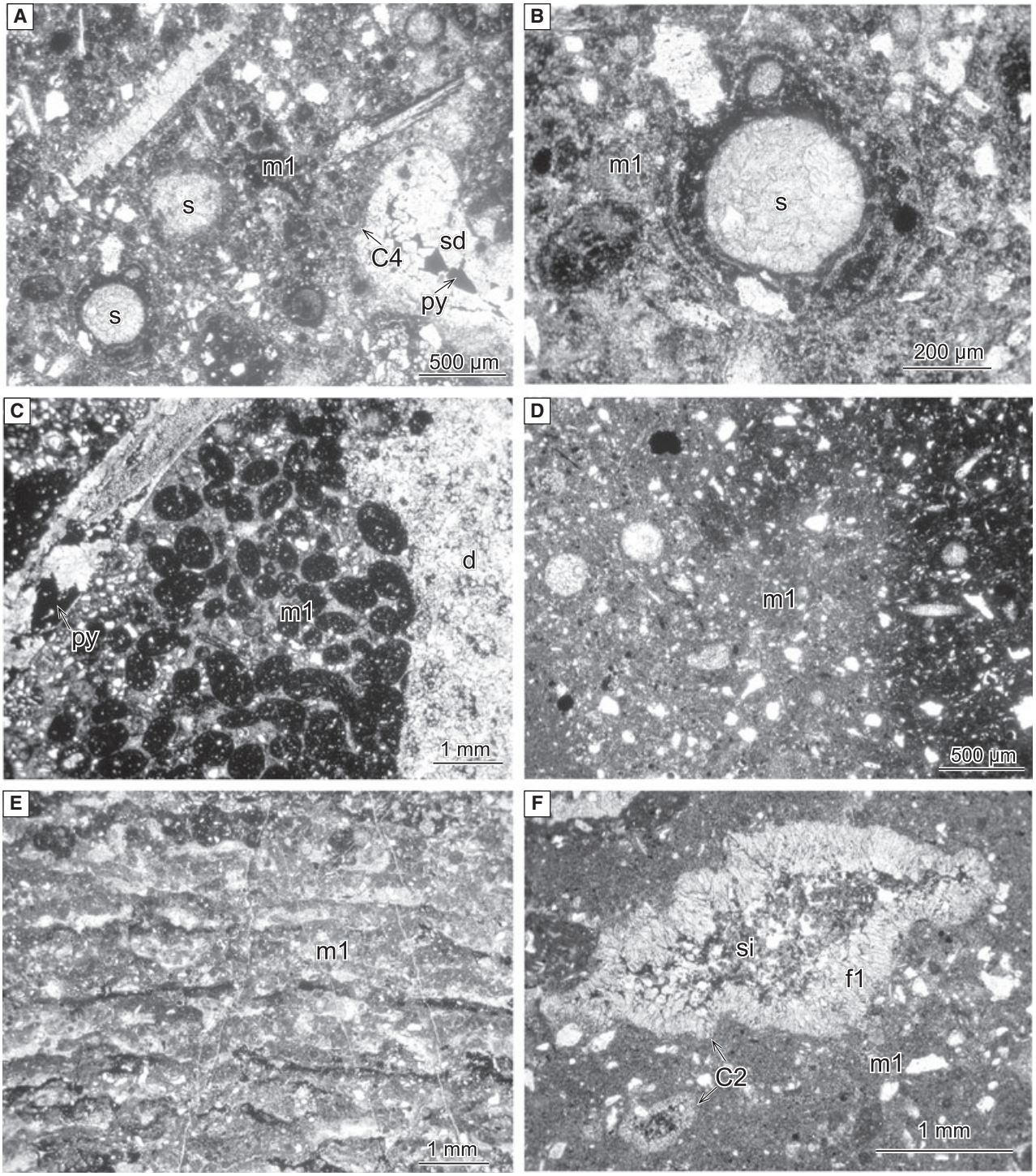

Fig. 7. (A) Micrite 1 (m1) with bored bivalve fragment (upper left), radiolaria with encrusted laminated micrite and filled with sparry calcite (s), corrosion pore (C4) filled with saddle dolomite (sd) and pyrobitumen (py). KAR-21. (B) Detail of (A) showing a laminated micrite crust around a radiolaria with internal sparry calcite cement (s). (C) Bivalve internal micrite 1 (m1) fill showing numerous faecal pellets and replacive dolomite (d) (note pellet ghosts). Bivalve shell (upper left) partially dissolved and filled with pyrobitumen (py). KAR-21a. (D) Micrite 1 (m1) showing framboidal pyrite (black particles) and oil-stain (to the right). KAR-20b. (E) Laminated micrite 1 (m1) from a stromatolite. Note convex-upward alternating laminae of fenestral micrite (grey to white) and pyrite (black). KAR-20c. (F) Dissolution pores (C2) enclosed in micrite 1 (m1) and filled with fibrous calcite 1 (f1) and siliciclastics (si). ALK-13. All microphotographs with transmitted light.

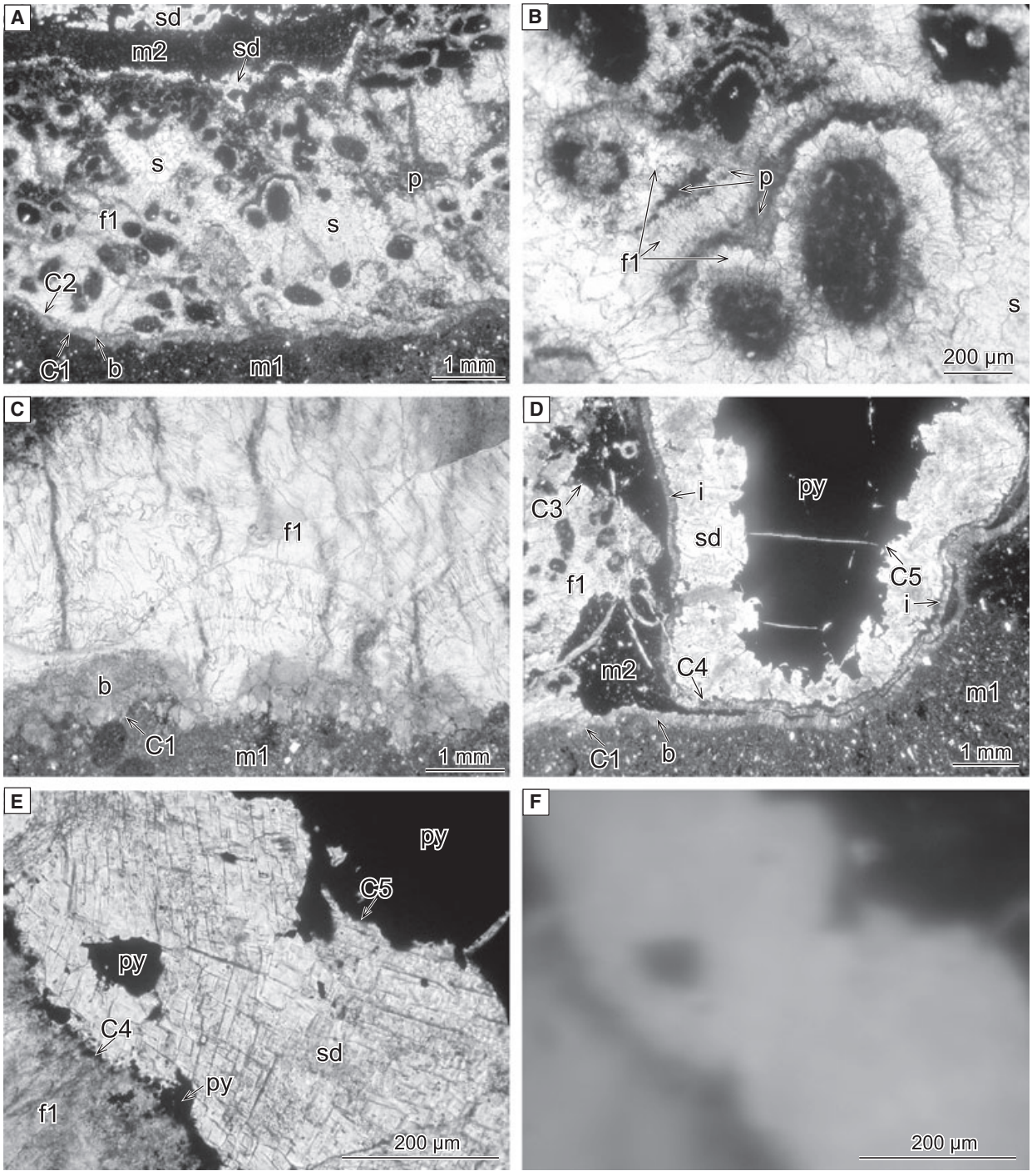

Fig. 8. (A) Partial view of a tubular concretion showing cement stratigraphy. Outer micrite 1 (m1) and inner conduct fill composed of brown calcite isopachous cement (b), fibrous calcite 1 (f1) enclosing bacterially mediated peloids, peloidal calcite (p), sparry calcite (s), micrite 2 (m2) and saddle dolomite (sd). Note corrosion surfaces (C1 and C2) and dark inclusion (organics?) trails crossing fibrous and sparry calcites. Top upright. KAR-2. (B) Detail of (A) showing bacterially mediated peloids coated by alternating fibrous calcite (f1) and peloidal calcite (p) layers. Top upright. (C) Corrosion vug on micrite 1 (m1) filled with brown (b) and botryoidal fibrous calcite 1 (f1). Note inclusion-rich (organics?) growing bands and sub-perpendicular trails. ALK-12. (D) Partial view of a tubular concretion showing micrite 1 (m1) and open conduit fill composed of isopachous brown calcite (b), fibrous calcite 1 (f1) enclosing peloids, micrite 2 (m2), isopachous calcite (i), saddle dolomite (sd) and pyrobitumen (py). C1 and C3 to C5 correspond to corrosion surfaces. Top to right. KAR-27. (E) Fibrous calcite 1 (f1), saddle dolomite (sd), pyrobitumen (py) and intervening corrosion surfaces (C4 and C5). LK-20a. (F) Same view as in (E), under UV light. Note non-fluorescent pyrobitumen. (A) to (E) microphotographs with transmitted light.

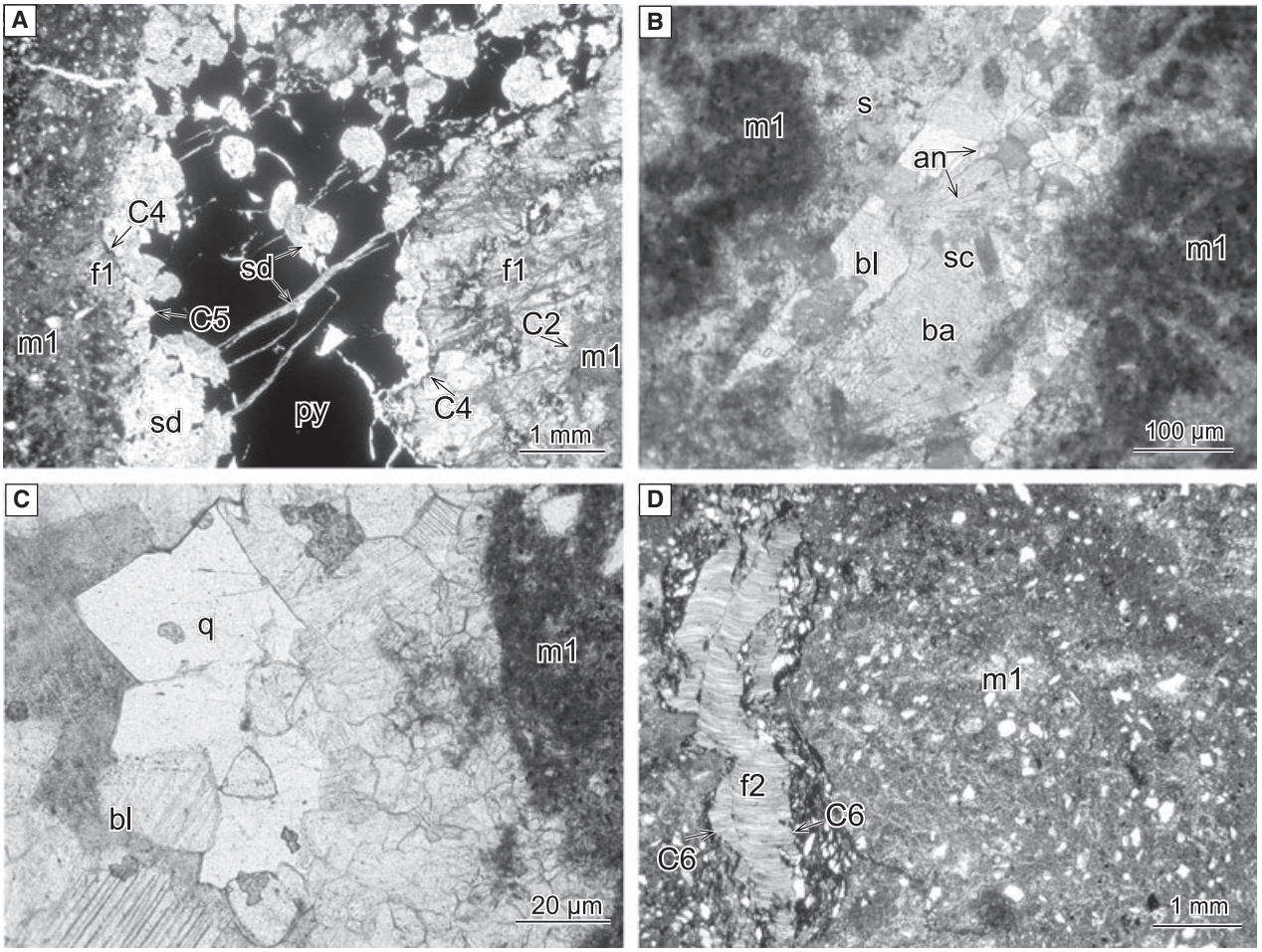

Fig. 9. (A) Micrite 1 (m1) and corrosion vug (C2) filled with fibrous calcite 1 (f1), saddle dolomite (sd) and pyrobitumen (py), the latter enclosing spherules and fracture fills of saddle dolomite (sd); saddle dolomite on corrosion surface (C4) post-dates numerous inclusion trails along microfractures (right); saddle-dolomite fracture-fill (C4) revealed in upper left corner. LK-20a. (B) Replacive sulphate and carbonate mixture (sc) and blocky calcite (bl) in host micrite 1 (m1) and sparry calcite (s); note needles of anhydrite (an) enclosed in barite (ba). ALK-11a. (C) Blocky calcite (bl) and clear, limpid quartz (q). ALK-13. (D) Micrite 1 (m1) and a fracture (C6) filled with fibrous calcite 2 (f2) which exhibits fibres oriented perpendicular to the fracture surface. ALK-8a. (A), (C) and (D) are microphotographs with transmitted light, and (B) is with plane-polarized light.

to 15%), grains of silt to fine sand-sized quartz (9% to 15%) and feldspar (albite) (3% to 5%), framboidal pyrite (5% to 9%) and organic matter. Micrite 1 embeds abundant radiolaria tests, planktonic and benthonic foraminifera tests, sponge spicules, wood fragments, sub-spherical faecal peloids, as well as ammonites and belemnites (Fig. 7A to D). In domal stromatolites or around microfossils the micrite shows wavy lamination (Figs 5D and 7A,B,E). Pyrite is usually present as both disseminated framboids (2 to 100 μm) and, in stromatolitic lamination, as massive crusts, up to 60 to 110 μm thick, upon micrite laminae (Fig. 7D and E). The micrite is recrystallized locally to a microspar with crystals ranging in size from 5 to 20 μm. In places, the micritic carbonate is bioturbated and brecciated extensively. Weak corrosion and fragmentation during the following phase (C1, event 2) created irregular surfaces that post-date the micrite (Fig. 8A, C and D).

The corrosion surfaces were coated and lined subsequently by an anhedral, locally recrystallized, brown to dark yellow calcite (b, event 3). The calcite is relatively rich in organic matter inclusions and forms irregular to isopachous cement layers (Fig. 8A, C and D) which alternate with layers of fibrous calcite 1 (f1, event 5). The fibrous calcite coats and lines a corrosion and fracturing surface (C2; Figs 7F, 8A and 9A) which had formed previously (event 4). It is also characterized by pyrite-free and siliciclastic-free

botryoids or isopachous layers of light yellow radiating calcite fans (event 5), displaying rolling extinctions under crossed nichols and rhomb-tip terminations (Figs 7F, 8A to E and 9A). Growth lines in the botryoids are marked by submicrometric inclusion-rich (solid bitumen?) bands (Fig. 8C). Trails of dark micro-inclusions (organics?) occur along and cross-cut the calcite fibres (Figs 8A,C and 9A). Locally, in the interior of tubular concretions from the Kardala site, fibrous cements grew around micrite peloids (Fig. 8A,B and D). Encased peloids are different from faecal pellets of the micrite 1 phase and generally rest on the bottom of voids (geopetal structures), showing a loose packing. These detrital-free and pyrite-rich peloids are variable in shape and size, ranging from 0·05 to 0·55 mm in diameter, and exhibit indistinct (gradational) margins and dark organic matter. The interiors of these peloids are characterized by a brownish and cloudy microcrystalline texture with abundant framboidal pyrite. Lumps of peloids were also observed.

Late diagenesis

The record of late diagenetic events (Fig. 6, events 6 to 20) is more complete at the Kardala site than at Alkolea. A peloidal calcite phase formed as both a thin lamina coating on previous fibrous calcite and pore-filling masses (pc, event 6). This detrital-free phase constitutes a brown to grey clotted peloid microspar microfabric (Fig. 8A and B). The pyrite-rich peloids range widely in size but are generally < 100 μm, and most commonly < 60 μm; their shape is roughly spherical and their margins are typically poorly defined or gradational. Some of the peloids form irregular clusters, creating a complex clotted fabric within fenestral microspar. Some pores from the Alkolea carbonates were filled with a detrital silt (si, event 7) composed of clays, quartz and organic matter, which appear golden-brown to dark-brown in thin sections (Fig. 7F). Local corrosion and fracturing (C3) subsequently cross-cut previous phases (event 8). Locally, recrystallization of previous calcite phases took place during this event. Then sparry calcite precipitated to partially or completely fill previous porosity (event 9), constituting irregular masses of clear dentate crystals (Figs 7A,B and 9B).

Geopetal fillings or linings of micrite (micrite 2) were observed within the conduits of the tubular concretions (event 10). This non-detrital to poorly detrital micrite shows a recrystallized clotted texture and abundant framboidal pyrite (Fig. 8A and D). In some conduits of the tubular concretions, a further lining phase of thin (< 150 μm thick laminae) isopachous calcite was observed (i, event 11). This phase is a brown, recrystallized, turbid calcite with abundant organic inclusion trails sub-perpendicular to the pore surface (Fig. 8D). The recrystallized calcite shows fan-like inclusion trails, slight rolling extinctions under crossed nichols and rhomb-tip terminations, suggesting recrystallization from a previous fibrous calcite or aragonite. Subsequently, an extensive phase of corrosion and fracturing (C4) took place (event 12), which created a very irregular dissolution surface (preferentially along previous pores), V-shaped fractures and microfractures (Figs 7A, 8D and 9A). This event is characterized by widespread inclusion trails cross-cutting the fibrous calcite 1 (f1) and sparry calcite, coinciding with microfracture development (Figs 8A,C and 9A).

The following phase of carbonate precipitation corresponds to pore-filling saddle (baroque) dolomite, only recorded in the Kardala carbonates. The cement formed during this phase lines and/or fills pores and vugs (sd, event 13), and consists of coarse, clear crystals with turbid, inclusion-rich axial zones which exhibit conspicuous curved faces and undulose extinctions under crossed nichols (Figs 7A, 8A,D to F and 9A). In addition, the dolomite crystals exhibit solid bitumen inclusions, aligned parallel to cleavage. Thin (< 0·1 mm), discontinuous laminae of saddle dolomite were observed prior to micrite 2 formation (Fig. 8A). Locally, matrix-replacive dolomite occurs, showing ghosts of original carbonate particles (Fig. 7C). Saddle dolomite constitutes a good geothermometer, indicating formation at temperatures between 60° or 80° and 150 °C (Radke & Mathis, 1980; Warren, 2000), coinciding with the oil window. The formation of similar dolomites has been related to hydrothermal fluids elsewhere (Davis & Smith, 2006), as well as the thermochemical sulphate reduction of petroleum at high temperatures (Machel, 1987). The following paragenetic event includes corrosion and indentation of the saddle dolomite crystals located in the outer parts of the linings (event 14), producing an irregular surface with embayments (C5) (Figs 8D to F and 9A). The porosity (up to several centimetres long) is filled completely or partially with widespread black solid bitumen (event 15) (Figs 7A, 7C, 8D to F and 9A). This material is opaque in transmitted light, black under incident light, non-fluorescent with epifluorescence microscopy (UV) (Fig. 8E and F)

Table 2. Stable carbon and oxygen isotope values for Kardala and Alkolea carbonates.

Carbonate phase	Sample ID	$\delta^{13}C$‰ (PDB)*	$\delta^{18}O$‰ (PDB)*
Kardala			
Belemnite (rostrum)	KAR-39	0·11	−3·37
Lucinid shell	KAR-40-A	−4·78	−12·44
Lucinid shell	KAR-40-B	−4·46	−12·38
Lucinid shell	KAR-40-C	−5·82	−11·53
Micrite 1 (m1)	KAR-2	−12·06	−8·15
Micrite 1 (m1)	KAR-3	−17·29	−8·08
Micrite 1 (m1)	KAR-3i	−16·52	−7·51
Micrite 1 (m1)	KAR-8	−14·98	−8·16
Micrite 1 (m1)	KAR-9	−12·17	−9·10
Micrite 1 (m1)	KAR-14	−16·42	−8·07
Micrite 1 (m1)	KAR-15	−14·78	−8·43
Micrite 1 (m1)	KAR-16	−16·84	−7·44
Micrite 1 (m1)	KAR-20	−12·90	−7·14
Micrite 1 (m1)	KAR-27	−16·59	−7·66
Micrite 1 (m1)	KAR-28-A	−11·25	−7·47
Micrite 1 (m1)	KAR-28-B	−10·96	−8·55
Micrite 1 (m1)	KAR-28-C	−12·39	−7·10
Fibrous calcite 1 (f1)	KAR-2-B	−20·70	−5·73
Fibrous calcite 1 (f1)	KAR-27-C	−18·70	−7·07
Fibrous calcite 1 (f1), marginal septaria	KAR-30	−5·78	−3·32
Fibrous calcite 1 (f1), marginal septaria	KAR-33	−15·14	−2·47
Fibrous calcite 1 (f1), marginal septaria	KAR-34	−4·43	−5·29
Fibrous calcite 1 (f1), marginal septaria	KAR-35	−11·54	−3·16
Micrite 2 (m2)	KAR-27-D	−10·34	−10·06
Saddle dolomite (sd)	KAR-2-A	0·94	−9·97
Saddle dolomite (sd)	KAR-27-A	0·74	−10·07
Saddle dolomite (sd)	KAR-36	2·25	−8·96
Alkolea			
Micrite 1 (m1)	ALK-8	−24·42	−3·72
Micrite 1 (m1)	ALK-8i	−23·87	−3·18
Micrite 1 (m1)	ALK-9	−21·09	−5·54
Micrite 1 (m1)	ALK-10	−22·48	−3·17
Micrite 1 (m1)	ALK-11	−24·36	−5·68
Micrite 1 (m1)	ALK-13	−5·62	−4·11
Micrite 1 (m1)	ALK-16	−14·47	−4·53
Fibrous calcite 1 (f1)	ALK-12	−41·49	−1·24
Fibrous calcite 1 (f1)	ALK-12i	−41·50	−0·92

i, Replicate samples.
*Uncertainty: ±0·2‰.

and shows very low solubility. All these characteristics are indicative of overmature pyrobitumen, probably impsonite (Gómez de Llarena, 1958). Locally, a thin pyrobitumen lamina occurs between the C4 corrosion surface and the saddle dolomite (Fig. 8E). Pyrobitumen interiors show both dispersed spherules up to 1 mm (diameter) and fracture fills composed of saddle dolomite and/or blocky calcite (event 18) (Fig. 9A).

The following minor paragenetic phase constitutes rare, up to decimetre-sized, elongate, porous masses of a white mineral mixture found only at Alkolea (sc, event 16; Fig. 6). Microscopic and XRD analysis of these minerals revealed a complex mixture composed of sulphates (celestine, barite, gypsum and anhydrite), carbonates (strontianite and calcite) and albite, which replaced previous carbonate phases (Fig. 9B), or filled pores and vugs. The mineral association of these mixtures is indicative of a late diagenetic hydrothermal origin (Klein & Dutrow, 2008). The subsequent pore-filling cements consist of coarse blocky calcite and authigenic quartz (Fig. 9C) which precipitated synchronously and completely filled any remaining porosity associated with both carbonates and pyrobitumens (events 17 and 18, bl and q, respectively; Fig. 6). Blocky calcite is composed of coarse, clear to turbid spar

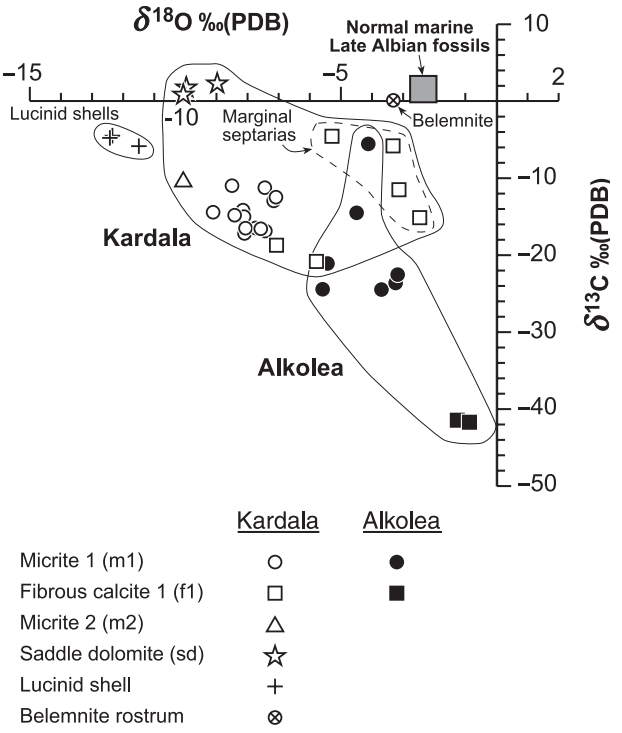

Fig. 10. Stable carbon versus oxygen isotopic cross-plot for Kardala and Alkolea carbonates (encircled fields).

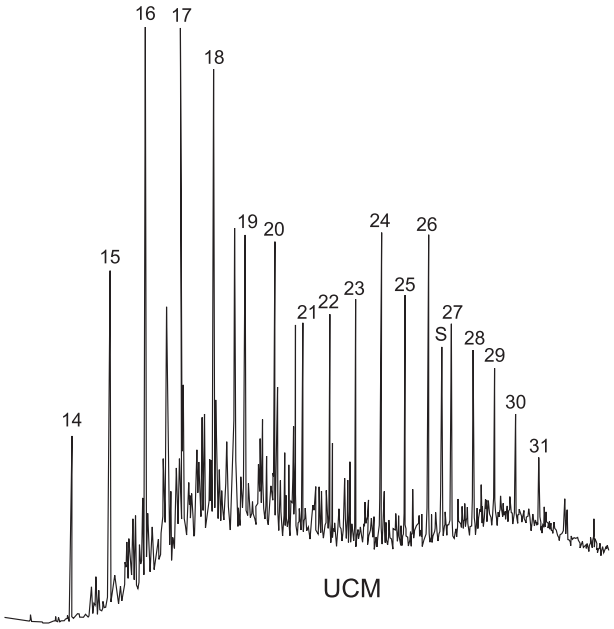

Fig. 11. Expanded gas chromatographic traces showing the composition of the major hydrocarbons in a pyrobitumen-rich sample (Chaler *et al.*, 2005). UCM, unresolved complex mixture; S, squalene.

crystals (Fig. 9C), which locally enclose fragments of pyrobitumen, indicating a solid state at this time. Millimetre-sized, clear crystals of authigenic quartz usually exhibit prismatic shapes (Fig. 9C), but anhedral, poikilotopic crystals, including solid bitumen fragments, are also present. Finally, extensional fractures opened (event 19) and filled with fibrous calcite 2 (event 20, Fig. 6). The most fibrous veins are sub-vertical and local around carbonate concretions (Fig. 9D). Crystal fibres are perpendicular to oblique in orientation with respect to the walls of the fractures.

GEOCHEMISTRY

Carbonate carbon and oxygen isotopes

The results of stable carbon and oxygen isotope analyses of the Kardala and Alkolea carbonates are summarized in Table 2 and plotted in Fig. 10. The material analysed corresponds to volumetrically major carbonate phases (micrite 1, fibrous calcite 1, micrite 2 and saddle dolomite), a belemnite (rostrum) and three lucinid shells. Minor phases of carbonate cements were not sampled because of the limited spatial resolution of the microdrill. Most samples were depleted in both ^{13}C and ^{18}O compared with sea water values. Individual carbonate phases constitute discrete isotope groups and authigenic carbonates can also be discriminated by locality.

The data cluster into four distinct fields, comprising the carbonates from each of the two localities, the lucinid shells and the belemnite (Fig. 10). Stable ^{13}C data from the Kardala and Alkolea carbonate carbons generally overlap. However, the Alkolea carbonate ^{13}C generally shows greater depletion than the Kardala carbonate ^{13}C when mean values of the same carbonate phases are compared. The $\delta^{13}C$ values of Kardala carbonates range between −20·7‰ and +2·2‰, showing a marked grouping for each carbonate phase. The lowest values correspond to fibrous calcite 1, micrite 1 and micrite 2 phases of the inner part of the carbonate lens (−19·7‰, −14·2‰, −10·3‰ mean values, respectively) and fibrous calcite 1 phase of the outer part of the lens (−9·2‰ average value). In contrast, with light carbon phases, $\delta^{13}C$ values of Kardala saddle dolomites range between +0·9‰ and +2·2‰.

The carbonates from Alkolea present a wide range of $\delta^{13}C$ values, −41·5‰ for fibrous calcite and −24·4‰ to −5·6‰ for micrite 1. The isotopic signatures of the belemnite rostrum and the three lucinid shells are grouped into two separate fields, yielding $\delta^{13}C$ values of +0·1‰ and −4·4‰ to −5·8‰, respectively.

Table 3. Stable organic carbon isotope values for Kardala carbonates and hosting Black Flysch succession.

Sample rock	Sample ID	$\delta\ ^{13}C_{org}$‰ (PDB)*
Carbonate deposits (Kardala)		
Pyrobitumen-fill (chimney)	KAR-27-B	−25·26 ± 0·12
Pyrobitumen-fill (chimney)	KAR-3	−24·27 ± 0·25
Oil-stain micrite 1 (concretion)	KAR-17	−26·33 ± 0·31
Hosting Black Flysch succession		
Lutite (underlying Berriatua unit)	SAT-3	−24·73 ± 0·47
Lutite (underlying Mutriku unit)	BURU-3	−25·20 ± 0·16
Lutite (underlying Mutriku unit)	BURU-5	−24·90 ± 0·08
Lutite (underlying Mutriku unit)	BURU-6	−25·43 ± 0·04
Lutite (adjacent, Kardala unit)	HH-26	−24·87 ± 0·05

*Standard deviation is indicated.

Oxygen isotopic values of carbonate phases from both localities exhibit two overlapping fields. Kardala carbonates show more negative $\delta^{18}O$ values overall (−10·06‰ to −2·47‰) than Alkolea carbonates (−5·68‰ to −0·92‰). Moreover, comparison of $\delta^{18}O$ values of similar, individual, early diagenetic carbonate phases from both localities reveals that the Kardala phases exhibit more negative values than Alkolea phases. In particular, Kardala micrite 1 and fibrous 1 carbonates from inner lens precipitates yielded values from −9·10‰ to −7·10‰ and −7·07‰ to −5·73‰, respectively, and fibrous calcite 1 from marginal precipitates showed values from −5·29‰ to −2·47‰. The same carbonate phases from Alkolea show values of −5·68‰ to −3·17‰ and −1·24‰ to −0·92‰, respectively. The $\delta^{18}O$ values of the three lucinid shells and belemnite rostrum are clustered into two different fields, yielding values of −12·44‰ to −11·53‰ and −3·37‰, respectively.

Organic matter

Three logs of TOC were measured. Two logs crossed the carbonate lens at both Kardala and Alkolea and a further log was carried out across the lutite deposits adjacent to the Kardala carbonates (Fig. 4). The log across the Kardala carbonates (log 1, Fig. 4B) reveals that both carbonates and interbedded lutites have a high TOC content, up to 3·62%, while underlying and overlying deposits have values of about 1% (background TOC value for Black Flysch deposits; Agirrezabala *et al.*, 2008). In contrast, the log across adjacent lutite deposits (log 2, Fig. 4B) exhibits relatively constant background TOC values, ranging between 0·70% and 0·98%. The Alkolea TOC log presents a serrated shape with minimum values coinciding with carbonates and maximum values with lutites. Carbonates exhibit very low TOC values, ranging from 0·17% to 0·27% (mean 0·20%), whereas lutites show background values between 0·71% and 1·27% (mean 0·90%). An expanded gas chromatogram (Fig. 11) corresponding to a pyrobitumen-rich sample from Kardala (Chaler *et al.*, 2005) shows a relatively low unresolved complex mixture (UCM) and the presence of a squalene biomarker. On the other hand, three samples of pyrobitumen and oil-stained micrites from Kardala yielded a $\delta^{13}C_{org}$ mean value of −25·28‰ (−24·27‰ to 26·33‰) which is very similar to the mean value of −25·02‰ (−24·73‰ to −25·43‰) corresponding to five samples of the host Black Flysch Group organic matter (Table 3).

INTERPRETATIONS AND DISCUSSION

Fossil biota

The Kardala and Alkolea carbonate lenses yielded fossil invertebrate taxa that have been reported from both modern and ancient vents and seeps and a bivalve not reported previously from vents and seeps. At Kardala, the most common molluscan fossils are lucinid and large clams. Modern lucinid bivalves are known to harbour symbiotic, chemoautotrophic sulphur-oxidizing bacteria; they are common members of biological communities inhabiting present-day seeps and vents (Dame, 1996; Sibuet & Olu, 1998; Desbruyères *et al.*, 2006). Although the identification of the large clams is problematic, they resemble symbiont-containing big bivalves that colonize present-day seeps and vents. Some ancient vent and seep carbonates also contain lucinid and large clams in their fossil biota (Peckmann *et al.*, 2002; Goedert *et al.*, 2003;

Majima *et al.*, 2005; Campbell, 2006). The two gastropod specimens (abyssochrysid? and trochoid?) found at Kardala are also indicative of vent-dwelling biota. Gastropods associated with vents and seeps are recognized increasingly elsewhere (Campbell, 2006). Both symbiont-containing and non-symbiont-containing gastropods occur in present-day hydrocarbon seeps and vents; non-symbiotic gastropods act as predators of autochthonous organic matter (Sibuet & Olu, 1998; Van Dover, 2000). The stromatolites found at Kardala suggest that microbial mats developed on the sea floor during fluid flow; their internal lamination and the deep-water depositional setting suggest that their formation mechanism was a process of binding fine sediment to bacterial mats, together with encrustation by the precipitating carbonate. Deep-water, vent-related and seep-related stromatolites have been described in a few present and past examples (Greinert *et al.*, 2002; Gómez-Pérez, 2003).

The radiolitid found at Kardala constitutes the first rudist bivalve documented in a vent-related or seep-related precipitate. Rudists are an abundant and significant constituent of Tethyan Cretaceous carbonate platforms and are commonly absent from deep-water deposits; they are usually considered to be shallow-water bivalves adapted to living in symbiosis with photosynthesizing zooxanthellae algae (Kauffman & Johnson, 1988). However, the occurrence of Late Cretaceous radiolitid rudists (e.g. *Durania* gen.) in deep-water pelagic deposits in Israel and Kansas, as well as the radiolitid specimen from the Kardala carbonates, suggests that some rudists were living in deeper water conditions than previously thought and that they did not need the putative endosymbiotic algae (Lewy, 1995).

All the macrobenthonic fossils observed at Alkolea are small sponges with the exception of a plate-like coral. Sponges are epibenthonic, filtering organisms which are relatively common in both present-day and ancient vents and seeps (Sibuet & Olu, 1998; Peckmann *et al.*, 1999; Desbruyères *et al.*, 2006), as well as in 'normal' marine environments. Recently, some carnivorous sponges with internal methanotrophs have been documented from a mud volcano (seep) in the Barbados Trench (Vacelet *et al.*, 1995).

Authigenic carbonate precipitation

The ^{13}C depletion of pyrite-rich, early micrite measured in samples from both Kardala and Alkolea carbonates indicates that carbon is derived from the anaerobic bacterial oxidation of methane and other hydrocarbons in the sulphate reduction zone (Han *et al.*, 2004). Moreover, the occurrence of organic-rich, anhedral brown to yellow calcite at both localities is indicative of bacterial oxidation of hydrocarbons under anoxic conditions, as demonstrated previously for Jurassic and Cretaceous seeps (Beauchamp & Savard, 1992; Campbell *et al.*, 2002). In present-day hydrothermal vents and seeps, this process is carried out by a syntrophic consortium of methane-oxidizing archaea and sulphate-reducing bacteria, although the exact nature of the interactions is understood poorly (Boetius *et al.*, 2000; Michaelis *et al.*, 2002; Orphan *et al.*, 2002; Valentine, 2002). The net chemical reaction involves oxidation of methane (and other hydrocarbons) and reduction of sulphate (Ritger *et al.*, 1987; Paull *et al.*, 1992):

$$CH_4 + SO_4^{2-} \rightarrow HCO_3^- + HS^- + H_2O \qquad (1)$$

The precipitation of carbonate takes place as a consequence of an increase in alkalinity, whereby HS^- reacts with iron from the detrital minerals to produce pyrite (Berner, 1984). The observed detrital richness in the micritic cement (m1) suggests that the micrite grew within a pre-existing fine sediment and/or that detrital grains and carbonate were mixed by intense biological activity in the shallow sub-sea floor realm (e.g. bioturbation, faecal pellets and fossil remains) (Diaz-del-Río *et al.*, 2003; Mazzini *et al.*, 2005). Evidence for carbonate precipitation at, or immediately beneath, the sediment–water interface on the sea floor is inferred in this study from bioturbated fossiliferous micrite and the occurrence of borings and stromatolites. The very high carbonate content (average 67·7%) also suggests that carbonate precipitation took place at a shallow depth prior to sediment compaction (Peckmann *et al.*, 1999; Clari & Martire, 2000).

Fibrous calcite 1 (formerly aragonite?) is interpreted as a cement derived from the anaerobic bacterial oxidation of thermogenic methane (and other hydrocarbons) because of the extremely negative $\delta^{13}C$, particularly at Alkolea. Relatively high $\delta^{18}O$ values suggest a low formation temperature and precipitation at the sea bottom (Fig. 10). Fibrous calcite is a common mineral phase in seep and vent carbonates and has usually been interpreted as a cement formed in association with sulphate-rich diagenetic environments where calcite precipitation is inhibited (Aloisi *et al.*, 2002).

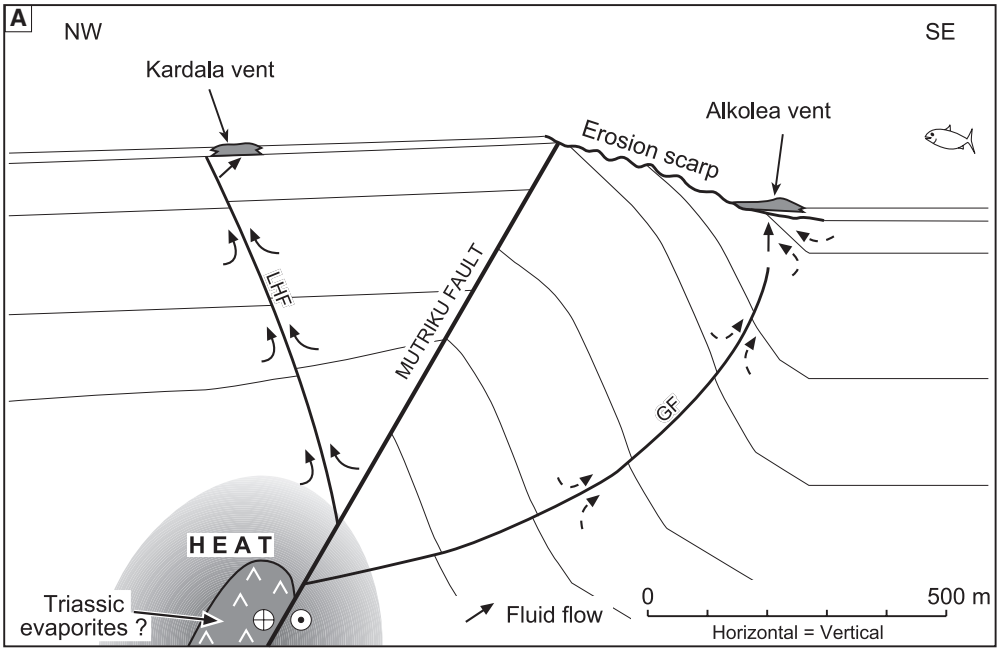

B

Kardala vent	Comparison	Alkolea vent
	data	
High	• TOC	Low
High	• Carbonate $\delta^{13}C$	Low
Low	• Carbonate $\delta^{18}O$	High
Abundant	• Tubular concretions	Absent
Abundant	• Chemosymbiotic fauna	Absent
	Interpretation	
Oil > Methane	• Vented hydrocarbon	Methane > Oil
High	• Fluid temperature	Low
High	• Flow intensity	Low

Fig. 12. (A) Interpreted transpressive geological setting of Kardala and Alkolea vents in Late Albian times (modified from Agirrezabala *et al.*, 2002). Hydrothermal fluids altered host Black Flysch organic matter generating hydrothermal petroleum (oil and methane). In the Kardala vent, fluid expulsion was controlled by a fault-zone (Laugarren Hondartza fault: LHF), whereas at the Alkolea locality erosive scarp [and Garate (GF) and bedding-parallel faults?] focused expelled fluids. (B) Comparative summary of data from and interpretations of the Kardala and Alkolea vents.

Bacterially mediated carbonate formation is also supported by the microtextures formed during the early diagenetic and earliest late diagenetic phases. These microtextures include: (i) laminated early micrite (m1) as both microfossil coating (Fig. 7A and B) and domal stromatolites (Figs 5D and 7E) (Campbell *et al.*, 2002; Greinert *et al.*, 2002); (ii) pyrite-rich peloids with indistinct margins (Fig. 8A and B) (Chafetz, 1986; Peckmann *et al.*, 2002; Shapiro, 2004); (iii) clotted peloid microspar as both coating laminae or pore-filling masses (Fig. 8A and B) (Chafetz, 1986; Cavagna *et al.*, 1999; Riding & Tomás, 2006); and (iv) clotted late micrite (m2), which lined or filled previous pores (Fig. 8A and D) (Cavagna *et al.*, 1999; Peckmann *et al.*, 1999, 2003; Campbell *et al.*, 2002). The Basque examples are texturally similar to the microbial fabrics documented in seep carbonates from the Italian Miocene (Cavagna *et al.*, 1999; Peckmann *et al.*, 1999; Clari & Martire, 2000) and the Californian Mesozoic (Campbell *et al.*, 2002).

The ^{18}O depletion of the saddle dolomite suggests that, during late diagenesis, hydrothermal fluids reached their highest temperatures. Considering that saddle dolomite-forming hydrothermal fluids are typically hypersaline brines (Davis & Smith, 2006), it is possible that fluids at Kardala had a salinity higher than that of normal sea water. In this respect, outcropping Triassic evaporites within the study area are invoked as the probable source of hypersaline fluids (Figs 1B and 12). On

the other hand, the presence of coarse-grained saddle dolomite overgrowths on a pyrobitumen-encrusted corrosion surface and the very low solubility of the pyrobitumen suggest thermochemical sulphate reduction conditions (Machel *et al.*, 1995) which take place at temperatures higher than 100 °C (Machel, 2001). Carbonate spherules enclosed in the pyrobitumen-fills are interpreted as original spherical pores corresponding to gas bubbles within the original petroleum, whereas carbonate-filled fractures are similar to typical alteration cracks present in pyrobitumens (Jacob, 1989). These characteristics suggest that the original petroleum was in a semi-solid to solid state during formation of saddle dolomite and blocky calcite. Widespread pyrobitumen fills demonstrate that porous carbonates were once charged pervasively with a mixture of oil and gas, which was then altered to pyrobitumen by thermal cracking. Similar late diagenetic pyrobitumen fills have been documented in Palaeozoic hydrocarbon-seep carbonates from Germany and Morocco (Peckmann *et al.*, 2001, 2007). The mineral association of the complex mixture of sulphates and carbonates from the Alkolea carbonates is indicative of a shallow burial hydrothermal origin. Finally, fibrous calcite 2 (Fig. 9D) indicates a progressive fracture opening and simultaneous fibre precipitation because of compaction or tectonic processes.

The six corrosion/fracturing events alternating with carbonate precipitation recorded in the paragenetic sequence (surfaces C1 to C6, Fig. 6) indicate changes in fluid composition-pH and/or brittle fracturing during the Basque vent carbonate development. Corrosion surfaces have been documented in many seep carbonates (Beauchamp & Savard, 1992; Campbell *et al.*, 2002; Peckmann *et al.*, 2003; Peckmann & Thiel, 2004). These surfaces are often encrusted with pyrite rims that precipitated due to the migration of Fe^{2+} and H_2S from the reduction site to the reaction place (Coleman & Raiswell, 1995; Peckmann *et al.*, 2003; Peckmann & Thiel, 2004). In this scenario, pyrite formation is accompanied by an increase in acidity that could be responsible for carbonate corrosion. In the case of the Kardala and Alkolea carbonates, the absence of pyrite coatings on corrosion surfaces could be due to the low availability of reduced iron whereas the input of weak acidic H_2S-charged fluids could have lead to corrosion of the nearby carbonates.

The most complete record of the paragenetic events found at the two sites occurs in carbonate tubular concretions, probably because they acted as open conduits for fluid flow during both the early and the late diagenetic stages. The occurrence of carbonate breccias and local sedimentary folds is interpreted either as the product of authigenic carbonate resedimentation by gravity-driven flows (Agirrezabala *et al.*, 2002) or by sudden hydrocarbon blowouts. Nevertheless, if down slope movement occurred, this would have been over short distances, as suggested by the outcrop-scale lateral transition between resedimented and autochthonous carbonates.

Carbonate isotopic signature

Carbon isotopes

Inorganic ^{13}C depletion in the carbonates studied, with $\delta^{13}C$ as low as −41·5‰, indicates a hydrocarbon-derived origin (Aharon, 2000; Campbell *et al.*, 2002; Peckmann & Thiel, 2004). At the Kardala locality, the lowest inorganic $\delta^{13}C$ values, corresponding to fibrous calcite 1, micrite 1 and micrite 2 phases of the inner part of the carbonate lens (−19·7‰, −14·2‰, −10·3‰ mean values, respectively) and the fibrous calcite 1 phase of the outer part of the lens (−9·2‰ average value), are consistent with the principal source being oil. This observation is also consistent with the presence of common pyrobitumen-fills, organic matter inclusions, pervasive oil-staining of carbonates, their high TOC content (up to 3·6%) and the $\delta^{13}C_{org}$ (−25·28‰, mean value) of pyrobitumen and oil-rich samples (Table 3, see the section *Organic matter* below). In this regard, Joye *et al.* (2004) observed, in cold-seep sediments from the Gulf of Mexico, that the carbon isotopic composition of carbonate (−10‰ to −20‰) was typically heavier (up to 15‰) than those of the oil (−23‰ to −26‰) from which it was derived; the ranges of these values are very similar to those of the present study. The enrichment in inorganic ^{13}C exhibited by the fibrous calcite 1 cement from inner to outer carbonates in the Kardala lens indicates a progressive diminishing of hydrocarbon-derived carbon (and a concomitant increment of sea water inorganic carbon) from the inner to the outer part of the lens. It suggests that there was a gradient in the hydrocarbon input to the vent sediments from the lens centre (high input) towards the outer areas (low input). In contrast with light carbon phases, the $\delta^{13}C$ values of Kardala saddle dolomites (+0·9‰ to +2·2‰) are consistent with an early Late Albian sea water signature (about +1·8‰; Wilson & Norris, 2001). These isotopic values could be interpreted as indicative of hydrothermal fluids composed of heated, infil-

trated sea water. Nevertheless, similar values have also been documented in some examples of authigenic carbonates derived from other processes, such as the alteration and oxidation of hydrocarbons by high-temperature thermochemical sulphate reduction (Machel *et al.*, 1995), carbonate dissociation (Hoefs, 1997) and exsolution of volatiles from magmas (Botz *et al.*, 2002).

At the Alkolea locality, the most ^{13}C-depleted fibrous calcite values (−41·5‰) indicate a principal source of thermogenic methane, given the evidence for active petroleum generation in the area (Sackett, 1978; Aharon, 2000; Campbell *et al.*, 2002). The more enriched values (−24·4‰ to −5·6‰) of micrite 1 reflect mixing of hydrocarbon-derived carbon (thermogenic methane) and sea water inorganic carbon during its formation (Haggerty, 1991).

The belemnite value is near 0‰, which is consistent with carbonate secretion near isotopic equilibrium with sea water bicarbonate (Anderson & Arthur, 1983). The slight isotopic depletion shown by the lucinid shells could suggest a contribution from hydrocarbon-derived carbon via endosymbiotic chemosynthesis (Rio *et al.*, 1992; Hein *et al.*, 2006), or could indicate a diagenetic overprint on the shells (Martin *et al.*, 2007).

Oxygen isotopes

Kardala and Alkolea carbonates show ^{18}O-depleted compositions. Similar ^{18}O-depleted carbonates are not uncommon and a variety of processes have been invoked to explain their origins. The most common processes are: (i) influx of meteoric water; (ii) recrystallization during burial diagenesis; and (iii) precipitation at high temperatures.

In this example, a possible influence of meteoric waters in the carbonate cements seems improbable because the sediments embedding the carbonates were deposited in a wide, deep-water (600 to 2500 m depth; García-Mondéjar *et al.*, 2004), turbiditic trough corresponding to the central axis of the basin, far from continental areas. Low δ^{18}O values of lutite-hosted lucinids (−12·44‰ to −11·53‰) point to an important diagenetic neomorphic alteration of their shells, confirmed by petrological analysis (partial dissolution and recrystallization), while the belemnite isotopic value (−3·37‰) is close to the early Late Albian deep-water fossil value (−2·3‰; Wilson & Norris, 2001), consistent with no significant diagenetic resetting. Lucinid shells in many ancient rocks are recrystallized easily or replaced during burial diagenesis (Clari & Martire, 2000; Martin *et al.*, 2007). However, the following isotope and mineralogical characteristics indicate that the analysed carbon and oxygen isotopic data of the carbonate phases probably are not altered significantly compared with the primary precipitate: Firstly, the most enriched isotopic values of both early diagenetic Alkolea phases and the sampled belemnite are similar to a sea water isotopic signal. Secondly, early diagenetic δ^{18}O values are substantially higher than late diagenetic values. Thirdly, late diagenetic δ^{18}O values and saddle dolomite are consistent with high temperature fluids. Fourthly, the observed isotopic trend constitutes a common pattern in hydrocarbon seeps, reflecting an increase in temperature and/or burial (Campbell *et al.*, 2002). Therefore, primary hydrothermal fluids are the most probable source of the ^{18}O-depleted cements, as the occurrence of shallow burial saddle dolomite suggests.

Increasing ^{18}O depletion in the diagenetic sequence of the Kardala carbonates suggests precipitation from hot waters with progressively higher temperatures. This interpretation is consistent with the occurrence of late diagenetic saddle dolomite, a palaeothermometer indicative of temperatures higher than 60 to 80 °C (Radke & Mathis, 1980; Warren, 2000). In contrast, the less negative δ^{18}O values of the Alkolea early diagenetic phases indicate cold to warm sea water conditions during their formation. The enrichment in ^{18}O observed in the Kardala fibrous calcite 1 from the inner to the outer part of the carbonate lens, although based on a small data set, denotes a progressive cooling of hydrothermal fluids towards the outside of the carbonate body.

Organic matter

The TOC content of the authigenic carbonates from Kardala (up to 3·62%) is significantly higher than that of the embedding deposits (about 1%), reflecting an organic carbon source linked to the carbonate precipitate area. Overall, the high TOC content, as well as the observed pervasive oil-staining, organic inclusions, abundant void-fill pyrobitumen and the carbonate isotopic signature, suggest that oil is the primary source of the hydrocarbons that fuelled sulphate reduction at Kardala. It is also suggested that systematically lower TOC values of the authigenic carbonates with respect to the embedding deposits at Alkolea are not a consequence of lower input of organic

matter, but are rather due to a dilution of the organic matter by the addition of diagenetic carbonate. The expanded gas chromatogram corresponding to a pyrobitumen-rich sample from Kardala (Fig. 11) indicates a slight to moderate biodegradation on the basis of the relatively low unresolved complex mixture (UCM) and the distribution of n-alkanes (Wenger & Isaksen, 2002). Moreover, the presence of a squalene biomarker in these samples is indicative of anoxic environments and a methanogenic archaea source (Brassel *et al.*, 1981; Elvert *et al.*, 2000; Peckmann & Thiel, 2004).

Hydrocarbon sources

The ^{13}C depletion of the Alkolea and Kardala carbonate phases, with the exception of the saddle dolomite, indicates that the carbon was derived from hydrocarbon sources. The carbonates at Alkolea show overall lower $\delta^{13}C$ values than those at Kardala and the early carbonate phases are also more ^{13}C-depleted at Alkolea than at Kardala (Figs 10 and 12). Such a depletion difference between contemporaneous vent carbonates is interpreted as being the result of distinct hydrocarbon sources. The $\delta^{13}C$ values of Alkolea fibrous calcite 1 and early micrite (mean values −41·5‰ and −19·4‰, respectively), together with the presence of pyrobitumen, suggest a thermogenic methane primary source (Aharon, 2000; Campbell *et al.*, 2002). Nevertheless, a minor input of biogenic methane can be inferred from the presence of the squalene biomarker (Fig. 11). In contrast, $\delta^{13}C$ values of the Kardala fibrous calcite 1, early micrite and late micrite (mean values −19·7‰, −14·2‰ and −10·3‰, respectively) are consistent with an oil source (Aharon, 2000; Joye *et al.*, 2004). The $\delta^{13}C$ values of Kardala could be explained by the mixing of methane-derived carbon and sea water inorganic carbon. However, the pervasive oil-staining of carbonates, abundant solid bitumen fills and high TOC content (up to 3·6%) are indicative of oil as a principal source. The higher TOC values found at Kardala are very similar to those associated with bacterial oxidation petroleum in the Gulf of Mexico (Anderson *et al.*, 1983).

Flow intensities

The abundance of lucinid and large clams at the Kardala locality contrasts with the absence of chemosymbiotic taxa at the contemporaneous Alkolea vent. This relationship is interpreted as caused by differences in intensity of fluid venting in the two localities. A similar relationship between chemosymbiotic megafauna type/abundance and fluid flow intensity has been documented in several modern seeps and vents (Olu *et al.*, 1996, 1997, 2004; Barry *et al.*, 1997; Sibuet & Olu, 1998; Orange *et al.*, 1999; Sahling *et al.*, 2002; Levin *et al.*, 2003; Levin, 2005). Therefore, the occurrence of fossil clams at Kardala suggests a relatively vigorous hydrocarbon flow and high rates of supply of H_2S, high enough to maintain endosymbiotic chemoautotrophic bacteria in their megainvertebrate hosts. In contrast, the absence of a chemosynthesis-based fauna at Alkolea could be explained by fluid flow too low to support them (Fig. 12) or, alternatively, by sub-surface carbonate formation. However, the latter hypothesis is unlikely, as the presence of sessile epibenthonic fauna in the carbonates (sponges and a coral) suggests that at least some of them formed at the sea bed.

Another indicator of flow intensity and style of fluid expulsion is the morphology of carbonate precipitates. Nodular or tabular carbonates are usually associated with diffuse and low intensity flows, whereas tubular concretions indicate high and/or discrete fluid venting (Kulm & Suess, 1990; Campbell & Bottjer, 1993; Orange *et al.*, 1999). Accordingly, the relative abundance of tubular carbonate concretions only in the Kardala outcrop indicates intense or, at least, concentrated conditions of hydrocarbon flow. Conversely, the tabular shapes of the Alkolea carbonates and the absence of tubular concretions suggest diffuse, low intensity fluid venting (Fig. 12). Moreover, the most complete sequences were detected in the tubular carbonate concretions, suggesting that they acted as open conduits for fluid flows during both early and late diagenetic stages.

Fluid palaeotemperatures

Low $\delta^{18}O$ values in carbonates have often been interpreted as a consequence of diagenesis. However, as discussed earlier, the isotopic signatures of the studied carbonates from both Kardala and Alkolea probably were not altered significantly after carbonate precipitation. The influence of meteoric waters has also been excluded. In this scenario, low $\delta^{18}O$ values in authigenic carbonates are commonly interpreted as the result of precipitation under elevated temperatures (Friedman & O'Neil, 1977). On the basis of this assumption, precipitation palaeotemperatures

can be calculated using the isotopic equilibrium equation of Anderson & Arthur (1983) for calcites and that of Friedman & O'Neil (1977) for saddle dolomites, by assuming that the parent fluid is heated Late Albian sea water. The local $\delta^{18}O$ standard mean ocean water (SMOW) of Late Albian sea water is +0·5‰ (from Wilson & Norris, 2001). Hence, the Alkolea and Kardala carbonates precipitated from warm to hot hydrothermal fluids. At Kardala, the mean temperature estimates obtained from micrite 1, fibrous calcite 1, micrite 2 and saddle dolomite are 60°, 51°, 74° and 109 °C, respectively. At Alkolea, the mean temperatures estimated from micrite 1 and fibrous calcite 1 are 39° and 23 °C, respectively. A comparison of these results indicates that hydrothermal fluids were hotter at Kardala than at Alkolea (Fig. 12B). Moreover, a comparison of the temperatures of early carbonate phases from both localities shows 21° to 27 °C hotter temperatures for Kardala. At Kardala, the temperatures of carbonate precipitation increase with the paragenetic sequence (except for the fibrous calcite 1). This relationship is interpreted as the result of the burial process and the geothermal gradient in the hydrothermal system. At the Kardala locality, the calculated temperature of formation of micrite 1 indicates that embedded mega-invertebrates lived in 60 °C waters. In present-day hydrothermal vents, dense invertebrate communities have usually been documented in waters up to 40 °C (Van Dover, 2000; Desbruyères *et al.*, 2006). This fact suggests that the micrites may have been overprinted during late diagenesis by warm burial fluids, thereby affecting their oxygen isotopic signature. The lowest precipitation temperatures were found for the fibrous calcite 1 phase at both localities, and are consistent with their precipitation in contact with cold to warm sea waters.

In the case of saddle dolomite-forming fluids, estimated palaeotemperatures may be erroneously low, as the assumed parent fluid is sea water. Parent fluids of hydrothermal systems are, however, typically hypersaline brines enriched in ^{18}O compared with contemporaneous sea water (Spencer, 1987; Davis & Smith, 2006). Assuming this typical enrichment in ^{18}O, estimated temperatures could be up to 50 to 100 °C higher than that calculated for a sea water parent fluid.

Hydrocarbon source and petroleum formation

The Kardala and Alkolea vent carbonates are hosted by the Black Flysch Group, an organic-rich, deep-water turbiditic unit. Since TOC values from the Black Flysch Group are 1% on average (Agirrezabala *et al.*, 2008), they constitute a potential source rock for hydrocarbons (Tissot & Welte, 1984). The analysed pyrobitumen-fills and oil-stained micrite from the Kardala carbonates showed a mean $\delta^{13}C_{org}$ value of −25·28‰. In comparison, the embedding Black Flysch siliciclastic deposits yielded a mean $\delta^{13}C_{org}$ value of −25·02‰, consistent with that of contemporaneous terrestrial organic matter from the North Atlantic Ocean (Hofmann *et al.*, 2000). Because there is negligible isotopic fractionation between organic source and hydrocarbons produced during hydrothermal alteration (Schoell *et al.*, 1990), the carbon isotope value of the pyrobitumen can be used to constrain the source from which it was derived. Accordingly, the similarity in isotope values for pyrobitumen and the Black Flysch Group deposits suggests that the latter was the source of oil and methane at Kardala and Alkolea (Fig. 12). In conventional basins, the onset of petroleum generation begins at 50 °C and at depths greater than 1 km, with peak generation occurring at about 80° to 100 °C and depths of 3 km (Tissot & Welte, 1984; Hunt, 1996). In contrast, hydrothermal petroleum is produced by the rapid diagenetic/catagenetic alteration of sedimentary organic matter which occurs within a higher temperature window (100° to 400 °C; Hunt, 1996; Rushdi & Simoneit, 2002a). In the present case, recorded fluid palaeotemperatures up to 109 °C (or higher, assuming ^{18}O-rich parent fluids) indicate that Late Albian hydrothermal fluids were hot enough for rapid hydrothermal petroleum formation sourced from shallow-depth Black Flysch deposits.

Structural and hydrothermal controls on fluid expulsion

Kardala and Alkolea hydrothermal vent activity was contemporaneous with the transpressive tectonics associated with the synsedimentary activity of the Mutriku fault and the growth of the adjacent Aitzeta fold during the Late Albian *C. auritus* Subzone (Agirrezabala, 1996; Agirrezabala *et al.*, 2002, 2003). This coincidence in space and time suggests a possible link between tectonism, hot fluids and hydrocarbon-rich fluid expulsion (Fig. 12). The formation of transpressional structures indicates that tectonically induced compression, pore-space reduction and overpressuring could have been the main driving forces controlling fluid movement and expulsion.

Similar processes have been documented at many modern accretionary complexes (Bray & Karig, 1985; Lewis & Marshall, 1996), and in modern and fossil transpressive margins (Orange *et al.*, 1999; Aiello, 2005), where initially hydrocarbon-rich, water-saturated sediments were squeezed and fluids expelled. In the study area, transpression-induced fluid expulsion around the Mutriku fault could have allowed the focusing of fluid venting in two different settings in relation to the local structure and geomorphic environment. The Kardala vent developed adjacent to the Laugarren Hondartza fault, a minor branch of the Mutriku fault on the uplifted ridge (hangingwall) (Fig. 12). Fluids migrated up the fault through fractured rocks of the Black Flysch Group and updip to the crest of the ridge (Fig. 12), as the orientation of tubular carbonate concretions (sub-perpendicular to the north-east-trending structural ridge) indicates. In this sense, tubular concretions would be part of the sub-surface plumbing system of the Kardala vent. A similar structural control of fluid migration has been documented in modern vents and seeps of accretionary prisms and transpressive margins (Kulm & Suess, 1990; Orange *et al.*, 1999; Eichhubl *et al.*, 2000; Aiello, 2005). In contrast, the Alkolea vent developed at the base of a south-east-facing, erosional tectonic scarp, corresponding to the local high-angle, angular unconformity which post-dated the first growth pulse of the Aitzeta monoclinal syncline, located on the downward footwall of the Mutriku fault (Fig. 12). This geomorphic indentation localized diffuse flow of warmer hydrothermal fluids because of the relatively low permeability (intergranular) of the underlying sandy mudstone deposits (Agirrezabala *et al.*, 2002). A similar control of fluid focusing has been documented in modern seeps developed on submarine scarps and canyons (Orange *et al.*, 1999). In addition to geomorphic indentation, rock fracturing related to the Garate fault and bedding-parallel faults (Agirrezabala *et al.*, 2002) is also considered as a possible cause of flow focusing at the Alkolea site.

The hydrothermal petroleum (oil and hydrocarbon gas) that sourced the authigenic carbonates was probably generated from Black Flysch organic matter by hydrothermal activity at shallow depth. In the present-day Guaymas Basin and North-eastern Pacific Ocean, hydrothermal petroleum is produced at shallow depths from sedimentary organic matter by contact alteration with hydrothermal fluids related to intrusion of basaltic sills (Einsele *et al.*, 1980; Simoneit & Lonsdale, 1982; Rushdi & Simoneit, 2002a,b). In the northern margin of the Basque-Cantabrian Basin, thick volcanic successions and magmatic intrusions formed during the Late Albian and Late Cretaceous (Rossy, 1988). Moreover, the main volcanic activity phase occurred during the *auritus* Subzone (Castañares *et al.*, 2001), penecontemporaneously with the development of the vents studied. Volcanic materials do not crop out in the study area, but the Mutriku fault trace connects this area with the nearby (*ca* 6 km) southern volcanic region where very thick volcanic successions and intrusive basalts occur (Rossy, 1988; Agirrezabala, 1996). Taking into account this relationship, it is possible that a deep magmatic intrusion existed near the study area; this would account for the high heat flow that supported the hydrothermal activity and petroleum generation at a shallow depth (Fig. 12). In this respect, magmatism-related hydrothermal fluids have also been documented from Late Albian mineralizations in other localities of the basin (Aranburu *et al.*, 2002).

CONCLUSIONS

Combined petrographic, geochemical and palaeontological analyses indicate that the mid-Cretaceous authigenic carbonates exposed at Kardala and Alkolea constitute microbially mediated by-products of hydrocarbon-rich (oil and thermogenic methane) hydrothermal venting associated with the episodic activity along the Mutriku fault. These two contemporaneous vent carbonates exhibit a consistent, complex paragenetic sequence indicative of similar fluid generation processes and pore-water evolution. Nevertheless, the comparison of the geochemical and palaeontological data, as well as of the morphologies of the concretions between the carbonate localities, is indicative of differences in vented fluid and flow characteristics. The carbon isotopic signatures, the relative abundance of oil-stainings and pyrobitumen-fills, and the total organic carbon values of the authigenic carbonates indicate that oil was the main hydrocarbon expelled at the Kardala vent whereas thermogenic methane-rich fluids sourced the carbon for the authigenic carbonates at Alkolea. Fluid palaeotemperatures estimated from the $\delta^{18}O$ of carbonates, assuming that the parent fluid was contemporaneous sea water, suggest hotter hydrothermal fluids at Kardala (maximum 109 °C) than at Alkolea (maximum 39 °C). Considering

that the formation of saddle dolomite is indicative of ^{18}O-rich hypersaline parent fluid, fluid temperatures could have been even higher than calculated. Both chemosymbiotic fauna and tubular carbonate concretions are relatively abundant at the Kardala vent whereas they are absent at the Alkolea. This fact suggests a stronger fluid flow at Kardala and a more diffuse flow at Alkolea.

The previous differences are interpreted as the result of contrasting local tectonic and geomorphic settings at the vent sites studied. At the Kardala, the highly permeable fault zone provided a conduit for hot hydrothermal fluids to flow to the surface. In contrast, at Alkolea the relatively low permeability (intergranular) of the underlying deposits at the base of the erosive scarp caused diffuse flow of warmer hydrothermal fluids.

Tectonically induced compression, pore-space reduction and overpressuring were the main driving forces that controlled hydrothermal fluid movement and expulsion, as the contemporaneous growth of transpressive structures indicates. Estimated fluid palaeotemperatures, together with organic geochemical data, suggest that vented oil and methane were generated at shallow depths from Black Flysch organic matter by contact alteration with hydrothermal fluids. The heat source for hydrothermal activity is related to the regional contemporaneous volcanism in the basin, and a possible connection with deep magmatic intrusion is invoked.

ACKNOWLEDGEMENTS

This research was supported by the Ministerio de Educación y Ciencia (projects CGL2006-05491/BTE and BTE2003-04823) and the Euskal Herriko Unibertsitatea (projects EHU06/62, UNESCO06/03 and 9/UPV00121.310-13556/2001). The XRD analyses were carried out with the participation of the Ministerio de Ciencia y Tecnología and the European Social Fund. I would like to thank S. Calzada for classification of some lucinid clams and C. Recio for technical assistance with isotopic analyses. The manuscript was improved by comments from K. Campbell (University of Aukland, Aukland), I.W. Aiello (Moss Landing Marine Laboratories, California) and T. van Weering (NIOZ, Texel). Special thanks are due to J.J.G. Reijmer (VU University Amsterdam) for editorial work. Thanks are also due to the agency Quattro (http://www.euskalnet.net/acts) for improving the English of this paper.

REFERENCES

Agirrezabala, L.M. (1996) *El Aptiense-Albiense del Anticlinorio Nor-Vizcaíno entre Gernika y Azpeitia*. PhD Thesis, Euskal Herriko Unibertsitatea, Bilbo, 429 pp.

Agirrezabala, L.M., Owen, H.G. and **García-Mondéjar, J.** (2002) Syntectonic deposits and punctuated limb rotation in an Albian submarine transpressional fold (Mutriku village, Basque-Cantabrian basin, northern Spain). *Geol. Soc. Am. Bull.*, **114,** 281–297.

Agirrezabala, L.M., Owen, H.G. and **García-Mondéjar, J.** (2003) Errata. Syntectonic deposits and punctuated limb rotation in an Albian submarine transpressional fold (Mutriku village, Basque-Cantabrian basin, northern Spain). *Geol. Soc. Am. Bull.*, **115,** 765–768.

Agirrezabala, L.M., Dorronsoro, C. and **Permanyer, A.** (2008) Geochemical correlation of pyrobitumen fills with host mid-Cretaceous Black Flysch Group (Basque-Cantabrian Basin, western Pyrenees). *Org. Geochem.*, **39,** 1185–1188.

Aharon, P. (2000) Microbial processes and products fueled by hydrocarbons at submarine seeps. In: *Microbial Sediments* (Eds R.E. Riding and S.M. Awramik), pp. 270–281. Springer-Verlag, Berlin.

Aiello, I.W. (2005) Fossil seep structures of the Monterey Bay region and tectonic/structural controls on fluid flow in an active transform margin. *Palaeogeogr. Palaeoclimatol. Palaeoecol.*, **227,** 124–142.

Aloisi, G., Bouloubassi, I., Heijs, S.K., Pancost, R.D., Pierre, C., Sinninghe Damste, J.S., Gottschal, J.C., Forney, L.J. and **Rouchy, J.-M.** (2002) CH_4-consuming microorganisms and the formation of carbonate crusts at cold seeps. *Earth Planet. Sci. Lett.*, **203,** 195–203.

Anderson, F.F. and **Arthur, M.A.** (1983) Stable isotopes of oxygen and carbon and their application to sedimentologic and paleoenvironmental problems. *SEPM Short Course*, **10,** 1–151.

Anderson, R.K., Scalan, R.S., Parker, P.L. and **Behrens, E.W.** (1983) Seep oil and gas in Gulf of Mexico slope sediments. *Science*, **222,** 619–622.

Aranburu, A., Fernández-Mendiola, P.A., López-Horgue, M. and **García-Mondéjar, J.** (2002) Syntectonic hydrothermal calcite in a faulted carbonate platform margin (Albian of Jorrios, northern Spain). *Sedimentology*, **49,** 875–890.

Barry, J.P., Kochevar, R.E. and **Baxter, C.H.** (1997) The influence of pore-water chemistry and physiology in the distribution of vesicomyid clams at cold seeps in Monterey Bay: implications for patterns of chemosynthetic community organization. *Limnol. Oceanogr.*, **42,** 318–328.

Beauchamp, B. and **Savard, M.** (1992) Cretaceous chemosynthetic carbonate mounds in the Canadian Arctic. *Palaios*, **7,** 434–450.

Beauchamp, B. and **von Bitter, P.** (Eds) (1992) Chemosynthesis:geological processes and products. *Palaios*, **7,** 337–484.

Berner, R.A. (1984) Sedimentary pyrite formation: an update. *Geochim. Cosmochim. Acta*, **48,** 605–615.

Boetius, A., Ravenschlag, K., Schubert, C.J., Rickert, D., Widdel, F., Gieseke, A., Amann, R., Jørgensen, B.B., Witte, U. and **Pfannkuche, O.** (2000) A marine microbial consortium apparently mediating anaerobic oxidation of methane. *Nature*, **407,** 623–626.

Botz, R., Wehner, H., Schmitt, M., Worthington, T.J., Schmidt, M. and **Stoffers, P.** (2002) Thermogenic hydrocarbons from the offshore Calypso hydrothermal field, Bay of Plenty, New Zealand. *Chem. Geol.*, **186,** 235–248.

Brassel, S.C., Wardroper, A.M.K., Thompson, I.D., Maxwell, J.R. and **Eglinton, G.** (1981) Speciphic acyclic isoprenoids as biological markers of methanogenic bacteria in marine sediments. *Nature*, **290,** 693–696.

Bray, C.J. and **Karig, D.E.** (1985) Porosity of sediments in accretionary prisms and some implications for dewatering processes. *J. Geophys. Res.*, **90,** 768–778.

Campbell, K.A. (2006) Hydrocarbon seep and hydrothermal vent paleoenvironments and paleontology: Past developments and future research directions. *Palaeogeogr. Palaeoclim. Palaeoecol.*, **232,** 362–407.

Campbell, K.A. and **Bottjer, D.J.** (1993) Fossil cold seeps. *Natl Geogr. Res. Explor.*, **9,** 326–343.

Campbell, K.A., Farmer, J.D. and **Des Marais, D.** (2002) Ancient hydrocarbon seeps from the Mesozoic convergent margin of California: carbonate geochemistry, fluids and paleoenvironments. *Geofluids*, **2,** 63–94.

Castañares, L.M., Robles, S., Gimeno, D. and **Vicente-Bravo, J.C.** (2001) The submarine volcanic system of the Errigoiti Formation (Albian-Santonian of the Basque-Cantabrian Basin, northern Spain): stratigraphic framework, facies and sequences. *J. Sed. Res.*, **71,** 318–333.

Cavagna, S., Clari, P. and **Martire, L.** (1999) The role of bacteria in the formation of cold seep carbonates: geological evidence from Monferrato (Tertiary, NW Italy). *Sed. Geol.*, **126,** 253–270.

Chafetz, H.S. (1986) Marine peloids: a product of bacterially induced precipitation of calcite. *J. Sed. Res.*, **56,** 812–817.

Chaler, R., Dorronsoro, C., Grimalt, J.O., Agirrezabala, L.M., Fernández-Mendiola, P.A., García-Mondéjar, J., Gómez-Pérez, I. and **López-Horgue, M.** (2005) Distributions of C_{22}-C_{30} even-carbon-number *n*-alkanes in Oceanic Anoxic Event 1 samples from the Basque-Cantabrian Basin. *Naturwissenschaften*, **92,** 221–225.

Clari, P.A. and **Martire, L.** (2000) Cold seep carbonates in the Tertiary of northwest Italy: evidence of bacterial degradation of methane. In: *Microbial Sediments* (Eds R.E. Riding and S.M. Awramik), pp. 261–269. Springer-Verlag, Berlin.

Coleman, M.L. and **Raiswell, R.** (1995) Source of carbonate and origin of zonation in pyritiferous carbonate concretions: evaluation of a dynamic model. *Am. J. Sci.*, **295,** 282–308.

Craig, H. (1957) Isotopic standards for carbon and oxygen and correlation factors for mass spectrometric analysis of carbon dioxide. *Geochim. Cosmochim. Acta*, **12,** 133–149.

Dame, F.R. (1996) *Ecology of Marine Bivalves. An Ecosystem Approach*. CRC Press, Boca Raton, FL, 254 pp.

Davis, G.R. and **Smith, L.B. Jr** (2006) Structurally controlled hydrothermal dolomite reservoir facies: an overview. *AAPG Bull.*, **90,** 1641–1690.

Desbruyères, D., Segonzac, M. and **Bright, M.** (Eds) (2006) *Handbook of Deep-sea Hydrothermal Vent Fauna*. Denisia, Linz, Vol. 18, 544pp.

Diaz-del-Río, V., Somoza, L., Martínez-Frias, J., Mata, M.P., Delgado, A., Hernández-Molina, F.J., Lunar, R., Martín-Rubí, J.A., Maestro, A., Fernández-Puga, M.C., León, R., Llave, E., Medialdea, T. and **Vázquez, J.T.** (2003) Vast fields of hydrocarbon-derived carbonate chimneys related to the accretionary wedge/olistostrome of the Gulf of Cádiz. *Mar. Geol.*, **195,** 177–200.

Eichhubl, E., Greene, H.G., Naehr, T. and **Maher, N.** (2000) Structural control of fluid flow: offshore fluid seepage in the Santa Barbara Basin, California. *J. Geochem. Explor.,* **69-70,** 545–549.

Einsele, G., Gieskes, J.M., Curray, J., Moore, D.M., Aguayo, E., Aubry, M.-P., Fornari, D., Guerrero, J., Kastner, M., Kelts, K., Lyle, M., Matoba, Y., Molina-Cruz, A., Niemitz, J., Rueda, J., Saunders, A., Schrader, H., Simoneit, B. and **Vacquier, V.** (1980) Intrusion of basaltic sills into highly porous sediments, and resulting hydrothermal activity. *Nature*, **283,** 441–445.

Elvert, M., Suess, E., Greinert, J. and **Whiticar, M.J.** (2000) Archaea mediating anaerobic methane oxidation in deep-sea sediments at cold-seeps of the eastern Aleutian subduction zone. *Org. Geochem.*, **31,** 1175–1187.

Flügel, E. (2004) *Microfacies of Carbonate Rocks: Analysis, Interpretation and Application*. Springer, Berlin, 976 pp.

Folk, R.L. (1987) Detection of organic matter in thin-sections of carbonate rocks using a white card. *Sed. Geol.*, **54,** 193–200.

Friedman, I. and **O'Neil, J.R.** (1977) Compilation of stable isotope fractionation factor of geochemical interest. In: *Data of Geochemistry* (Ed. M. Fleischer), 6th edn. *US Geol. Surv. Prof. Pap.*, **440-KK,** 1–12.

Gaillard, C., Rio, M., Rolin, Y. and **Roux, M.** (1992) Fossil chemosynthetic communities related to vents or seeps in sedimentary basins: the pseudobioherms of southeastern France compared to other world examples. *Palaios*, **7,** 451–465.

García-Mondéjar, J., Fernández-Mendiola, P.A., Agirrezabala, L.M., Aranburu, A., López-Horgue, M.A., Iriarte, E. and **Martínez de Rituerto, S**. (2004) El Aptiense-Albiense de la Cuenca Vasco-Cantábrica. In: *Geología de España* (Ed. J.A. Vera), pp. 291–296. SGE-IGME, Madrid.

Goedert, J.L., Thiel, V., Schmale, O., Rau, W.W., Michaelis, W. and **Peckmann, J.** (2003) The Late Eocene ''Whiskey Creek'' methane-seep deposit (western Washington State). Part I: Geology, paleontology, and molecular geobiology. *Facies*, **48,** 223–240.

Gómez de Llarena, J. (1958) Datos paleontológicos del flysch litoral de Guipuzcoa: el Vraconiense de septarias de Motrico. *Notas Com. Inst. Geol. Min. Esp., II*, **50,** 5–21.

Gómez-Pérez, I. (2003) An Early Jurassic deep-water stromato litic bioherm related to possible methane seepage (Los Molles Formation, Neuquén, Argentina). *Palaeogeogr. Palaeoclimatol. Palaeoecol.*, **201,** 21–49.

Greinert, J., Bohrmann, G. and **Elvert, M.** (2002) Stromatolitic fabric of authigenic carbonate crusts: result of anaerobic methane oxidation at cold seeps in 4,850 m water depth. *Int. J. Earth Sci.*, **91,** 698–711.

Haggerty, J.A. (1991) Evidence from fluid seeps atop serpentine seamounts in the Marianas Forearc: clues for emplacement of the seamounts and their relationships to forearc tectonics. *Mar. Geol.*, **102,** 293–309.

Han, X., Suess, E., Sahling, H. and **Wallman, K.** (2004) Fluid venting activity on the Costa Rica margin: new results from authigenic carbonates. *Int. J. Earth Sci.*, **93,** 596–611.

Hein, J.R., Normark, W.R., McIntyre, B.R., Lorenson, T.D. and **Powell, C.L.** (2006) Methanogenic calcite, ^{13}C-depleted bivalve shells, and gas hydrate from mud volcano offshore southern California. *Geology*, **34,** 109–112.

Hoefs, J. (1997) *Stable Isotope Geochemistry*. Springer-Verlag, Berlin, 201 pp.

Hofmann, P., Ricken, W., Schwark, L. and **Leythaeuser, D.** (2000) Carbon-sulfur-iron relationships and δ^{13}C of organic matter for late Albian sedimentary rocks from the North Atlantic Ocean: paleoceanographic implications. *Palaeogeo gr. Palaeoclimatol. Palaeoecol.*, **163,** 97–113.

Hunt, J.M. (1996) *Petroleum Geochemistry and Geology*. W.H. Freeman, New York, 743 pp.

Jacob, H. (1989) Classification, structure, genesis and practical importance of natural solid oil bitumen (''migrabitumen''). *Int. J. Coal Geol.*, **11,** 65–79.

Joye, S.B., Boetius, A., Orcutt, B.N., Montoya, J.P., Schulz, H.N., Erickson, M.J. and **Lugo, S.K.** (2004) The anaerobic oxidation of methane and sulfate reduction in sediments from Gulf of Mexico cold seeps. *Chem. Geol.*, **205,** 219–238.

Judd, A.G. and **Hovland, M.** (2007) *Seabed Fluid Flow: The Impact on Geology, Biology and the Marine Environment*. Cambridge University Press, Cambridge, 475 pp.

Kauffman, E.G. and **Johnson, C.C.** (1988) The morphological and ecological evolution of Middle and Upper Cretaceous reef-building rudists. *Palaios*, **3,** 194–216.

Kauffman, E.G., Arthur, M.A., Howe, B. and **Scholle, P.A.** (1996) Widespread venting of methane-rich fluids in Late Cretaceous (Campanian) submarine springs (Tepee Buttes), Western Interior seaway, U.S.A. *Geology*, **24,** 799–802.

Kelly, S.R.A., Ditchfield, P.W., Doubleday, P.A. and **Marshall, J.D.** (1995) An Upper Jurassic methane-seep limestone from the fossil Bluff Group forearc basin of Alexander Island, Antarctica. *J. Sed. Res.*, **65,** 274–282.

Kelly, S.R.A., Blanc, E., Price, S.P. and **Whitham, A.G.** (2000) Early Cretaceous giant bivalves from seep-related limestone mounds, Wollaston Forland, Northeast Greenland. In: *The Evolutionary Biology of the Bivalvia* (Eds E.M. Harper, J. D. Taylor and J.A. Crame), *Geol. Soc. Spec. Publ.*, **177,** 227–246.

Klein, C. and **Dutrow, B.** (2008) *Mineral Science*. John Wiley & Sons, Hoboken, NJ, 675 pp.

Kulm, L.D. and **Suess, E.** (1990) Relationship of carbonate deposits and fluid venting: Oregon accretionary prism. *J. Geophys. Res.*, **95,** 8899–8916.

Levin, L.A. (2005) Ecology of cold seep sediments: interactions of fauna with flow, chemistry and microbes. *Oceanogr. Mar. Biol. Annu. Rev.*, **43,** 1–46.

Levin, L.A., Ziebis, W., Mendoza, G., Growney, V., Tryon, M., Brown, K., Mahn, C., Gieskes, J. and **Rathburn, A.** (2003) Spatial heterogeneity of macrofauna at northern California methane seeps: the influence of sulfide concentration and fluid flow. *Mar. Ecol. Progr. Ser.*, **265,** 123–139.

Lewis, K.B. and **Marshall, B.A.** (1996) Seep faunas and other indicators of methane-rich dewatering on New Zealand convergent margins. *NZ J. Geol. Geophys.*, **39,** 181–200.

Lewy, Z. (1995) Hypothetical endosymbiontic zooxanthellae in rudists are not needed to explain their ecological niches and thick shells in comparison with hermatypic corals. *Cretaceous Res.*, **16,** 25–37.

Little, C.T.S., Herrington, R.J., Maslennikov, V.V., Morris, N.J. and **Zaykov, V.V.** (1998) The fossil record of hydrothermal vent communities. In: *Modern Ocean Floor Processes and the Geological Record* (Eds R.A. Mills and K. Harrison), *Geol. Soc. Spec. Publ.*, **148,** 259–270.

Little, C.T.S., Danelian, T., Herrington, R.J. and **Haymon, R.M.** (2004) Early Jurassic hydrothermal vent community from the Franciscan Complex, California. *J. Paleontol.*, **78,** 542–559.

Machel, H.G. (1987) Saddle dolomite as a by-product of chemical compaction and thermochemical sulphate reduction. *Geology*, **15,** 936–940.

Machel, H.G. (2001) Bacterial and Thermochemical sulfate reduction in diagenetic settings – old and new insights. *Sed. Geol.*, **140,** 143–175.

Machel, H.G., Krouse, H.R. and **Sassen, R.** (1995) Products and distinguishing criteria of bacterial and thermochemical sulfate reduction. *Appl. Geochem.*, **10,** 373–389.

Majima, R., Nabuhara, T. and **Kitazaki, T.** (2005) Review of fossil chemosynthetic assemblages in Japan. *Palaeogeogr. Palaeoclim. Palaeoecol.*, **227,** 86–123.

Martin, R.A., Nesbitt, E.A. and **Campbell, K.A.** (2007) Carbon stable isotopic composition of benthic foraminifera from Pliocene cold methane seeps, Cascadia accretionary margin. *Palaeogeogr. Palaeoclim. Palaeoecol.*, **246,** 260–277.

Mazzini, A., Aloisi, G., Akhmanov, G.G., Parnell, J., Cronin, B.T. and **Murphy, P.** (2005) Integrated petrographic and geochemical record of hydrocarbon seepage on the Vøring Plateau. *J. Geol. Soc.*, **162,** 815–827.

McCrea, J.M. (1950) On the isotopic chemistry of carbonates and a palaeotemperature scale. *J. Chem. Phys.*, **18,** 849–857.

Michaelis, W., Seifert, R., Nauhaus, K., Treude, T., Thiel, V., Blumenberg, M., Knittel, K., Gieseke, A., Peterknecht, K., Pape, T., Boethius, A., Amann, R., Jorgensen, B.B., Widdel, F., Peckmann, J., Pimenov, N.V. and **Gulin, M.B.** (2002) Microbial reefs in the Black Sea fueled by anaerobic oxidation of methane. *Science*, **299,** 1013–1015.

Montadert, L., Winnock, E., Delteil, J.R. and **Grau, G.** (1974) Continental margins of Galicia-Portugal and Bay of Biscay. In: *Geology of Continental Margins* (Eds C.A. Burk and C.L. Drake), pp. 223–342. Springer-Verlag, Berlin.

Moore, R.C. (Ed.) (1956) *Treatise on Invertebrate Paleontology, Part F Coelenterata*. Geological Society of America and University of Kansas Press, Boulder, CO, 498 pp.

Ogg, J.G., Agterberg, F.P. and **Gradstein, F.M.** (2004) The Cretaceous Period. In: *A Geologic Time Scale 2004* (Eds F.M. Gradstein, J.G. Ogg and A.G. Smith), pp. 344–383. Cambridge University Press, Cambridge.

Olu, K., Duperret, A., Sibuet, M., Foucher, J.-P. and **Fiala-Médioni, A.** (1996) Structure and distribution of cold seep communities along the Peruvian active margin: relationship to geological and fluid patterns. *Mar. Ecol. Progr. Ser.*, **132,** 109–125.

Olu, K., Lance, S., Sibuet, M., Henry, P., Fiala-Médioni, A. and **Dinet, A.** (1997) Cold seep communities as indicators of fluid expulsion patterns through mud volcanoes seaward of the Barbados accretionary prism. *Deep-Sea Res. I*, **44,** 811–841.

Olu, K., Sibuet, M., Fiala-Médioni, A., Gofas, S., Salas, C., Mariotti, A., Foucher, J.-P. and **Woodside, J.** (2004) Cold seep communities in the deep eastern Mediterranean Sea: composition, symbiosis and spatial distribution on mud volcanoes. *Deep-Sea Res. I*, **51,** 1915–1936.

Orange, D.L., Greene, H.G., Reed, D., Martin, J.B., McHugh, C.M., Ryan, W.B.F., Maher, N., Stakes, D. and **Barry, J.** (1999) Widespread fluid expulsion on a translational continental margin: Mud volcanoes, fault zones, headless canyons, and organic-rich substrate in Monterey Bay, California. *Geol. Soc. Am. Bull.*, **111,** 992–1009.

Orphan, V.J., House, C.H., Hinrichs, K.U., McKeegan, K.D. and **DeLong, E.F.** (2002) Multiple archaeal groups mediate methane oxidation in anoxic cold seep sediments. *Proc. Natl Acad. Sci. USA*, **99,** 7663–7668.

Paull, C.K., Chanton, J.P., Neumann, A.C., Coston, J.A. and **Martens, C.S.** (1992) Indicators of methane-derived carbonates and chemosynthetic organic carbon deposits: examples from the Florida Escarpment. *Palaios*, **7,** 361–375.

Peckmann, J. and **Thiel, V.** (2004) Carbon cycling at ancient methane-seeps. *Chem. Geol.*, **205,** 443–467.

Peckmann, J., Thiel, V., Michaelis, W., Clari, P., Gaillard, C., Martire, L. and **Reitner, J.** (1999) Cold seep deposits of Beauvoisin (Oxfordian; southeastern France) and Marmorito (Miocene; northern Italy): microbially induced authigenic carbonates. *Int. J. Earth Sci.*, **88,** 60–75.

Peckmann, J., Gischler, E., Oschmann, W. and **Reitner, J.** (2001) An Early Carboniferous seep community and hydrocarbon-derived carbonates from the Harz Mountains, Germany. *Geology*, **22,** 271–274.

Peckmann, J., Goedert, J.L., Thiel, V., Michaelis, W. and **Reitner, J.** (2002) A comprehensive approach to the study of methane-seep deposits from the Lincoln Creek Formation, western Washington State, USA. *Sedimentology*, **49,** 855–873.

Peckmann, J., Goedert, J.L., Heinrichs, T., Hoefs, J. and **Reitner, J.** (2003) The Late Eocene ''Whiskey Creek'' methane-seep deposit (western Washington State). Part II: petrology, stable isotopes, and biogeochemistry. *Facies*, **48,** 241–254.

Peckmann, J., Campbell, K.A., Walliser, O.H. and **Reitner, J.** (2007) A Late Devonian hydrocarbon-seep deposit dominated by deimerelloid brachiopods, Morocco. *Palaios*, **22,** 114–122.

Puigdefábregas, C. and **Souquet, P.** (1986) Tecto-sedimentary cycles and depositional sequences of the Mesozoic and Tertiary from the Pyrenees. *Tectonophysics*, **129,** 173–203.

Radke, B.M. and **Mathis, R.L.** (1980) On the formation and occurrence of saddle dolomite. *J. Sed. Res.*, **50,** 1149–1168.

Riding, R.T. and **Tomás, S.** (2006) Stromatolite reef crust, Early Cretaceous, Spain: bacterial origin of *in situ*-precipitated peloid microspar? *Sedimentology*, **53,** 23–34.

Rio, M., Roux, M., Renard, M. and **Schein, E.** (1992) Chemical and isotopic features of present day bivalve shells from hydrothermal vents or cold seeps. *Palaios*, **7,** 351–360.

Ritger, S., Carson, B. and **Suess, E.** (1987) Methane-derived authigenic carbonates formed by subduction-induced pore-water expulsion along the Oregon/Washington margin. *Geol. Soc. Am. Bull.*, **98,** 147–156.

Rossy, M. (1988) *Contribution a l'étude du magmatisme Mésozoique du domaine Pyrénnéen*. PhD Thesis, Université de Franche-Comté, France, 368 pp.

Rushdi, A.I. and **Simoneit, B.R.T.** (2002a) Hydrothermal alteration of organic matter in sediments of the Northeastern Pacific Ocean: Part 1. Middle Valley, Juan de Fuca Ridge. *Appl. Geochem.*, **17,** 1401–1428.

Rushdi, A.I. and **Simoneit, B.R.T.** (2002b) Hydrothermal alteration of organic matter in sediments of the Northeastern Pacific Ocean: Part 2. Escanaba Trough, Gorda Ridge. *Appl. Geochem.*, **17,** 1467–1494.

Sackett, W.M. (1978) Carbon and hydrogen isotope effects during the thermocatalytic production of hydrocarbons in laboratory simulation experiments. *Geochim. Cosmochim. Acta*, **42,** 571–580.

Sahling, H., Rickert, D., Lee, R.W., Linke, P. and **Suess, E.** (2002) Macrofaunal community structure and sulfide flux at gas hydrate deposits from the Cascadia convergent margin. *Mar. Ecol. Progr. Ser.*, **231,** 121–138.

Schoell, M., Hwang, R.J. and **Simoneit, B.R.T.** (1990) Carbon isotope composition of hydrothermal petroleums from Guaymas Basin, Gulf of California. *Appl. Geochem.*, **5,** 65–69.

Schultz, L.G. (1964) Quantitative interpretation of mineralogical composition from X-ray and chemical data for Pierre Shales. *US Geol. Surv. Prof. Pap.*, **391-C,** 1–31.

Shapiro, R.S. (2004) Recognition of fossil prokaryotes in Cretaceous methane seep carbonates: relevance to astrobiology. *Astrobiology*, **4,** 438–449.

Sibuet, M. and **Olu, K.** (1998) Biogeography, biodiversity and fluid dependence of deep-sea cold-seep communities at active and passive margins. *Deep-Sea Res. II*, **45,** 517–567.

Simoneit, B.R.T. and **Lonsdale, P.F.** (1982) Hydrothermal petroleum in mineralised mounds at the seabed of Guaymas Basin. *Nature*, **295,** 198–202.

Souquet, P., Debroas, E.J., Boirie, J.M., Pons, P., Fixari, G., Roux, J.C., Dol, J., Thieuloy, J.P., Bonnemaison, M., Manivit, H. and **Peybernes, B.** (1985) Le Groupe du Flysch Noir (Albo-Cénomanien) dans les Pyrénées. *Bull. Centres Rech. Explor.-Produd. Elf-Aquitaine*, **9,** 183–252.

Spencer, R.J. (1987) Origin of Ca-Cl brines in Devonian formations, Western Canada sedimentary basin. *Appl. Geochem.*, **2,** 373–384.

Tissot, B.P. and **Welte, D.H.** (1984) *Petroleum Formation and Occurrence*. Springer-Verlag, Berlin, 538 pp.

Vacelet, J., Boury-Esnault, N., Fiala-Médioni, A. and **Fisher, C.R.** (1995) A methanotrophic carnivorous sponge. *Nature*, **377,** 296.

Valentine, D.L. (2002) Biogeochemistry and microbial ecology of methane oxidation in anoxic environments: a review. *Antonie Van Leeuwenhoek*, **81,** 271–282.

Van Dover, C.L. (2000) *The Ecology of Deep-Sea Hydrothermal Vents*. Princeton University Press, Princeton, NJ, 424 pp.

Warren, J. (2000) Dolomite: occurrence, evolution and economically important associations. *Earth-Sci. Rev.*, **52,** 1–81.

Wenger, L.M. and **Isaksen, G.H.** (2002) Control of hydrocarbon seepage intensity on level of biodegradation in the sea bottom sediments. *Org. Geochem.*, **33,** 1277–1292.

Wilson, P.A. and **Norris, R.D.** (2001) Warm tropical ocean surface and global anoxia during the mid-Cretaceous period. *Nature*, **412,** 425–429.

Manuscript received 27 March 2007; revision accepted 11 August 2008

Geol. Mag. **150** (*6*), *2013, pp. 986–1001.* © *Cambridge University Press 2013*
doi:10.1017/S0016756813000149

Albian syndepositional block rotation and its geological consequences, Basque–Cantabrian Basin (western Pyrenees)

LUIS MIGUEL AGIRREZABALA*† & JAUME DINARÈS-TURELL‡

*Estratigrafia eta Paleontologia Saila, Euskal Herriko Unibertsitatea UPV/EHU, 644 PK, 48080 Bilbo, Spain
‡Istituto Nazionale di Geofisica e Vulcanologia. Via di Vigna Murata 605, 00143 Roma, Italy

(*Received* 13 November 2012; *accepted* 24 January 2013; *first published online* 2 May 2013)

Abstract – Stratigraphic, structural, palaeocurrent and palaeomagnetic analyses of Upper Albian deep-water deposits in and around the Deba block (Northern Iberia) are presented. Results indicate an anticlockwise vertical-axis rotation of this block by 35° during a maximum time span of *c.* 1 Ma (Late Albian intra-*C. auritus* ammonite Subzone). This Albian syndepositional block rotation is interpreted to be the consequence of the coeval activity of conjugate major sinistral strike-slip faults and minor (antithetic) dextral strike-slip faults, which border the Deba block. On the base of conservative estimations, a minimum block-rotation rate of 35° Ma^{-1} and a sinistral strike-slip rate of 1.2 km Ma^{-1} are calculated. As a consequence of the interaction of the rotated Deba block with adjacent non-rotated blocks, its corners experienced coeval transpressive (NW and SE corners) and transtensional deformations (SW and, possibly, NE corners). At the transtensional SW corner, two domal high-reflective seismic structures have been recorded and interpreted as high-level magmatic laccoliths. These magmatic intrusions triggered the development of a mineralizing hydrothermal system, which vented to the Late Albian seafloor warm to hot hydrocarbon-rich fluids. Vented hydrocarbon was generated from Albian organic-rich sediments by contact alteration with hydrothermal fluids.

Keywords: block rotation, palaeocurrent, palaeomagnetism, Albian, Basque–Cantabrian Basin.

1. Introduction

Crustal block rotation about vertical axes is a common feature of intra-continental strike-slip fault zones, in particular of areas in which deformation is distributed over a wide zone (e.g. Ron *et al.* 1984; Luyendyk *et al.* 1985; McKenzie & Jackson, 1986; Nicholson *et al.* 1986; Mattei *et al.* 2012). Classically, palaeomagnetic, geodetic, seismic and structural studies have provided compelling evidence for block rotation. In addition, in a few cases palaeocurrent directions have been used as geometric markers for tracking strain in areas of tectonic vertical axis rotation or orocline bending with variable success (e.g. Shaw *et al.* 2012). Debate over models for block rotation has concentrated on two main groups, continuum and discrete models (e.g. McKenzie & Jackson, 1986; King *et al.* 1994; Peacock *et al.* 1998). Discrete models involve rigid block rotation accommodated by sets of large faults, which causes the development of triangular overlaps (shortening) and voids (extension) at the zone margins. In areas of overlap local convergence produces folding and reverse faulting (e.g. Şengör *et al.* 1985), while areas of voids are filled by magmatic intrusions (Tikoff & Teyssier, 1992), salt diapirs (Hudec & Jackson, 2007) or sedimentary basins (Luyendyk *et al*. 1980).

The Pyrenean domain has been traditionally considered the Cretaceous transcurrent boundary between Europe and Iberia plates. Most studies point out a distributed wide wrench boundary where sinistral strike-slip movements along E–W to NW–SE faults were responsible for transtension (e.g. Van der Voo, 1969; Puigdefàbregas & Souquet, 1986; Choukroune, 1992; Larrasoaña *et al.* 2002) (Fig. 1a). In the western Pyrenees, the mid-Cretaceous tectonic pattern of the Basque–Cantabrian Basin indicates that the filling of this basin was mainly controlled by transtension, particularly during Albian times. In this basin, a lot of different syndepositional tectonic structures and other features related to strike-slip tectonics have been documented (García-Mondéjar *et al.* 1996). Besides sedimentation, other coeval geological processes such as hydrothermal venting and mineralization (Aranburu *et al.* 2002; Agirrezabala 2009; López-Horgue *et al.* 2010), iron carbonate ore formation, magmatism (Castañares *et al*. 2001; Fernández-Mendiola & García-Mondéjar, 2003) and hydrocarbon accumulation has been interpreted as controlled by Albian tectonic structures (García-Mondéjar, 1989). The aim of this work is to provide new stratigraphic, structural, palaeocurrent and palaeomagnetic data supporting Albian vertical-axis rotation of the *c.* 7 km^2 Deba block. The obtained results allow us to construct a comprehensive block rotation model which explains coeval tectonic deformations, emplacement of magmatic intrusions, hydrocarbon venting and hydrothermal mineral formation recorded in the margins of the Deba block.

2. Geological setting

The Basque–Cantabrian Basin in the western Pyrenees (Fig. 1a) was a Mesozoic peri-cratonic rift related to the

†Author for correspondence: l.agirrezabala@ehu.es

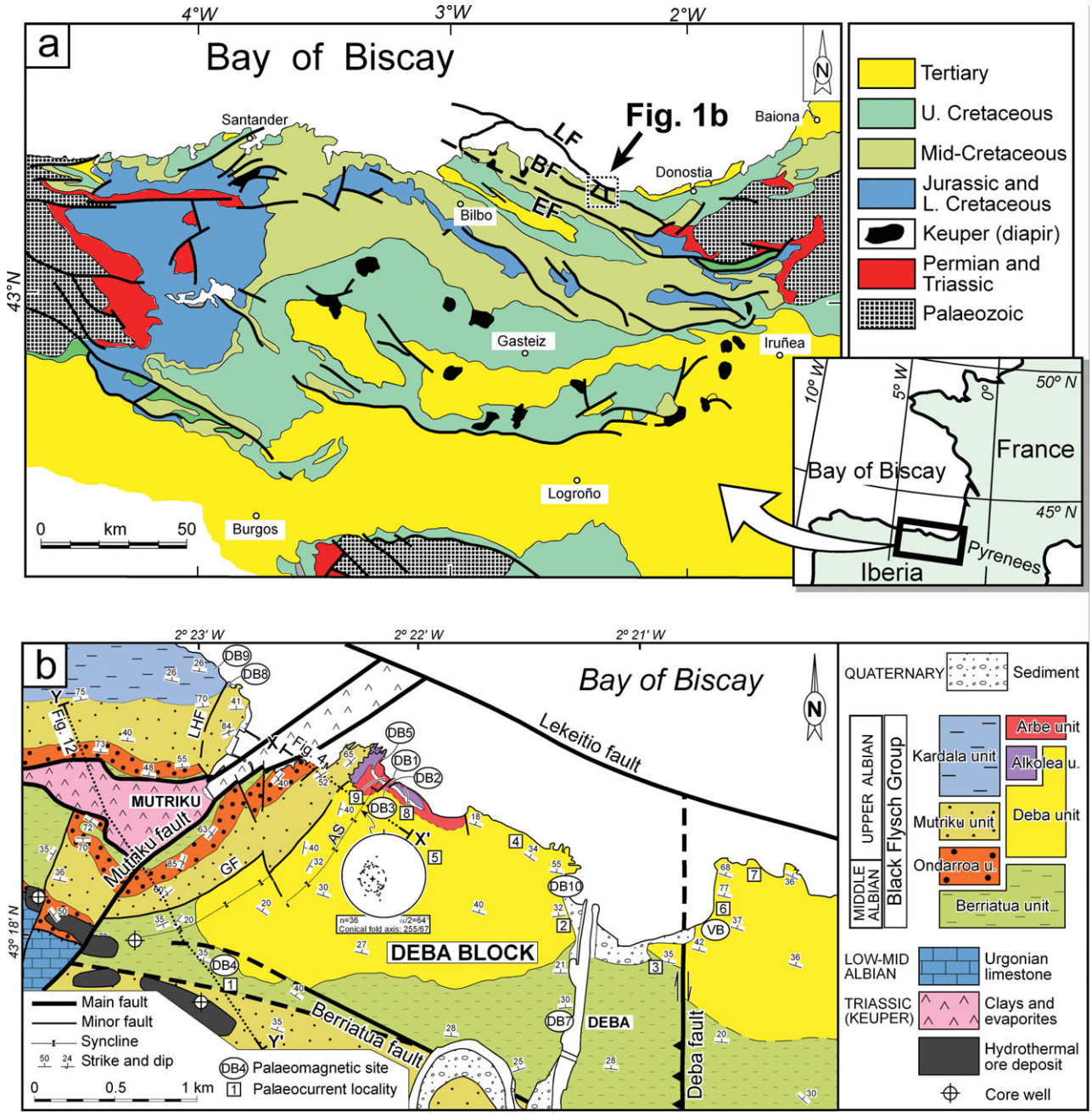

Figure 1. (Colour online) (a) Geological map of the Basque–Cantabrian Basin with indication of the study area depicted in (b). LF: Lekeitio fault; BF: Berriatua fault; EF: Elgoibar fault. (b) Detailed geological map of the Deba block and neighbouring areas. Palaeocurrent localities (squares) and palaeomagnetic sites (circles) are indicated. Inset shows equal-area stereographic projection of stratification poles of the conical Aitzeta syncline (AS) and resulting best-fit small circle, conical fold axis and its semi-apical angle ($\alpha/2$). X–X′ indicates the trace of the cross-section shown in Figure 4b, and Y–Y′ indicates the trace of the seismic section shown in Figure 12.

opening of the Bay of Biscay and North Atlantic Ocean (Montadert *et al.* 1974; Choukroune & Mattauer, 1978; Rat *et al.* 1983; Engeser & Schwentke, 1986; Rat, 1988; García-Mondéjar, 1989) and inverted during Tertiary compression (Cámara, 1997; Gómez *et al.* 2002). The basin experienced a mid-Cretaceous phase of quick subsidence in a regional transtensional regime related to the left-lateral drift of Iberia (Van der Voo, 1969; Rat *et al.* 1983; Puigdefàbregas & Souquet, 1986; García-Mondéjar, 1989; García-Mondéjar *et al.* 1996, 2004*a*, *b*; Olivet, 1996). Resulting sinistral strike-slip movements were distributed in a wide zone along the Iberia–Europe plate boundary (Choukroune, 1992; García-Mondéjar *et al.* 1996). The extreme stretching and thinning of the crust reached a maximum during mid-Cretaceous times (Pedreira *et al.* 2003, 2007; García-Mondéjar *et al.* 2004*a*; Jammes *et al.* 2009), with the occurrence of submarine volcanism and shallow-level magmatic intrusions (Rossy, 1988; Castañares *et al.* 2001; Fernández-Mendiola & García-Mondéjar, 2003) but without full development of an ocean. Magmatic intrusions emplaced in organic-rich deposits triggered

contact metamorphism of host organic matter and the generation of hydrocarbon-rich fluids, which seeped to the Albian palaeoseabed (Agirrezabala *et al.* 2013). In addition, local high-temperature metamorphism (Azambre & Rossy, 1976) and hydrothermal Zn–Pb (among others) ore formation (García-Mondéjar, 1989; Agirrezabala & García-Mondéjar, 2001*a*; Aranburu *et al.* 2002; López-Horgue *et al.* 2010) took place in the basin during the mid-Cretaceous period. The local distribution of magmatic rocks, hydrothermal ore deposits and hydrocarbons in the basin is interpreted to have been controlled by the intersection of two NW- and SE-trending fault systems (García-Mondéjar, 1989; García-Mondéjar *et al.* 1996; Castañares *et al.* 2001).

Mid-Cretaceous strike-slip tectonics affected mainly the northern margin of the Basque–Cantabrian Basin, where both syndepositional transtensional and transpressive deformations (faults and folds) and vertical-axis block rotations have been documented (Agirrezabala & García-Mondéjar, 1992, 1994; García-Mondéjar *et al.* 1996; Agirrezabala *et al.* 2002; Larrasoaña *et al.* 2002). This margin constituted in Albian–Cenomanian times a sinistral wrench corridor composed of both ESE- to E-trending strike-slip major faults and transversal NE- to N-trending minor faults which compartmentalized the margin in small blocks (the Deba block studied here), creating small deep-water sub-basins (Agirrezabala & García-Mondéjar, 1994, 2001*a*; García-Mondéjar *et al.* 1996). These sub-basins were filled by NE-derived siliciclastic turbidite systems, which constitute the Middle Albian – Lower Cenomanian Black Flysch Group (Souquet *et al.* 1985). Regional turbiditic dispersion systems and palaeocurrents were parallel to the confining tectonic structures, usually showing a L-shaped pattern with SSW-directed proximal dispersion and palaeocurrents and ESE-directed distal dispersion and palaeocurrents within the inner part of the basin (Agirrezabala & García-Mondéjar, 1994; García-Mondéjar *et al.* 2004*b*; Agirrezabala & Bodego, 2005).

3. Stratigraphy

Rocks cropping out in the Deba block and adjacent areas belong mainly to the Black Flysch Group, which is subdivided into seven informal Middle – Late Albian lithostratigraphic units (Figs 1b, 2). Stratigraphic, sedimentological, geochemical and structural data and interpretations relative to these deep-water units have been documented in detail by L. M. Agirrezabala (unpub. Ph.D.thesis, Euskal Herriko Unibertsitatea, 1996), Agirrezabala *et al.* (2002, 2003, 2008) and Agirrezabala (2009). The stratigraphic record of the area is marked by two important tectono-sedimentary events that occurred at the Late Albian *C. auritus* ammonite Subzone (*M. inflatum* Zone). Ammonite biozonation has been the traditional primary standard for subdividing most of the Cretaceous period and yields the maximum biostratigraphic resolution for the Albian stage. The Albian absolute time scale and durations of its biozones are derived from cyclostratigraphy (Grippo *et al*. 2004; Ogg *et al.* 2004). In the case of the Late Albian *M. inflatum* ammonite Zone, a duration of 5.5 Ma is estimated. That zone is composed of four subzones with an assigned equal duration of 1.3 Ma (Ogg *et al.* 2004).

At the north-western margin of the Deba block, a wedge of syntectonic deposits with abundant coarse breccias and two (high-angle) angular unconformities (AU1 and AU2) of *C. auritus* Subzone age (Alkolea unit, Figs 1b, 2) record the growth of a monoclinal syncline interpreted to be associated with the Mutriku fault (Agirrezabala *et al.* 2002). Overlying post-*auritus* turbidites (Arbe unit) onlap north-westwards and fossilize the resultant fold (Figs 1b, 2) (Agirrezabala *et al.* 2002). Two contemporaneous authigenic carbonate lenses occur in *C. auritus* syntectonic deposits adjacent to the Mutriku fault (Fig. 2). A multidisciplinary study of these carbonates indicates that they constitute microbially mediated by-products of hydrocarbon-rich hydrothermal venting associated with the activity of the Mutriku fault (Agirrezabala, 2009). Estimated fluid palaeotemperatures up to 109 °C, together with organic geochemical correlation, indicate that vented oil and thermogenic methane were generated at shallow depths from Black Flysch organic matter by contact alteration with hydrothermal fluids (Agirrezabala *et al.* 2008; Agirrezabala, 2009). Pre-*auritus* rocks of the south-western part of the study area host hydrothermal mineralizations, Pb–Zn deposits (EEE, 2003) and pyrobitumen fills (Figs 1b, 2).

4. Block bordering faults and deformation structures

The Deba block is bordered by two ESE-trending main faults, namely the Lekeitio fault to the NE and the Berriatua fault to the SW, and two transversal NE- and N-trending minor faults, namely the Mutriku fault to the NW and the Deba fault to the E. These define a trapezoidal-shaped non-faulted rock unit of *c.* 7 km^2 (Fig. 1b). Based on different geological data, ESE- and E-trending major faults of the northern margin of the basin have been traditionally interpreted as mid-Cretaceous sinistral strike-slip faults along which eastwards movement of the Iberian plate took place (Rat *et al.* 1983; García-Mondéjar *et al.* 1996; Larrasoaña *et al.* 2002; Iriarte, 2005). Moreover, kinematic indicators from the fault zones confirm left-lateral movements along them (Agirrezabala & García-Mondéjar, 2001*a*), although no displacement magnitudes for individual faults are available. Stratigraphic and structural analysis of the minor NE-trending Mutriku fault and associated Aitzeta growth fold (Fig. 1b) suggests Late Albian right-lateral movements along this fault (Agirrezabala *et al.* 2002). The N-trending Deba fault zone shows kinematic indicators such as striation on shear planes, slickenfibres, en échelon extensional veins and foliation indicative of dextral strike-slip faulting (Fig. 3). Additionally,

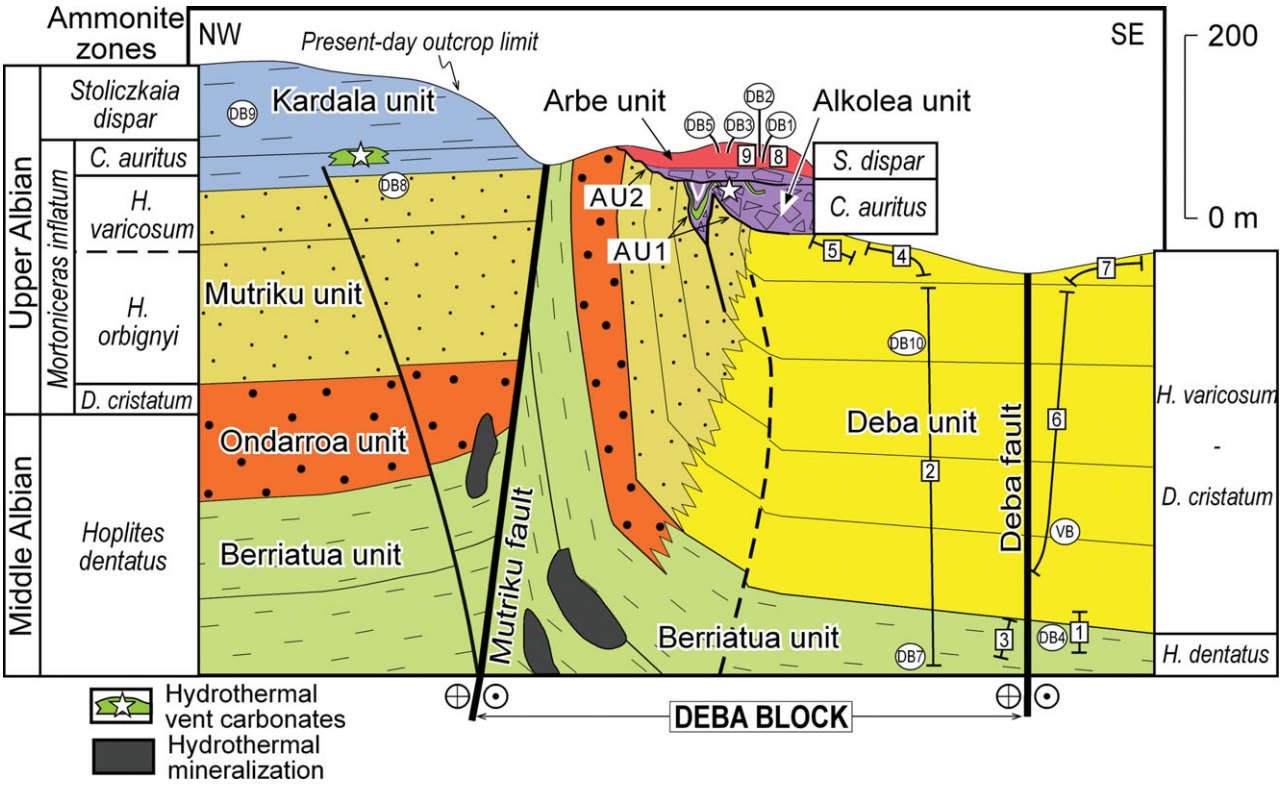

Figure 2. (Colour online) Lithostratigraphy and ammonite biostratigraphy of the Black Flysch Group deposits in the study area. Palaeocurrent localities (squares) with their corresponding succession interval (segment line) and palaeomagnetic sites (circles) are shown. AU1 and 2 are angular unconformities.

mapping of the Deba fault also shows a right-lateral offset of 200 m and a reverse dip-slip component in its southern part of *c.* 200–300 m (Fig. 1b).

In the NW corner of the Deba block, the Aitzeta monoclinal syncline (Figs 1b, 4) appears adjacent and parallel to the Mutriku fault (Agirrezabala *et al.* 2002). At present, it reaches 2 km (minimum) in strike length and 0.5 km (maximum) in dip-direction width and strikes NE. The Aitzeta monocline depicts a vertical limb striking NE which crops out for 2 km immediately west of the Mutriku fault while its horizontal limb is interpreted to underlie the rest of the Deba block. The vertical limb brings up to 500 m of the Middle–Upper Albian rocks to the surface in the NW, while it becomes narrower to the SW until it disappears. Both mapping and bedding attitudes indicate that the Aitzeta syncline is a conical fold (axis: 255/67°; semi-apical angle $\alpha/2$: 64°) (Fig. 1b). The wedge of syntectonic deposits (Alkolea unit) that overlaps the south-eastern margin of the structure and related angular unconformities (AU1 and 2) record the two-pulse growth of the Aitzeta monoclinal syncline during the Late Albian *auritus* Subzone. A cross-section of the structure restored at the end of *auritus* Subzone time shows that it constitutes the subvertical limb of a fault-related syncline (Fig. 4). Structural analysis and clast stratigraphy of syntectonic deposits indicate that the growth of this structure carried out the uplift and erosive denudation of 350–390 m (minimum) of underlying rocks (Agirrezabala *et al.* 2002). The presence of bedding-parallel faults which cut overlying angular unconformity 1 and cause drape folding of the syntectonic deposits (Fig. 4) is interpreted as a result of flexural slip folding (Alonso, 1989). During the rotation and uplift of the limb a SE-facing erosive talus developed; fragments of underlying units were resedimented at the base of this (Fig. 4).

5. Palaeocurrents

A total of 282 palaeocurrents distributed at 9 localities were measured from sole mark structures (flute, prod, crescent, groove, bounce and skip casts) of sandy turbidite successions (Figs 1b, 2, 5). Four of these successions were also sampled for palaeomagnetic analyses. Obtained palaeocurrent data and statistical parameters are listed in Table 1 and corresponding rose diagrams are plotted in Figure 6a. They were collected from pre- and post-*auritus* strata both inside and outside of the Deba block. No palaeocurrents have been measured NW of the Mutriku fault because of the absence of good-quality outcrops of turbiditic strata. Folds in the measured sections indicate a horizontal axis; tilting of sedimentary structures was therefore corrected by rotation about the horizontal axis.

5.a. Palaeocurrent results

The palaeocurrent rose diagrams for each locality show low dispersion (Table 1, Fig. 6a). The palaeocurrent

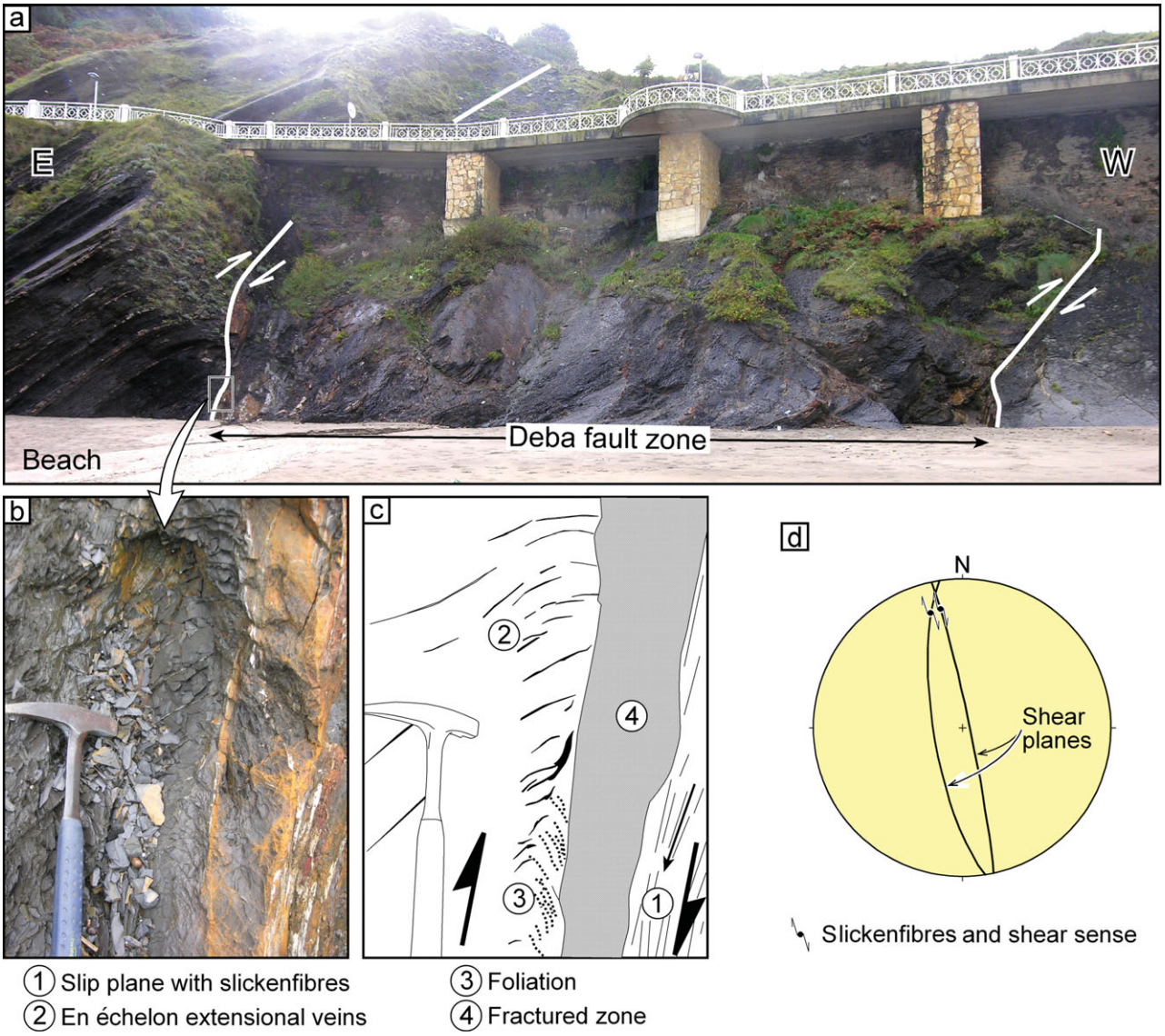

Figure 3. (Colour online) Outcrop of the Deba fault zone at the Deba beach. (a) Photograph of the Deba fault zone and adjacent thin-bedded turbidite succession (Deba unit); (b) detail photograph of (a); (c) drawing of (b) showing different kinematic indicators (slip plane, slickenfibres, en échelon extensional veins, foliation and fractured zone) suggesting dextral strike-slip faulting; and (d) equal-area stereographic projection of two major shear planes and associated slickenfibres from the Deba fault zone indicative of dextral strike-slip movements.

Table 1. Palaeocurrent statistical data. Measured sedimentary structures are sole marks from sandy turbidites. Location numbers correspond to those in Figures 1b, 2; *N* population size; *L*% vector length (%); *k* concentration factor.

Setting	Age	Location	Unit	*N*	Vector mean (°)	*L*%	*k*
Deba block	Post-*auritus*	8	Arbe	12	215	98	69.2
		9	Arbe	21	222	98	48.3
	Pre-*auritus*	2	Berriatua and Deba	49	65	89	9.3
		3	Berriatua	7	68	94	17.7
		4	Deba	38	64	93	15.5
		5	Deba	31	79	99	164.8
Outside Deba block	Pre-*auritus*	1	Berriatua and Deba	14	101	97	42.7
		6	Deba	83	110	66	2.9
		7	Deba	27	96	87	7.8

directions map indicates three directional groups of palaeocurrent roses related by their stratigraphic and structural position (Fig. 6a). In the Deba block, palaeocurrents from pre-*auritus* rocks yield mean palaeoflow directions toward N 64° E to N 79° E whereas mean palaeocurrents from post-*auritus* strata indicate palaeoflows toward N 215° E to N 222° E. Outside of the Deba block, mean palaeocurrents from pre-*auritus* rocks indicate N 96° E- to N 110° E-directed palaeoflows. Among the three directional groups there are no transitional palaeocurrent directions even between very close localities.

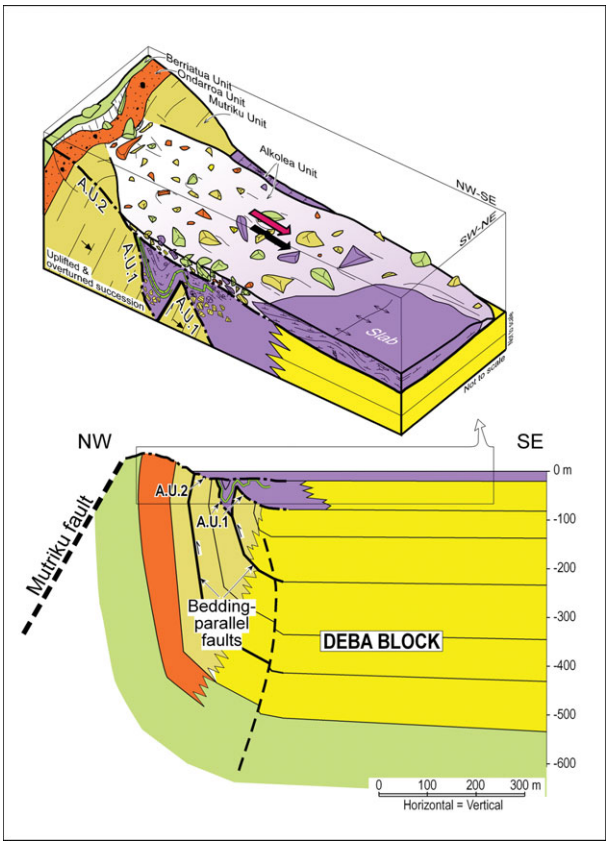

Figure 4. (Colour online) Cross-section of the NW margin of the Deba block restored at the end of *auritus* Subzone, showing the Aitzeta monoclinal syncline adjacent to the Mutriku fault (modified from Agirrezabala *et al.* 2002) (lower). For location, see Figure 1b. Interpretative block diagram illustrating limb rotation, uplift, denudation and resedimentation processes as a consequence of the growth of the Aitzeta syncline at the end of the *auritus* Subzone (upper).

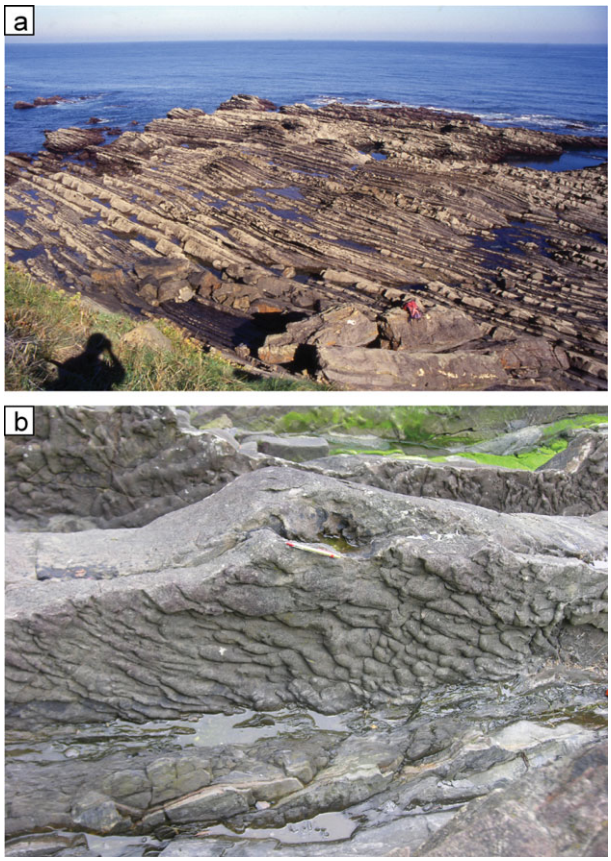

Figure 5. (Colour online) (a) Outcrop of a distal sandy turbidite succession of the Deba unit. All the palaeocurrent measurements and most of the palaeomagnetic data were obtained from similar turbidite successions. (b) Detail photograph of a sandy turbidite sole with flute casts (flow to the right). Pencil for scale (centre of the photograph).

6. Palaeomagnetism

A total of 75 samples for palaeomagnetic study were collected from 9 sites corresponding to the turbiditic Black Flysch Group deposits (lutites and siderites) (Figs 1b, 2, 5a). Five of these palaeomagnetic sites coincide with palaeocurrent localities. Samples were collected and oriented *in situ* with a gasoline-powered drill and orienting device, respectively. Core samples were cut in the laboratory in standard palaeomagnetic samples for measurements. Natural remanent magnetization (NRM) and remanence following demagnetization steps were measured on a 2G Enterprises DC SQUID (superconducting quantum interference device) high-resolution pass-through cryogenic magnetometer (manufacturer noise level of 10^{-12} A m^2) operated in a shielded room at the Istituto Nazionale di Geofisica e Vulcanologia (INGV) in Rome, Italy. A Pyrox oven in the shielded room was used for thermal demagnetizations and alternating field (AF) demagnetization was performed with three orthogonal coils installed inline with the cryogenic magnetometer. A stepwise AF protocol and a combined AF and thermal protocol were used for demagnetization of samples. The presence of siderite (antiferromagnetic) in much of the studied samples (Gil *et al.* 1986), which easily oxidizes to secondary magnetic minerals (magnetite, maghemite and hematite; e.g. Ellwood *et al.* 1988; Pan *et al.* 2000), prompted us to use a specifically designed thermal demagnetization protocol. Samples were initially demagnetized in four AF steps up to 20 mT before stepwise thermal demagnetization. After each thermal step remanence was measured, a single step of 20 mT was applied and remanence was remeasured before the next thermal step. This strategy aimed to minimize spurious secondary remanence acquisition produced by the by-products of eventual siderite alteration upon heating.

Demagnetization data were plotted on standard orthogonal plots. NRM components were calculated using principal component analysis and standard Fisher statistics was applied to compute mean directions. For samples demagnetized using the combined AF and thermal protocol, the characteristic remanent magnetization (ChRM) is computed using only the measurement after the 20 mT step after the heating step (Fig. 7). In addition, inclination-only means were computed using the software PmagTools (Mark W. Hounslow, CEMP, Lancaster, UK) using statistics in

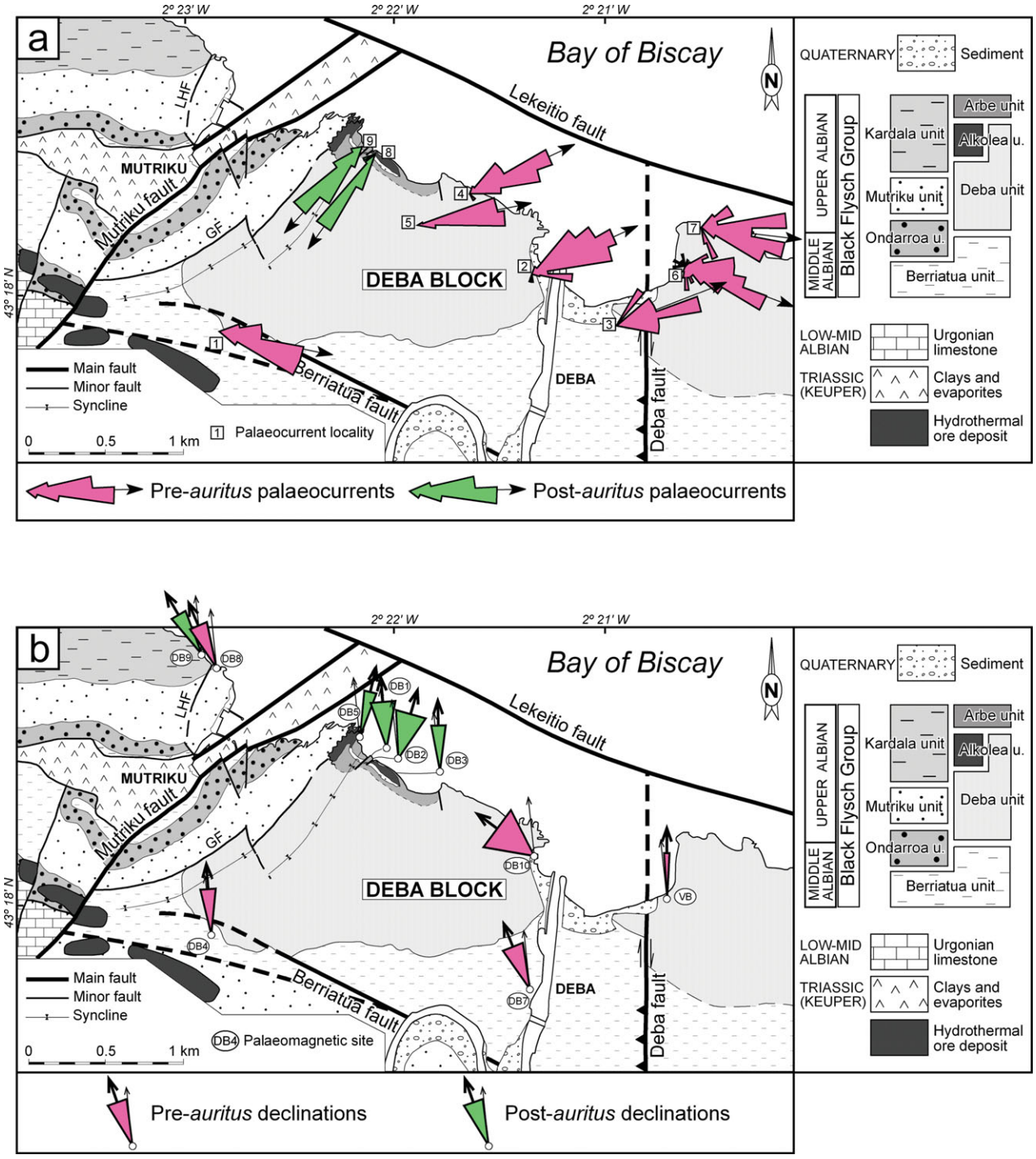

Figure 6. (Colour online) Palaeocurrent and palaeomagnetic declination data obtained from the study area. (a) Palaeocurrent map showing rose diagrams of pre-*auritus* and post-*auritus* localities (Table 1). (b) Mean palaeomagnetic declinations obtained for pre-*auritus* and post-*auritus* sites (Table 2).

McFadden & Reid (1982). Tectonic-corrected data implied a simple bedding correction with the exception of data from site DB5 which is affected by a plunging cylindrical fold (Aitzeta syncline) (Fig. 1b). Consequently, palaeomagnetic declination has been corrected for apparent palaeomagnetic rotation (*sensu lato*) by –26° following Pueyo *et al.* (2003, p. 354).

In order to evaluate the presence of tectonic rotations around the vertical axis in the studied zone, the European reference direction has been used. The western Pyrenees, and more specifically the studied zone, has been traditionally considered as part of the European plate; the European reference direction has therefore usually been used in palaeomagnetic studies (Vandenberg, 1980; Schott & Peres, 1988; Van der Voo, 1993; Schott & Parés, 1996; Larrasoaña *et al.* 2002). The mean Lower Cretaceous (Kl, 98–144 Ma) palaeopole for the European plate computed by Van der Voo (1993) from a selection of four poles with reliability criteria $Q>3$ (Lat/Long = 70/193)

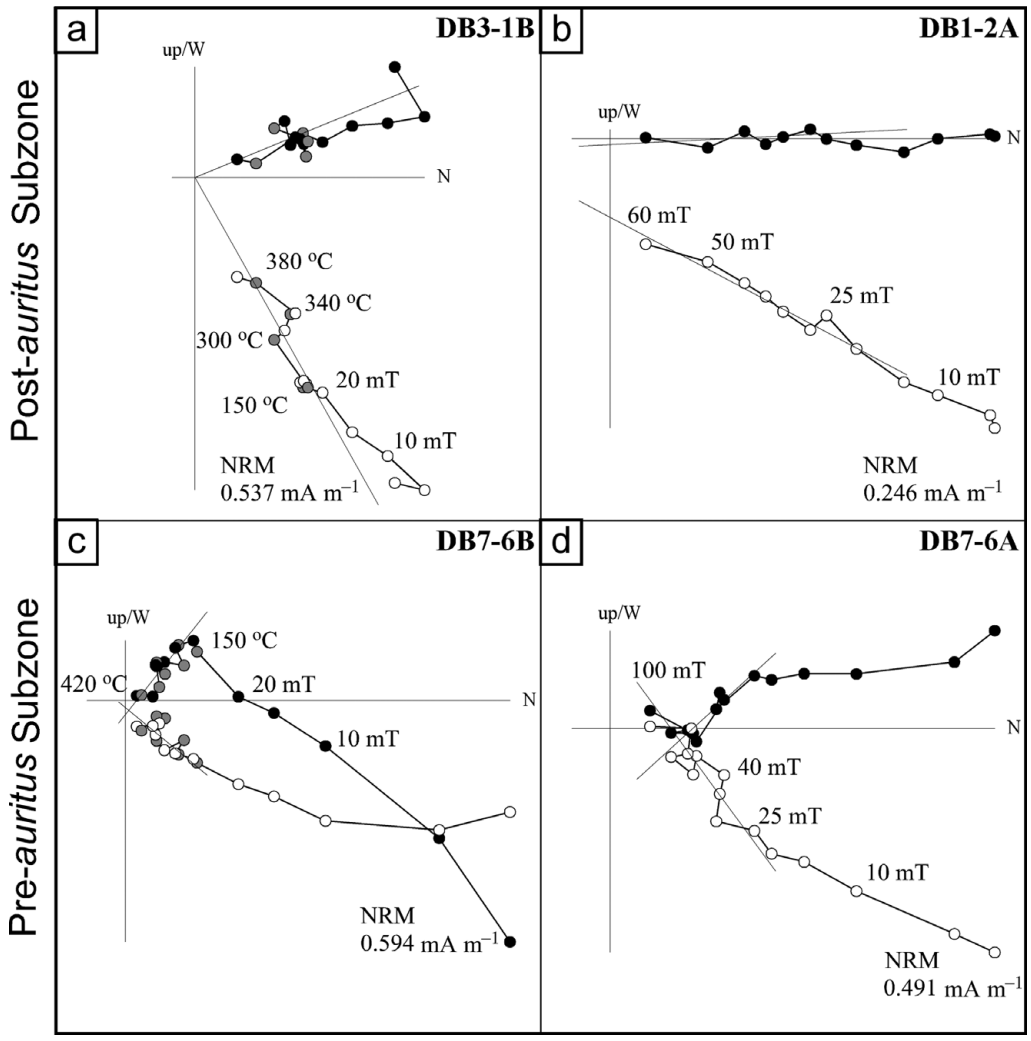

Figure 7. (a)–(d) Bedding-corrected orthogonal plots of demagnetization data from representative pre-*auritus* and post-*auritus* rocks. Solid (open) circles represent projections onto the horizontal (vertical) plane. The fitted ChRM component is shown. For the combined AF and thermal demagnetization (a, c) shaded points indicate the heating step excluded for the ChRM calculation. The intensity of the initial NRM and the demagnetization treatment for some steps are indicated.

implies a reference direction of declination/inclination or $D/I = 354/42$ in the study area.

6.a. Palaeomagnetic results

NRM intensities were of the order 0.05–0.8 mA m^{-1}. AF and combined thermal demagnetization protocols provide similar results (Fig. 7). Samples normally unblock a viscous component at 5 mT probably related to drilling or storage. A low-coercivity and low-temperature component is then removed by fields of *c.* 25–20 mT or 150–200 °C. This component represents a recent secondary overprint conforming to the present geomagnetic field. At higher fields up to 100 mT and maximum temperatures of 420–500 °C a characteristic component (ChRM) that normally trends to the origin of the diagram is finally removed. Data from a Deba site in Vandenberg (1980) has also been taken into account in this study. Palaeomagnetic data and statistical parameters for all sites are listed in Table 2 and corresponding site means are plotted in Figures 6b, 8, 9b, c. The polarity of all ChRM components is normal as it would correspond to a primary direction of the Albian age of the rocks, which falls in the Cretaceous Long Normal superchron. The distribution of sites in different tectonic blocks and their limited bedding attitudes prevents a proper fold test being performed. Moreover, the presence of internal vertical-axis rotation in the Deba block also hampers a regional fold test. An inclination-only mean considering all sites has been computed at sample level. The mean inclination after tectonic correction ($I = 41.9$, $\alpha_{95} = 3.8$, $k = 14.26$, $N = 79$) has only slightly better statistical parameters than the mean inclination before tectonic correction ($I = 54.6$, $\alpha_{95} = 4.7$, $k = 15.36$, $N = 79$) denoting the overall similar bedding attitude. Despite no conclusive field test, we interpret the computed ChRM as representative of a primary Albian direction that records vertical-axis block rotation. The mean directions for the pre- and post-*auritus* rocks from the Deba block calculated at sample level are listed in Table 3. The angle of rotation

Table 2. Site mean palaeomagnetic results (*N*/*n* number of samples measured/used to compute mean direction; *D* declination; *I* inclination; *k* Fisher's precision parameter; α_{95} radius of the 95% confidence cone)

									In situ		Tectonic corrected	
Setting	Age	Site	Unit	Lat (N)	Long (W)	*N*/*n*	α_{95}	*k*	*D*	*I*	*D*	*I*
Deba block	Post-*auritus*	DB1	Arbe	43° 18′ 31.15″	2° 22′ 06.44″	15/12	15.4	8.9	337.2	56.6	355.1	37.3
		DB2	Arbe	43° 18′ 30.65″	2° 22′ 06.73″	10/6	18.7	13.8	10.8	51.4	15.7	27.0
		DB3	Arbe	43° 18′ 30.25″	2° 22′ 08.73″	6/5	9.0	73.3	333.3	77.4	358.2	64.7
		DB5	Arbe	43° 18′ 34.55″	2° 22′ 10.54″	10/10	7.8	39.5	16.4	46.1	15.3	51.4
	Pre-*auritus*	DB7	Berriatua	43° 17′ 44.10″	2° 21′ 21.26″	9/9	13.2	16.1	306.5	69.4	338.1	40.5
		DB10	Deba	43° 18′ 11.36″	2° 21′ 21.21″	8/3	26.8	22.3	254.7	48.2	306.5	52.5
Outside Deba block	Post-*auritus*	DB9	Kardala	43° 18′ 53.24″	2° 22′ 54.97″	11/10	9.8	25.5	300.5	56.6	329.6	37.3
	Pre-*auritus*	DB8	Kardala	43° 18′ 50.19″	2° 22′ 52.00″	12/10	11.3	19.3	315.5	52.1	336.7	37.0
		VB*	Deba	43° 18′ 00.32″	2° 20′ 46.14″	27/27	3.4	–	–	–	359.6	45.0
		DB4	Berriatua	43° 17′ 55.76″	2° 22′ 51.76″	18/14	9.6	18.0	235.2	59.5	355.8	51.2

*Vandenberg's (1980) Deba site data

Table 3. Site group mean palaeomagnetic results for the Deba block data calculated at sample level (*N*/*n*, *D*, *I*, *k*, α_{95} as for Table 2; *R* angle of rotation; ΔR error)

				In situ				Tectonic corrected					
Setting	Age	Sites	*N*/*n*	*D*	*I*	α_{95}	*k*	*D*	*I*	α_{95}	*k*	*R*	ΔR
Deba block	Post-*auritus*	DB1+DB2+DB3+DB5	41/33	359.3	57.1	7.9	11.1	5.9	44.6	7.8	11.3	11.9	±7.0
	Pre-*auritus*	DB7+DB10	17/12	286.5	66.2	11.9	13.1	331.5	44.3	12.0	14.0	–22.5	±9.5

R calculated by comparing the measured declination with the European reference direction and its error ΔR following the statistical method proposed by Demarest (1983) are provided.

7. Discussion

7.a. Evidence for Albian block rotation

Different contemporaneous geological processes such as local deformation, hydrothermal venting and possibly magmatic and/or salt diapiric intrusions recorded at the corners of the Deba block are interpreted to have occurred as the consequences of the anticlockwise rotation of this block during Late Albian *auritus* Subzone. This block rotation is supported by obtained palaeocurrent directions and palaeomagnetic results.

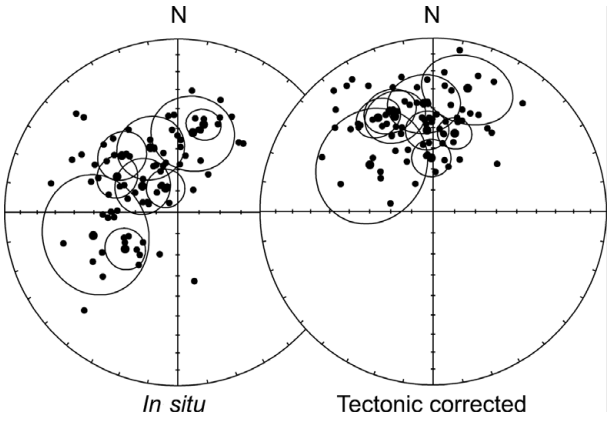

Figure 8. Equal-area projections of the ChRM directions before (*in situ*) and after tectonic correction for all sites (Table 2). The 95% confidence ellipse for the mean directions is plotted.

7.a.1. Local transpression

In the NW corner of the Deba block, syntectonic deposits of *auritus* Subzone age (Figs 1b, 2) record the growth of the NE-trending SE-facing Aitzeta monoclinal syncline, interpreted as the subvertical limb of a fault-related syncline (Agirrezabala *et al.* 2002). A restored cross-section to the top of growth deposits indicates that tectonic shortening for the end of *auritus* Subzone is *c.* 500 m (Fig. 4). It formed in response to local NW–SE compressive stress along the northeastern part of the dextral-reverse Mutriku fault. The attenuation and end of the Aitzeta syncline to the SW indicates the progressive diminishing of the shortening in the same sense, from at least 0.5 km (Fig. 4) to zero. This differential shortening along the Mutriku fault suggests an anticlockwise rotational movement of the adjacent Deba block.

Rigid block rotation can happen in synthetic or antithetic senses. A synthetically rotated block model postulates block bordering antithetic minor faults at high angles to the main faults (Freund, 1974; Nicholson *et al.* 1986). An antithetically rotated block model predicts block bordering synthetic minor faults at low angles to the main faults (Jordan, 1991; Gross *et al.* 1997). In the Deba case, sinistral block rotation occurs between left-lateral major strike-slip faults and is bordered by minor antithetic right-lateral faults, as the synthetically rotated block model postulates. This block rotation model also predicts the formation of transpressive structures at opposite corners and transtensive structures at the other two corners as a solution to the space problems (Fig. 10). Following this model, we interpret the transpressive Aitzeta fold formation at the NW corner of the Deba block as the

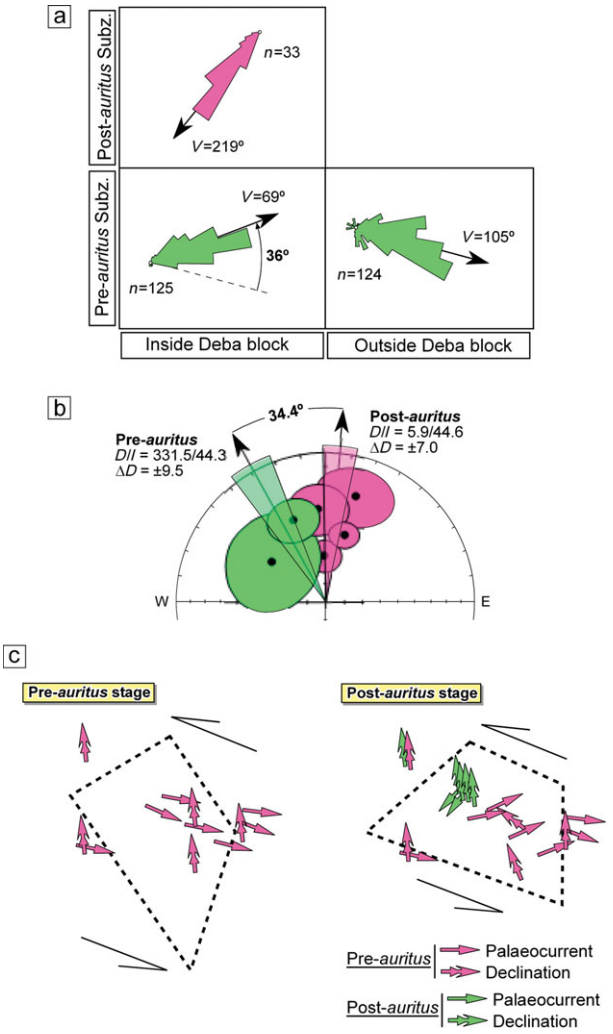

Figure 9. (Colour online) (a) Palaeocurrent roses of pre-*auritus* and post-*auritus* rocks from inside and outside the Deba block. (b) Stereographic projection of pre-*auritus* and post-*auritus* site means (Table 2) from the Deba block and group mean directions calculated at sample level (Table 3). (c) Two-stage (pre- and post-*auritus*) sketch showing palaeocurrent and palaeomagnetic declination mean directions and interpreted rotation of the Deba block.

direct consequence of the local compression resulting from the anticlockwise rotation of that block (Fig. 11). In the opposite SE corner of the block, the southern part of the Deba fault shows a dextral-reverse character affecting pre-*auritus* rocks (Figs 1b, 3). Although the dextral-reverse movement cannot be precisely dated because of a lack of *auritus* and post-*auritus* deposits, we interpret this movement as the result of local E–W compression triggered by the Deba block rotation during *C. auritus* Subzone times (Fig. 11).

7.a.2. Hydrothermal vents and magmatic intrusions

In recent studies, two hydrothermal vent carbonate lenses and associated chemosymbiotic fauna hosted in the syn-rotational *auritus* Subzone deposits from both sides of the Mutriku fault (Figs 1b, 2) have been documented in detail (Agirrezabala *et al.* 2008;

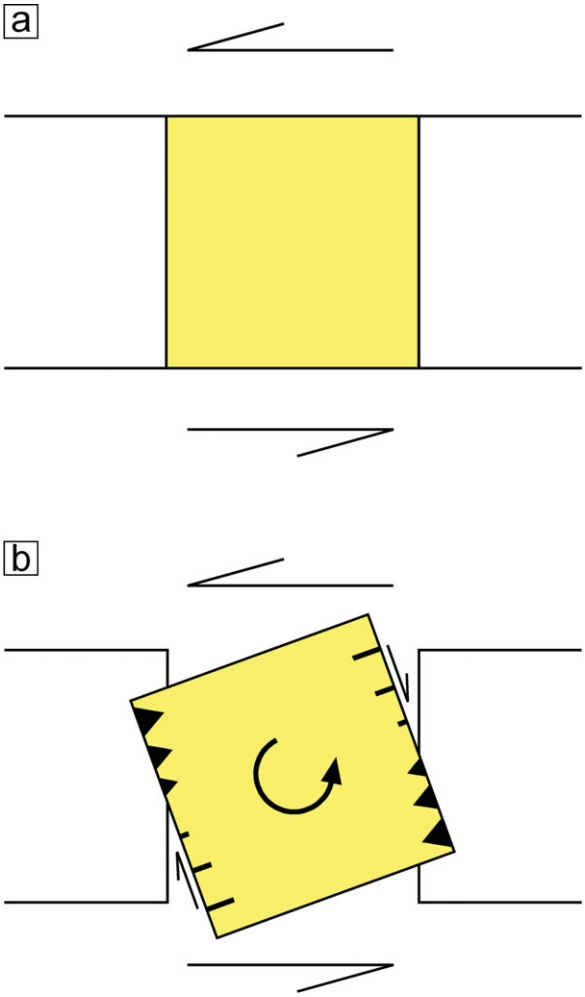

Figure 10. (Colour online) Sketch of synthetic block rotation model: (a) initial situation and (b) synthetically rotated block bordered by antithetic minor faults and formation of transpressive structures (teeth) at opposite corners and transtensive structures (hachures) at the other two corners.

Agirrezabala, 2009). These carbonates have been interpreted as microbially mediated by-products of hydrocarbon-rich (oil and termogenic methane) hot fluids (up to 109 °C) expelled to the Late Albian sea floor (Agirrezabala, 2009). Geochemical correlation between pyrobitumen-fills from vent carbonates and host rock organic matter suggests that the hydrocarbon source was the Black Flysch Group (Agirrezabala *et al.* 2008). Magmatic intrusion-related contact metamorphism of these organic-rich sediments would have triggered the generation of hydrocarbons, which migrated updip through the Mutriku fault and the steep limb of the Aitzeta monocline to the sea floor.

In the present-day Guaymas Basin and NE Pacific Ocean, hydrothermal petroleum and methane is produced at shallow depths from sedimentary organic matter by contact metamorphism around shallow-level magmatic intrusions (Einsele *et al.* 1980; Simoneit & Lonsdale, 1982; Rushdi & Simoneit, 2002). Similarly, this hydrocarbon-generating process has also been interpreted from magmatic sill-intruded ancient sedimentary basins worldwide (Jamtveit *et al.* 2004;

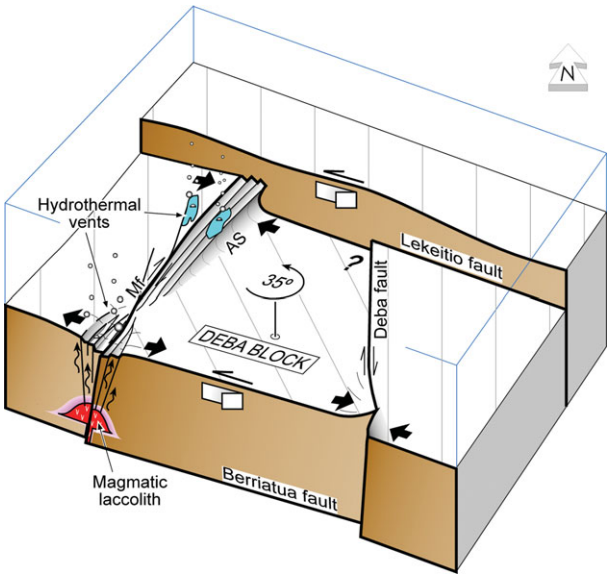

Figure 11. (Colour online) Schematic block diagram showing anticlockwise rotation of the Deba block during Late Albian *auritus* Subzone times. Contemporaneous to block rotation and, as a consequence of the space problem, transpressive deformations took place in its NW and SE corners and transtension in its SW (and NE?) corner. In the transtensive SW corner, magmatic intrusions emplaced by the local discharge of lithostatic pressure triggered the development of a hydrothermal system. This hydrothermal system mineralized host rocks and vented warm to hot fluids rich in oil and methane to the Albian seafloor. These hydrocarbons were generated at shallow depths from Black Flysch organic matter by contact alteration with hydrothermal fluids. AS: Aitzeta monoclinal syncline; Mf: Mutriku fault.

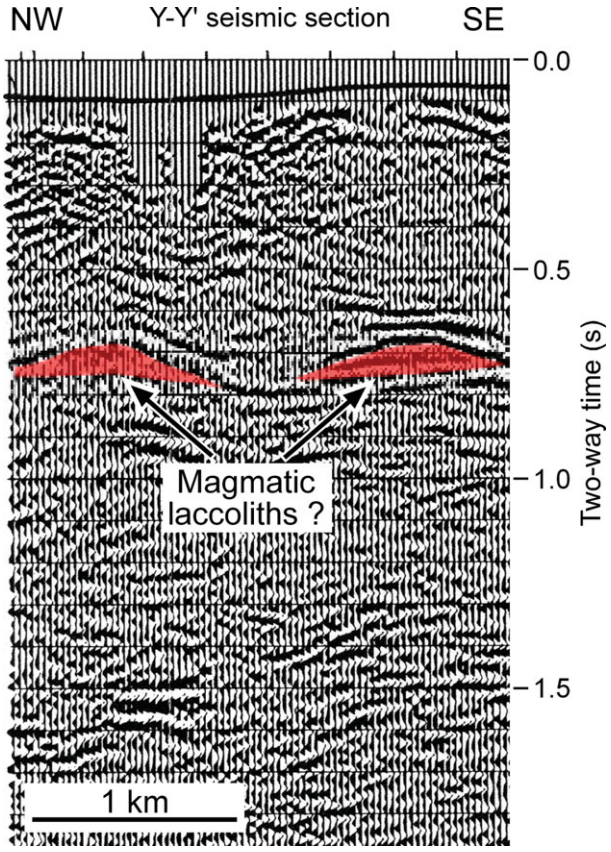

Figure 12. (Colour online) Seismic section across the SW corner of the Deba block showing two highly reflective domal structures. Based on their geometries, dimensions and relationship with the overlying hydrothermal system they are interpreted as magmatic laccoliths. For location see Figure 1b.

Svensen *et al.* 2004, 2009; Ganino & Arndt, 2009). In the Basque–Cantabrian Basin, intrusive and extrusive volcanic activity was important in Late Albian and Late Cretaceous times (Rossy, 1988), distinguishing a main activity phase during the *auritus* Subzone (Castañares *et al.* 2001) penecontemporaneously with the development of the hydrothermal vents here. In this respect, a seismic profile across the SW corner of the Deba block shows the presence of two domal, highly reflective structures at *c.* 0.7 s depth (Fig. 12). Their concordant, high-amplitude reflections, convex-up tops and flat bottoms and dimensions are compatible with an interpretation of both structures as magmatic laccoliths (Corry, 1988; Thompson, 2007) and salt-related domes (Talbot, 1993; Schultz-Ela & Jackson, 1996; Hudec & Jackson, 2006). An interpretation of the structures as magmatic intrusions is favoured based on the local high heat flow that supported the hydrothermal activity and hydrocarbon generation at a shallow depth as well as the occurrence of pervasive hydrothermal mineralizations, Pb–Zn deposits and abundant pyrobitumen-fills (EEE, 2003) concentrated in rocks over the domal seismic structures (Figs 1b, 2). In addition, the features have length/thickness ratios comparable to documented magmatic laccoliths from different geological settings (Corry, 1988; McCaffrey & Petford, 1997). The igneous character of the seismic structures is also favoured by the important Late Albian magmatism in the area, recorded by the presence of: (1) pyroclastic beds within the studied succesions (*auritus* and *varicosum* subzones) (Agirrezabala & García-Mondéjar, 2001*b*); (2) mapped magmatic intrusions enclosed in pre-*auritus* rocks 4 km to the SW (EEE, 2003); and (3) thick volcanic successions and magmatic intrusions along the northern margin of the basin, where the main volcanic activity phase occurred during the *auritus* Subzone (Rossy, 1988; Castañares *et al.* 2001).

Magmatic intrusions (and related hydrothermal fluids) in strike-slip settings are usually emplaced in areas subjected to transtension (e.g. Aydin *et al.* 1990; Ventura, 1994; Chetty, 1995; Aranguren *et al.* 1996; Marra, 2001; Adiyaman & Chorowicz, 2002; Breitkreuz & Mock, 2004; Sapiie & Cloos, 2004; Busby *et al.* 2005; Tibaldi *et al.* 2010). In these areas, a discharge of lithostatic pressure favours the emplacement of magmatic intrusions, and the faults provide preferential magma conduits. In this study, we interpret the emplacement of possible magmatic intrusions and the formation of hydrothermal deposits at the SW corner of the Deba block to have taken place under local extension (Fig. 11). This is in agreement with the SW termination of the compressive Aitzeta fold, which does not reach the SW corner of the Deba block (Fig. 1b). This fact could indicate a transition

from compression at the NW corner to extension at the SW corner (Fig. 11).

7.a.3. Palaeocurrent and palaeomagnetic evidence

At the Deba block, pre-*auritus* palaeocurrent rose diagrams (ENE-directed) show a systematic anticlockwise deviation if comparing with contemporaneous adjacent (and regionally distal) palaeocurrents (ESE-directed) (Fig. 6a). The average of all pre-*auritus* palaeocurrent directions from the Deba block localities shows a mean palaeoflow direction toward N 69° E, while the sum of coeval palaeocurrents at localities outside the Deba block yields a mean palaeoflow direction towards N 105° E, resulting in a mean deviation of 36° (Fig. 9a). Moreover, the magnetic declinations of pre-*auritus* rocks at Deba block sites also show a similar anticlockwise deviation of 22° (± 9) from the Albian European magnetic reference direction (N 354° E; Van der Voo, 1993) (Table 3, Fig. 9b). In contrast, overlying post-*auritus* rocks at the Deba block yield palaeocurrent roses concordant with a 'normal' regional proximal direction (towards SSW) (Fig. 9a), and the mean of their magnetic declinations shows a clockwise deviation of 12° (±7) from the Albian magnetic reference direction (Table 3, Fig. 9b). Consequently, the anticlockwise rotation of the Deba block is pre-dated by pre-*auritus* rocks and post-dated by post-*auritus* rocks, constraining the age of the rotation process to the Late Albian *auritus* Subzone.

In summary, the palaeocurrent results suggest an anticlockwise rotation of the Deba block of 36° (Fig. 9a) and the palaeomagnetic results indicate a similar rotation of 34° (difference between pre- and post-*auritus* means at the Deba block; Table 3 and Fig. 9b). The agreement of results obtained from independent datasets provides strong support for the interpretation of the Deba block rotation of *c.* 35° (mean value between palaeocurrent and declination rotations; Fig. 9c). Moreover, the similar results obtained from palaeocurrent and palaeomagnetic data from the same localities reinforce the inferred rotation of the Deba block. This anticlockwise rotation is in concordance with the Albian sinistral strike-slip tectonics deduced by many authors for both the Basque–Cantabrian Basin (Rat *et al.* 1983; García-Mondéjar, 1989; García-Mondéjar *et al.* 1996) and the Pyrenean realm (Choukroune & Mattauer, 1978; Puigdefàbregas & Souquet, 1986; Olivet, 1996, Larrasoaña *et al.* 2002).

West of the Deba block two sites of pre- and post-*auritus* rocks (DB8 and DB9) show anticlockwise declination deviation of 18° and 33°, respectively, from Albian magnetic reference direction, suggesting for that area an anticlockwise rotation process younger than Late Albian *rostratum* Subzone (Figs 6b, 9c). Based on geological maps and structural criteria, rotation of this area has been related to the Tertiary inversion tectonics of the basin (L. M. Agirrezabala, unpub. PhD thesis, Euskal Herriko Unibertsitatea, 1996). On the other hand, palaeocurrent directions of the study area show a sharp change from ESE to SSW, coinciding with the *auritus* Subzone (Figs 6a, 9a, c). This fact suggests that the same tectonic pulse that triggered the rotation of the Deba block also caused the disappearance of the confining southern structural slope responsible of the ESE deflection of pre-*auritus* turbidity flows. The disappearance of that topographic barrier allows post-*auritus* turbidity currents to flow in a SSW direction.

7.b. Block rotation rates

Recent work based on sedimentological and structural analyses, combined with precise biostratigraphy of ammonites, documents in detail the growth history of the Aitzeta syncline in the NW corner of the Deba block (Agirrezabala *et al.* 2002, 2003). It developed in two main pulses that were recorded in the Late Albian syntectonic deposits as two high-angle, angular unconformities (AU1 and AU2, base and top of *auritus* Subzone, respectively; Figs 1b, 2). These two unconformities and related resedimented deposits record strong limb-rotation and uplift of the syncline limb (42° and 250 m in the first pulse and 66° and 100–140 m in the second pulse). Nevertheless, the occurrence of hemipelagic deposits between both angular unconformities indicates an intervening phase of tectonic calm, which lasted *c.* 0.29 Ma (minimum duration estimated by using average sedimentation rates of hemipelagic sediments; Agirrezabala *et al.* 2002). If the *auritus* Subzone spans 1.3 Ma (Ogg *et al.* 2004), and 0.29 Ma (minimum) of this represents the tectonic calm (hemipelagic sedimentation), the duration of all deformation phases or angular unconformities is *c.* 1 Ma (maximum). Consequently, if there is a cause–effect relationship between the Aitzeta fold growth and the Deba block rotation, then two phases can also be invoked for the Deba block rotation with an estimated time span equal to the duration of the two folding pulses, that is, 1 Ma (maximum) for the sum of both pulses. If this duration is assumed for the total rotation (35°) of the Deba block, the minimum block rotation rate calculated is 35° Ma^{-1}. Similar rapid rotation rates have been documented in other strike-slip basins, particularly in areas where blocks are small. Based on palaeomagnetic data from California, Johnson *et al.* (1983) estimated Quaternary rates of 35° rotation in less than 0.9 Ma for the Vallecito–Fish Creek Basin; Seeber & Bogen (1985) documented 20–30° rotation in the past 0.7–1 Ma in sediments adjacent to the San Jacinto Fault; and Horns & Verosub (1995) documented rotation rates of 20° Ma^{-1} in the San Gregorio fault zone. Rapid rates of rotation of small blocks have also been observed in geodetic data from central California (17° Ma^{-1}; Prescott *et al.* 1981) and Alpine fault system in New Zealand (8° Ma^{-1}; Walcott, 1984). Simple trigonometry and 35° rotation of the 2.1-km-wide Deba block gives 1.2 km displacement (strike-slip component); we therefore

derive an estimate of 1.2 km Ma^{-1} for minimum slip rate on the two major faults.

7.c. Block rotation model

Stratigraphic, structural, subsurface, palaeocurrent and palaeomagnetic data described above support the anticlockwise rotation of the Deba block by *c.* 35° during Late Albian times (Figs 9c, 11). The rotation of the Deba block is interpreted as related to the left-slip of the NW-trending Lekeitio and Berriatua boundary faults, which belong and are parallel to the wider sinistral wrench corridor defined in the northern margin of the basin (Agirrezabala & García-Mondéjar, 1994, 2001*a*; García-Mondéjar *et al.* 1996; Agirrezabala *et al.* 2002). Second-order bordering Mutriku and Deba faults trend NE and N, respectively, and show right-lateral slip. Because these faults are oriented at high angles to the general trend of the wrench corridor, and because the sense of slip is in the opposite sense, they can be considered as antithetic strike-slip faults or conjugate Riedel (R') shears (Tchalenko, 1970) characteristics of strike-slip regimes (e.g. Christie-Blick & Biddle, 1985; Sylvester, 1988). This structural scenario is concordant with the anticlockwise synthetic rotation of the Deba block (Fig. 11), as the block rotation models predict (e.g. Freund, 1974; Ron *et al*. 1984; McKenzie & Jackson, 1986; Nicholson *et al.* 1986; Jordan, 1991).

In models of rigid block rotation, blocks do not show internal strain and involved rotation is accommodated by sets of bordering faults (e.g. Ron *et al*. 1984; McKenzie & Jackson, 1986). Rotation of rigid blocks causes a space problem at the boundaries between rotated and non-rotated blocks, resulting in triangular areas of overlap (transpression) and void (transtension) in the opposite corners (Fig. 10). This is concordant with the anticlockwise rotation of the Deba block transpressive deformations (reverse faulting, uplift and fold growth) recorded in the opposite NW and SE corners of the block, whereas coeval transtension took place in the alternate SW (and NE) corner where high-level magmatic laccoliths emplaced and the related hydrothermal system developed (Figs 11, 12). In this respect, it has been shown that in a block rotation scenario magmatic intrusions and hydrothermal fluid flow usually locate in transtension corners as a result of local lithostatic discharge (Christie-Blick & Biddle, 1985). These corners may be likely sites for decompression melting, and the faults and fractures could provide preferential conduits for magma and hydrothermal fluids (Chetty, 1995; Marra, 2001; Sapiie & Cloos, 2004; Tatar *et al.* 2004; Tibaldi *et al.* 2010).

8. Conclusions

Studied deep-water deposits record the syndepositional vertical-axis rotation of the Deba block during Late Albian *C. auritus* Subzone times. Stratigraphic, structural, subsurface, palaeocurrent and palaeomagnetic data suggests 35° anticlockwise rotation of the Deba block during that time. Deduced anticlockwise block rotation is consistent with the ESE-trending sinistral wrench system of the Basque–Cantabrian Basin. Published biostratigraphic data based on ammonites allow us to constrain the block rotation process to a maximum period of 1 Ma. On the basis of conservative estimations, the block rotation took place at a minimum rate of 35° Ma^{-1} resulting in a sinistral strike-slip minimum rate of 1.2 km Ma^{-1}.

Vertical-axis rotation of the Deba block caused geometric problems along its contacts with non-rotated adjacent blocks, triggering coeval transpressive and transtensive deformation around its corners. At the NW and SE opposite corners, syndepositional compressive faulting, folding and uplift took place, whereas alternate SW and, possibly, NE corners would have experienced extensional faulting and fracturing. In the extensional SW corner two domal high-reflective structures recorded by seismic profiles have been interpreted as high-level magmatic laccoliths emplaced by local discharge of lithostatic pressure. The emplacement of these magmatic intrusions triggered the development of a mineralizing hydrothermal system, which expelled warm to hot fluids rich in hydrocarbon (oil and methane) to the Albian seafloor. Vented hydrocarbons were generated at shallow depths from Black Flysch organic matter by contact alteration with hydrothermal fluids. The applicability of the comprehensive model is apparent, and it could be relevant to mineral and hydrocarbon exploration in the Basque–Cantabrian Basin and other strike-slip basins.

Acknowledgements. We would like to thank Allen Frankovik and Alex Franco (Energiaren Euskal Erakundea) for their help with interpreting seismic profiles and providing well data, respectively. Gabriel Gutiérrez-Alonso and one anonymous reviewer are thanked for their useful and constructive comments, which help greatly to improve the manuscript. This research was supported by the Euskal Herriko Unibertsitatea (project EHU11/42) and the Ministerio de Ciencia e Innovación (projects CGL2006-05491/BTE and CGL2009-08545).

References

ADIYAMAN, O. & CHOROWICZ, J. 2002. Late Cenozoic tectonics and volcanism in the northwestern corner of the Arabian Plate; a consequence of the strike-slip Dead Sea fault zone and the lateral escape of Anatolia. *Journal of Volcanology and Geothermal Research* **117**, 327–45.

AGIRREZABALA, L. M. 2009. Mid-Cretaceous hydrothermal vents and authigenic carbonates in a transform margin, Basque-Cantabrian Basin (western Pyrenees): a multidisciplinary study. *Sedimentology* **56**, 969–96.

AGIRREZABALA, L. M. & BODEGO, A. 2005. Interbedded mudstone slope and basin-floor sandy deposits in the Ondarroa turbidite system (Albian, Basque-Cantabrian Basin). *Geogaceta* **38**, 83–6.

AGIRREZABALA, L. M., DORRONSORO, C. & PERMANYER, A. 2008. Geochemical correlation of pyrobitumen fills with host mid-Cretaceous Black Flysch Group

(Basque-Cantabrian Basin, western Pyrenees). *Organic Geochemistry* **39**, 1185–8.

AGIRREZABALA, L. M. & GARCÍA-MONDÉJAR, J. 1992. Tectonic origin of carbonate depositional sequences in a strike-slip setting (Aptian, Northern Iberian). *Sedimentary Geology* **81**, 163–72.

AGIRREZABALA, L. M. & GARCÍA-MONDÉJAR, J. 1994. A coarse-grained turbidite system with morphotectonic control (middle Albian, Ondarroa, North Iberia). *Sedimentology* **41**, 383–407.

AGIRREZABALA, L. M. & GARCÍA-MONDÉJAR, J. 2001*a*. Kinematic indicators and mineralization on the Elgoibar fault (Basque-Cantabrian Basin). *Geogaceta* **30**, 7–10.

AGIRREZABALA, L. M. & GARCÍA-MONDÉJAR, J. 2001*b*. Deep-water fallout tephra deposits in the Black Flysch of Deba (Upper Albian, Basque-Cantabrian Basin). *Geotemas* **3**, 123–6.

AGIRREZABALA, L. M., KIEL, S., BLUMENBERG, M., SCHÄFER, N. *et al.* 2013. Outcrop analogues of pockmarks and associated methane-seep carbonates: a case study from the Lower Cretaceous (Albian) of the Basque-Cantabrian Basin, western Pyrenees. *Palaeogeography, Palaeoclimatology, Palaeoecology*, published online 5 December 2012. doi: 10.1016/j.palaeo.2012.11.020.

AGIRREZABALA, L. M., OWEN, H. G. & GARCÍA-MONDÉJAR, J. 2002. Syntectonic deposits and punctuated limb rotation in an Albian submarine transpressional fold (Mutriku village, Basque-Cantabrian basin, northern Spain). *Geological Society of America Bulletin* **114**, 281–97.

AGIRREZABALA, L. M., OWEN, H. G. & GARCÍA-MONDÉJAR, J. 2003. Errata. Syntectonic deposits and punctuated limb rotation in an Albian submarine transpressional fold (Mutriku village, Basque-Cantabrian basin, northern Spain). *Geological Society of America Bulletin* **115**, 765–8.

ALONSO, J. L. 1989. Fold reactivation involving angular unconformable sequences: theoretical analysis and natural examples from the Cantabrian Zone (Northwest Spain). *Tectonophysics* **170**, 57–77.

ARANBURU, A., FERNÁNDEZ-MENDIOLA, P. A., LÓPEZ-HORGUE, M. & GARCÍA-MONDÉJAR, J. 2002. Syntectonic hydrothermal calcite in a faulted carbonate platform margin (Albian of Jorrios, northern Spain). *Sedimentology* **49**, 875–90.

ARANGUREN, A., TUBIA, J. M., BOUCHEZ, J. L. & VIGNERESSE, J. L. 1996. The Guitiriz Granite, Variscan Belt of northern Spain; extension-controlled emplacement of magma during tectonic scape. *Earth and Planetary Science Letters* **139**, 165–76.

AYDIN, A., SCHULTZ, R. A. & CAMPAGNA, D. 1990. Fault-normal dilatation pull-apart-basins: implications for relationship between strike-slip fault and volcanic activity. In *Active and Recent Strike-slip Tectonics* (eds M. Boccaletti & A. Nur), pp. 45–52. Annales Tectonicae Special Issue.

AZAMBRE, B. & ROSSY, M. 1976. Le magmatisme alcalin d'âge crétacé dans les Pyrénées occidentales de l'Arc basque; ses relations avec le métamorphisme et la tectonique. *Bulletin de la Société Géologique de France* **18**, 1725–8.

BREITKREUZ, C. & MOCK, A. 2004. Are laccolith complexes characteristic of trantensional basin systems? Examples from the Permo-Carboniferous of Central Europa. In *Physical Geology of High-level Magmatic Systems* (eds C. Breitkreuz & N. Petford), pp. 13–31. Geological Society of London, Special Publications no. 234.

BUSBY, C. J., BASSETT, K. N., STEINER, M. B. & RIGGS, N. R. 2005. Climatic and tectonic controls on Jurassic intra-arc basins related to northward drift of North America. *Geological Society of America Special Paper* **393**, 359–76.

CÁMARA, P. 1997. The Basque-Cantabrian basin's Mesozoic tectono-sedimentary evolution. *Mémoires de la Société Géologique de France* **171**, 187–91.

CASTAÑARES, L. M., ROBLES, S., GIMENO, D. & VICENTE-BRAVO, J. C. 2001. The submarine volcanic system of the Errigoiti Formation (Albian-Santonian of the Basque-Cantabrian Basin, northern Spain): stratigraphic framework, facies and sequences. *Journal of Sedimentary Research*, **71**, 318–33.

CHETTY, T. R. K. 1995. Significance of the block rotation model in tectonics and mineralization in Precambrian terrains – An example from the South Indian shield. *Journal of Geodynamics* **20**, 255–66.

CHOUKROUNE, P. 1992. Tectonic evolution of the Pyrenees. *Annual Review of Earth and Planetary Sciences* **20**, 143–58.

CHOUKROUNE, P. & MATTAUER, M. 1978. Tectonique des plaques et Pyrénées: sur le fonctionnement de la faille transformante nord-pyrénéenne; comparaisons avec des modèles actuels. *Bulletin de la Société Géologique de France* **20**, 689–700.

CHRISTIE-BLICK, N. & BIDDLE, K. T. 1985. Deformation and basin formation along strike-slip faults. In *Strike-slip Deformation, Basin Formation, and Sedimentation* (eds K. T. Biddle & N. Christie-Blick), pp. 1–34. Society of Economic Paleontologists and Mineralogists, Special Publications no. 37.

CORRY, C. E. 1988. *Laccoliths: Mechanics of Emplacement and Growth*. Geological Society of America, Special Paper **220**, 110 pp.

DEMAREST, H. H. JR. 1983. Error analysis for the determination of tectonic rotation from paleomagnetic data. *Journal of Geophysical Research* **88**, 4321–8.

EEE 2003. *1:25000 Eskalako Euskal Herriko Mapa Geologikoa*. Eusko Jaurlaritza, Bilbo. CD-ROM.

EINSELE, G., GIESKES, J. M., CURRAY, J., MOORE, D. M. *et al.* 1980. Intrusion of basaltic sills into highly porous sediments, and resulting hydrothermal activity. *Nature* **283**, 441–5.

ELLWOOD, B. B., CHRZANOWSKI, T. H., HROUDA, F., LONG, G. J. *et al.* 1988. Siderite formation in anoxic deep-sea sediments: A synergetic bacteria controlled process with important implications in paleomagnetism. *Geology* **16**, 980–2.

ENGESER, T. & SCHWENTKE, W. 1986. Towards a new concept of the tectogenesis of the Pyrenees. *Tectonophysics* **129**, 233–42.

FERNÁNDEZ-MENDIOLA, P. A. & GARCÍA-MONDÉJAR, J. 2003. Carbonate platform growth influenced by contemporaneous basaltic intrusion (Albian of Larrano, Spain). *Sedimentology* **50**, 961–78.

FREUND, R. 1974. Kinematics of transform and transcurrent faults. *Tectonophysics* **21**, 93–134.

GANINO, C. & ARNDT, N. T. 2009. Climate changes caused by degassing of sediments during the emplacement of large igneous provinces. *Geology* **37**, 323–6.

GARCÍA-MONDÉJAR, J. 1989. Strike-slip subsidence of the Basque-Cantabrian Basin of Northern Spain and its relationship to Aptian-Albian opening of Bay of Biscay. In *Extensional Tectonics and Stratigraphy of the North Atlantic Margins* (eds A. J. Tankard & H. R. Balkwill),

pp. 395–409. American Association of Petroleum Geologists, Memoir no. 46.

García-Mondéjar, J., Agirrezabala, L. M., Aranburu, A., Fernández-Mendiola, P. A. *et al.* 1996. The Aptian-Albian tectonic pattern of the Basque-Cantabrian Basin (Northern Spain). *Geological Journal* **31**, 13–45.

García-Mondéjar, J., Fernández-Mendiola, P. A., Agirrezabala, L. M., Aranburu, A. *et al.* 2004*a*. Extensión del Aptiense-Albiense en la Cuenca Vasco-Cantábrica. In *Geología de España* (ed. J. A. Vera), pp. 340–3. Sociedad Geológica de España-Instituto Geológico y Minero de España.

García-Mondéjar, J., Fernández-Mendiola, P. A., Agirrezabala, L. M., Aranburu, A. *et al.* 2004*b*. El Aptiense-Albiense de la Cuenca Vasco-Cantábrica. In *Geología de España* (ed J. A. Vera), pp. 291–6. Sociedad Geológica de España-Instituto Geológico y Minero de España.

Gil, P. P., Yusta, I., Herrero, J. M. & Velasco, F. 1986. Mineralogía y geoquímica de las concreciones carbonatadas del Flysch Negro (Albiense sup.-Cenomaniense inf.) de Armintza (Vizcaya). *Boletín de la Sociedad Española de Mineralogía* **9**, 347–56.

Gómez, M., Vergés, J. & Riaza, C. 2002. Inversion tectonics of the northern margin of the Basque Cantabrian Basin. *Bulletin de la Société Géologique de France* **173**, 449–59.

Grippo, A., Fischer, A., Hinnov, L. A., Herbert, T. D. *et al.* 2004. Cyclostratigraphy and chronology of the Albian stage (Piobicco core, Italy). In *Cyclostratigraphy: An Essay of Approaches and Case Histories* (eds B. D'Argenio, A. G. Fischer, I. Premoli Silva, H. Weissert & V. Ferreri), pp. 57–81. Society of Economic Paleontologists and Mineralogists, Special Publication no. 81.

Gross, M. R., Becker, A. & Gutiérrez-Alonso, G. 1997. Transfer of displacement from multiple slip zones to a single detachment due to rigid block rotation: example from the Dead Sea Rift, Israel. *Geological Society of America Bulletin* **109**, 1021–35.

Horns, D. M. & Verosub, K. L. 1995. Investigation of late Neogene vertical axis rotation and remagnetization in central coastal California. *Journal of Geophysical Research* **100**, 3873–84.

Hudec, M. R. & Jackson, M. P. A. 2006. Advance of allochthonous salt sheets in passive margins and orogens. *American Association of Petroleum Geologists Bulletin* **90**, 1535–64.

Hudec, M. R. & Jackson, M. P. A. 2007. Terra infirma: understanding salt tectonics. *Earth Science Reviews* **82**, 1–28.

Iriarte, E. 2005. Tectosedimentary phases along the Leitza wrench fault related to Cretaceous Iberia/Europe plate boundary evolution. *Tectonics of Strike-slip Restraining & Releasing Bends in Continental and Oceanic Setting*. Conference abstract book. The Geological Society of London.

Jammes, S., Manatschal, G., Lavier, L. & Masini, E. 2009. Tectonosedimentary evolution related to extreme crustal thinning ahead of a propagating ocean: example of the western Pyrenees. *Tectonics* **28**, TC4012, doi:10.1029/2008TC002406.

Jamtveit, B., Svensen, H., Podladchikov, Y. & Planke, S. 2004. Hydrothermal vent complexes associated with sill intrusions in sedimentary basins. In *Physical Geology of High-Level Magmatic Systems* (eds C. Breitkreuz & N. Petford), pp. 233–41. Geological Society of London, Special Publications no. 234.

Johnson, N. M., Opdyke, N. D., Woodard, G. D., Zeitler, P. K. *et al.* 1983. Rates of late Cenozoic tectonism in the Vallecito-Fish Creek basin, western Imperial Valley, California. *Geology* **11**, 664–7.

Jordan, P. G. 1991. Development of asymmetric shale pull-aparts in evaporite shear zones. *Journal of Structural Geology* **13**, 399–409.

King, G., Oppenheimer, D. & Amelung, F. 1994. Block versus continuum deformation in the western United States. *Earth and Planetary Science Letters* **128**, 55–64.

Larrasoaña, J. C., Parés, J. M., del Valle, J. & Millán, H. 2002. Triassic paleomagnetism from the Western Pyrenees revisited: implications for the Iberian-Eurasian Mesozoic plate boundary. *Tectonophysics* **362**, 161–82.

López-Horgue, M. A., Iriarte, E., Schröder, S., Fernández-Mendiola, P. A. *et al.* 2010. Structurally controlled hydrothermal dolomites in Albian carbonates of the Asón Valley, Basque Cantabrian Basin, Northern Spain. *Marine and Petroleum Geology* **27**, 1069–92.

Luyendyk, B. P., Kamerling, M. J. & Terres, R. 1980. Geometric model for Neogene crustal rotations in southern California. *Geological Society of America Bulletin* **91**, 211–17.

Luyendyk, B. P., Kamerling, M. J., Terres, R. & Hornafius, J. S. 1985. Simple shear of southern California during Neogene time suggested by paleomagnetic declinations. *Journal of Geophysical Research* **90**, 12454–66.

Marra, F. 2001. Strike-slip faulting and block rotation: a possible triggering mechanism for lava flows in the Alban Hills? *Journal of Structural Geology* **23**, 127–41.

Mattei, M., Cifelli, F., Muttoni, G., Zanchi, A. *et al.* 2012. Neogene block rotation in central Iran: Evidence from paleomagnetic data. *Geological Society of America Bulletin* **124**, 943–56.

McCaffrey, K. J. W. & Petford, N. 1997. Are granitic intrusions scale invariant? *Journal of the Geological Society of London* **154**, 1–4.

McFadden, P. L. & Reid, A. B. 1982. Analysis of palaeomagnetic inclination data. *Geophysical Journal of the Royal Astronomical Society* **69**, 307–19.

McKenzie, D. & Jackson, J. 1986. A block model of distributed deformation by faulting. *Journal of the Geological Society of London* **143**, 349–353.

Montadert, L., Winnock, E., Deltiel, J. R. & Grau, G. 1974. Continental margins of Galicia-Portugal and Bay of Biscay. In *Geology of Continental margins* (eds C. A. Burk & C. L. Drake), pp. 323–42. Springer Verlag.

Nicholson, C., Seeber, L., Williams, P. & Sykes, L. R. 1986. Seismic evidence for conjugate slip and block rotation within the San Andreas Fault System, Southern California. *Tectonics* **5**, 629–48.

Ogg, J. G., Agterberg, F. P. & Gradstein, F. M. 2004. The Cretaceous Period. In *A Geologic Time Scale 2004* (eds F. M. Gradstein, J. J. Ogg, & A. G. Smith), pp. 344–83. Cambridge University Press.

Olivet, J. L. 1996. Kinematics of the Iberian Plate. *Bulletin des Centres de Recherche Exploration-Production Elf Aquitaine* **20**, 131–95.

Pan, Y. X., Zhu, R. X. & Banerjee, S. K. 2000. Rock magnetic properties related to thermal treatment of siderite: Behavior and interpretation. *Journal of Geophysical Research* **105**, 783–94.

Peacock, D. C. P., Anderson, M. W., Morris, A. & Randall, D. E. 1998. Evidence for the importance of

"small" faults on block rotation. *Tectonophysics* **299**, 1–13.

PEDREIRA, D., PULGAR, J. A., GALLART, J. & DÍAZ, J. 2003. Seismic evidence of Alpine crustal thickening and wedging from the western Pyrenees to the Cantabrian Mountains (north Iberia). *Journal of Geophysical Research* **108** (B4), 2204. doi:10.1029/2001JB001667.

PEDREIRA, D., PULGAR, J. A., GALLART, J. & TORNÉ, M. 2007. Three-dimensional gravity and magnetic modeling of crustal indentation and wedging in the western Pyrenees-Cantabrian Mountains. *Journal of Geophysical Research* **112**, B12405. doi:10.1029/2007JB005021.

PRESCOTT, W. H., LISOWSCKI, M. & SAVAGE, J. C. 1981. Geodetic measurement of crustal deformation on the San Andreas, Hayward, and Calaveras faults near San Francisco, California. *Journal of Geophysical Research* **86**, 10853–69.

PUEYO, E. L., PARÉS, J. M., MILLÁN, H. & POCOVÍ, A. 2003. Conical folds and apparent rotations in paleomagnetism (a case study in the Southern Pyrenees). *Tectonophysics* **362**, 345–66.

PUIGDEFÀBREGAS, C. & SOUQUET, P. 1986. Tecto-sedimentary cycles and depositional sequences of the Mesozoic and Tertiary from the Pyrenees. *Tectonophysics* **129**, 173–203.

RAT, P. 1988. The Basque-Cantabrian basin between the Iberian and European plates. Some fact but still many problems. *Revista de la Sociedad Geológica de España* **1**, 327–48.

RAT, P., AMIOT, M., FEUILLÉE, P., FLOQUET, M. *et al.* 1983. Vue sur le Crétacé Basco-Cantabrique et Nord-Ibérique. Une marge et son arrière-pays, ses environments sédimentaires. *Mémoires Géologiques de l'Université de Dijon* **9**, 191 pp.

RON, H., FREUND, R. & GARFUNKEL, Z. 1984. Block rotation by strike-slip faulting: structural and paleomagnetic evidence. *Journal of Geophysical Research* **89**, 6256–70.

ROSSY, M. 1988. *Contribution a l'étude du magmatisme Mésozoique du domaine Pyrénnéen*. PhD thesis, Université de Franche-Comté. Published thesis.

RUSHDI, A. I. & SIMONEIT, B. R. T. 2002. Hydrothermal alteration of organic matter in sediments of the Northeastern Pacific Ocean: Part 1. Middle Valley, Juan de Fuca Ridge. *Applied Geochemistry* **17**, 1401–28.

SAPIIE, B. & CLOOS, M. 2004. Strike-slip faulting in the core of the Central Range of west New Guinea: Ertsberg Mining District, Indonesia. *Geological Society of America Bulletin* **116**, 277–93.

SCHOTT, J. J. & PARÉS, J. M. 1996. Paleomagnetisme. In *Synthèses Géologique et Gèophysique des Pyrénées, Volume 1* (eds A. Barnolas, J. C. Chiron & B. Guérangé), pp. 41–9. Bureau de Recherches Géologiques et Minières-Instituto Tecnológico y Geominero de España.

SCHOTT, J. J. & PERES, A. 1988. Paleomagnetism of Permo-Triassic red beds in the western Pyrenees: evidence for strong clockwise rotations of the Paleozoic units. *Tectonophysics* **156**, 75–88.

SCHULTZ-ELA, D. D. & JACKSON, M. P. A. 1996. Relation of subsalt structures to suprasalt structures during extension. *American Association of Petroleum Geologists Bulletin* **80**, 1896–924.

SEEBER, L. & BOGEN, N. L. 1985. Block rotation along the southern San Jacinto fault zone. *Eos* (Transactions, American Geophysical Union) **66**, p. 953.

ŞENGÖR, A. M., GÖRÜR, N. & ŞAROĞLU, F. 1985. Strike-slip faulting and related basin formation in zones of tectonic escape: Turkey as a case study. In *Strike-Slip Deformation, Basin Formation, and Sedimentation* (eds K. T. Biddle & N. Christie-Blick), pp. 227–64. Society of Economic Paleontologists and Mineralogists Special Publication no. 37.

SHAW, J., JOHNSTON, S T., GUTIÉRREZ-ALONSO, G. & WEIL, A. B. 2012. Oroclines of the Variscan orogen of Iberia: paleocurrent analysis and paleogeographic implications. *Earth and Planetary Science Letters* **329–330**, 60–70.

SIMONEIT, B. R. T. & LONSDALE, P. F. 1982. Hydrothermal petroleum in mineralised mounds at the seabed of Guaymas Basin. *Nature* **295**, 198–202.

SOUQUET, P., DEBROAS, E. J., BOIRIE, J. M., PONS, P. *et al.* 1985. Le Groupe du Flysch Noir (Albo-Cénomanien) dans les Pyrénées. *Bulletin des Centres de Recherche Exploration-Production Elf Aquitaine* **9**, 183–252.

SVENSEN, H., PLANKE, S., MALTHE-SØRENSSEN, A., JAMTVEIT, B. *et al.* 2004. Release of methane from a volcanic basin as a mechanism for the initial Eocene global warming. *Nature* **429**, 542–5.

SVENSEN, H., PLANKE, S., POLOZOV, A., SCHMIDBAUER, N. *et al.* 2009. Siberian gas venting and the end-Permian environmental crisis. *Earth and Planetary Science Letters* **277**, 490–500.

SYLVESTER, A. G. 1988. Strike-slip faults. *American Association of Petroleum Geologists Bulletin* **100**, 1666–703.

TALBOT, C. J. 1993. Spreading of salt structures in the Gulf of Mexico. *Tectonophysics* **228**, 151–66.

TATAR, O., PIPER, J. D. A., GÜRSOY, H., HEIMANN, A. *et al.* 2004. Neotectonic deformation in the transition zone between the Dead Sea Transform and the East Anatolian Fault Zone, Southern Turkey: a paleomagnetic study of the Karasu Rift Volcanism. *Tectonophysics* **385**, 17–43.

TCHALENKO, J. S. 1970. Similarities between shear zones of different magnitudes. *Geological Society of America Bulletin* **81**, 1625–40.

THOMPSON, K. 2007. Determining magma flow in sills, dykes and laccoliths and their implications for sill emplacement mechanisms. *Bulletin of Volcanology* **70**, 183–201.

TIBALDI, A., PASQUARÈ, F. & TORMEY, D. 2010. Volcanism in reverse and strike-slip fault settings. In *New Frontiers in Integrated Solid Earth* Science (eds S. Cloetingh & J. Negendank), pp. 315–48. Springer-Verlag.

TIKOFF, B. & TEYSSIER, C. 1992. Crustal-scale, en echelon "P-shear" tensional bridges: a possible solution to the batholithic room problem. *Geology* **20**, 927–30.

VANDENBERG, J. 1980. New paleomagnetic data from the Iberian Peninsula. *Geologie en Mijnbouw* **59**, 49–60.

VAN DER VOO, R. 1969. Paleomagnetic evidence for the rotation of the Iberian Peninsula. *Tectonophysics* **7**, 5–56.

VAN DER VOO, R. 1993. *Paleomagnetism of the Atlantic, Tethys and Iapetus Oceans*. Cambridge University Press, 411 pp.

VENTURA, G. 1994. Tectonics, structural evolution and caldera formation on Vulcano Island (Aeolian Archipielago, southern Tyrrhenian Sea). *Journal of Volcanology and Geothermal Research* **60**, 207–24.

WALCOTT, R. I. 1984. The kinematics of the plate boundary zone through New Zealand: a comparison of short- and long-term deformation. *Geophysical Journal of the Royal Astronomical Society* **79**, 613–33.

Journal of Sea Research xxx (xxxx) xxx–xxx

Contents lists available at ScienceDirect

Journal of Sea Research

journal homepage: www.elsevier.com/locate/seares

Environmental and ammonoid faunal changes related to Albian Bay of Biscay opening: Insights from the northern margin of the Basque-Cantabrian Basin

Luis M. Agirrezabala*, Mikel A. López-Horgue

Estratigrafia eta Paleontologia Saila, Euskal Herriko Unibertsitatea UPV/EHU, 48080 P.K., 644 Bilbo, The Basque Country, Spain

ARTICLE INFO

Keywords:
Environmental changes
Ammonoids
Albian
Bay of Biscay opening
Basque-Cantabrian Basin
Northern margin

ABSTRACT

The opening and ocean floor spreading of the Bay of Biscay began in the earliest Albian. The integrative study of the Albian sedimentary record and its ammonoid fauna (around 250 specimens) from the northern margin of the Basque-Cantabrian Basin indicates that environmental changes, occurred as a consequence of the Bay of Biscay opening, triggered significant ammonoid bioevents. Main bioevents are diversity changes in the ammonoid associations, occurrence of large forms (diameter up to 0.45 m) and the incursion of elements from other basins. Time-correlation of faulting pulses with ammonoid bioevents indicates that transtensive tectonics was ultimately the major control on the marine environmental conditions such as depth, sea bottom physiography, seaways, sedimentary systems and sea-water chemistry. The pulsating faulting during the Albian led to the increment of the subsidence rate, the deepening and widening of the margin and the progressive increase in the oceanic circulation between the margin and the nascent Bay of Biscay and North Atlantic. In addition, Albian synsedimentary faults constituted conduits for ascending magmas and hydrocarbon-rich hydrothermal fluids, which expelled to the seafloor, causing changes in the sediments, the sea-water chemistry (fertilization) and biota. The integration of sedimentological and palaeontological data has given the basis for a conceptual model of the ammonoid habitats.

1. Introduction

Mesozoic rocks deposited in the northern margin of the Basque Cantabrian Basin (BCB) record rifting processes that led to the opening of the Bay of Biscay (Rat, 1988). During the Albian, and coeval to the beginning of the seafloor spreading in the western part of the Bay of Biscay, hyperextension of the crust caused faulting, maximum subsidence and deepening of the margin (Jammes et al., 2009). This allowed for the deposition of a thick succession of deep-water sediments, i.e. the Black Flysch Group, which host a rich and diverse fauna of ammonoids. Besides the biostratigraphical value of these ammonoid associations, which have been the basis for timing the otherwise difficult to date the thick and facies-changing sedimentary successions, their value to understand the environmental conditions and changes in a deepening marine basin are of key interest.

In the last years, ammonoid habitats have been inferred from the study of the conch parameters and hydrodynamic characteristics (e. g., Westermann, 1996) and from the relationship to the sedimentary facies (e. g., Batt, 1993). Recently, new evaluations of the morphology (e. g., Ritterbush and Bottjer, 2012) and the use of stable isotope analysis of the conch (Lukeneder et al., 2010), in addition to new advances in their palaeobiology, have permitted to better understand the environments inhabited by ammonoids (e. g., Lukeneder, 2015). Based on collected ammonoids, this study establishes an Albian biozonation for the entire northern margin of the Basque Cantabrian Basin, distinguishes several local bioevents and addresses the response of the ammonoid fauna to environmental changes inferred from the accurately studied Albian sedimentary record. The integration of these sedimentological and palaeontological data is the basis for the construction of a conceptual model of the ammonoid habitats which provides an improved understanding on the environments in which they thrived and on the environmental changes in a fastly evolving margin of the Bay of Biscay.

2. Geological and palaeontological background

The studied Albian sedimentary rocks and their ammonoid fauna belong to the northern margin of the Basque-Cantabrian Basin (BCB), a Mesozoic peri-cratonic rift basin related to the opening of the North Atlantic and the Bay of Biscay (Fig. 1). The Bay of Biscay is a V-shaped oceanic embayment widened toward the west, formed between Early

* Corresponding author.
E-mail address: l.agirrezabala@ehu.eus (L.M. Agirrezabala).

http://dx.doi.org/10.1016/j.seares.2017.04.002
Received 6 November 2016; Received in revised form 1 March 2017; Accepted 4 April 2017

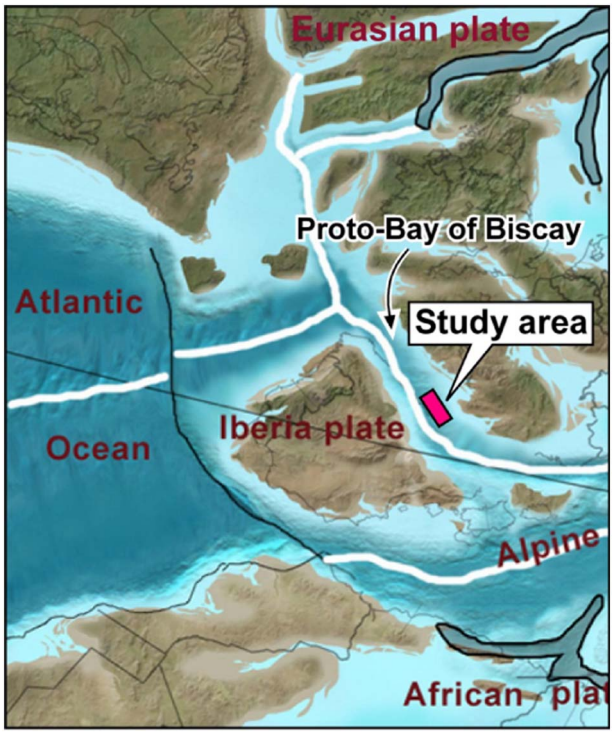

Fig. 1. Albian (100 Ma) palaeogeographic map of the North Atlantic showing the nascent Bay of Biscay between Iberia and Laurasia plates. The studied northern margin of the BCB is indicated.
Source: http://cpgeosystems.com.

Albian and Santonian times (Montadert et al., 1974). The oceanic floor spreading led to the anticlockwise rotation of the Iberian plate by 35–37° with respect to Eurasia and the opening of the Bay of Biscay (Van der Voo, 1969). In the front of this propagating ocean three main Mesozoic rift basins, i.e. Basque-Cantabrian, Parentis and Maule-Arzacq basins, were formed (Vergés et al., 2001). These basins experienced an Albian phase of maximum extension and subsidence coincident with the initiation of the sea floor spreading in the Bay of Biscay (Brunet, 1994). Recent works interpret these basins as magma-poor hyperextended rifts characterized by extremely thinned crust and locally also exhumed mantle (Jammes et al., 2009), but without oceanization. Cenozoic inversion of the BCB led to intense folding and thrusting of their sedimentary records (Vergés et al., 2001).

The Cretaceous northern margin of the BCB belongs to the European plate and exhibits a main NW-SE structural orientation (Fig. 2). This margin is adjacent to the Landes Palaeozoic massif (European plate) by the NE and is limited to the SW by the Leitza-Elgoibar fault which is assigned to the plate boundary between the Iberia and Eurasia plates (Agirrezabala, 1996; García-Mondéjar et al., 1996; and references therein). The stratigraphic architecture and sedimentologic characteristics of the Albian sedimentary record of the margin indicate an overall southwest sedimentary polarity (Agirrezabala, 1996). During the Albian the northern margin was sited at a palaeolatitude of ca. 35° with a subtropical warm and wet climate (Dercourt et al., 2000). Open sea waters on the margin were warm and with a normal salinity (García-Mondéjar, 1990).

In the last thirty years, the collection of an important sample of Middle and Upper Albian ammonoids hosted in offshore marine successions made possible the accurate dating of these successions. This collection is today hosted in the Department of Stratigraphy and Palaeontology of the University of the Basque Country (UPV/EHU; Leioa), in the Museo de Ciencias Naturales de Araba (MCNA; Vitoria-Gasteiz) and in the Nautilus Museum of the Basque Coast Geopark (NM; Mutriku, Gipuzkoa). However, no Lower Albian ammonoids have been found up to date; the dating of this part of the succession has been possible by means of orbitolinids (foraminifers). The first references to ammonoids in the study area come from Gómez de Llarena (1958), Rat (1959) but they only refer to identifications of scarce specimens with biostratigraphic value. The only descriptive works on ammonoids of the study area are those of Wiedmann and Boess (1984) and Agirrezabala et al. (1992). Afterwards, the accurate biostratigraphy for the Middle-Upper Albian with indication of the associated species has been given in Agirrezabala (1996) and Agirrezabala et al. (2002) for the eastern part of the study area, and in López-Horgue et al. (2009) and López-Horgue and Bodego (2012) for the western part.

3. Methods

This paper presents a synthesis of stratigraphic, sedimentological and palaeontological data from twelve main Albian sections distributed along the northern margin of the BCB, summarized in a cross-margin transect to illustrate the history of the Albian environmental changes and local bioevents. In each section, detailed description and interpretation of sedimentary facies and collecting and study of fossils (principally ammonoid) have been carried out. A total of > 250 ammonoid specimens have been considered, spanning from the basal Middle Albian to the Upper Albian. These ammonoids were published in two previous papers by Agirrezabala et al. (2002) and López-Horgue et al. (2009). The correlation among the sections is based on ammonoid biostratigraphic data and, to a lesser extent, on inoceramid and foraminifera data. In addition, published detailed mapping of lithostratigraphic units, physical event deposits (megabeds, bentonite beds, volcanic flows) and erosional/non-depositional features (unconformities), and chemostratigraphic intervals (^{13}C–depleted deposits) are used as complementary correlation tools (Robles et al., 1988; Agirrezabala, 1996, 2009; Agirrezabala and García-Mondéjar, 1989). Thus, a margin-scale robust chronostratigraphic framework was obtained in which 6 ammonoid zones and subzones are distinguished, previously recognized by Agirrezabala et al. (2002) and López-Horgue et al. (2009). Although the specimen richness of collected ammonoids is not enough for an exhaustive statistical analysis, it is high enough for inferring major changes in the ammonoid assemblages, which may be related to environmental perturbations.

The study and correlation of the ammonoid faunas from the northern margin of the BCB allows us: i) to discriminate stratigraphic intervals with different diversities (number of species) at a resolution level of ammonoid biozones (maximum resolution for margin-scale correlations); ii) to distinguish ammonoid associations with different features (morphology, ornamentation and size of the conch, and palaeogeographical affinity); and iii) to recognize local bioevents. In this paper, we use the term “local bioevent” as a short-term evolutionary, ecologic and biogeographic change recorded in the fossil biota of a limited area (100 mi) in response to rapid environmental changes (see Kauffman and Hart, 1996); these environmental changes (tectonics, climate, sea-level, volcanism, chemistry, etc.) may also cause correlative changes in the sedimentological record (Kauffman and Hart, 1996). Finally, we discuss the interrelationships between the ammonoid record and the environmental changes deduced from both the sedimentary facies and depositional architecture.

4. Results

4.1. Albian sedimentary record

The main stratigraphic and sedimentologic characteristics of the Albian sedimentary record of the northern margin are documented in Robles et al. (1988), Agirrezabala and García-Mondéjar (1989) and Agirrezabala (1996). In addition, many specific and detailed geological studies have been recently carried out in the area. Fig. 3 depicts a synthetic NE-SW stratigraphic cross-section for the Albian record of the

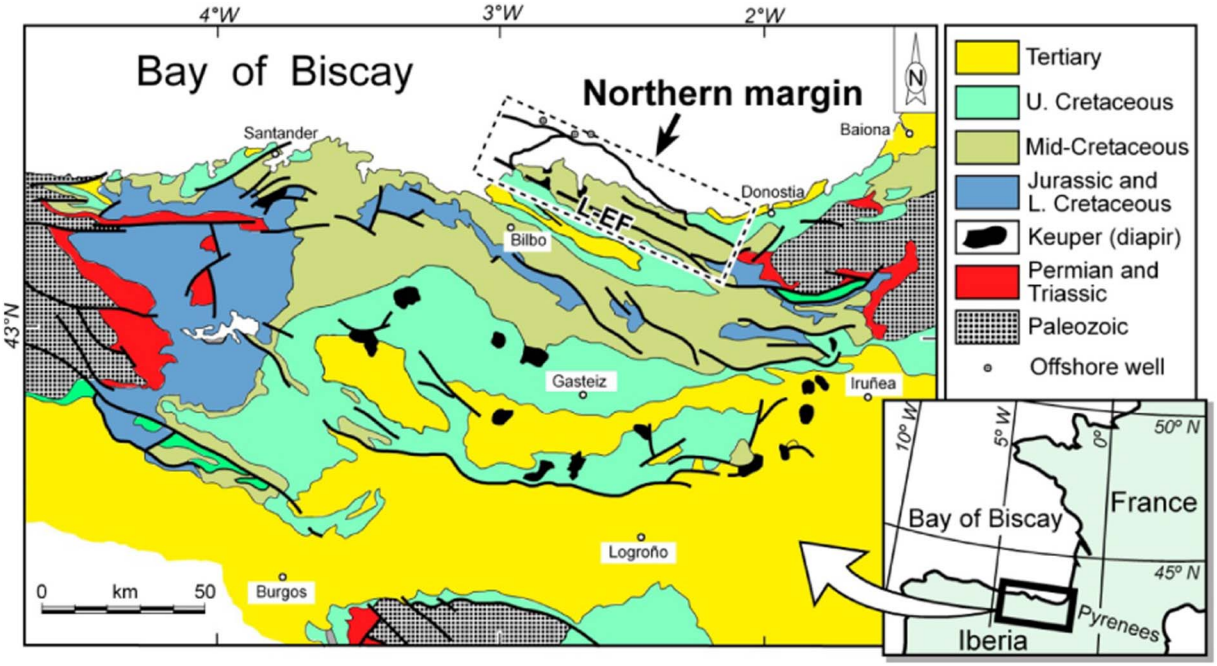

Fig. 2. Geologic map of the BCB with indication of the studied northern margin. L-E F: Leitza-Elgoibar fault.

northern margin where main sedimentary facies, stratigraphic sequences, and ammonoid biozones are shown. The Albian stratigraphic record can be divided into four main sequences bounded by the intervening unconformities U1 to U4. The sequence 1 is composed of deltaic to shallow-water marine deposits, and sequences 2–4 consist of deep-water clastic deposits (Black Flysch Group) and local shallow-water carbonates. The cross-section shows in a southwestward direction that: i) the Albian sedimentary record thickens greatly, ii) clastic deposits are progressively finer, and iii) sedimentary facies are progressively deeper water, indicating that during the Albian the margin had a southwestward sedimentary polarity with increasing subsidence in the same direction. It also shows NE- and N-trending transverse synsedimentary faults that compartmented the margin during the Albian.

4.1.1. *Sequence 1 (uppermost Aptian–Lower Albian)*

The age of the bounding unconformity U1 and overlying basal deposits of this sequence is poorly constrained, ranging from uppermost

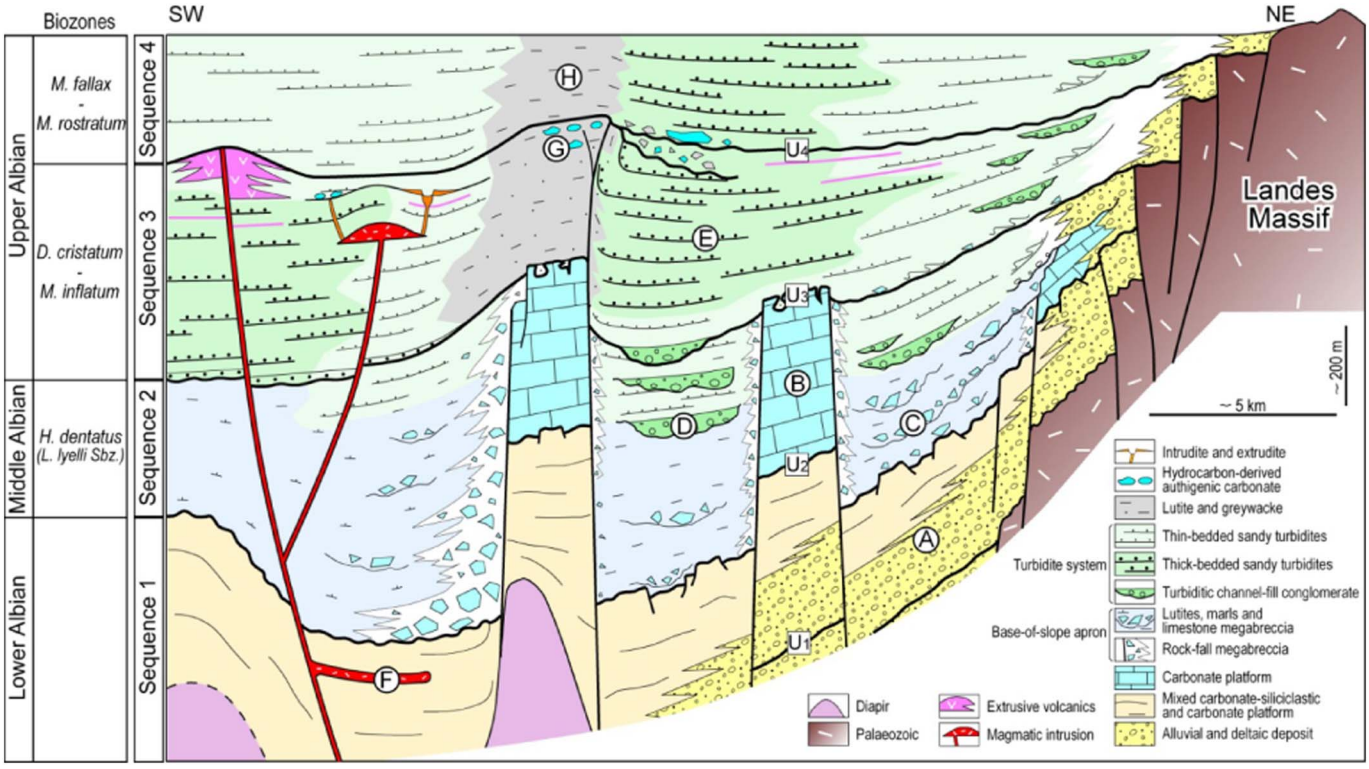

Fig. 3. Synthetic stratigraphic cross-section of the Albian northern margin deposits with indication of stratigraphic sequences (1–4), sequence boundaries (U2–U4) and main sedimentary facies. A–H letters indicate outcrop photographs shown in Fig. 4.

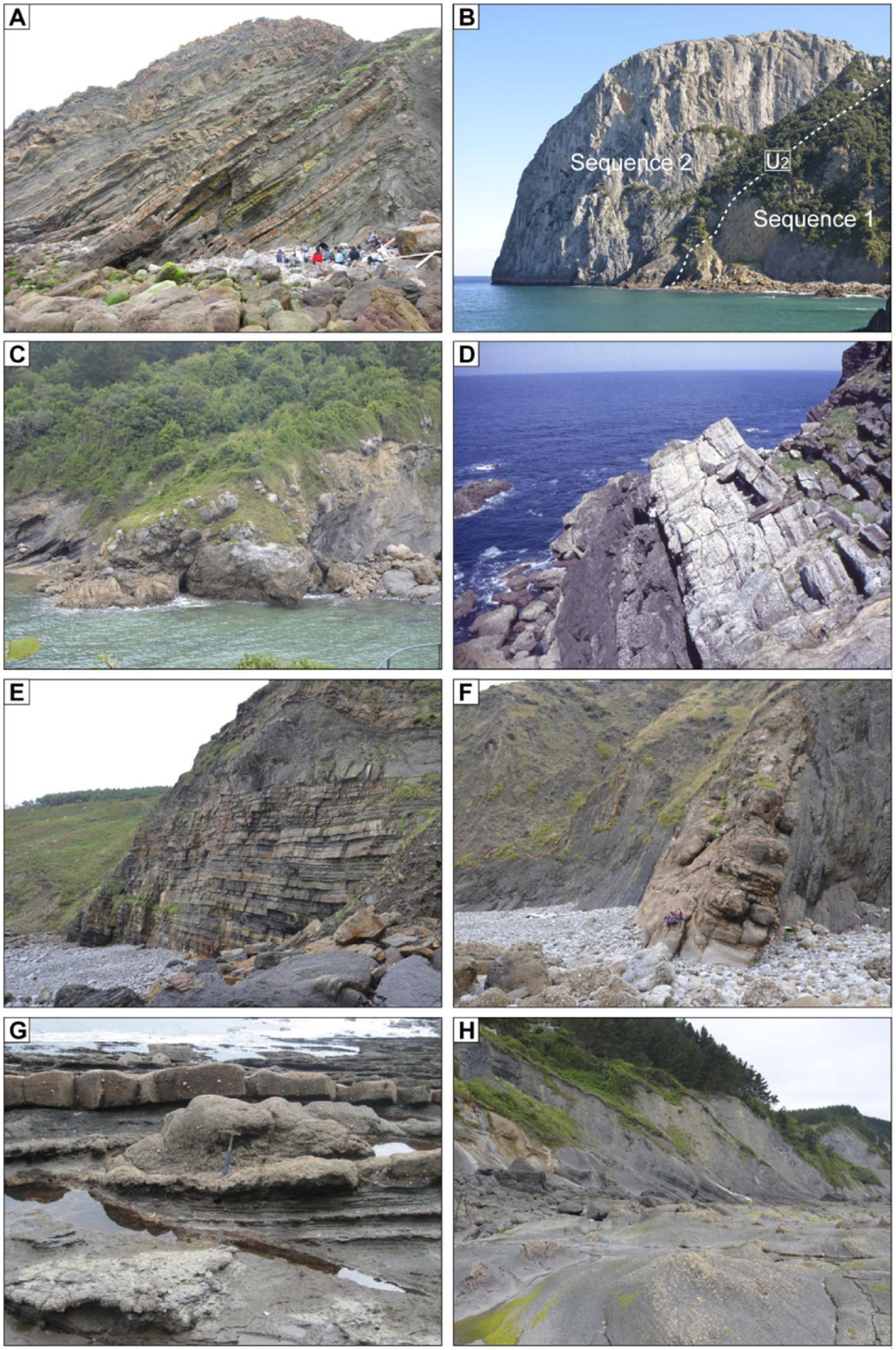

Fig. 4. Outcrop photographs of Albian tectono-stratigraphic sequences and main sedimentary facies (for location see Fig. 3). A) Deltaic sandstones and lutites arranged in thickening- and coarsening-upward sequences (sequence 1, Gorliz locality). B) Deltaic sandstone and lutites (sequence 1) overlaid by shallow-water massive limestones corresponding to a carbonate bank (sequence 2, Ogoño cape). C) Wedge-shaped limestone megabreccias with olistoliths up to 30 m long interbedded with organic-rich lutites (sequence 2, Ea locality). D) Turbiditic channel-fill composed of conglomerates and sandstones (sequence 2, Ea locality). Note a person for scale at the base of the channel-fill. E) Thick, parallel turbidite sandstones interpreted as turbidite lobe deposits (sequence 3, Bakio locality). F) 5 m-thick magmatic sill (sequence 3) intruded in organic-rich lutites (sequence 2). Contact aureole records formation of thermogenic methane, oil and CO_2 which migrated upward and escaped to the palaeoseabed (Gorliz locality). G) Hydrocarbon-derived authigenic carbonate lens filling a palaeopockmark (sequence 3, Ispaster locality). H) Mudstones deposited on a submarine structural palaeohigh under quiet, hemipelagic conditions (sequence 4, Mutriku locality).

Aptian to lowermost Albian. In the NE part of the margin, this sequence is composed of conglomerates, sandstones and organic-rich mudstones (Fig. 4A,B) interpreted as deposited in two retreating fan-delta systems (Robles et al., 1988; Agirrezabala, 1996) sourced from the NE. These deltaic systems pass southwestward to interbedded sandstones, mudstones and fossil-rich (rudists, corals, ostreids, orbitolinids, etc.) micritic and calcarenitic limestones deposited in a siliciclastic-carbonate mixed platform (Agirrezabala, 1996). More to the southwest, rudist- and coral wackestones dominate in a shallow-water carbonate platform. Marl deposits of slightly deeper intra-platform troughs occur locally and adjacent to carbonate platforms. This sequence was deposited in a general shallow-water marine environment with relatively gentle depositional gradients.

4.1.2. Sequence 2 (Middle Albian, H. dentatus Zone)

Basal bounding unconformity U2 is an erosive surface cross-cut by coeval NW- to NE-trending normal fault scarps. Some fault scarps show hardground features (borings, encrusting oysters and Fe mineral crusts), indicating their submarine exposition. Overlying deposits onlap fault scarps. The sequence is composed of two distinct deposit types: shallow-water limestones and adjacent deep-water resedimented clastic deposits. The boundaries between both deposit types are sharp and subvertical and are interpreted as syndepositional fault scarps. The shallow-water limestones are composed of massive rudistid and coral wackestones constituting lithosomes of reduce area (1–5 km^2) but great thickness (up to 400 m) surrounded by deep-water deposits (Fig. 4B). They are interpreted as small aggrading carbonate banks formed on horsts or diapirs (Agirrezabala and García-Mondéjar, 1989; Poprawski et al., 2014).

The deep-water resedimented clastic deposits occur between the carbonate banks and fill NE-SW oriented fault-bounded grabens. They belong to the lowest part of the Black Flysch Group characterized by the presence of relatively organic-rich (TOC ca. 1%), black to dark gray lutites with abundant framboidal pyrite and *Zoophycos* ichnofacies; petrographic and Rock-Eval analyses indicate that organic matter was mainly of detrital character and derived from the continent (Agirrezabala et al., 2008, 2014). These deposits present two main parts, a lower calciclastic part and an upper siliciclastic part. The lower part is composed mainly of organic-rich lutites and thick limestone orto- and para-megabreccias with olistoliths up to 40 m long (Fig. 4C), with minor sandy turbidites. These deposits are interpreted as formed in a deep-water base-of-slope environment where quiet sedimentation (mud) was punctuated by down-slope catastrophic debris flow and rock falls (megabreccias) sourced from northern carbonate platforms. The upper part of the sequence is composed of coarse-grained siliciclastic turbidite systems characterized by proximal thick conglomeratic channel-fills (Fig. 4D) which pass down-slope to thinner tabular sandy turbidites interpreted as fan lobe and fan fringe deposits. These turbidite systems were sourced from northern fan-deltas and filled L-shaped pull-apart sub-basins (Agirrezabala and García-Mondéjar, 1994). In addition, limestone megabreccias with very limited lateral extension (200–400 m) and olistoliths with dimensions up to 280 × 40 m occur adjacent to carbonate banks, which are interpreted as rock fall deposits piled at the base of fault scarps (Agirrezabala and García-Mondéjar, 1988; Poprawski et al., 2014).

4.1.3. Sequence 3 (Upper Albian, D. cristatum–M. inflatum Zones)

Northern offshore wells document the presence of Upper Albian thin siliciclastic deposits overlying Palaeozoic rocks of the Landes Massif. Onshore, the lower boundary of the sequence (U3) is either a palaeokarst surface (top of the underlying carbonate banks) or an erosive surface. The existence of local angular unconformities and megabeds (seismites?) related to the lower boundary suggests a tectonic origin. The sequence boundary is overlaid by widespread deep-water siliciclastic deposits recording the drowning (after subaerial exposition) of the previous carbonate banks. The sequence consists of thick turbidite systems filling fault-bounded subsident depocenters separated by structural highs. Turbidite systems are composed of tabular sandy turbidites showing *Nereites* ichnofacies, relatively organic-rich lutites (TOC ca. 1%) and siderite thin beds (Fig. 4E) interpreted as turbiditic lobe and fan fringe deposits. On structural palaeo-highs, bioturbated (*Zoophycos* ichnofacies) sandy lutites with scattered thin-bedded sandy turbidites and siderite beds are interpreted as the result of relatively quiet hemipelagic deposition punctuated by occasional diluted turbidity currents.

In addition, in the upper part of the sequence (*H. binum* Subzone–*M. inflatum* Zone), sedimentary deposits record different contemporaneous *syn*-depositional process, i.e. tectonic, magmatic, metamorphic and fluid expulsion processes. Local angular unconformities and related megabreccias record the transpressive deformation and uplift caused by sinitral vertical-axis block rotation of small cortical blocks in a strike-slip context (Agirrezabala et al., 2002; Agirrezabala and Dinarès-Turell, 2013). Basalts and pyroclastic deposits are interbedded with deep-water deposits (Agirrezabala and García-Mondéjar, 2001; Castañares et al., 2001), and magmatic laccoliths and sills intrude Albian sedimentary units (Fig. 4F). Intrusion of magmas caused syndepositional folding and fracturing of overburden rocks and formation of intrudites and extrudites (Agirrezabala et al., 2013; Agirrezabala, 2015). In the contact aureole of those magmatic intrusions, metamorphism of organic-rich host lutites led to the formation of overpressured hydrothermal fluids rich in thermogenic methane, oil and CO_2, which migrated upward and were expelled to the seabed (Agirrezabala et al., 2008, 2014). ^{13}C-depleted authigenic carbonates occur in these seep areas (Fig. 4G) and enclose chemosymbiotic fauna, archea biomarkers, bitumen and non-obligate relatively rich fauna, i.e. abundant radiolarian and planktonic foraminifers, gastropods, bivalves, ammonoids, arthropods, sponges and rare corals (e.g. Agirrezabala, 2009, 2015; Agirrezabala et al., 2013). Some of these corals are zooxanthellate (Hannes Loeser, 2016, personal communication).

4.1.4. Sequence 4 (Upper Albian, M. fallax Zone)

In onshore outcrops, the basal bounding unconformity U4 shows different features basinwide: erosive surface, angular unconformity or onlap surface. The sequence is composed of thick- to thin-bedded tabular sandy turbidites showing *Nereites* ichnofacies interpreted as deposited in the distal part of submarine fans. These relatively thick turbidite deposits filled subsident depocentres separated by faulted ridges where hemipelagic mudstones were deposited (Fig. 4H). Locally, adjacent to these ridges, occurrence of angular unconformities and megabreccias record fault-related transpressive folding.

4.2. Albian ammonoid fauna

More than 250 specimens have been collected from the Albian succession of the northern margin of the BCB, spanning from the lower Middle Albian to the Upper Albian (see Fig. 2: sequences 2, 3 and 4); despite of the accurate field-exploration, Upper Aptian-Lower Albian sediments (sequence 1) did not yield ammonoids. In this sample, compiled in Table 1, a total of 58 species assignated to 34 genera and subgenera have been identified from all recognized biozones (Agirrezabala et al., 2002; López-Horgue et al., 2009). Ammonoids occur in 44 distinctive intervals of limited thickness, ranging between 5 and 6 cm and 4–5 m. Ammonoid occurrences are then widely distributed along the succession but are representative of the relative richness in these expanded series.

4.2.1. Ammonoid biostratigraphy

Ammonoid associations are representative of their corresponding biozones (Table 1). Biostratigraphy is well discussed and ammonoid associations represented in the works of Agirrezabala et al. (2002) and López-Horgue et al. (2009), where they follow the Albian zonal scheme for the Tethyan province proposed in López-Horgue et al. (1999) and

Table 1
Albian ammonite zones, subzones and ammonite content in the northern margin of the BCB. Data are compiled from Agirrezabala et al. (2002, 2003) and López-Horgue et al. (2009). We introduce here some modifications concerning the former Upper Albian *Stoliczkaia dispar* Zone, previously discussed in Gale et al. (2011) and Reboulet et al. (2014).

Zones, subzones and levels[a]	Ammonites
M. fallax–M. rostratum Zones. Levels: P, R, meters 551–563	
Anisoceras cf. *perarmatum* (Pictet & Campiche)	*Mortoniceras* (*Mortoniceras*) cf. *pachys* (Seeley)
Anisoceras picteti Spath	*Mortoniceras* (*Mortoniceras*) sp.
Anisoceras pseudoelegans (Pictet & Campiche)	*Anisoceras saussureanum* (Pictet)
Mortoniceras (*Mortoniceras*) *alstonense* (Breistroffer)	*Anisoceras armatum* (J. Sowerby)
Mortoniceras (*Mortoniceras*) *arietiforme* group Spath	*Mortoniceras* (*Mortoniceras*) sp. indet. cf. gr. *rostratum*
Mortoniceras (*Mortoniceras*) *rugosum* Spath	
M. inflatum Zone. Levels: N, meter 536	
Hamitoides cf. *studerianus* Pictet	*Lechites* sp.
Cantabrigites cf. *nanoides* Wiedmann	*Mortoniceras* (*M.*) *crassinodatum* (van Hoepen)
H. varicosum Zone (*H. choffati* Subzone). Levels: K, L, meters 468–528	
Puzosia cf. *provincialis* (Parona & Bonarelli)	*Hypophylloceras velledae* (Michelin)[d]
Hysteroceras cf. *varicosum* (J. Sowerby)	*Idiohamites turgidus* (J. Sowerby)[d]
Mortoniceras (*Mortoniceras*) sp.	*Anisoceras arrogans* (Giebel)[d]
Hamites sp.	*Puzosia mayoriana* (d'Orbigny)
Craginites sp.	*Pachydesmoceras* cf. *denisonianum*[d]
Mortoniceras (*Deiradoceras*) *exilis* (van Hoepen) & cf. *ex.*	*Idiohamites* sp.[c]
Arestoceras cf. *splendidum* van Hoepen	*Mortoniceras* sp.[c]
Mortoniceras (*Deiradoceras*) *bispinosum* (Spath)	
H. varicosum Zone (*H. binum* Subzone). Levels: J, meters 455–475	
Labeceras sp.	*Desmoceras latidorsatum* (Michelin)
Bhimaites sp.	*Desmoceras* sp. juv.
Hamites sp. juv.	*Hypophylloceras moreti* (Mahmoud)
Hysteroceras sp. juv.	*Hypophylloceras subalpinum* (d'Orbigny)
Kossmatella oosteri Breistroffer	*Hypophylloceras seresitense* (Pervinquière)
Hypophylloceras sp.	cf. *Anagaudryceras* sp.
Bhimaites cf. *aontzyensis* Collignon	*Kossmatella schindewolfi* Wiedmann and Dieni
Puzosia (*Anapuzosia*) sp. juv.	*Kossmatella muhlenbecki* (Fallot)
Kossmatella romana Wiedmann	*Parasilesites kilianiformis* (Fallot)
Tetragonites sp. juv.	*Hysteroceras varicosum* (J. de C. Sowerby)
Jauberticeras jaubertianum (d'Orbigny) & cf. *jaubert.*	*Hysteroceras binum* (J. Sowerby)
Protetragonites sp. juv.	*Puzosia* (*Anapuzosia*) *tucuyensis* (von Buch) and cf. *tuc.*
Puzosia mayoriana (d'Orbigny)	
D. cristatum Zone–*H. varicosum* Zone (*H. orbigyi* Subzone). Levels: G, I	
Puzosia sp.	*Oxytropidoceras* (*Oxytropidoceras*) cf. *cantianum* Spath
Kossmatella cf. *schindewolfi* Wiedmann & Dieni	*Kossmatella*[b]
Hemiptychoceras sp.	*Dipoloceras*?[b]
Puzosia (*Puzosia*) sp.	*Epihoplites*?[b]
Hysteroceras sp.	
H. dentatus Zone (*L. lyelli* Subzone). Levels: A, B, C, D, E, F, meter 430	
Metahamites cf. *elegans* (d'Orbigny)	*Lyelliceras pseudolyelli* (Parona & Bonarelli)
Kossmatella cf. *muhlenbecki* (Fallot)	*Lyelliceras* cf. *lyelli* (d'Orbigny)
Metahamites sp.	*Lyelliceras* cf. *gevreyi* (Jacob)
Parasilesites cf. *kilianiformis* (Fallot)	*Lyelliceras* sp. *peruvianum*-group
Kossmatella sp.	*Cleoniceras* (*Cleoniceras*) cf. *devisensis* Spath
Eogaudryceras sp.	*Protanisoceras* (*Protanisoceras*) sp.
Dipoloceroides sp.	*Puzosia* sp.
Hemiptychoceras gaultinum (Pictet)	*Oxytropidoceras* (*Oxytropidoceras*) sp.
Kossmatella agassizianum (Pictet)	*Oxytropidoceras* cf. *roissyanum* (d'Orbigny)

[a] Letters A-R indicate levels of Agirrezabala et al. (2002, 2003; Table A1 and Fig. A1) and meters indicate levels of López-Horgue et al. (2009; Fig. 5).
[b] Ammonites after Rat (1959).
[c] Ammonites after Reitner (1987)
[d] Ammonites after Pletsch (1990).

Owen (1999) with discussions in Wiedmann and Owen (2001) and Owen and Mutterlose (2006).

The Middle Albian is only represented by its basal biozone, the *Lyelliceras lyelli* Subzone of the *Hoplites dentatus* Zone, with 7 stratigraphic levels distributed in a sedimentary succession 100 to 500 m thick (sequence 2 in Fig. 3). Typical elements of this association, with 15 species from 11 genera/subgenera, are the marker *Lyelliceras lyelli* and *Oxytropidoceras* cf. *roissyanum*. A basin-wide unconformity separates Middle Albian sediments from the overlying Upper Albian succession (sequences 3 and 4 in Fig. 3).

The Upper Albian sequence 3 in the study area is represented by the *Dipoloceras cristatum*, *Hysteroceras varicosum* and *Mortoniceras inflatum* Zones. Basal sediments of this sequence yield 2 levels with 7 species from 7 genera/subgenera corresponding to the *Dipoloceras cristatum* Zone and to the *Hysteroceras orbignyi* Subzone of the *H. varicosum* Zone, with characteristic *Dipoloceras* sp. and *Hysteroceras* sp. Overlying *Hysteroceras binum* Subzone of the *H. varicosum* Zone is well represented by 6 levels; the marker *H. binum* occurs among 20 species distributed in 14 genera/subgenera. *Hysteroceras choffati* Subzone of the *H. varicosum* Zone has been distinguished from an interval bearing 8 levels with a total of 13 species from 11 genera; typical elements of this Subzone are *Mortoniceras* spp. with a tendency to show a subtle mid-flank tubercle. *Mortoniceras inflatum* Zone sediments are characterized by an interval with 5 levels bearing *Mortoniceras* spp. with a mid-flank tubercle from a total of 4 species distributed into 4 genera/subgenera.

The Upper Albian sequence 4 is represented by the *Mortoniceras fallax* Zone and part of the *Mortoniceras rostratum* Zone, so not reaching the uppermost Albian. Corresponding sediments crop out in the Kardala and Armintza sea-cliffs, showing 16 levels with at least 10 species from 2 genera/subgenera; this association is characterized by *Mortoniceras* spp. transitional to typical *M. rostratum*. Ammonoids of the *M. inflatum*, *M. fallax* and *M. rostratum* biozones are currently being studied in more detail and will constitute the basis of a new paper.

4.2.2. Ammonoid-bearing levels and preservation

Ammonoids occur mainly in thin intervals of fine-grained siliciclastic sediments and associated diagenetic carbonates, being very scarce in coarse-grained sediments. Most of these levels originated in offshore marine areas adjacent to main terrigenous-dispersal systems, being rich in terrestrial organic matter.

Ammonoids from the lutites and calcareous muddy siltstones are preserved as crushed internal moulds with dissolved conch or replaced by diagenetic calcite, a finely preserved sculpture, entire body chambers and no signs of epibiont encrustation or boring (e.g. Fig. 5 A–D, K); in some intervals, the phragmocone is preserved as undistorted pyritic nucleus (e.g. Fig. 5 E, F). Ammonoids hosted in local hydrocarbon seep carbonates are common (Agirrezabala, 2009); hosted fossils usually preserve their original dimension (phragmocone and body chamber) but a shell replaced by diagenetic calcite. Siderite concretions are widespread in some fine-grained intervals and atop of some diluted turbidites; they bear well preserved undistorted ammonoids, with the conch (phragmocone and body chamber) preserved as diagenetic calcite, occasionally with its upper part dissolved, and no signs of epibionts (e.g. Fig. 5 G–J, L, M). In this type of concretions, delicate structures such as apertural rostra of *Mortoniceras* spp. are preserved.

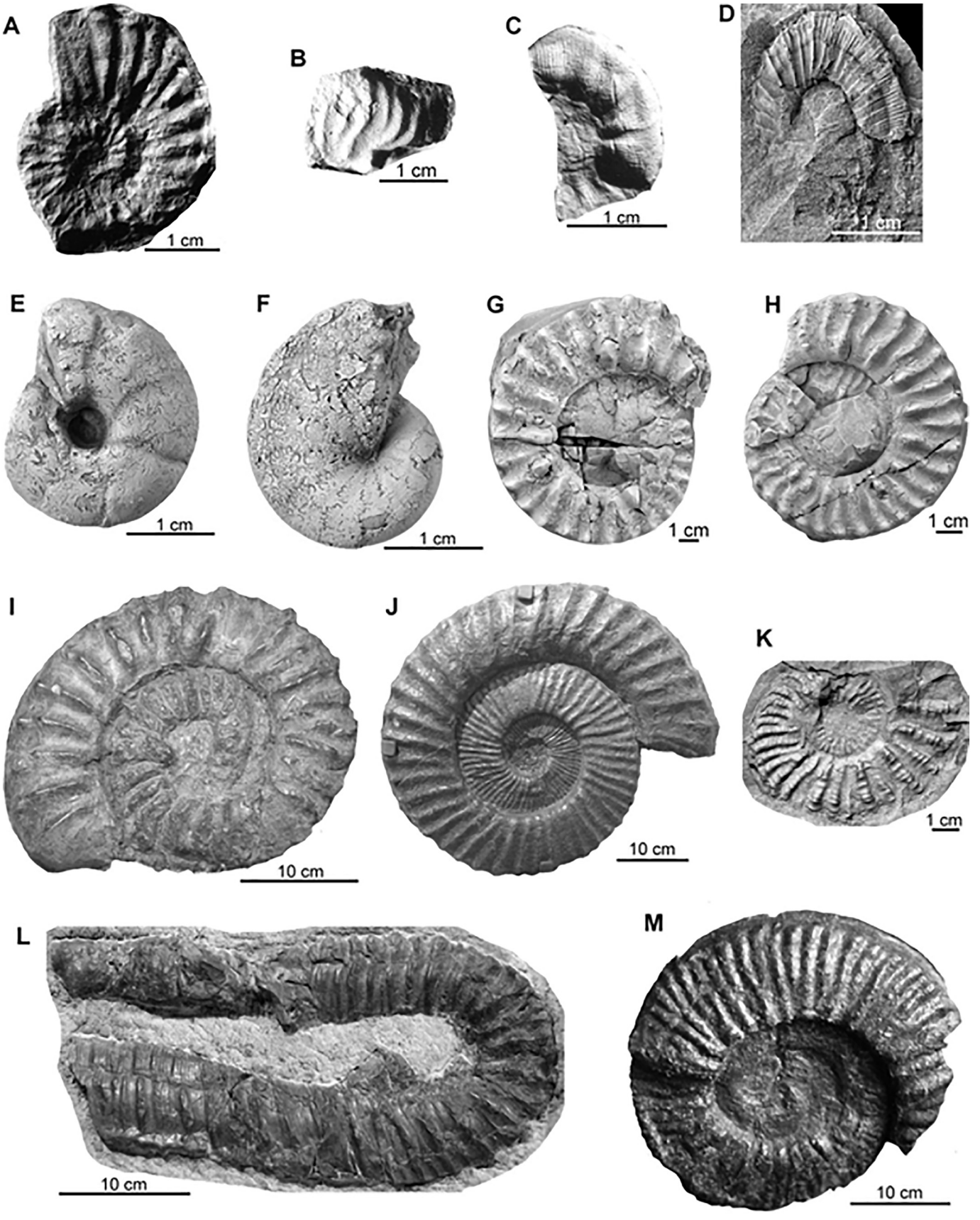

(caption on next page)

Fig. 5. Ammonoids from the study area: examples of morphotypes and biogeographical/biostratigraphical references. A. *Lyelliceras* cf. *lyelli* (d'Orbigny) (UPV/EHU). B. *Cleoniceras* (*C.*) cf. *devisensis* Spath (UPV/EHU). C. *Kossmatella* cf. *schindewolfi* Wiedmann and Dieni (UPV/EHU). D. *Labeceras* sp. (MCNA 13472). E. *Desmoceras latidorsatum* (Michelin) (MCNA 13487). F. *Hypophylloceras subalpinum* (d'Orbigny) (MCNA 13502). G. *Mortoniceras* (*Deiradoceras*) *exilis* (van Hoepen) (MCNA 13513). H. *Mortoniceras* (*Deiradoceras*) *bispinosum* (Spath) (MCNA 13520). I. *Mortoniceras* (*M.*) *rugosum* Spath (NM). J. *Mortoniceras* (*M.*) *arietiforme* Spath (NM). K. *Craginites* sp. (UPV/EHU). L. *Anisoceras* sp. (NM). M. *Mortoniceras* (*M.*) cf. *pachys* (Seeley) (NM). Specimens deposited in the collections of: UPV/EHU, the University of the Basque Country, department of Stratigraphy and Palaeontology, Leioa, Basque Country; MCNA, Museo de Ciencias Naturales de Álava, Gasteiz, Basque Country; NM, Nautilus Museum, Mutriku, Gipuzkoa, Basque Country.

Biozones		Morphotypes (%)	Examples
M. rostratum / *M. fallax*		1- Planorbicone to serpenticone (35) 2- Platycone to serpenticone (30) 3- Ancylocone (25) 4- Discocone (10)	1- *Puzosia* 2- *Mortoniceras* 3- *Anisoceras* 4- *Hypophylloceras*
M. inflatum		1- Spherocone to planorbicone-like (>35) 2- Planorbicone to serpenticone (35) 3- Platycone to serpenticone (<10) 4- Ancylocone (<10) 5- Orthocone (<10)	1- *Desmoceras* 2- *Puzosia* 3- *Mortoniceras* 4- *Hamitoides* 5- *Lechites*
H. varicosum	*H. choffati*	1- Platycone to serpenticone (45) 2- Planorbicone to serpenticone (20) 3- Ancylocone (20) 4- Discocone (5) 5- Hamiticone (5) 6- Spherocone to planorbicone-like (5)	1- *Deiradoceras* 2- *Puzosia* 3- *Idiohamites* 4- *Hypophylloceras* 5- *Hamites* 6- *Pachydesmoceras*
	H. binum	1- Spherocone to planorbicone-like (>25) 2- Planorbicone to serpenticone (>25) 3- Discocone (20) 4- Platycone to serpenticone (15) 5- Ancylocones (<10)	1- *Desmoceras*, *Tetragonites* 2- *Puzosia*, *Kossmatella* 3- *Hypophylloceras* 4- *Parasilesites*, *Hysteroceras* 5- *Labeceras*
	H. orbignyi / *D. cristatum*	1- Planorbicone to serpenticone (>70) 2- Platycone (<10) 3- Platycone to serpenticone (<10) 4- Hamiticone (<10)	1- *Puzosia*, *Kossmatella* 2- *Oxytropidoceras* 3- *Hysteroceras* 4- *Hemiptychoceras*
H. dentatus		1- Platycone to serpenticone (40) 2- Planorbicone to serpenticone (35) 3- Platycone (15) 4- Hamiticone and Ancylocone (10)	1- *Parasilesites*, *Lyelliceras* 2- *Puzosia*, *Kossmatella*, *Dipoloceroides* 3- *Oxytropidoceras* 4- *Hemiptychoceras*, *Protanisoceras*

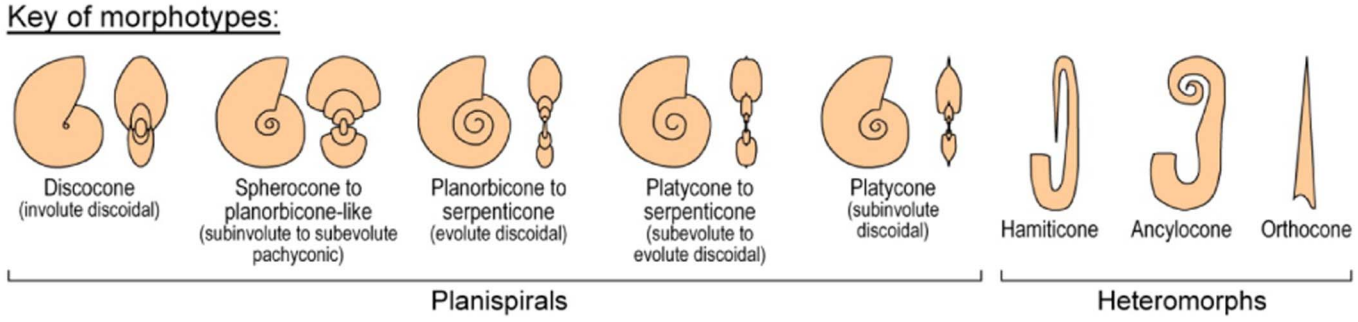

Fig. 6. Ammonoid morphotypes distinguished among studied associations with indication of the relative proportion in a given assemblage and representative examples. Based on the proportion of different morphotypes, associations are distinguished according to their zonal distribution. Morphotypes are illustrated in the lower part of the figure. Morphotypes after Westermann (1996) and Ritterbush and Bottjer (2012), with precisions on the planispiral shape sensu Korn (2010).

Fragments of ammonoids are rarely found in sandy turbidites, usually preserved as internal moulds.

4.2.3. Ammonoid morphology and size

We focus here on the description of the main ammonoids morphologies present in the studied area, their occurrence and variability through time. We follow the terminology of Westermann (1996) with the updates given by Ritterbush and Bottjer (2012) and compare them to the conch terminology of Korn (2010). Accordingly, we present here eight morphological groups or morphotypes, each of them comprising related forms of different taxa, which are representative of life modes in the marine environment. In the Fig. 6 we summarize the distinguished morphotypes and their relative proportion in a given sample according to their zonal scheme. Despite the ammonoid sample is quite good with about 250 specimens distributed in 44 levels, the aim of this work is not to make an accurate analysis of the conch parameters and indeed the morphological variation, but to make a first attempt to present the main ammonoid morphotypes and their occurrences in a stratigraphic and

sedimentological frame.

Ammonite sizes range in diameter from several mm to almost 500 mm, being common up to 100 mm size. Biggest forms occur mainly in the *M. inflatum* to *M. rostratum* Zones interval where they are common. According to the size groups defined by Stevens (1988), these ammonites are of the "large" size-class; however, they really represent oversized (giant) forms if considering the median sizes of their family-level representatives. Concerning the conch ornamentation, we only differentiate planispiral leiostracan elements (such as the genera *Hypophylloceras, Desmoceras and Tetragonites*), planispiral trachyostracan elements (such as the genera *Lyelliceras*, *Mortoniceras* and *Cantabrigites*), and finely ribbed/strongly ribbed heteromorphs (e.g. *Labeceras/Anisoceras*) as a first attempt to differentiate conch sculptures from smooth to finely ribbed and strongly ribbed/tuberculated. In the BCB, we observe that less ornamented forms are common in offshore deeper environments, meanwhile ornamented forms are comparatively more abundant in offshore shallower areas (e.g. López-Horgue et al., 1999, 2009).

4.2.4. Ammonoid bioevents

Bioevents are levels or thin stratigraphic intervals with a distinctive fossil association characterized by exotic elements, striking abundance of a taxon and/or morphological changes (e.g. Wilmsen, 2008); they respond to short-term (up to ~100 kyr) evolutionary, ecologic and/or biogeographic turnovers of organisms due to changing environmental conditions, occurring at local, regional or global scale (Kauffman and Hart, 1996). The relative abundance of the ammonoids in the expanded sediment successions of the northern margin of the BCB, the accuracy of the stratigraphic studies (e.g. Agirrezabala et al., 2002) and the known biogeographical affinities of the ammonoids (López-Horgue et al., 1999, 2009) allow us to distinguish bioevents of the following types: a- evolutive changes, with first and last occurrences at generic level; b- palaeobiogeographical changes, determined by the variations of taxa of different affinities; c- abundance and diversity changes; d- changes in the morphotype composition of the ammonoid associations and in the shell size. These bioevents are shown in Fig. 7 and are the following: 1- sudden basal Middle Albian occurrence of the first ammonoids in the area after the total absence during the Late Aptian and Early Albian; the association is diverse and of Tethyan affinities, but with scarce typical South American and European elements; 2- first occurrences of cosmopolitan *Hysteroceras* sp. and European *Epihoplites* sp. in the Upper Albian *D. cristatum* Zone to *H. orbignyi* Subzone transition, after an interval without sedimentary record of most of the Middle Albian; 3- incursion of the South African *Labeceras* sp. (López-Horgue et al., 2009) during the *H. orbignyi* to *H. binum* subzones transition-time; 4- Tethyan leiostracan elements dominate in a well diversified association of mainly juveniles of the *H. binum* Subzone; 5- incursion of the typical North American *Craginites* sp. during times of the basal *H. choffati* Subzone (López-Horgue et al., 2009); trachyostracan ammonoids (cosmopolitan but essentially Tethyan Mortoniceratinae) dominate with some South African elements; 6- last occurrence of *Hysteroceras* sp.; 7- first occurrence of *Mortoniceras* sp. in the area at around the middle part of the *H. choffati* Subzone; 8- first occurrences of the heteromorphs *Idiohamites* sp. and *Anisoceras* sp. at around the middle part of the *M. inflatum* Zone, together with giant leiostracan forms of Tethyan affinities; 9- abundance of cosmopolitan ammonoids at the upper part of the *M. inflatum* Zone; and 10- giant trachyostracan (cosmopolitan but essentially Tethyan Mortoniceratinae), leiostracan (typically Tethyan Desmoceratidae) and spiny heteromorphs (Anisoceratidae) occur at the base of the *M. fallax* Zone, being the most common forms up to basal *M. rostratum* Zone.

5. Discussion: Albian environmental changes and bioevents

In this chapter we will focus on the integration of mainly ammonoid-based palaeontological data with stratigraphic and sedimentological data from the studied Albian sedimentary record. Fossil preservation and host rock characteristics make the ammonoid associations be considered autochthonous, with null or very low degree of lateral transport (e.g. Fernández-López, 1991). Ammonoids are not considered facies-dependent (e.g. Lukeneder, 2015). Their common occurrence in fine-grained facies in domains without important coarse-grained input, suggest they were inhabitants of offshore (oceanic) waters with an important siliciclastic suspension input. Conch morphology and ontogenetic stages are primary elements to understand interpretations on ammonoid habitat, which together with their palaeobiogeographical affinities and the information obtained from the facies analysis, allow us to make a conceptual model of the environment inhabited by them in the northern margin of the Basque-Cantabrian Basin.

5.1. Margin water depth, width and connectivity

The Albian sequences record an important pulsating deepening and widening of the margin, which coincides with back-faulting pulses occurred at the sequence boundaries (U2–U4). During the Early Albian (sequence 1) the development of deltaic to platform environments indicates coastal to neritic water depths with low bathymetric gradients. At the earliest Early Albian (sequence 2), an important transtensive tectonic pulse faulted the northern margin and created a horst and graben system where shallow-water conditions maintained only on small, isolated uplifted blocks adjacent to deep-sea troughs developed on grabens. The deepening of these syn-tectonic depositional systems suggests that back-faulting widened the margin northeastward. During the Late Albian, after an erosion/non-deposition phase (Middle Albian pro parte), the instauration of an extensive and more distal deep-water environment (sequences 3 and 4) indicates a new deepening and back-faulting pulse. It is also supported by the occurrence in offshore wells of Upper Albian deposits overlying the Landes Palaeozoic massif (NE part in Fig. 3), as well as on other Palaeozoic massifs around the BCB (e.g. Bodego et al., 2015). The proliferation of planktonic microfossils (foraminifers and radiolarian) suggests that the deepening and widening of the margin led to the link with the open ocean (Bay of Biscay). Biofacies data suggest that most of the margin sea floor was located at mesopelagic depths (Castañares et al., 2001; García-Mondéjar et al., 2004). In this deep-water realm, structural ridges constituted hemipelagic palaeohighs, in which the presence of rare zooxanthellate corals and rudist indicates photic conditions and epipelagic water depths (< 200 m).

The sequence 2 yields a diverse association in which sculptured ammonoids (both trachyostracan planispirals and heteromorphs) comprise < 50% of the sample with respect to leiostracan planispirals. This ratio indicates offshore waters (e.g. Westermann, 1996; Kawabe, 2003) compatible with the suggested epipelagic to upper mesopelagic depths after sedimentological data. Despite being a less rich association, ammonoids from the basal sequence 3 (*D. cristatum* and *H. orbignyi* biozones) also suggest a similar offshore environment. The association of the *H. binum* Subzone (sequence 3) is dominated by planispiral leiostracan juveniles, usually pyritized; there are also some inoceramids *Actinoceramus*. These Upper Albian inoceramids occur in variable oxygenated conditions (Crampton and Gale, 2005); their occurrence in the study area in muddy intervals with very scarce bioturbation and pyritic ammonoids may suggest hypoxic bottoms and a likely expansion of the oxygen minimum zone, in contrast to other muddy intervals with more bioturbation and lack of inoceramids and pyritic ammonoids. This interpretation is compatible with relative deeper conditions that can also be suggested by the dominance of leiostracan planispirals. The upper part of the sequence 3 and sequence 4 yield ammonoid associations in which leiostracan represent about 2/3 of the sample. This reflects the persistence of the offshore conditions in the study area.

Sea-water masses of different origin can be mixed due to the opening of seaways after different mechanisms such as tectonics and relative sea-level rises. The admixtures of ammonoids of different

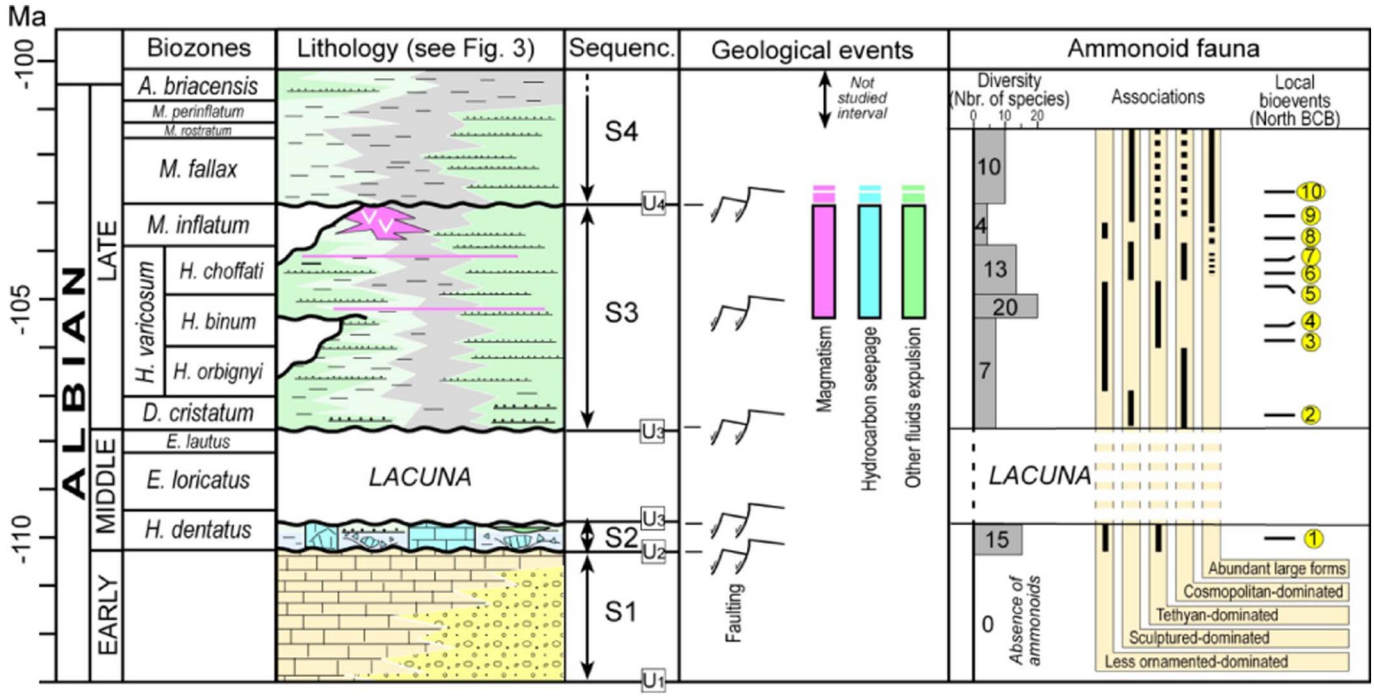

Fig. 7. Characteristics of ammonoid fauna from the northern margin of the BCB and time-correlation to the main geological events that controlled environmental conditions and basin development. Ammonoid biostratigraphy and other ammonoid occurrences as in López-Horgue et al., 2009. Other sources: Agirrezabala et al., 2013; Rat, 1959; Gómez de Llarena, 1958; Reitner, 1987; Pletsch, 1990. U: Sequence-bounding unconformities. Circled numbers refer to main local bioevents and related steps of ammonoid turnover: 1- sudden occurrence of ammonoids (of the L. *Lyelli* Subzone) considered as the FO (first occurrence) for Albian ammonoids in the Northern margin of the Basque Cantabrian Basin; mainly a Tethyan association with cosmopolitan elements, western Tethys elements (*Lyelliceras* gr. *peruvianum*) and one specimen typical of the European province (*Cleoniceras* cf. *devisense*). 2- FO of *Hysteroceras* sp. and incursion of European *Epihoplites* sp. 3- Incursion of South African *Labeceras* sp. 4- Abundance of Tethyan elements and FO of *Desmoceras latidorsatum*. 5- Incursion of North American *Craginites* sp. 6- LO (last occurrence) of *Hysteroceras* sp. 7- FO of *Mortoniceras* sp. 8- FO of *Anisoceras* sp. and *Idiohamites* sp. 9- Abundance of cosmopolitan elements. 10- Onset of abundant cosmopolitan and Tethyan large elements.

biogeographical affinities or the punctuated introduction of species typical of other areas are evidences of sea connections (e.g. Lehmann et al., 2015). The studied area is dominated by Tethyan and cosmopolitan elements with punctuated incursions of exotic elements (as also indicated in the southern BCB; López-Horgue et al., 1999). Middle Albian is typically Tethyan but with elements from South America and Europe, indicative of a net connection of the basin after an important faulting phase. The margin preserved its connectivity for the entire Late Albian with punctuated incursions of ammonoids from other regions, mostly associated with tectonic pulses (Fig. 7): 1- north European elements during the early Late Albian; and 2- typical South African (e.g. Fig. 5 G) and North American (e.g. Fig. 5 K) elements, also coinciding with the onset of magmatism and seepage of hydrocarbons and other fluids in the margin.

5.2. Sea water column and sediment characteristics

The Early Albian shallow submarine environment (sequence 1) was subject to extensive reworking by waves and currents and was well oxygenated (García-Mondéjar, 1990). In Middle to Late Albian times (sequences 2–4) the deposition of deep-water black to dark gray lutites rich in organic matter, framboidal pyrite and siderite concretions indicate a muddy dysoxic sea floor (Potter et al., 2005). Here, aerobic oxidation of the organic matter caused depletion of oxygen in the shallowest sediments. At some greater burial depth (several centimetres) organic matter was oxidized in suboxic conditions by bacteria-mediated iron reduction, leading formation of early diagenetic pyrite and siderite (Gil et al., 1986). The quiet sedimentation of mud in the deep-sea was punctuated by gravity-driven flows of different concentrations, increasing temporary the energy, turbidity and oxygenation of the bottom waters.

Ammonoid morphotypes from the study area are indicative of a demersal to planktic lifestyle in an offshore environment (e.g. Westermann, 1996; Ritterbush and Bottjer, 2012). The occurrence of demersal morphotypes (e.g. brancoceratids such as *Mortoniceras* sp.) is indicative of an oxygenated water column, since these forms do not survive in hypoxic conditions (e.g. Batt, 1993). Actually, these demersal forms are scarce or absent in the intervals with pyritized juveniles (e.g. *H. binum* Subzone), suggesting that oxygenated waters were only in the upper water column. Both planktic vertical migrants, such as *Hypophylloceras* sp. and *Jauberticeras* sp., and planktic drifters, such as *Desmoceras* sp., *Tetragonites* sp. and probably *Puzosia* sp., are abundant throughout the Upper Albian succession. Ammonoids are suggested to be of high metabolism (Lukeneder, 2015) and so they needed oxygenated waters. However, there are examples of associations of small heteromorphs in hypoxic facies (e.g. Lukeneder, 2007) which are interpreted to have been adapted to oxygen-deficient conditions for short time for preying or migrations; this scenario might be also suggested, although with cautions, for the abundant juveniles and small adults of the *H. binum* Subzone.

5.3. Magmatism, geofluids emissions and trophic level

During the early Late Albian (sequence 3, *H. binum* Subzone-*M. inflatum* Zone) magmatic activity led formation of high-level magmatic intrusions and submarine deposition of extrusive (effusive and explosive) rocks. Hydrothermal and submarine alteration of these magmatic rocks may have provided a larger-than-normal iron flux to the sea water. Many evidences link iron fertilization from volcanic eruptions to increases of primary productivity and fish abundance (Cather et al., 2009; Langmann et al., 2010). In the case of the northern margin of the BCB, the relatively abundance of altered magmatic rocks suggest that they may have constituted a significant iron source which could promote fertilization of the Albian sea waters.

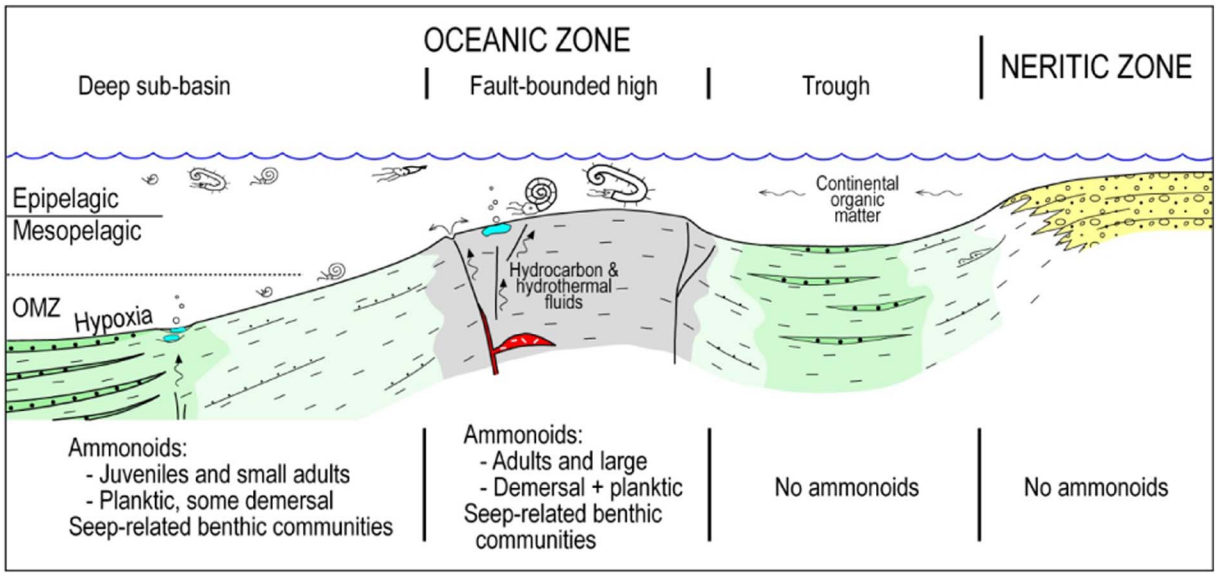

Fig. 8. Conceptual model of the different ammonoid habitats for the Late Albian of the northern margin of the BCB based on the integration of sedimentological and palaeontological data. Both groups of data suggest epipelagic to upper mesopelagic depths in an oceanic zone with distinct shallow areas on uplifted tectonic blocks surrounded by deeper sub-basins. Deeper areas were prone to develop hypoxia in the lower waters. Continent-derived organic matter and seepage of hydrocarbons and other hydrothermal fluids were the main nutrient sources. OMZ: oxygen minimum zone.

The formation of authigenic carbonates during the early Late Albian (sequence 3, *H. binum* Subzone-*M. inflatum* Zone) records the expulsion to the northern margin palaeoseabed of thermogenic methane, oil and CO_2 formed by contact metamorphism around magmatic intrusions (Agirrezabala et al., 2008, 2013, 2014; Agirrezabala, 2009, 2015). In these seeps, expelled hydrocarbons were anaerobically oxidized by microbial communities at or just below the seabed, promoting the precipitation of carbonate and constituting chemosynthetic oases in the largely deserted deep seabed (Agirrezabala, 2009; Agirrezabala et al., 2013). Here bacteria and archea flourished and abundant chemosymbiotic megafauna inhabited the seabed, leading to an important biomass increment. This biomass may have constituted a food source which attracted non-obligate diverse megafauna species, finally contributing to an increase in the biomass. Moreover, seep carbonate formation at or near the seabed created local hardground substrates which could have been attractive to attached species, fishes and other megafauna (Judd and Hovland, 2007). The likely escape to the sea of hydrocarbons in the northern margin of the BCB could have also caused a fertilizing effect on the water column with an increase in the total nutrients and primary production, as invoked for present-day highly productive seas (Hovland et al., 2012; and references therein).

The relatively abundant organic matter of terrestrial origin throughout the studied succession suggests that the water-column was rich in continent-derived nutrients. Late Albian ammonoid associations changed due to variations in the primary production in the water column inferred from the study of calcareous nannofossils (SE France, Tethyan; Reboulet et al., 2005), recording changes from mesotrophic to oligotrophic conditions in the surface waters. *Anisoceras* sp. from offshore epipelagic habitats is suggested to be dominant, together with other heteromorphs, during mesotrophic conditions and more competitive than planispirals during oligotrophic conditions in surface waters; planispiral *Mortoniceras* sp. was suggested to inhabit the lower epipelagic zone with a demersal mode of life (Reboulet et al., 2005). Both morphotypes are common in the study area, being forms representative of planktic and demersal feeders in an area with fertilization in both deep and surficial waters.

5.4. Conceptual model on ammonoid habitats

Accordingly to the discussed environmental characteristics, ammonoids in the study area thrived in good conditions for most of the Late Albian: warm temperatures, enough nutrients, epipelagic to upper mesopelagic depths in oceanic waters (Fig. 8). Frequent incursions of other Tethyan elements and only one typical European specimen suggest no substantial changes in the water temperature. In this scenario, marine areas above shallower uplifted tectonic blocks in the study area show examples of large ammonoids. Temperature and nutrient availability may have triggered growth and maturity (Reboulet, 2001; Lukeneder, 2015). Size variations along a depth gradient, with larger forms in shallow waters, have been studied in the Early Cretaceous of South France (e.g. Reboulet, 1996); besides, dwarfed forms have been interpreted as size dependency on higher hydrostatic pressure (Reboulet, 2001). Isotopic studies in Cretaceous ammonoid conchs show an ontogenetic change of habitat, with early and adult stages inhabiting deeper and shallow areas respectively (e.g. Lukeneder et al., 2010), in accordance with previous studies suggesting a sexual and age separation in many ammonoid taxa (Kennedy and Cobban, 1976).

6. Conclusions

Albian ammonoids from the northern margin of the BCB provide a biostratigraphic framework for the sedimentary succession of the whole margin and allow us to distinguish 10 bioevents of three types: evolutionary changes, palaeobiogeographical changes, and abundance and diversity changes. The integration of ammonoid-based palaeontological data with stratigraphy and sedimentology data from the studied Albian sedimentary rocks indicates that bioevents are coeval to environmental and sedimentary changes. Time-correlation of faulting pulses with ammonoid bioevents indicates that Albian transtensive tectonics was ultimately the major control of the marine environmental changes. Transtensive tectonics triggered changes in the water depth, sea bottom physiography, seaways, sedimentary systems and sea-water chemistry. Accordingly, this two-fold study is the base for a conceptual model of the ammonoid habitats, in which adult and large forms dominated in fault-bounded epipelagic highs and juvenile and small ammonoids in deeper mesopelagic sub-basins.

Acknowledgements

We especially thank Jesús María Narvaez and his wife Esperanza Azkarraga for their essential contribution to the collection, preparation and preservation of the large ammonoids of the Mutriku area, now deposited in the Nautilus Museum. We thank two anonymous reviewers for their constructive comments. Financial support was substantially provided by the Euskal Kostako Geoparkea (GEOGARAPEN 2015-16). LMA acknowledges financial support from the Eusko Jaurlaritza (Ikerketa Taldeak IT631-13 and IT930-16). MAL-H research has been supported partially by the Eusko Jaurlaritza (projects IT834-13 and IT1044-16).

References

Agirrezabala, L.M., 1996. Estratigrafía y Sedimentología del Aptiense-Albiense del Anticlinorio Nor-Vizcaíno entre Gernika y Azpeitia. (Ph. D. Dissertation) Euskal Herriko Unibertsitatea (429 pp.).

Agirrezabala, L.M., 2009. Mid-cretaceous hydrothermal vents and authigenic carbonates in a transform margin, Basque-Cantabrian Basin (western Pyrenees): a multidisciplinary study. Sedimentology 56, 969–996. http://dx.doi.org/10.1111/j.1365-3091.2008.01013.x.

Agirrezabala, L.M., 2015. Syndepositional forced folding and related fluid plumbing above a magmatic laccolith: insights from outcrop (Lower Cretaceous, Basque-Cantabrian Basin, western Pyrenees). Geol. Soc. Am. Bull. 127, 982–1000.

Agirrezabala, L.M., Dinarès-Turell, J., 2013. Albian syndepositional block rotation and its geological consequences, Basque-Cantabrian Basin (western Pyrenees). Geol. Mag. 150, 986–1001. http://dx.doi.org/10.1017/S0016756813000149.

Agirrezabala, L.M., García-Mondéjar, J., 1989. Evolución tectosedimentaria de la plataforma urgoniana entre Cabo Ogoño e Itziar durante el Albiense inferior y medio (Región Vasco-Cantábrica nor-oriental). Simposio del XII Congreso Español de Sedimentología. Leioa 11-20.

Agirrezabala, L.M., García-Mondéjar, J., 1994. A coarse-grained turbidite system with morphotectonic control (Middle Albian, Ondarroa, North Iberia). Sedimentology 41, 383–407.

Agirrezabala, L.M., García-Mondéjar, J., 2001. Deep-water fallout tephra deposits in the Black Flysch of Deba (Upper Albian, Basque-Cantabrian Basin). Geotemas 3, 123–126.

Agirrezabala, L.M., Martinez, R., García-Mondéjar, J., 1992. Fauna de Ammonites del tránsito Complejo Urgoniano-Flysch Negro entre Gernika y Deba (Albiense medio y superior, región Vascocantábrica Septentrional). Treballs del Museu de Geologia de Barcelona 2, 143–169.

Agirrezabala, L.M., Owen, H.G., García-Mondéjar, J., 2002. Syntectonic deposits and punctuated limb rotation in an Albian submarine transpressional fold (Mutriku village, Basque-Cantabrian basin, northern Spain). Geol. Soc. Am. Bull. 114, 281–297.

Agirrezabala, L.M., Dorronsoro, C., Permanyer, A., 2008. Geochemical correlation of pyrobitumen fills with host mid-Cretaceous Black Flysch Group (Basque-Cantabrian Basin, western Pyrenees). Org. Geochem. 39, 1185–1188. http://dx.doi.org/10.1016/j.orggeochem.2008.03.012.

Agirrezabala, L.M., Kiel, S., Blumenberg, M., Schäfer, N., Reitner, J., 2013. Outcrop analogues of pockmarks and associated methane-seep carbonates: a case study from the Lower Cretaceous (Albian) of the Basque-Cantabrian Basin, western Pyrenees. Palaeogeogr. Palaeoclimatol. Palaeoecol. 390, 94–115. http://dx.doi.org/10.1016/j.palaeo.2012.11.020.

Agirrezabala, L.M., Permanyer, A., Suárez-Ruiz, I., Dorronsoro, C., 2014. Contact metamorphism of organic-rich mudstones and carbon release around a magmatic sill in the Basque-Cantabrian Basin, western Pyrenees. Org. Geochem. 69, 26–35.

Batt, R., 1993. Ammonite morphotypes as indicators of oxygenation in a Cretaceous epicontinental sea. Lethaia 26, 49–63.

Bodego, A., Iriarte, E., Agirrezabala, L.M., García-Mondéjar, J., López-Horgue, M.A., 2015. Synextensional mid-Cretaceous stratigraphic architecture of the eastern Basque-Cantabrian basin margin (western Pyrenees). Cretac. Res. 55, 229–261.

Brunet, M.F., 1994. Subsidence in the Parentis Basin (Aquitaine, France): implications of the thermal evolution. In: Mascle, A. (Ed.), Hydrocarbon and Petroleum Geology of France: Special Publication of the European Association of Petroleum Geoscientists. Vol. 4. pp. 187–198.

Castañares, L.M., Robles, S., Gimeno, D., Vicente-Bravo, J.C., 2001. The submarine volcanic system of the Errigoiti formation (Albian–Santonian of the Basque-Cantabrian Basin, northern Spain): stratigraphic framework, facies and sequences. J. Sediment. Res. 71, 318–333.

Cather, S.M., Dunbar, N.W., McDowell, F.W., McIntosh, W.C., Scholle, P.A., 2009. Climate forcing by iron fertilization from repeated ignimbrite eruptions: the icehouse-silicic large igneous province (SLIP) hypothesis. Geosphere 5, 315–324.

Crampton, J.S., Gale, A.S., 2005. A plastic boomerang: speciation and intraspecific evolution in the Cretaceous bivalve *Actinoceramus*. Paleobiology 31, 559–577.

Dercourt, J., Gaetani, M., Vrielynk, B. (Eds.), 2000. Atlas Peri-Tethys, Palaeogeographical Maps. CCGM/CGMW, Paris.

Fernández-López, S., 1991. Taphonomic concepts for a theoretical biochronology. Revista Española de Paleontología 6, 37–49.

Gale, A.S., Bown, P., Caron, M., Crampton, J., Crowhurst, S.J., Kennedy, W.J., Petrizzo, M.R., Wray, D.S., 2011. The uppermost Middle and Upper Albian succession at the col de Palluel, Hautes-Alpes, France: an integrated study (ammonites, inoceramid bivalves, planktonic foraminifera, nannofossils, geochemistry, stable oxygen and carbon isotopes, cyclostratigraphy). Cretac. Res. 32, 59–130.

García-Mondéjar, J., 1990. The Aptian-Albian carbonate episode of the Basque-Cantabrian Basin (northern Spain): general characteristics, controls and evolution. Special Publication of the International Association of Sedimentologists 9, 257–290.

García-Mondéjar, J., Agirrezabala, L.M., Aranburu, A., Fernández-Mendiola, P.A., Gómez-Pérez, I., López-Horgue, M., Rosales, I., 1996. The Aptian-Albian tectonic pattern of the Basque-Cantabrian Basin (Northern Spain). Geol. J. 31, 13–45.

García-Mondéjar, J., Fernández-Mendiola, P.A., Agirrezabala, L.M., Aranburu, A., López-Horgue, M.A., Iriarte, E., Martínez de Rituerto, S., 2004. El Aptiense-Albiense de la Cuenca Vasco-Cantábrica. In: Vera, J.A. (Ed.), Geología de España. SGE-IGME, Madrid, pp. 291–296.

Gil, P.P., Yusta, I., Herrero, J.M., Velasco, F., 1986. Mineralogía y geoquímica de las concreciones carbonatadas del Flysch Negro (Albiense Sup.-Cenomaniense Inf.) de Arminza (Vizcaya). Boletin Sociedad Española Mineralogia 9, 347–356.

Gómez de Llarena, J., 1958. Datos paleontológicos del Flysch litoral de Guipuzcoa: El Vraconiense de septarias de Motrico. Notas y Comunicaciones del Instituto Geológico y Minero España 50, 5–20.

Hovland, M., Jensen, S., Fichler, C., 2012. Methane and minor oil macro-seep systems — their complexity and environments significance. Mar. Geol. 332-334, 163–173.

Jammes, S., Manatschal, G., Lavier, L., Masini, E., 2009. Tectonosedimentary evolution related to extreme crustal thinning ahead of a propagating ocean: example of the western Pyrenees. Tectonics 28, TC4012. http://dx.doi.org/10.1029/2008TC2406.

Judd, A., Hovland, M., 2007. Seabed Fluid Flow: The Impact on Geology, Biology and the Marine Environment. Cambridge University Press, Cambridge (475 pp.).

Kauffman, E.G., Hart, M.B., 1996. Cretaceous bio-events. In: Walliser, H. (Ed.), Global Events and Event Stratigraphy in the Phanerozoic. Springer Verlag, Berlin, Heidelberg, New York, pp. 285–312.

Kawabe, F., 2003. Relationship between mid-Cretaceous (upper Albian-Cenomanian) ammonoid facies and lithofacies in the Yezo forearc basin, Hokkaido, Japan. Cretac. Res. 24, 751–763.

Kennedy, W.J., Cobban, W.A., 1976. Aspects of ammonite biology, biogeography and biostratigraphy. Spec. Pap. Palaeontol. 17, 1–94.

Korn, D., 2010. A key for the description of Palaeozoic ammonoids. Fossil Record 13, 5–12.

Langmann, B., Zaksek, K., Hort, M., Duggen, S., 2010. Volcanic ash as fertiliser for the surface ocean. Atmos. Chem. Phys. 10, 3891–3899.

Lehmann, J., Ifrim, C., Bulot, L., Frau, C., 2015. Paleobiogeography of Early Cretaceous Ammonoids. In: Klug, C. (Ed.), Ammonoid Paleobiology: From Macroevolution to Paleogeography. Topics in Geobiology Vol. 44. pp. 229–257.

López-Horgue, M. A. and Bodego, A., 2012, Ar-Ar and Biostratigraphical Dating of Volcanism-related Hydrothermalism: Implications for Fluid-flow During the Mid-Cretaceous Extensional Episode in the Basque-Cantabrian Basin. Geofluids VII Meeting, Paris, Abstract book, 209-211.

López-Horgue, M.A., Owen, H.G., Rodríguez-Lázaro, J., Orue-Etxebarria, X., Fernández-Mendiola, P.A., García-Mondéjar, J., 1999. Late Albian-Early Cenomanian stratigraphic succession near Estella-Lizarra (Navarra, central northern Spain) and its regional and interregional correlation. Cretac. Res. 20, 369–402.

López-Horgue, M.A., Owen, H.G., Aranburu, A., Fernandez-Mendiola, P.A., García-Mondéjar, J., 2009. Early Late Albian (Cretaceous) of the central region of the Basque-Cantabrian Basin, northern Spain: biostratigraphy based on ammonites and orbitolinids. Cretac. Res. 30, 385–400. http://dx.doi.org/10.1016/j.cretres.2008.08.001.

Lukeneder, A., 2007. Cephalopod evolution: a new perspective-implications from two Early Cretaceous ammonoid suborders (Northern Calcareous Alps, Upper Austria). Denisia 20, 395–404.

Lukeneder, A., 2015. Ammonoid habitats and life history. In: Klug, C. (Ed.), Ammonoid Paleobiology: From Anatomy to Ecology. Topics in Geobiology Vol. 43. pp. 689–791.

Lukeneder, A., Harzhauser, M., Müllegger, S., Piller, W.E., 2010. Ontogeny and habitat change in Mesozoic cephalopods revealed by stable isotopes ($\delta^{18}O$, $\delta^{13}C$). Earth Planet. Sci. Lett. 296, 103–114.

Montadert, L., Winnock, E., Delteil, J.R., Grau, G., 1974. Continental margins of Galicia-Portugal and Bay of Biscay. In: Burk, C.A., Drake, C.L. (Eds.), Geology of Continental Margins. Springer-Verlag, Berlin, pp. 223–342.

Owen, H.G., 1999. Correlation of Albian European and Tethyan ammonite zonations and the boundaries of the Albian stage and substages: some comments. Scripta Geologica, Special Issue 3, 129–149.

Owen, H.G., Mutterlose, J., 2006. Late Albian ammonites from off-shore Suriname — implications for biostratigraphy and palaeobiogeography. Cretac. Res. 27, 717–727.

Pletsch, T., 1990. Kartierung, Sedimentologie und Stratigraphie im “Schwarzen Flysch von Deva” bei Saturraran, Prov. Bizkaia/Gipuzkoa, N-Spanien. (M. Sc. Thesis) University of Tübingen, Germany (103 pp.).

Poprawski, Y., Basile, C., Agirrezabala, L.M., Jaillard, E., Gaudin, M., Jacquin, T., 2014. Sedimentary and structural record of the Albian growth of the Bakio diapir (the Basque Country, northern Spain). Basin Res. 26, 746–766.

Potter, P.E., Maynard, J.B., Depetris, P.J., 2005. Mud and Mudstones: Introduction and Overview. Heidelberg, New York, Springer, Berlin (297 pp.).

Rat, P., 1959. Les pays crétacés basco-cantabriques (Espagne). (Thése) 18 Publ. Univ. Dijon (525 pp.).

Rat, P., 1988. The Basque-Cantabrian basin between the Iberian and European plates: some facts but still many problems. Rev. Soc. Geol. Esp. 1, 327–348.

Reboulet, S., 1996. L'evolution des ammonites du Valanginien-Hauterivien inférieur du bassin vocontien et de la plate-forme provençale (Sud-Est de la France): relations avec la stratigraphie séquentielle et implications bioestratigraphique. Doc. Labor.

Géol. Lyon 137, 371.
Reboulet, S., 2001. Limiting factors on shell growth, mode of life and segregation of Valanginian ammonoid populations: evidence from adult-size variations. Géobios 34, 423–435.
Reboulet, S., Giraud, F., Proux, O., 2005. Ammonoid abundance variations related to changes in trophic conditions across the oceanic anoxic event 1d (latest Albian, SE France). PALAIOS 20, 121–141.
Reboulet, S., Szives, O., Aguirre-Urreta, B., Barragán, R., Company, M., Idakieva, V., Ivanov, M., Kakabadze, M.V., Moreno-Bedmar, J.A., Sandoval, J., Baraboshkin, E.J., Çaglar, M.K., Özy, I., González-Arreola, C., Kenjo, S., Lukeneder, A., Raisossadat, S.N., Rawson, P.F., Tavera, J.M., 2014. Report on the 5th International Meeting of the IUGS Lower Cretaceous Ammonite Working Group, the Kilian Group (Ankara, Turkey, 31st August 2013). Cretac. Res. 50, 126–137.
Reitner, J., 1987. Mikrofazielle, palökologische und paläogeographische Analyse ausgewählter Vorkommen flachmariner Karbonate im Basko-Kantabrischen Strike-Slip Fault Becken System (Nord-spanien) an der Wenden von der Unterkreide zur Oberkreide. Documenta Naturae 40, 1–239.
Ritterbush, K.A., Bottjer, D.J., 2012. Westermann morphospace displays ammonoid shell shape and hypothetical paleoecology. Paleobiology 38, 424–446.
Robles, S., Pujalte, V., García-Mondéjar, J., 1988. Evolución de los sistemas sedimentarios del margen continental cantábrico durante el Albiense y Cenomaniense, en la transversal del litoral vizcaíno. Rev. Soc. Geol. Esp. 1, 409–441.
Stevens, G.R., 1988. Giant ammonites: a review. In: Wiedmann, J., Kullmann, J. (Eds.), Cephalopods — Present and Past, pp. 141–166.
Van der Voo, R., 1969. Paleomagnetic evidence for the rotation of the Iberian peninsula. Tectonophysics 7 (5-1).
Vergés, J., García-Senz, J.M., Ziegler, P.A., Cavazza, W., Robertson, A.H.F., Crasquin-Soleau, S., 2001. Mesozoic evolution and Cenozoic inversion of the pyrenean rift. In: Peri-Tethys Memoir 6: Pery-Tethyan Rift/Wrench Basins and Passive Margins. 186. Mémoires Muséum National d'Histore Naturelle, Paris, pp. 187–212.
Westermann, G.E.G., 1996. Ammonoid life and habitat. In: Landman, N.H., Tanabe, K., Davies, R.A. (Eds.), Ammonoid Paleobiology. Plenum, New York, pp. 607–707.
Wiedmann, J., Boess, J., 1984. Ammonitenfunde aus der Biskaya-Synkline (Nordspanien) - Kreidegliederung und Alter des Kreide-Vulkanismus. Eclogae Geol. Helv. 77, 483–510.
Wiedmann, J., Owen, H.G., 2001. Late Albian ammonite biostratigraphy of the Kirchrode I borehole, Hannover, Germany. Palaeogeogr. Palaeoclimatol. Palaeoecol. 174, 161–180.
Wilmsen, M., 2008. An Early Cenomanian (Late Cretaceous) maximum flooding bioevent in NW Europe: correlation, sedimentology and biofacies. Palaeogeogr. Palaeoclimatol. Palaeoecol. 258, 317–333.